Spring 1-1-2012

Stratigraphic architecture and connectivity of a low net-to-gross fluvial system: Combining outcrop analogs and multiple-point geostatistical modeling, lower Williams Fork Formation, Piceance Basin, Colorado

Jayne Alexandra Sloan
University of Colorado at Boulder, ali@sloanmail.com

STRATIGRAPHIC ARCHITECTURE AND CONNECTIVITY OF A LOW NET-TO-GROSS FLUVIAL SYSTEM: COMBINING OUTCROP ANALOGS AND MULTIPLE-POINT GEOSTATISTICAL MODELING, LOWER WILLIAMS FORK FORMATION, PICEANCE BASIN, COLORADO

by

JAYNE ALEXANDRA SLOAN

B.A., The College of Wooster, 2009

A thesis submitted to the

Faculty of the Graduate School of the

University of Colorado in partial fulfillment

Of the requirement for the degree of

Master of Science

Department of Geological Sciences

2012

This thesis entitled:

Stratigraphic architecture and three-dimensional connectivity of a low net-to-gross fluvial system: Combining outcrop analogs and multiple-point geostatistical modeling (MPS), lower Williams Fork Formation, Piceance Basin, Colorado

written by Jayne Alexandra Sloan

has been approved for the Department of Geological Sciences

_____

Matthew J. Pranter

_____

Rex D. Cole

_____

Hai-Zui Meng

Date _____

The final copy of this thesis has been examined by the signatories, and we find that both the content and the form meet acceptable standards of scholarly work in the above mentioned discipline.

ABSTRACT

Sloan, Jayne Alexandra (M.S. Geology [Department of Geological Sciences])

Stratigraphic architecture and connectivity of a low net-to-gross fluvial system: Combining outcrop analogs and multiple-point geostatistical modeling, lower Williams Fork Formation, Piceance Basin, Colorado.

Thesis directed by Associate Professor Matthew J. Pranter

Fluvial deposits of the lower Williams Fork Formation (Mesaverde Group; Upper Cretaceous) form the main reservoirs at Grand Valley Field in the Piceance Basin of Colorado. In the eight-section study area, the lower Williams Fork Formation consists of approximately 1,500 ft (457 m) of mudstone with numerous isolated-to-amalgamated, lenticular-to-channel-form sandstone deposited by meandering river systems within a coastal-plain setting. Given the uncertainty in the geometry and distribution of the fluvial reservoirs, this study addresses the field-scale architecture and distribution of the fluvial deposits by combining outcrop-analog data with 3-D reservoir modeling using multipoint statistical simulation (MPS).

Log data from 328 wells and core data from 10 wells were described to determine key facies (N=12), facies associations, and architectural elements (point bar, crevasse splay, coal, floodplain). These observations and interpretations were compared to existing outcrop data and observations to evaluate stratigraphic variability within the area.

Core-to-log comparison was used to develop criteria to calculate lithology logs and interpret architectural elements from conventional well logs. Both point bars and

crevasse splays form reservoir-quality sandstones. The range in thickness for point bars is 2-30 ft (0.6-9.0 m) with an average of 5.4 ft (1.6 m). Crevasse splays range in thickness from 0.5-20 ft (<0.2-6.1 m) with an average of 1.7 ft (0.5 m). For comparison, dimensional data from outcrops located approximately 20 mi (32 km) to the southwest show that point bars (N=116) range in thickness from 3.9-29.9 ft (1.2-9.1 m) and from 44.1-1699.8 ft (13.4-518.1 m) in apparent width, and crevasse splays (N=279) range in thickness from 0.5-15.0 ft (0.2-4.6 m) and from 40.1-843.3 ft (12.2-257.0 m) in apparent width.

Three-dimensional reservoir modeling was used to investigate three different scenarios, representing different spatial distributions of the fluvial deposits. A nested modeling approach was used to model sinuous channels that represent a “string-of-beads” pattern for comparison to individual, and partially disconnected point bars and crevasse splays that form isolated-to-amalgamated sandstones. Within modeled meander belts, MPS was used to model the detailed distribution of fluvial deposits to capture the inferred spatial patterns of the fluvial reservoirs. The differences between the scenarios were explored in terms of static and dynamic connectivity and dynamic fluid-flow simulation to address the potential impact on reservoir performance.

Dedication

I would like to dedicate this thesis to my husband Justin, and my parents, Rich and Josie, for their encouragement, guidance, and support throughout this process.

Acknowledgements

I would like to thank numerous people who have assisted in this research throughout the last two years. Most importantly, I would like to thank and acknowledge my adviser, Dr. Matthew Pranter, for his guidance, knowledge, and encouragement throughout this process. Next, I would like to thank my committee members and supporting faculty: Dr. Rex Cole, of Colorado Mesa University, and Dr. Hai-Zui Meng, of iReseroivr.com, Inc. I would like to thank the following professionals for their input and guidance throughout the duration of this project: Dr. Gus Gustason, EnerPlus, Jon Cantwell, Williams, Art Rawley, Williams, Steve Sturm, Schlumberger, and the United States Geological Survey (USGS) for providing core that was described. I would like to especially thank Williams for the contribution of v-clay and coal flag logs, and stratigraphic horizon tops.

This work would not have been possible without financial and technical support through the Reservoir Characterization and Modeling Laboratory (RCML) within the Energy and Minerals Applied Research Center (EMARC) of the Geological Sciences Department at the University of Colorado at Boulder. The following sponsors of the Williams Fork consortium - Phase V are also to thank for their financial and educational contributions: Williams Petroleum, iReservoir.com, Inc., Anadarko Petroleum Corporation, Marathon Oil Company, Bill Barrett Corporation, Newfield Energy, Chevron Corporation, Occidental Petroleum Corporation (Oxy), ConocoPhillips, ExxonMobil, Suncor Energy, and Schlumberger

Kim Hlava, Ericka Harper, Chris Rybowiak, Whitney Mathias, and Patrick Boulas are to thank for their time and efforts over the past two years in discussion, course work, and research collaboration. These results could not have been completed without the help of two outstanding undergraduate students at the University of Colorado at Boulder: Sara Heinle and Katerine Anarde.

Finally, I would like to acknowledge the loving support of my family for their never-ending support and care, with the most credit goes to my husband, Justin Sloan, for always believing in me and providing encouraging words throughout the past two years. I could not have done this without any of you.

CONTENTS

LIST OF TABLES

LIST OF FIGURES

CHAPTER ONE

INTRODUCTION

The Piceance Basin, located in northwestern Colorado, produces mainly natural gas from low-permeability (tight) sandstone reservoirs. The majority of production comes from the Williams Fork Formation of the Mesaverde Group. Mesaverde outcrops and producing gas fields within the basin are shown in Figure 1. The Williams Fork Formation is Late Cretaceous in age and predominately composed of meandering-to-braided fluvial deposits, with coastal-plain and shallow-marine deposits present in the southeastern portion of the basin.

Connectivity of sandstone-body deposits in the Williams Fork Formation has previously focused on the reservoir scale because reservoir quality sandstones are discontinuous and difficult to correlate in the sub-surface (Pranter et al., 2011; Pranter and Sommer, 2011). Because of the variable but commonly low connectivity of sandstone bodies, wells are drilled using a 10-ac [4-hectare; 430,600 ft^2 (40,468 m^2)] spacing.

Static connectivity of sandstone bodies tends to be underestimated in two dimensions (Pringle et al., 2004) and therefore 3-D modeling must be carried out to accurately assess these deposits in the sub surface or outcrop. Static connectivity is defined in this study as “a percentage that is calculated as the volume of sandstone bodies connected to a particular pattern of wells (directly or indirectly) divided by the total sandstone volume” (Pranter et al., 2011; pg. 3). Within the Williams Fork Formation, porosity and permeability values are low (6-18%, 0.1-2 microdarcies, respectively) and therefore sandstone reservoirs have the potential to be connected

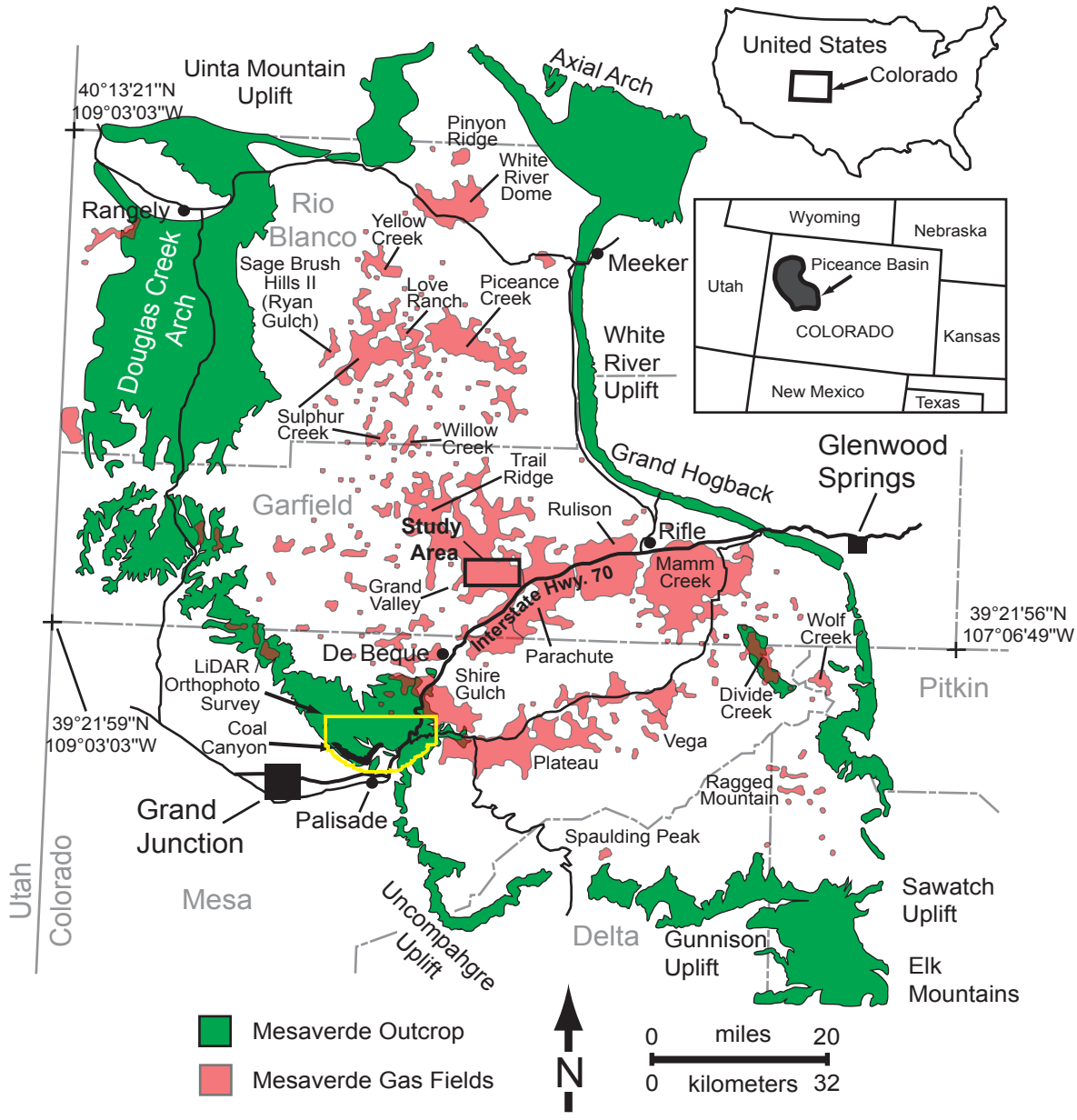

Figure 1: Map showing the extent of Mesaverde Group outcrops (green) and major gas fields (red) of the Piceance Basin. The study area at Grand Valley Field is highlighted by a black box. The location of previously collected outcrop dimensional statistics used in this study is Coal Canyon. Aerial LiDAR orthophoto survey is highlighted by a yellow polygon (Panjaitan, 2006; Pranter et al., 2009). Modified from Johnson (1989), Tyler and McMurry (1995), Hoak and Klawitter (1995), and Pranter et al. (2009).

statically but not dynamically in terms of fluid-flow (Pranter et al., 2011). Dynamic connectivity is evaluated based on the assumption that sandstone bodies can interact with others statically, but porosity and permeability values may prohibit the flow of hydrocarbons between the interacting sandstones. Sandstone bodies with minimal surface-area interaction are identified as statically connected, but might not be connected dynamically. Dynamic fluid-flow simulation is necessary to evaluate how fluids travel between sandstone bodies.

By using 3-D subsurface modeling of sandstone-body deposits a quantitative assessment of connectivity statically and dynamically can assist in creating accurate assessments of sandstone-body distribution, amalgamation, and connectivity.

This study addresses the stratigraphic architecture and 3-D connectivity of sandstone bodies of the lower Williams Fork Formation at Grand Valley Field (Figure 2 and 3) to answer three research questions: (1) What are the key facies, facies associations, and architectural elements and how are these expressed by well logs? (2) How do fluvial-sandstone deposits and the net-to-gross ratio vary spatially? (3) How do different interpretations of sandstone-body geometries and the presence of mudstone-plug deposits impact static and dynamic connectivity, original gas-in-place (OGIP), and long-term field recovery?

Grand Valley Field is located in the south-central Piceance Basin approximately 1 mi (1.6 km) north west of Parachute, Colorado (Figures 1 and 4). Outcrops of the lower Williams Fork Formation have been researched extensively and are located approximately 22 mi (35.4 km) southwest (Figure 1) of Grand Valley Field. The study area at Grand Valley Field covers 8 mi^2 (20.7 km^2; Figures 4 and 5)

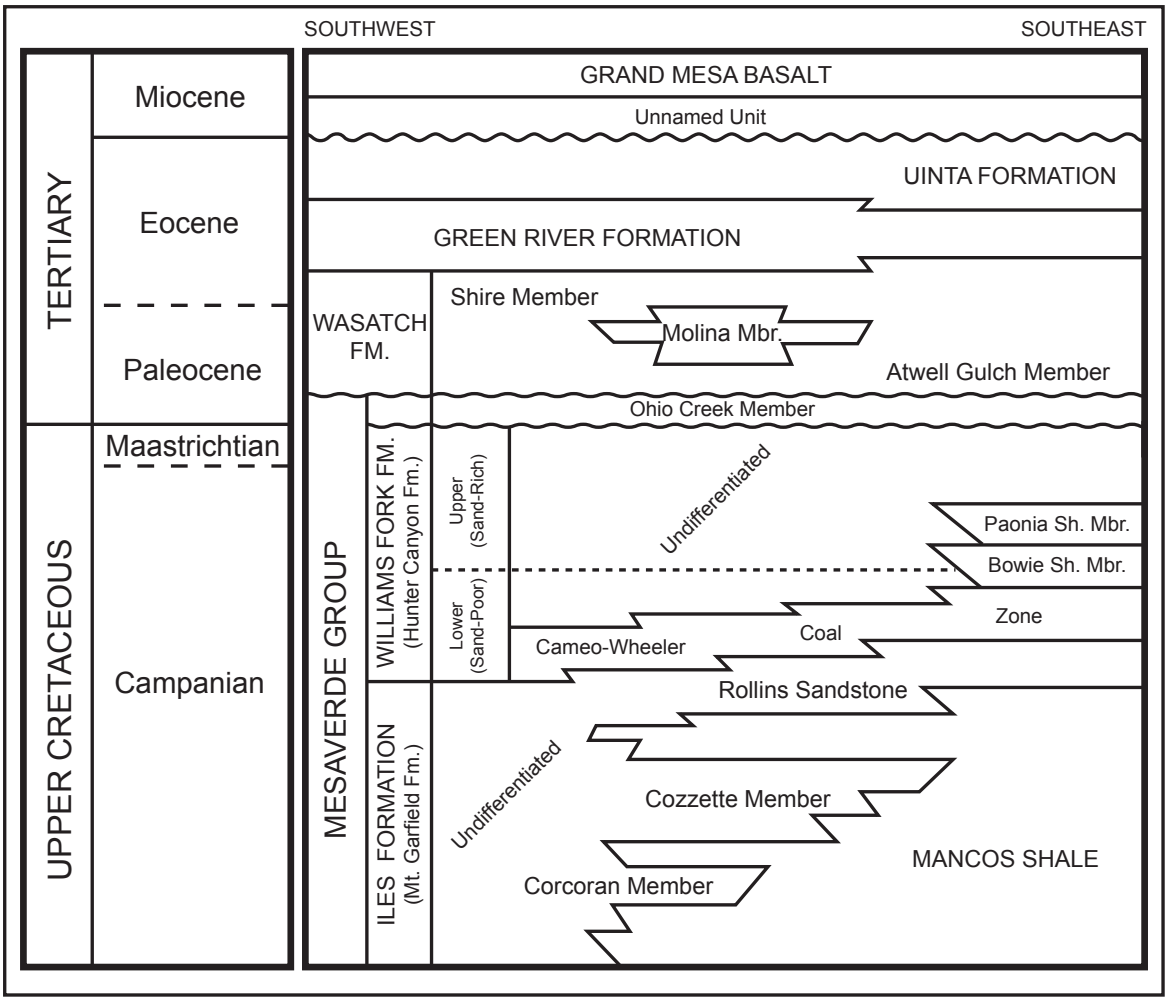

Figure 2: Stratigraphic nomenclature of the Upper Cretaceous and Tertiary strata within the southern Piceance Basin. The undifferentiated Williams Fork Formation is divided into a lower (sand-poor) interval and a middle to upper (sand-rich) interval. The stratigraphic interval of this study focuses on the undifferentiated, sand-poor, lower Williams Fork Formation. Modified from Young (1955, 1966), Fisher al. (1960), Donnell (1961), Collins (1976), Johnson and May (1980), Tyler et al. (1996), Hettinger and Kirschbaum (2002), Cole and Cumella (2003, 2005) , Hettinger et al. (2003), Johnson and Roberts (2003), Patterson et al. (2003), German (2006), Burger (2007), and Pranter et al. (2009).

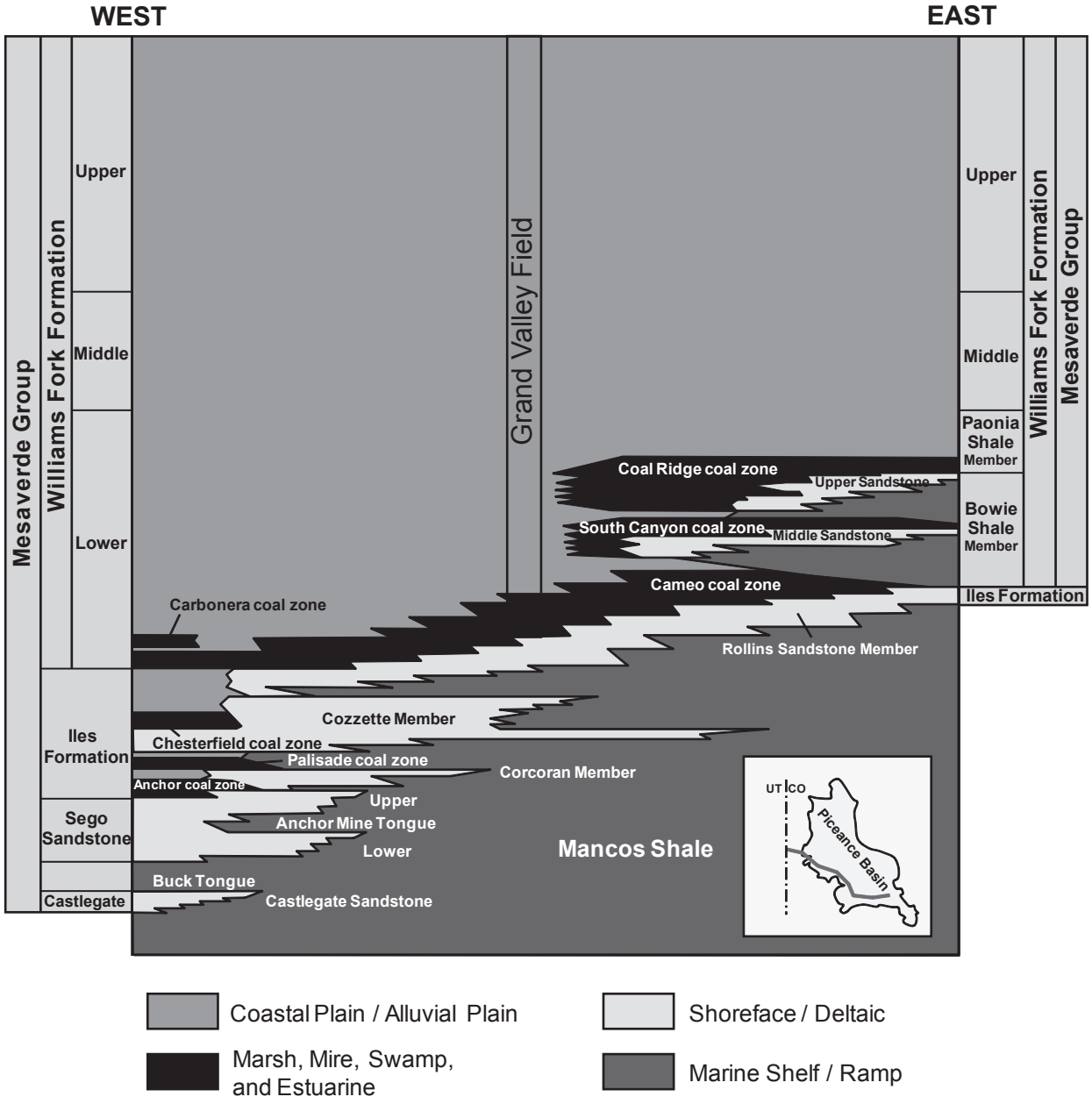

Figure 3: Stratigraphic nomenclature of Upper Cretaceous strata of the southeastern Piceance Basin. The Williams Fork Formation is formally differentiated into lower, middle, and upper. This study focuses on the lower (sand-poor) Williams Fork Formation at Grand Valley Field. Approximate location of the study area is shown. Modified from Carroll et al. (2004) and Pranter et al. (2011).

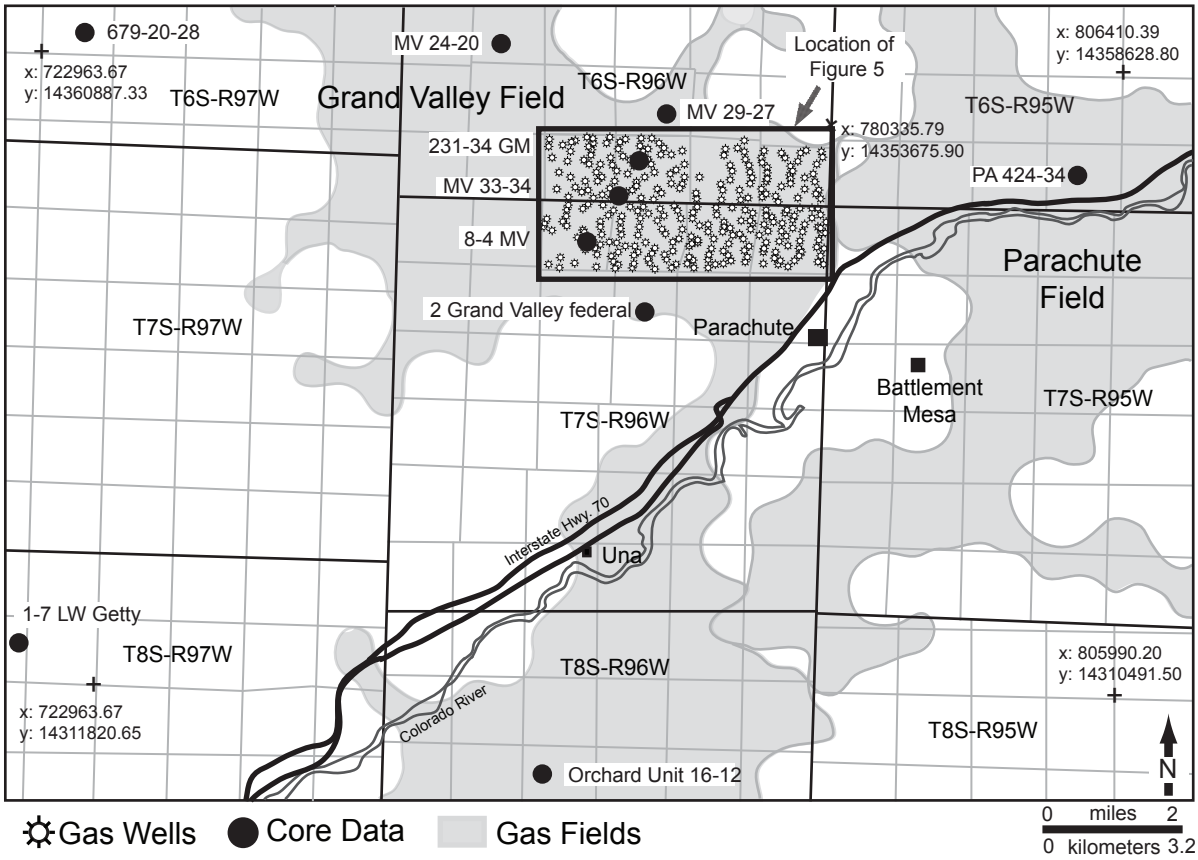

Figure 4: Map of the study area in the Piceance Basin. Location of this map is shown on Figure 1. The subsurface well log suite is outlined in black. Gas fields are shown in gray. Core locations are shown by black dots.

and was chosen due to the dense, irregular 10-ac [4-hectare; 430,600 ft^2 (40,468 m^2)] spacing [330 ft (100 m) north to south and 1,320 ft (402 m) east to west] of wells (Figure 5). The data set includes wireline logs for 328 wells and ten cores that total 896.3 ft (273.2 m) in length (Figures 4 and 5). Within the study area, a 1 mi^2 (1.6 km^2) area was selected for detailed 3-D reservoir modeling of the Lower Williams Fork Formation (Figure 5).

The stratigraphic interval of this study is from the top of the Rollins Sandstone Member of the Iles Formation to the top of the lower Williams Fork Formation (Figures 2 and 3). For a complete list of stratigraphic horizons and the measured depth (ft) of each horizon, see Appendix B. Two type logs are chosen for the study area to illustrate the stratigraphic variability of the deposits (Figure 6). Well logs used in this study include: V-Clay, Coal Flag, Gamma Ray (GR), Neutron-Porosity (NPHI), and Density-Porosity (DPHI).

TECTONIC AND STRATIGRAPHIC SETTING

The Piceance Basin is an elongate, asymmetrical basin, created during the Laramide orogeny (Johnson, 1989). During Late Cretaceous time (95-67 Ma), the Piceance Basin was situated on the western shoreline of the epeiric seaway, known as the Western Interior Seaway (Johnson, 1989; Hettinger and Kirschbaum, 2002; Blakey, 2004; Figure 7). The interior seaway stretched from present-day Canada to the Gulf of Mexico, covering the central portion of North America (Johnson, 1989). The shoreline was constantly migrating throughout the Rocky Mountain foreland basin during the Cretaceous and Johnson (1989) accounted for migration angles to

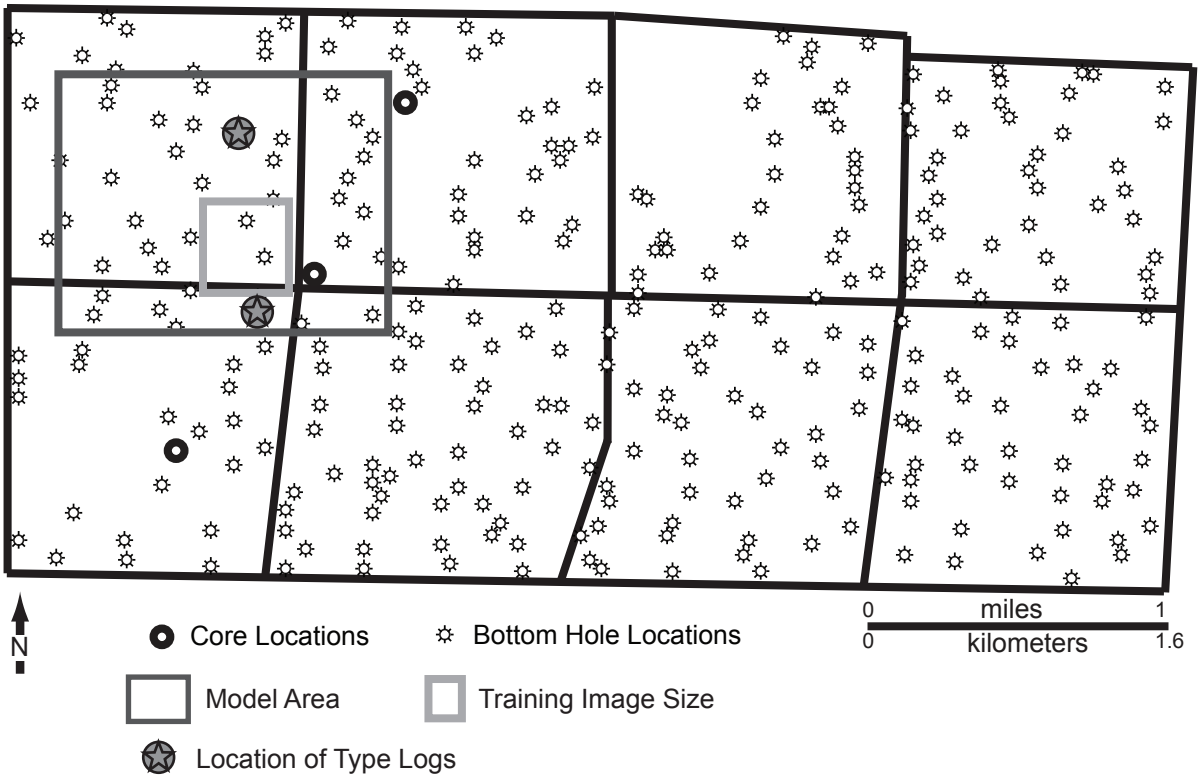

Figure 5: Eight-section study area at Grand Valley Field. The data set includes data for 328 well.

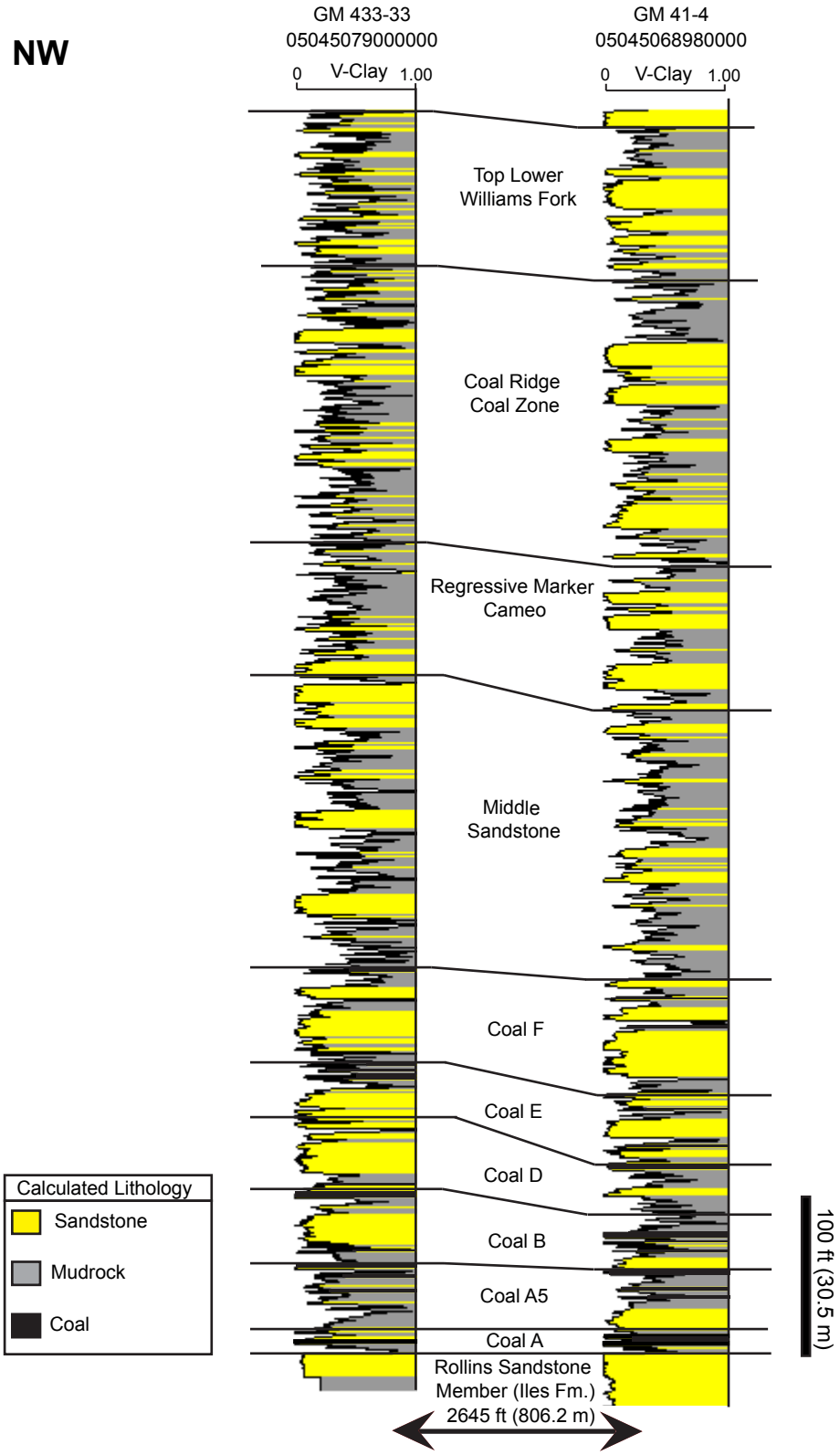

Figure 6: Type logs for the lower Williams Fork Formation at Grand Valley field. See figure 5 for the location of each well. Lithology was calculated using the following cut-off indicators: V-Clay 0-0.25 was sandstone; V-clay 0.25-1.00 considered mudrock; coal flag used to indicated location of coal deposits.

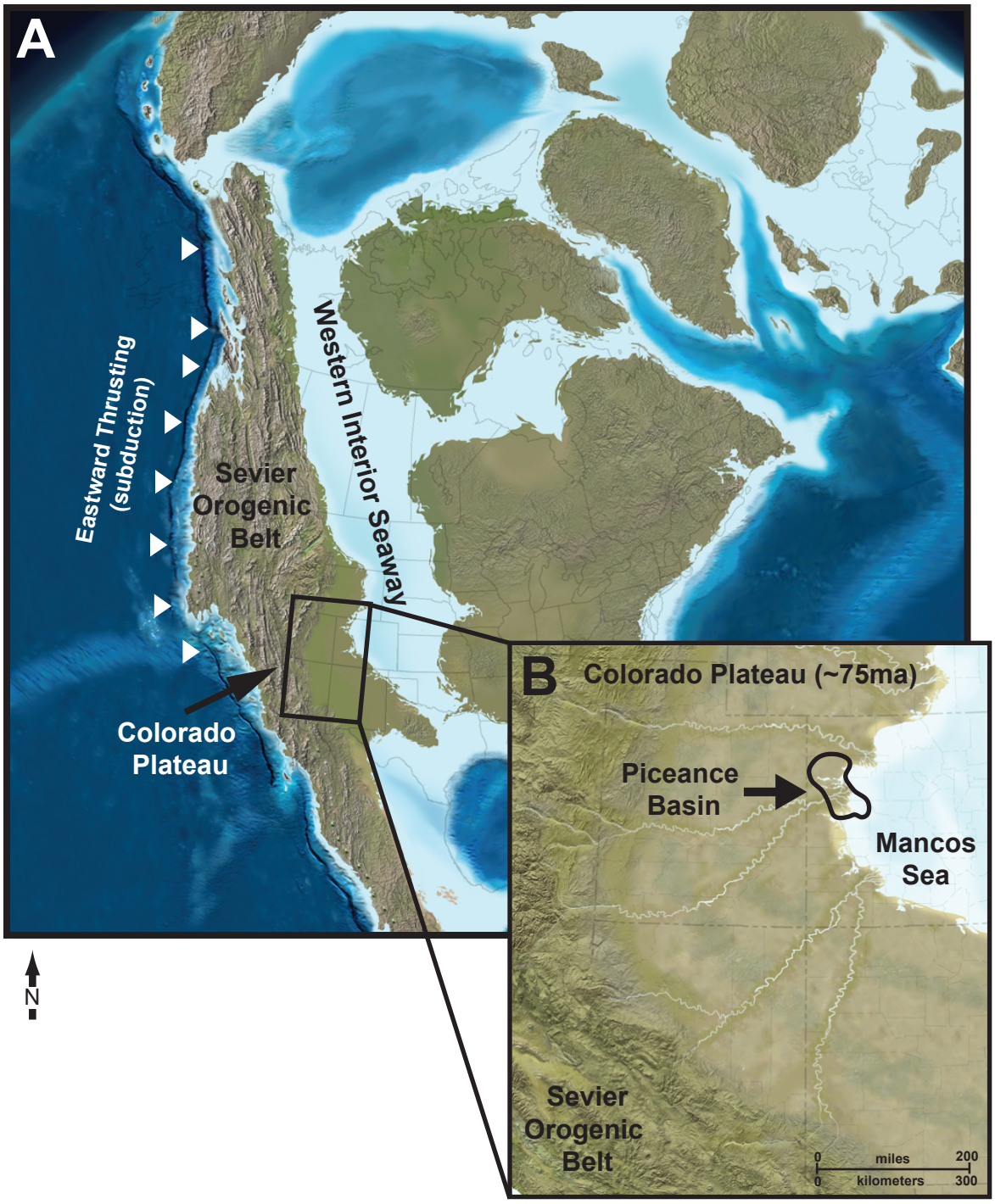

Figure 7: Paleogeographic reconstruction of the late Cretaceous Western Interior Seaway. (A) Reconstructrion of North America during the late Cretaceous (approximately 75ma). (B) Reconstruction of the Colorado Plateau during the same time frame with the current location of the Piceance Basin outlined. Modified from Blakey (2008), Hewlett (2010).

be between N65E and N15W at the location of the Piceance Basin during this time. The Rocky Mountain foreland basin developed during eastward thrusting of the Sevier orogenic belt (Johnson 1989). Thrusting is thought to have been the result of subduction taking place along the western margin of North America at this time (Figure 7).

The onset of the thick-skinned Laramide orogeny, involving reverse faulting, created several smaller basins within the central portion of the larger Rocky Mountain foreland basin (Johnson, 1989). It is speculated that the Piceance and Uinta basins were created due to deep troughs adjacent to thrust-bounded uplifts (Beck, 1985; Beck et al., 1988). Beck (1985) and Beck et al., (1988) speculate the troughs were created due to subsidence from frontal loading of the thrust sheets. Johnson (1989) suggests that loading from overriding thrust sheets was not the cause of subsidence within the now differentiated basins, due to the Piceance trough forming prior to the White River uplift.

As stated, the Piceance Basin is asymmetric with an elongate northwest to southeast axis orientation (Figure 1). Structural dip within the basin is gentle on the western and southwestern flanks of the basin with a range of 1 to 20 degrees (Cole and Cumella, 2005). The dip of the eastern margin steepens drastically and is overturned in places. This steeply dipping area is referred to as the Grand Hogback. The Grand Hogback is thought to have formed due to a westward trending thrust fault situated beneath the present-day outcropped area on the eastern margin (Johnson, 1989). Figure 8 shows a simplistic structural cross section from west to east across the southern portion of the Piceance Basin.

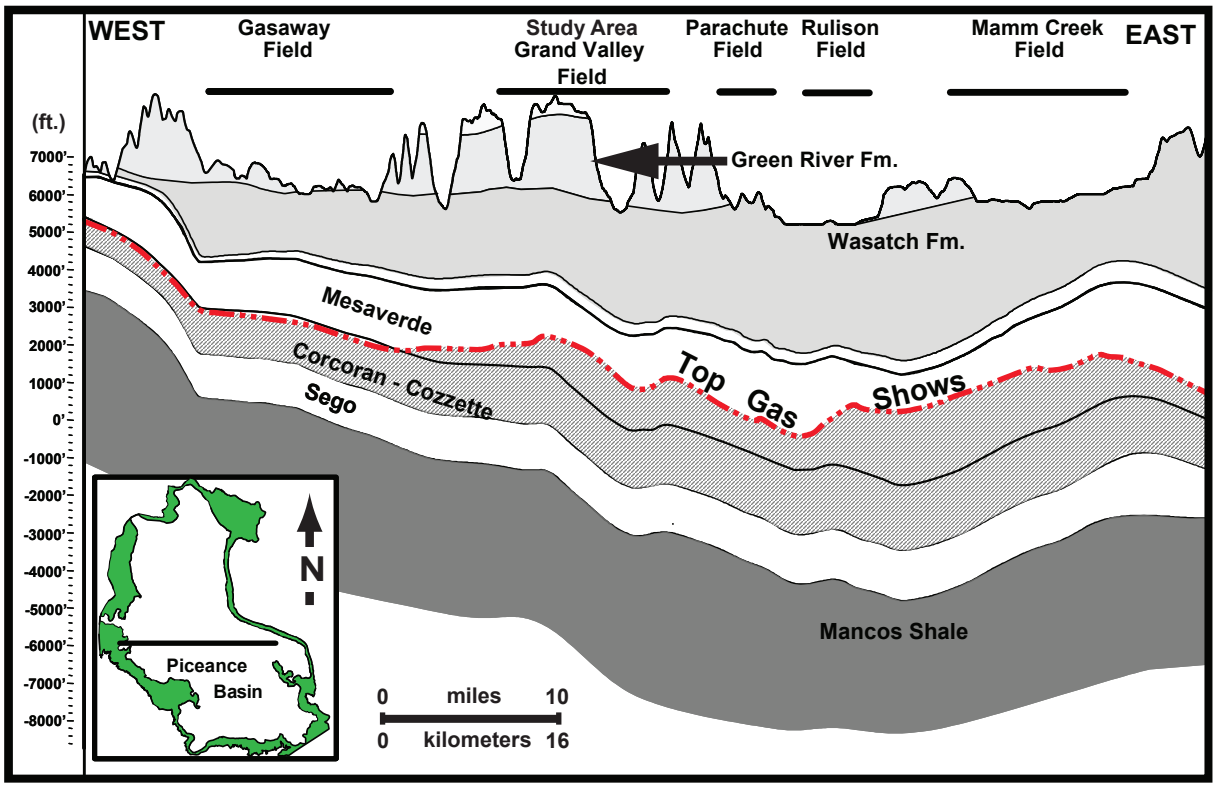

Figure 8: Schematic structural cross section from west to east across the southern portion of the Piceance Basin. Modified from Yuewicz et al. (2008) and Hewlett (2010).

Although adjacent, the Piceance Basin is now separated from the Uinta Basin by the Douglas Creek Arch to the northwest (Figure 1 and 9). Prior to being separated by the Douglas Creek Arch, the Uinta and Piceance Basins interacted throughout geologic time and were simultaneously filled by Lake Uinta during the Eocene (Johnson, 1989; Johnson and Flores, 2003).

The Uinta Uplift and Douglas Creek Arch now serve as the north and northwestern margins of the Piceance Basin respectively. Bounding the northeast portion of the basin is the Axial Basin Anticline, to the east by the White River Uplift and Elk Mountains, to the southeast by the Gunnison Uplift and Western Elk Mountains, and to the southwest by the Uncompagre uplift (Johnson, 1989; Cole and Cumella, 2003; Johnson and Roberts, 2003; Figure 9).

Structurally, the Piceance Basin contains multiple southeast-plunging anticlines, synclines, and monoclines. In the southeast portion of the basin lie three anticlines, which are underlain by west and southwest thrusting faults related to a major thrust fault created the Grand Hogback. These anticlines are referred to as Coal Basin, Divide Creek, and Wolf Creek Anticlines (Figure 9; Johnson, 1989).

The Department of Energy has promoted research in the Piceance Basin since 1977 (Johnson, 1989). This research has lead to simulations like the Multi-well Experiment (MWX) that was conducted to gather information on the tight-sandstone reservoirs within the Iles and Williams Fork Formations (Nelson, 2002). Nelson (2002) provides a detailed look at the MWX experiment. Regional fracture systems trend west-northwest and were a key component of the MWX (Nelson, 2002). Also, micro-seismic fracture mapping was tested in Mamm Creek Field to analyze the

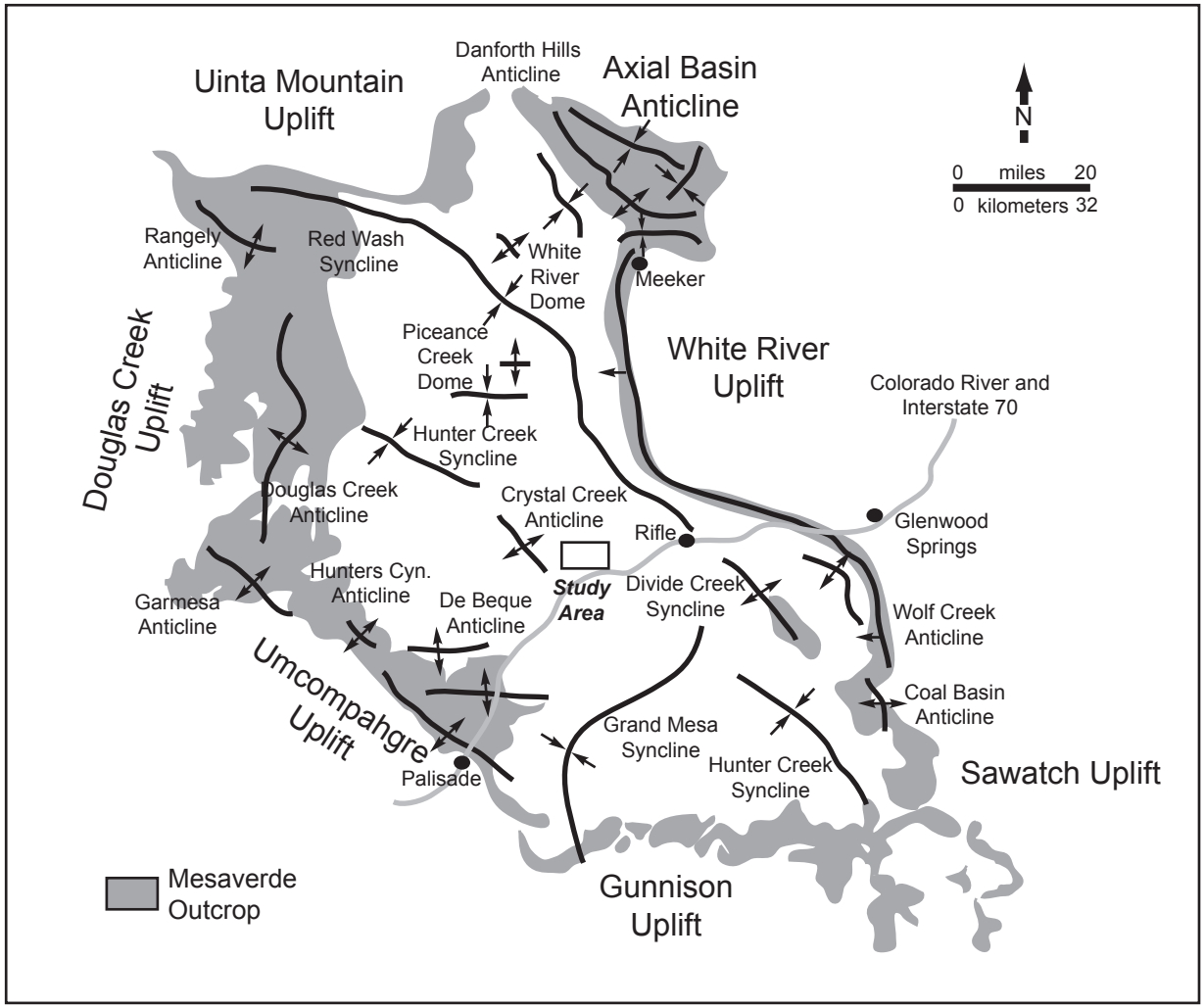

Figure 9: Structure map of anticlines and synclines within the Piceance Basin. Modified from Cashion (1973), Law and Spencer (1989), and Shaak (2010).

volume of fracturing needed to improve overall production (Weijers, et al., 2009). Baytok (2010) used attribute analysis of faults and fractures at Mamm Creek Field to identify type, distribution, and orientation of faults. Natural fractures are the main conduits for gas produced from sandstone reservoirs within the Piceance Basin (Johnson 1989; Johnson and Roberts, 2003; Cumella and Scheevel, 2005).

Sediments within the Mesaverde Group were shed off the Sevier highlands and transported into the basin by fluvial systems (Johnson, 1989; Hettinger and Kirschbaum, 2002). Coarser sediments remained in the highland areas, while finer-grained materials were transported into the middle of the Western Interior seaway. In the central portion of the Piceance Basin, the Mesaverde Group is differentiated into three members: the Iles Formation, Williams Fork Formation, and Ohio Creek Member (Figure 2). Stratigraphic nomenclature applied by Hettinger and Kirschbaum (2002, 2003) will be used throughout this study (Figure 2)

The Iles Formation is sub-divided into the Corcoran, Cozzette, and Rollins Sandstone Members (Hettinger and Kirschbaum, 2002, 2003). These members overlay and inter-tongue with the underlying Mancos Shale (Figure 2 and 3; Hettinger and Kirschbaum, 2002). The Corcoran Sandstone Member was named by Young (1955) and is composed of very fine to fine-grained sandstone, siltstone, shale, and coal. The environment of deposition ranges from offshore to coastal-plain environments. The Corcoran Member is differentiated from the overlying Cozzette and Rollins Sandstone members by tongues of the Mancos Shale (Figure 2; Hettinger and Kirschbaum, 2002).

The Cozzette Sandstone Member of the Iles Formation was also named by Young (1955) and contains very similar facies to the Corcoran. The environments of deposition were similar, transitioning from offshore marine to shoreface, estuarine and coastal plain strata.

The uppermost member of the Iles Formation is the Rollins Sandstone Member and was named by Lee (1909). Grain size increases from very fine to coarse-grained sand upward. This unit tends to be a cliff former and is representative of a regressive near-shore marine environment of deposition (Hettinger and Kirschbaum, 2002).

The Williams Fork Formation, named by Hancock (1925), is divided into the Bowie Shale Member, Paonia Shale Member, and undifferentiated Williams Fork Formation (Figure 2 and 3). The Williams Fork Formation was deposited in alluvial-plain, lower coastal-plain, and marginal-marine settings. The Williams Fork Formation is composed of inter-bedded mudstone, coal, and sandstone ranging in grain size from very fine-grained sandstone to conglomeratic. Within the lower Williams Fork Formation are substantial coal zones including: Cameo-Wheeler, overlying the Rollins Sandstone Member of the Iles Formation; South Canyon Coal zone, which inter-tongues with the middle sandstone of the Bowie Shale Member; and the Coal Ridge Coal zone that overlies and inter-tongues with the upper sandstone of the Bowie Shale member (Figure 2 and 3; Hettinger and Kirschbaum, 2002).

The Williams Fork Formation is informally divided throughout the southwestern portion of the basin into two intervals: the lower and upper Williams

Fork Formation (Figure 2). Today, three sub-divisions, the lower, middle, and upper are recognized (Figure 3). Differentiation in the southwest portion of the basin was originally based on the amount of sandstone present and overall net-to-gross ratio throughout the formation. The lower one-third of the formation was deposited in a coastal-plain setting and is relatively sand poor (approximately 30%-50% sandstone), while the upper two-thirds, deposited in an alluvial environment, tends to be sand rich with a net-to-gross ratio ranging from 50%-80% (Cole an Cumella, 2005; Pranter et al., 2009). The lower most portion of the Williams Fork Formation (Top of Rollins Sandstone member to top of the lower Williams Fork Formation) is predominately composed of mudrock with sinuous-to-lenticular sandstone bodies deposited by meandering fluvial systems and containing abundant coal deposits (Johnson, 1989; Hettinger and Kirschbaum, 2002; Ellison, 2004; Cole and Cumella, 2005; Panjaitan, 2006; Pranter et al., 2007, 2009). Overall, the lower Williams Fork Formation is considered to have a low net-to-gross ratio (less than 50%; Cole and Cumella, 2005; Pranter et al., 2009). Stratigraphically higher, the net-to-gross ratio increases. The middle and upper Williams Fork Formation are considered high net-to-gross (greater than 50%; Cole and Cumella, 2005; Pranter et al., 2009). Figure 3 shows the approximate stratigraphic location of the middle Williams Fork Formation that has now been differentiated from the lower and upper.

A sequence-stratigraphic framework developed by Patterson et al. (2003) within the Piceance Basin indicates deposits of the Mesaverde group represent progradational successions with seven composite sequences identified throughout the basin. Shaak (2010) focused on the sequence stratigraphy of the lower Williams

Fork Formation and mapped flooding surfaces in the subsurface. These flooding surfaces linked marine to non-marine strata. Shaak (2010) identified two higher frequency transgressive-regressive cycles in this unit that had not previously been identified.

Outcrop exposures on the southwestern side of the Piceance Basin have served as a primary location for studies investigating a variety of scales of heterogeneity (Figure 1). Sandstone bodies within the lower Williams Fork Formations have been measured to determine thickness, apparent width, and width-to-thickness ratio (Cole and Cumella, 2005; Pranter, et al., 2009; Table 1; Appendix A). Sandstone-body dimensional data were collected for the middle Williams Fork Formation at Plateau Creek Canyon (German, 2006).

Cole and Cumella (2005) identified four major sandstone-body types (Figure 10) and created a database of dimensional statistics of exposed Williams Fork outcrops in Coal Canyon (Figure 1). Panjaitan (2006) mapped and measured 668 sandstone-bodies at Coal Canyon using the following methods: 1) global positioning system (GPS) coupled with descriptions from field work and hand measurements, and 2) aerial light detection and ranging (LIDAR) data coupled with digital orthophotography and ground-based photomosaics (Cole and Cumella, 2005; Panjaitan, 2006; Pranter et al., 2009).

Dimensional statistics from Coal Canyon (Panjaitan, 2006; Pranter et al., 2009; Table 1) were used in conjunction with Cole and Cumella's (2005) specific sandstone-body types to create 3-D reservoir models at Rulison and Mamm Creek Fields (Vargas, 2004; Pranter et al., 2008; Hewlett, 2010; Pranter et al., 2011; Figure

Table 1 Statistical summary of sandstone-body dimensional data

Sandstone-Body Type	N	Min.	Mean	Median	Max.	Std. Dev.
Crevasse Splay	279					
Thickness (ft)		0.5	5.1	4.7	15.0	2.6
Apparent Width (ft)		40.1	231.1	198.7	843.3	136.4
Apparent Width at 75° (ft)*		45.9	242.5	214.9	869.4	133.0
Area (acres)*		0.15	5.5	3.3	54.5	7.2
Width:Thickness Ratio		9.8	94.6	79.5	718.2	80.9
Single Story Channel Fill	116					
Thickness (ft)		3.9	12.3	11.8	29.9	5.1
Apparent Width (ft)		44.1	339.5	274.7	1699.8	262.5
Apparent Width at 75° (ft)*		45.2	251.7	202.7	695.7	168.2
Area (acres)*		0.08	3.3	1.5	17.4	4.3
Width:Thickness Ratio		5.5	44.7	34.6	149.4	30.0
Multistory Channel Fill	273					
Thickness (ft)		5.0	19.1	17.8	47.1	8.2
Apparent Width (ft)		53.2	512.3	404.5	2791.1	433.5
Apparent Width at 75° (ft)*		38.2	398.1	297.9	2553.4	340.3
Area (acres)*		0.05	9.9	3.2	235.0	23.1
Width:Thickness Ratio		3.9	45.8	37.1	221.1	33.5
Total Population	668					
Thickness (ft)		0.5	12.1	9.7	47.1	8.7
Apparent Width (ft)		40.1	364.9	262.9	2791.1	335.8
Apparent Width at 75° (ft)*		38.2	309.3	240.4	2553.4	257.4
Area (acres)*		0.05	7.0	2.9	235.0	15.9
Width:Thickness Ratio		3.9	66.0	48.1	718.2	62.7

* Apparent width values at 75° and area values are reported for LiDAR-based measurements (N = 627). Area values for single-story and multistory sandstone bodies are reported for the average paleocurrent orientation of 75° for sandstone bodies in Coal Canyon.

Table 1: Outcrop dimensional data collected from the lower Williams Fork Formation at Coal Canyon in the Picenace Basin. Sandstone-body types A, B, and C were identified in the lower Wiliams Fork Formation. Outcrop statistics were used to guide the dimensions of training images created within this study. From Pranter et al. (2009).

10). Results of subsurface studies show the variability in net-to-gross ratio between the lower, middle, and upper Williams Fork Formations. As net-to-gross increases, overall connectivity of sandstone bodies increases (Vargas, 2004; Sommer, 2007; Pranter et al. 2008; Pranter and Sommer, 2011). Cole and Cumella (2005), Panjaitan (2006), Sommer (2007), and Pranter and Sommer (2011) addressed the issue of well spacing in the Piceance Basin, stating that the average width of most sandstone bodies within the Williams Fork Formation (528 ft; 160.9 m) are smaller than wells situated at 10-ac [4-hectare; 430,600 ft^2 (40,468 m^2)] spacing, therefore indicating a need for the dense spacing.

METHODS

Facies, facies associations, and architectural elements were described and interpreted in ten cores and compared to V-Clay well-log response to manually interpret architectural elements in non-cored wells. Point bars, crevasse splays, coal, and floodplain were modeled using multiple-point geostatistical modeling to create three scenarios. These scenarios determined effects of the presence and interaction mudstone-plugs have on sandstone connectivity throughout the system. Calculating static connectivity and conducting a dynamic fluid-flow simulation to quantitatively test reservoir quality sandstone-body connectivity compared these models.

To create three-dimensional subsurface models of sandstone bodies within the lower Williams Fork Formation, a detailed stratigraphic architecture was developed. Ten cores were described on half-foot increments to understand facies, facies associations, and architectural elements present at Grand Valley Field. Core

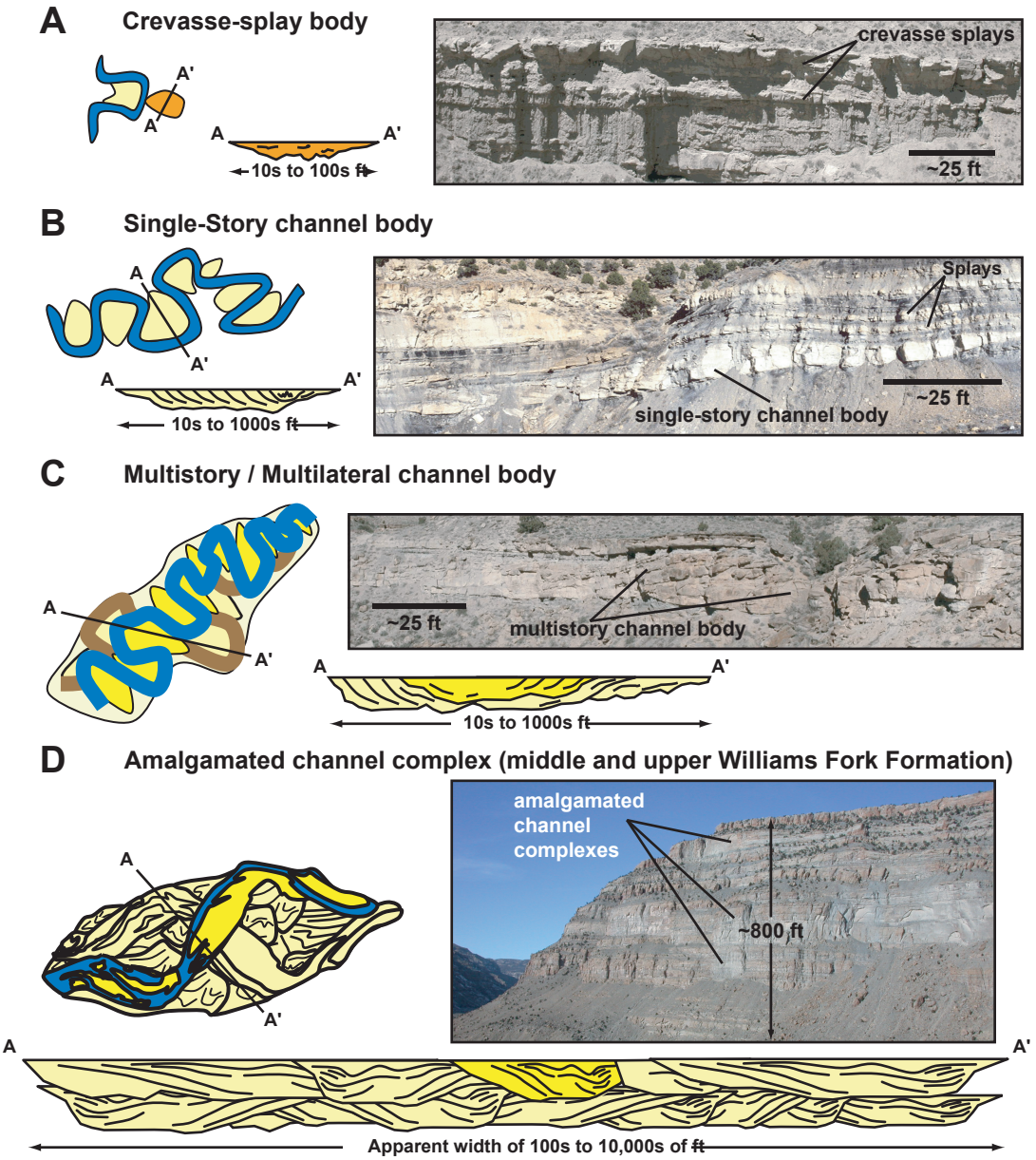

Figure 10: Sandstone-bodies identified in outcrop at Coal Canyon in the Piceance Basin. Sandstone-body types A, B, and C are present within the lower Williams Fork Formation at Grand Valley field. Dimensional statistics (thickness, apparent width, and width-to-thicknes ratio) are measured for N=668 total sandstone bodies.Outcrop statistics are used to constrain dimensions of sandstone-bodies drawn within training images created in this study. From Pranter et al. (2009).

descriptions were then related to well-log response to provide rationale for manual interpretation of fluvial architectural elements from well-log response.

Twelve stratigraphic surfaces were correlated throughout the field by creating a north-to-south and east-to-west grid of well-log cross sections through the eight-section area. To interpret spatial variability of sandstone deposits and architectural elements throughout the 8 mi^2 (20.7 km^2) study area, stratigraphic maps showing gross interval isopachs, percent sandstone, percent point-bar, and percent crevasse-splay were created for intervals within the 12 correlated stratigraphic surfaces.

Sandstone, mudstone, and coal were calculated from the lithology logs. Following calculation of lithology logs, architectural-element logs were manually interpreted for all wells in the data set. Using previously described outcrop statistics from the lower Williams Fork Formation at Coal Canyon, calculated lithology logs, manually interpreted architectural-element logs, and core descriptions, 3-D reservoir modeling was conducted to identify the static and dynamic connectivity and dynamic fluid-flow simulation results for the lower Williams Fork Formation at Grand Valley Field.

Three scenarios were modeled to compare the geometries of sandstone bodies and the presence of mudstone plugs within the system. Utilizing three scenarios of sandstone-body geometries and fluctuating the amount of mudstone plugs within the system, a conceptual fluid-flow simulation of 3-D static connectivity of sandstone bodies is assessed to determine the communication of sandstone bodies at Grand Valley Field.

Reservoir modeling scenarios of architectural-elements were populated with porosity and permeability values from core data. A conceptual dynamic simulation of the modeled fluvial sandstone deposits was conducted to assess long-term field recovery, OGIP, and dynamic connectivity. Petrophysical constraints, pressure data and hydraulic fractures were applied respectively. Long-term field recovery was calculated for thirty years at 10-ac [4-hectare; 430,600 ft^2 (40,468 m^2)], 20 [8-hectare; 871,200 ft^2 (80,937 m^2)], and 40-ac [16-hectare; 1,742,400 ft^2 (161,874 m^2)] spacing for all models, as well as OGIP, and 3-D connectivity. (T. Schaller, J. Gilman, personal communication).

PETROLEUM SYSTEM

The Piceance Basin is a major producer of natural gas within the Mesaverde Total Petroleum System (TPS; Johnson and Roberts, 2003). Yurewicz, et al. (2003) identified three main facies as potential source rocks for natural gas within the basin: (1) marine shale in the lower Mesaverde Group, (2) coal deposits within the Iles and Williams Fork formations, and (3) non-marine shale deposits within the Iles and Williams Fork formations. This study focuses on the lowest portion of the Williams Fork Formation and addresses the coal and carbonaceous shale deposits within the stratigraphic interval.

Source rocks in the Mesaverde Group are predominately mature for gas. The main coal, and source rock, within the Williams Fork Formation is referred to as the “Cameo zone” and interpreted as a transgressive systems track in the southeast portion of the basin by Patterson et. al. (2003). Coal thickness ranges from less than

1 ft (0.30 m) to 35 ft (10.7 m) (Yurewicz et. al., 2003). Also present within the Williams Fork Formation are non-marine shale deposits that act as potential source rocks for the basin-centered gas accumulation in the Piceance Basin. Yurewicz, et al. (2003) suggests the water table was high at this time, allowing for preservation of organic material within non-marine shale deposits.

Non-marine shales averages 2% total organic carbon (TOC) with low hydrogen indices. Coals in the Mesaverde Group average 65% TOC and moderate hydrogen indices (Yurewicz et al., 2003). Burial-history modeling conducted by Yurewicz et al. (2003) indicate coal deposits, although thin, within the Williams Fork Formation account for the majority of gas volumes throughout the basin. Gas generation began around 55 Ma and peaked between 47 and 39 Ma with the eastern half of the basin having an earlier peak generation time than the western (Johnson and Roberts, 2003; Yurewicz et al., 2003). Yurewicz et al. (2003) attribute this to the Wasatch Formation increasing in thickness on the western half of the basin.

During the Late Neogene, gas generation has decreased due to the down-cutting within the basin, however, generation may still be occurring. Coal-bearing intervals have the ability to reach temperatures exceeding 200 degrees F (Johnson and Roberts, 2003). Migration of hydrocarbons into sandstone reservoirs of the Williams Fork Formation occurs in a more vertical, rather than lateral sense, according to Johnson and Roberts (2003) and Yurewicz et al., (2003).

The fluvial-channel sandstone reservoirs exhibit low porosity and permeability, potentially due to early diagenesis throughout the basin (Johnson, 1989, Johnson

and Roberts, 2003, Cumella and Ostby, 2003; Cumella and Scheevel, 2005; Aboktef, in progress). Porosity ranges from approximately 5% - 8% while permeabilities range from 0.01 md to 0.1 md (Johnson and Roberts, 2003). Gas reservoirs are sealed through capillary seal and/or water block in the fluvial sandstone reservoirs of the Williams Fork Formation (Johnson and Roberts, 2003). Trapping mechanisms are also aided by lateral discontinuities between fluvial-sandstone reservoirs associated with structural and stratigraphic traps (Johnson and Roberts, 2003).

CHAPTER TWO

STRATIGRAPHIC ANALYSIS

To understand the coastal-plain deposits of the lower Williams Fork Formation at Grand Valley Field, ten cores totaling 890.3 ft (271.4 m) were described on 6 in (0.5 ft; 0.2 m) increments to determine facies, facies associations, and architectural elements (Figure 11). Cores were examined for grain size, sandstone percentage, sedimentary structures, amount of bioturbation, and other features such as siderite staining, fractures, and mudstone clasts. The cores represent intervals from the Rollins Sandstone Member (Iles Formation) to the lower and upper Williams Fork formations.

These different facies and architectural elements were described to identify major stratigraphic changes and to differentiate between the deposits by using their well-log signatures (Figure 11). Facies, facies associations, and architectural elements interpreted in cores were compared to their corresponding well-log response to identify log characteristics for architectural elements that might be diagnostic of those deposits. Recognition of representative well-log responses for architectural elements facilitates the interpretation of fluvial deposits in non-cored wells (Figure 12; Cant, 1992; Bridge and Tye, 2000).

Although cores were described within the Rollins Sandstone Member and upper Williams Fork Formation, percentages of facies were calculated for only the lower Williams Fork formation. A total of 654.7 ft (199.5 m) of core was described within the lower Williams Fork Formation within and surrounding Grand

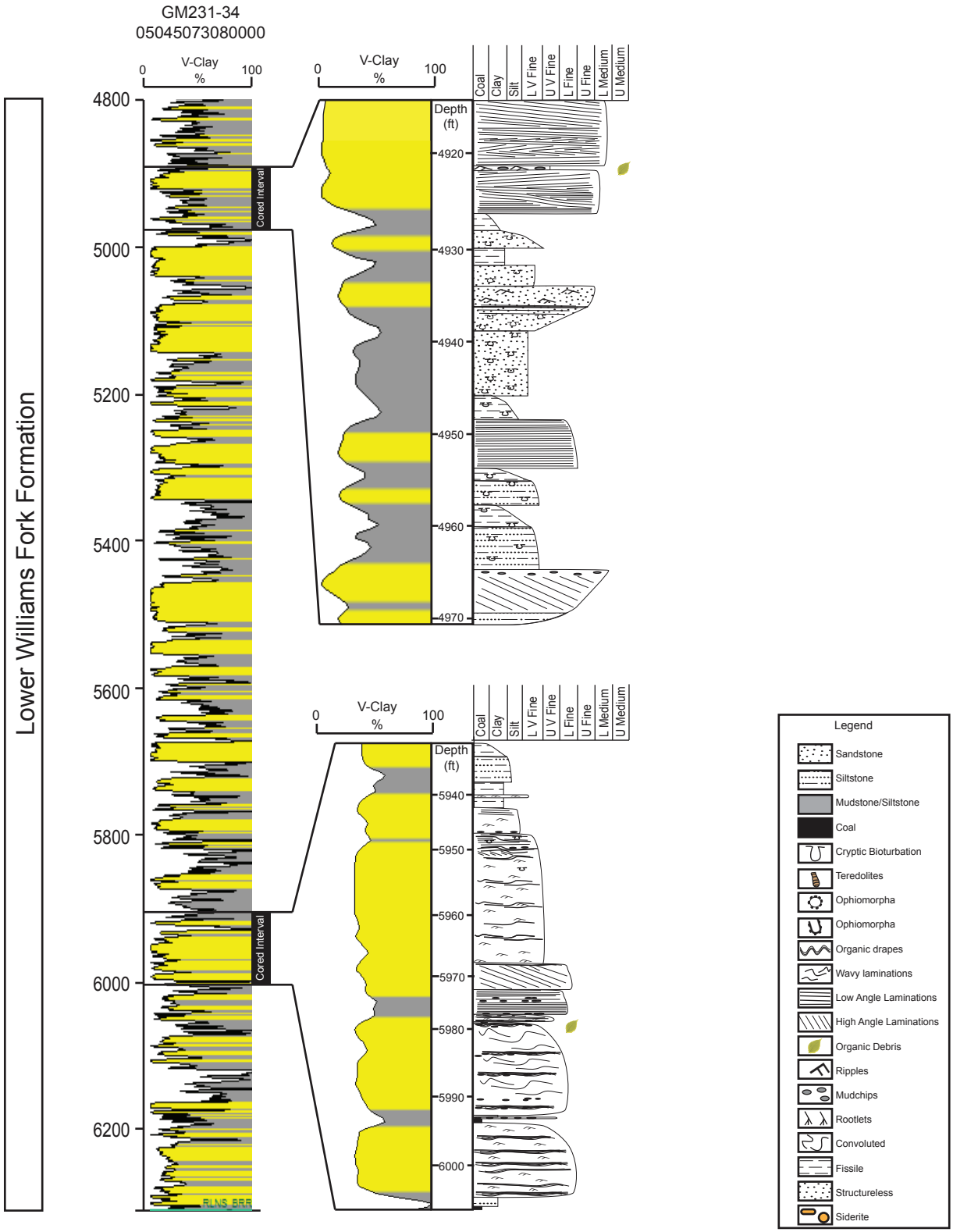

Figure 11: Diagrammatic sketch of core description for core GM231-34. Core GM231-34 transected through 127 ft (38.7 m) of the lower Williams Fork Formation.

Shape:	Cylindrical	Funnel Shaped	Bell Shaped	Symmetrical	Irregular
Trend:	Clean, No Trend	Abrupt Top Coarsening Upward	Abrupt Base Fining Upward	Rounded Base and Top	Mixed Clean and Shaly, No trend
Typical Gamma-Ray log response	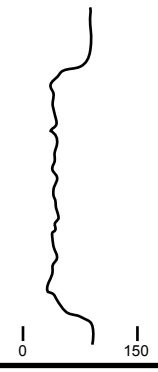				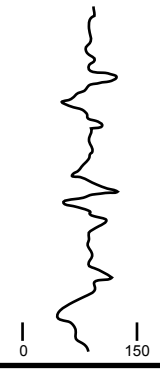
Interpre-tation:	aeolian, braded fluvial, carbonate shelf, reef, submarine canyon fill	crevasse splay, distributary mouth bar, clastic strand plain, barrier island, shallow marine sheet sand-stone, carbonate shoaling-upward sequence, submarine fan lobe.	fluvial point bar, tidal point bar, deep sea channel, some transgressive shelf sands	sandy offshore bar, some transgressive shelf sands, amalgamated CU and FU units	fluvial floodplain, carbonate slope, clastic slope, canyon fill

Figure 12: Typical gamma-ray log response examples interpreted based on log signature. This interpretation method, coupled with core-to-log comparison within the study area provides a framework to carry out the manual interpretation of architectural element logs based off log response. The main architectural elements interpreted from well-log character in this study are crevasse splays and fluvial point bars, which correlate to the funnel and bell shaped curves. Modified from Cant (1992).

Valley Field. Within the Rollins Sandstone Member, 60 ft (18.3 m) core were described, and 175.6 ft (53.5 m) in the upper Williams Fork Formation.

FACIES

Facies, are defined as: “a body of rock characterized by a particular combination of lithology, physical, and biological structures that bestow an aspect different from the bodies of rock above, below, and laterally adjacent (Walker 1992, p. 2).” Twelve facies are identified in cores and include: (A) contorted mudstone, (B) organic-rich (carbonaceous) mudstone, (C) laminated mudstone, (D) fissile mudstone, (E) silty mudstone, (F) coal, (G) ripple-laminated sandstone, (H) planar-laminated sandstone, (I) contorted sandstone, (J) bioturbated sandstone (Rollins Sandstone Member only, (K) wavy-laminated sandstone, (L) structureless sandstone (Table 2; Figures 13, 14).

Contorted Mudstone/Siltstone (M_C)

Contorted mudstone and/or siltstone (Figure 13) is dark to light gray. Interval thickness ranges from 1.5 ft (0.45 m) to 13.5 ft (4.11 m). This facies is contorted due to bioturbation by vertical and horizontal traces (specific trace fossils are not identified throughout core descriptions, but vertical versus horizontal burrows are distinguished), soft-sediment deformation, and often contains siderite staining. Grain-size is considered mudstone, however very-fine sandstone is present in some locations and burrows. The contact of this facies ranges from abrupt to gradational into other mudstone facies. Contorted mudstone/siltstone totals 12.4% of all facies described (Figure 15).

Table 1 Summary of facies

Facies Name	Facies Code	Description	Interpretation	Picture	Color
Contorted Mudstone	M_C	**Description**: contorted, bioturbated, silty mudstone with soft sediment deformation. Primarily silty mudstone with small amount of sandstone intermixed. Siderite staining present in some core locations. **Contact:** Abrupt and gradational **Thickness:** 1.5' - 13.5' **Internal Geometry:** Contorted, structureless, some cryptic bioturbation present; vertical and horizontal burrows visible in some cores	Floodplain Deposits or the top of an overall fining upward sequence wtihin the core that might correlate to the upper portion of a point bar.		
Organic rich (carbonaceous) Mudstone	M_O	**Description:** Organic (carbonaceous) rich silty mustone with siderite staining in some core locations (not in photo). **Contact:** Sharp, abrupt contacts overlain by sandstone. Gradational contacts wtih MC and Coal. **Thickness:** 2.5' - 13' **Internal Geometry:** Possibly some cryptic bioturbation present, overall look is structureless to highly contorted	Floodplain Deposits or the top of an overall fining upward sequence wtihin the core that might correlate to the upper portion of a point bar.		
Silty Laminated Mudstone	M_L	**Description:** Laminated silty mudstone. **Contact:** Sharp, abrupt contacts overlain by sandstone. Gradational contacts wtih SL and Coal. **Thickness**: 0.5' - 4' **Internal Geometry:** low angle crinkled laminations	Floodplain Deposits or the top of an overall fining upward sequence wtihin the core that might correlate to the upper portion of a point bar.	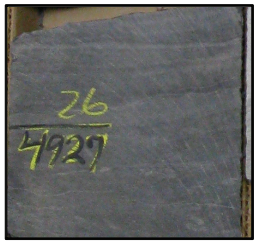	
Fissile Mudstone	M_F	**Description:** Fissile Mudstone **Contact:** Sharp, abrupt contacts overlain and underlain by sandstone. **Thickness**: >0.5' -8.5' **Internal Geometry:** low angle crinkled laminations Only occurs in GM231-34 Core	Floodplain Deposits or the top of an overall fining upward sequence wtihin the core that might correlate to the upper portion of a point bar.		

Table 2: Summary of facies for the lower Williams Fork Formation

Facies Name	Facies Code	Description	Interpretation	Picture	Color
Silty Mudstone	M_S	**Description:** silty mudstone with some sparse sand with fissile mudstone intermixed. **Contact:** Gradational into fissile mudstone (MF) Thickness: 3' - 4.5' **Internal Geometry:** contorted, structureless	Floodplain Deposits or the top of an overall fining upward sequence wtihin the core that might correlate to the upper portion of a point bar.		
Coal	C	**Description:** Coal **Contact:** Sharp **Thickness:** 0.5' - 12' **Internal Geometry:** contorted, structureless	marsh/floodplain		
Ripple-Laminated Sandstone (ripples are not distinguished by type for this study)	S_R	**Description**: ripple laminated sandstone, bi-modal grain size: very fine and fine lower; organic/mud drapes present sometimes **Contact:** gradational and interbedded within other facies Thickness: <0.5' - 16' **Internal Geometry:** a-symmetric, climbing, reactivation surfaces wtihin ripples, now contorted sections used to be rippled,difficult to see in specific areas (fuzzy)	Upper portion (coarsest section) of a crevasse splay) or sedimentary structure within a point bar	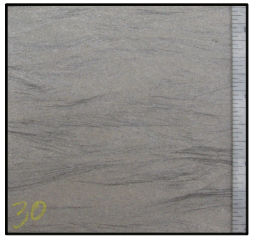	
Low-to-High Angle Laminated Sandstone	S_L	**Description:** low to high angle laminated sands with mudchips at the base, fine to upper-medium/lower-coarse grained **Contact:** gradational **Thickness:** 1' - 31.5' **Internal Geometry:** Low (>15 degrees) to high (<15 degrees) angle laminated sands.Sharp breaks associated with a change in angle (see photo) present throughout this facies.	Point Bar and/or Channel Bar	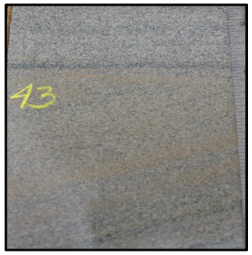	

Table 2: Summary of facies for the lower Williams Fork Formation

Facies Name	Facies Code	Description	Interpretation	Picture	Color
Contorted, Convoluted Sandstone	S_C	**Description:** contorted, convoluted interbedded sand and mud with potential cause from soft sediment deformation or bioturbation **Contact:** Gradational **Thickness**: 0.5' - 9' **Internal Geometry:** Highly contorted and bioturbated	Within Point Bar and Crevasse Splay sequence	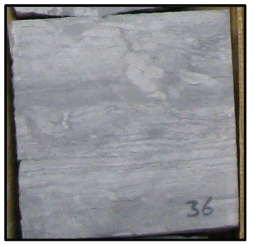	
Wavy Laminated Sandstone	S_{WL}	**Description:** shaly sandstone with organic drapes **Contact:** gradational between contorted and bioturbated sandstone **Thickness:** 1.5' **Internal Geometry:** Organically wavy laminated sandstone Photo curtesy of Core Lab and William	Upper portion (coarsest section) of a crevasse splay) or sedimentary structure within a point bar	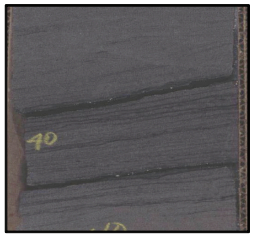	
Structureless Sandstone	S_S	**Description:** Structureless Sandstone **Contact:** Gradational **Thickness**: 2.4' - 11.7' **Internal Geometry:** Structureless Photo curtesy of Core Lab and Williams	Point Bar and/or Channel Bar	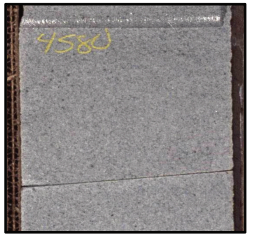	
Bioturbated Sandstone (present only in rollins sandstone member)	S_B	**Description:** bioturbated (ophiomorpha) sand in Rollins **Contact:** Gradational **Thickness:** 6.5' - 12' **Internal Geometry:** laminated to structureless medium sands with abundant ophiomorpha burrows	Sandstone with marine influence	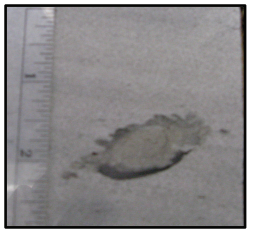	

Table 2: Summary of facies for the lower Williams Fork Formation

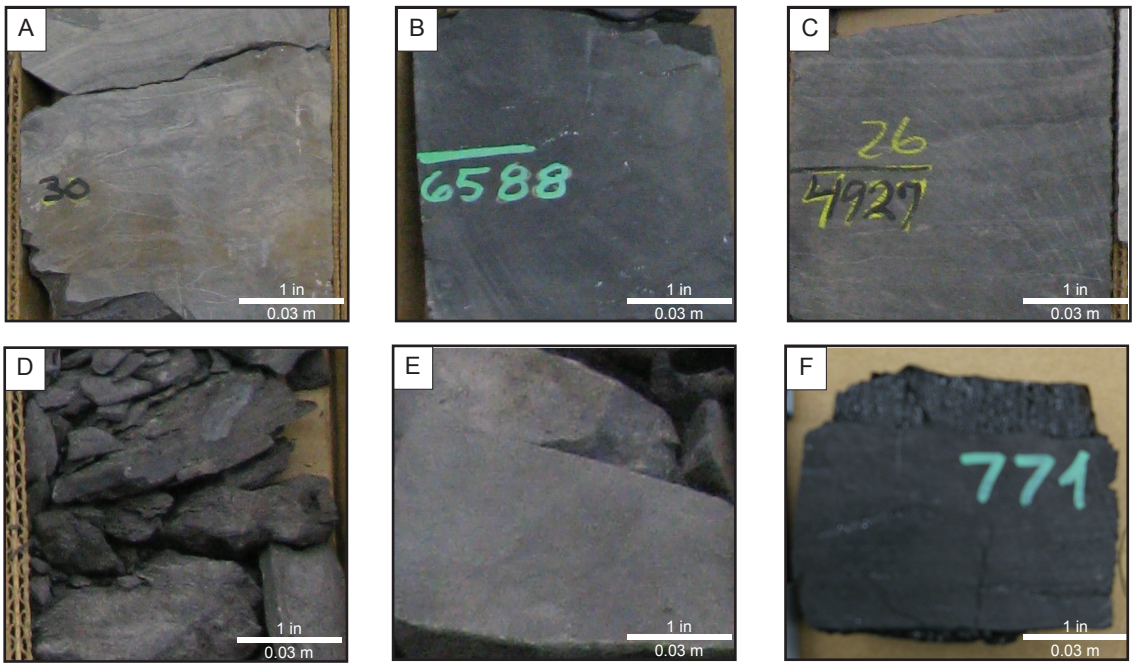

Figure 13: Mudstone-rich facies and coal. (A) Contorted mudstone, (B) organic rich mudstone, (C) silty laminated mudstone, (D) fissile mudstone, (E) silty mudstone, (F) coal.

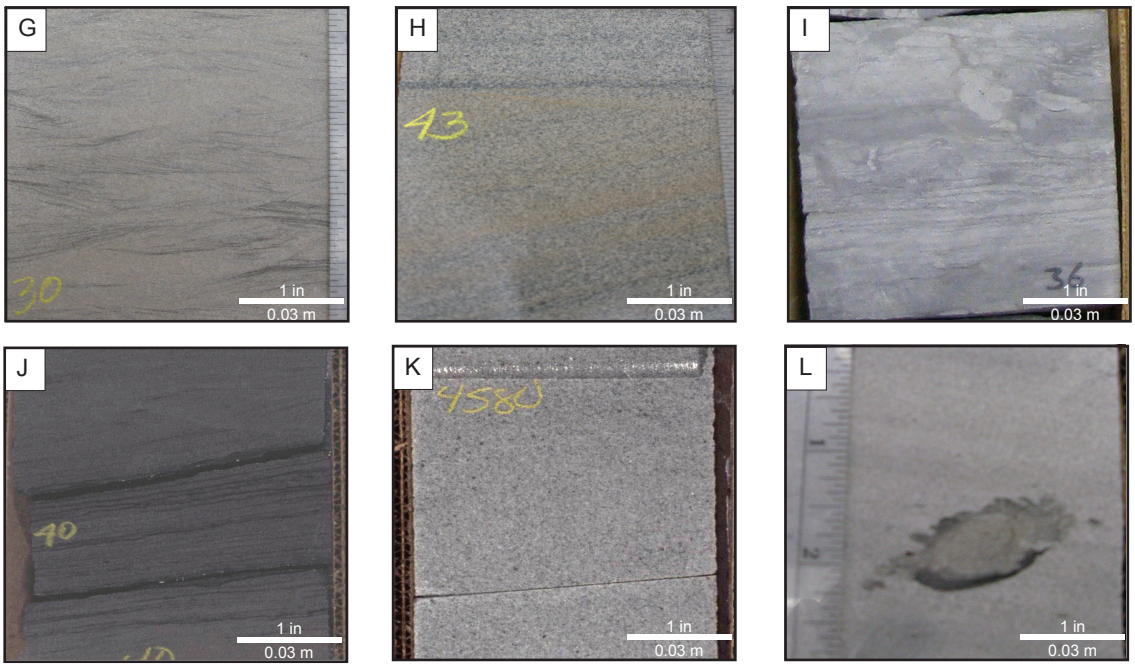

Figure 14: Sandstone-rich facies. (G) ripple-laminated sandstone,(H) low-to-high angle laminated sandstone, (I) convoluted sandstone, (J) wavy laminated sandstone, (L) bioturbated sandstone. Sandstone ranged in grain size from very fine-grained to coarse grained. Facies (L) was described in the Rollins Sandstone Member and is a marine sandstone.

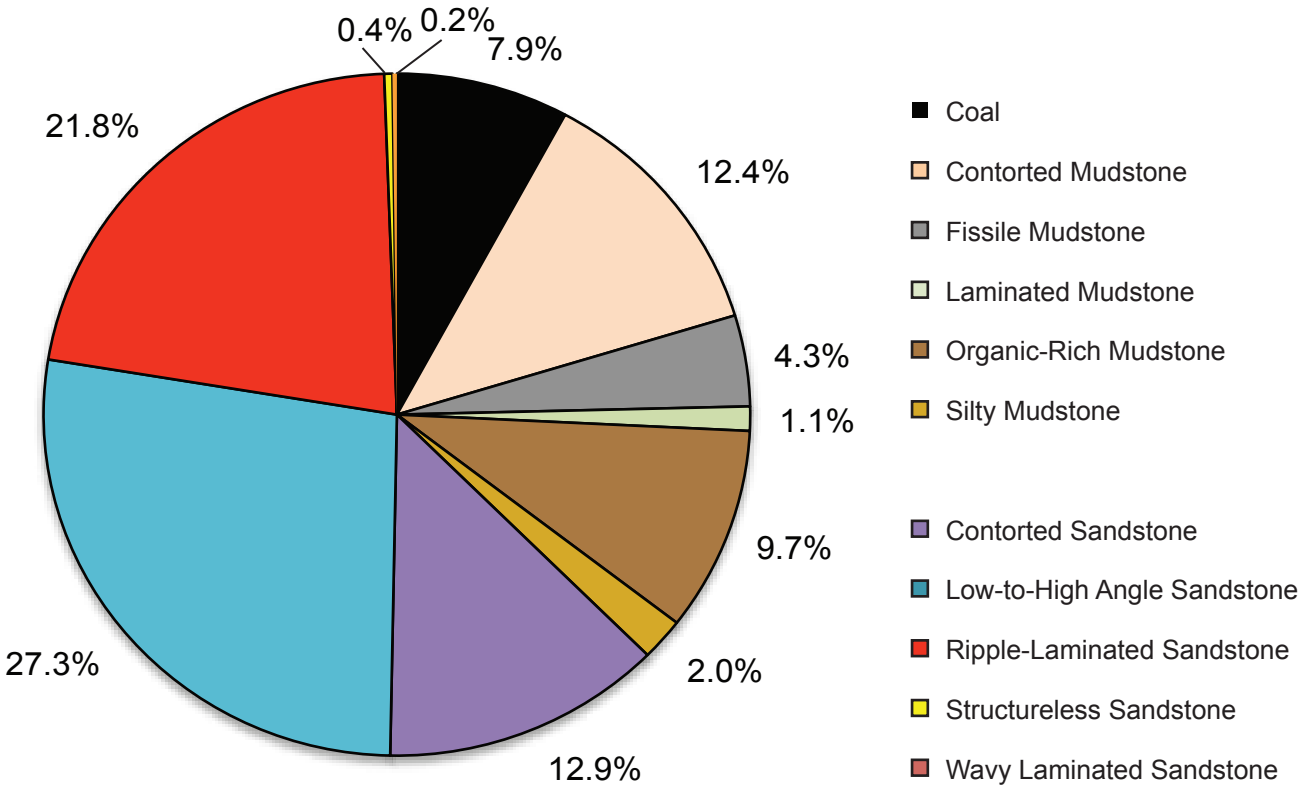

Figure 15: Percentage of the eleven facies described in the lower Williams Fork Formation: (C) coal, (MC) contorted mudstone, (MF) fissile mudstone, (ML) laminated mudstone, (MO) organic rich mudstone, (MS) silty mudstone, (SC) convoluted sandstone, (SL) low-to-high angle laminated sandstone, (SR) ripple-laminated sandstone, (SS) structureless sadnstone, (SWL) wavy laminated sandstone. Percentages are calculated by dividing the total footage of each described facies by the total footage of core described.

Organic-Rich (carbonaceous) Mudstone (M_O)

This dark-gray-to-black facies shows abrupt contacts with sandstone that lay stratigraphically higher and gradational contacts with contorted mudstone/siltstone and coal (Figure 13). This facies is differentiated from coal (facies F) by having no visible cleating, a silty grain-size, and the presence of cyptic bioturbation. This facies is commonly structureless and contains siderite staining. It ranges in thickness from 2.5 ft (0.76 m) to 13.0 ft (3.96 m) and accounts for 9.7% of the total examined facies (Figure 15).

Laminated Mudstone (M_L)

Laminated mudstone/siltstone (Figure 13) contains silt-sized material with very fine-grained sandstone and accounts for 1.1% of the facies examined (Figure 15). Dark-to-light gray, this facies exhibits crinkly laminations that are a darker colors then the surrounding rock. Similar to organic-rich (carbonaceous) mudstone, this facies is commonly overlain by sandstone with abrupt contacts and has gradational contacts with coal and laminated sandstone below. This facies is not as pronounced as other mudstone-dominated facies, and thickness ranges from 0.5 ft (0.2 m) to 4.0 ft (1.2 m).

Fissile Mudstone (M_F)

Fissile mudstone is dark-gray to black and extremely friable (Figure 13). Grain size ranges from silt to clay with low-angle crinkly internal laminations. This facies exhibits sharp contacts above and below with very fine-grained sandstone, and ranges in thickness from less than 0.5 ft (0.2 m) to 8.5 ft (2.6 m). Fissile mudstone is identified in 4.3% of the total cored interval described (Figure 15).

Silty Mudstone (M_S)

Silty mudstone (Figure 13) is internally structureless, lacks bioturbation, and is light to dark gray. This facies composes 2.0% (Figure 15) of the cored interval and is interbedded with fissile mudstone and rare very fine-grained sandstone. Contacts are gradational into fissile mudstone. This facies varies in thickness from 3 ft (0.9 m) to 4.5 ft (1.4 m).

Coal (C)

Coal in the lower Williams Fork Formation near Grand Valley Field ranges in thickness from 0.5 ft (0.2 m) to 12.0 ft (3.7 m) and is black (Figure 13). Cleats are visible and contacts with other facies are both sharp and gradational. Coal percentage within the described core is 7.9% (Figure 15).

Ripple-Laminated Sandstone (S_R)

Ripple-laminated sandstone (Figure 14) is abundant throughout the cored intervals of the lower Williams Fork Formation. The total percentage is second to planar-laminated sandstone at 21.8% (Figure 15). Grain size varies from very fine sand to lower-fine sand with carbonaceous debris highlighting the types of ripples present. This facies ranges in thickness from less than 0.5 ft (0.2 m) to 16 ft (4.9 m) and is commonly interbedded in less than 0.5 ft intervals with other mudstone facies. Specific types of ripples (i.e. symmetric and a-symmetric) were not differentiated in this facies.

Planar-Laminated sandstone (S_L)

Planar-laminated sandstone (Figure 14) is prevalent throughout all cores described for this study and therefore has the highest occurrence at 27.3%

(Figure 15). This facies exhibits low-to-high angle laminations and grain size ranges from fine to upper-medium/lower-coarse sand. An angle of 15 degrees is used to differentiate between low- and high-angle lamina. Erosional contacts, sharp changes in angle, degree of inclination, and direction of bedding are visible throughout this facies and are delineated on core descriptions (Figure 12; Appendix D). This facies composes the thickest continuous interval of the twelve facies identified with a range from 1 ft (0.30 m) to 31.5 ft (9.60 m). The contacts are commonly gradational with surrounding facies. Mudstone clasts are sometimes present at the base of the planar laminated sandstone facies.

Contorted Sandstone (S_C)

Contorted sandstone consists of inter-bedded sandstone and mudstone, with greater than 50% sandstone (Figure 14). The potential causes of convoluted bedding are soft-sediment deformation and cryptic bioturbation. Thickness ranges from 0.5 ft (0.2 m) to 9 ft (2.7 m). This facies accounts for 12.9% of facies and has gradational upper and lower contacts (Figure 15).

Wavy-Laminated Sandstone (S_{WL})

Wavy-laminated sandstone (Figure 14) contains carbonaceous debris within very fine to fine-grained sandstone. A minor amount of cryptic bioturbation is present. This facies exhibits a thickness of 1.5 ft (0.5 m) and accounts for 0.2% of the total facies (Figure 15). Organic (carbonaceous) drapes are considered low-angle (<15°) to crinkly. This facies shows gradational contacts with surrounding facies.

Structureless Sandstone (S_S)

Structureless sandstone is present in the upper portion of the lower Williams Fork Formation (Figure 14). Thickness ranges from 2.4 ft (0.7 m) to 11.7 ft (3.6 m) and accounts for 0.4% of facies (Figure 15). Grain size ranges from lower-medium to lower-coarse sand. Color of this facies is speckled black and white. No bioturbation or soft-sediment deformation is present. Contacts are gradational into other sandstone-dominated facies.

Bioturbated Sandstone (S_B)

Bioturbated sandstone (Figure 14) is identified within the Rollins Sandstone Member (Iles Formation; Figure 2, 3). Bioturbated sandstone was identified in 14.1 ft (4.3 m) of core and accounts for 23.5% of the facies examined in the Rollins Sandstone Member. Bioturbation is from *Ophiomorpha* burrows within fine-to medium-grained sandstone. The internal stratification varies from planar-parallel laminated to structureless sand. *Ophiomorpha* burrows range in size from the millimeters to inches in cross-sectional view (Figure 14). Thickness of this facies ranges from 6.5 ft (1.8 m) to 12 ft (3.7 m). The Rollins Sandstone Member is interpreted as a marine sandstone (Hettinger and Kirschbaum, 2002).

FACIES ASSOCIATIONS AND ARCHITECTURAL ELEMENTS

Facies associations are defined by Collinson (1969) as groups of facies that have a genetic relationship with one another, as well as some type of environmental significance. The 12 facies identified in core are grouped into three facies associations and four architectural elements (Table 3). Facies

Table 3 Summary of facies associations and archtiectural elements

Facies Association Name	Architectural Element Name	Description	Interpretation	Color
Fluvial Channel Sandstone	Point Bar	Overall fining upward sequence including all facies other than coal	Point Bar	
Crevasse Splay and Floodplain	Crevasse Splay	Coarsening upward sequence of facies	Crevasse Splay	
Crevasse Splay and Floodplain	Floodplain	Mudstone isolated within sandstone bodies and other mudstone facies without having an association to any other facies in the core.	Floodplain	
Coal	Coal	Carbonaceous black coal	Marsh	

associations include fluvial-channel sandstones, crevasse splays and floodplain, and coal (Table 3).

Architectural elements are a morphological subdivision of a depositional system characterized by a distinctive assemblage of facies, facies geometries, and depositional processes (Walker and James, 1992). Additionally, an architectural element is defined by the nature of the lower and upper bounding surfaces, internal geometry, thickness and lateral extent (scale), and internal geometry (Miall, 1985). Architectural elements defined include: point bar, crevasse splay, coal, and floodplain (Figure 16; Table 3).

Point Bar

Within the lower Williams Fork Formation, isolated-to-amalgamated sandstone bodies serve as the main reservoir units and are typically associated with fluvial systems (Cole and Cumella, 2005, Panjaitan, 2006; Pranter et al., 2007, 2008, 2009, 2011 *in press*; Pranter and Sommer, 2011). Highly sinuous meandering fluvial systems are the dominant transport and depositional mechanisms (Cole and Cumella, 2005, Panjaitan, 2006; Pranter et al., 2007, 2008, 2009, 2011 *in press*; Pranter and Sommer, 2011). Although lateral continuity of these sandstone deposits is not represented in core, outcrops have been analyzed to determine their spatial extent in the lower Williams Fork Formation (Table 1; Cole and Cumella, 2005, Panjaitan, 2006, Pranter et al., 2007, 2009; Pranter and Sommer, 2011).

Gamma-ray log response for point bars typically show an increase in gamma-ray values that is representative of an upward-fining grain-size trend

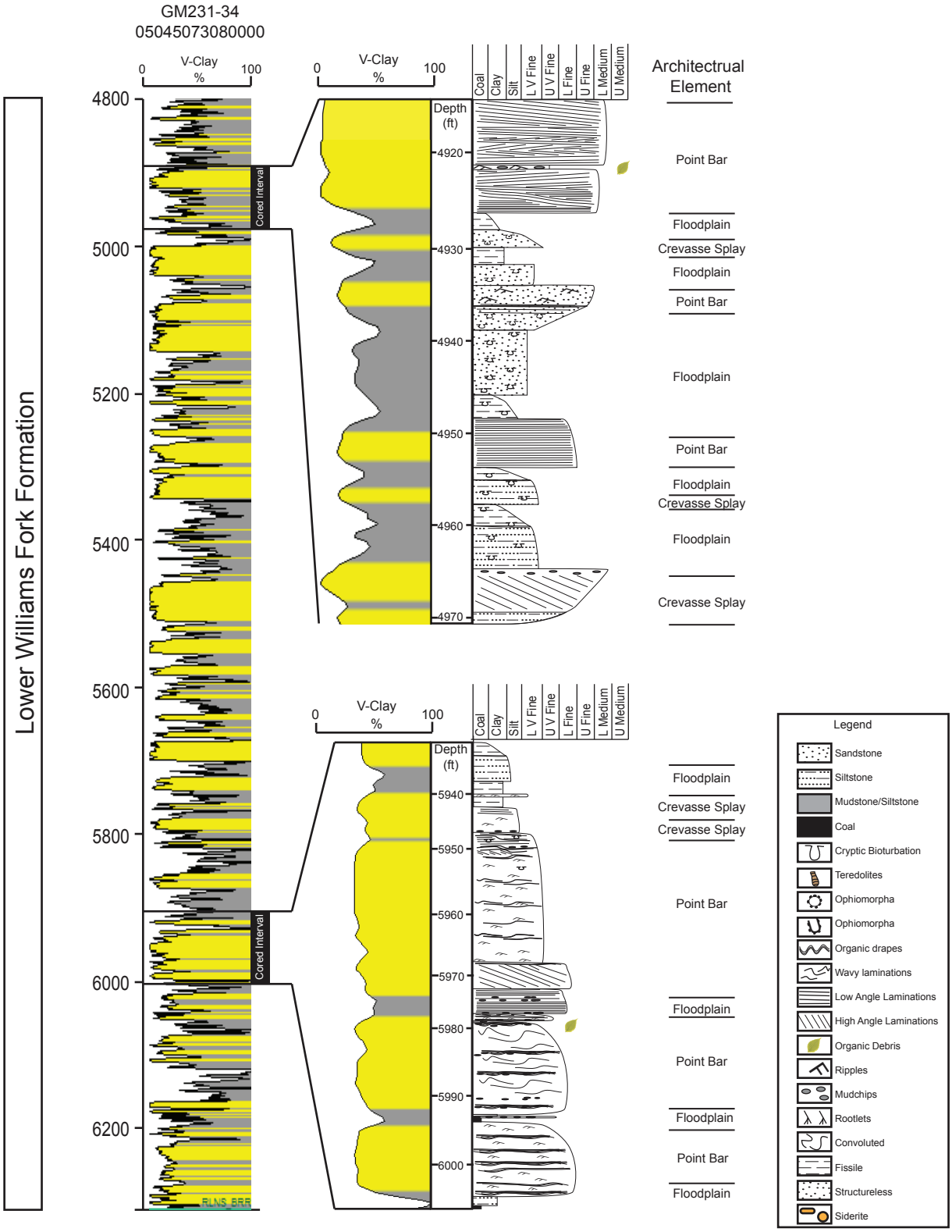

Figure 16: Diagrammatic sketch of core description for core GM231-34. Architectural elements shown in comparison to v-clay log response and core description.

(Figure 12). Typical vertical facies change from bottom to top is structureless sandstone to planar-laminated sandstone inter-bedded with ripple-laminated sandstone, and fine into contorted sandstone and wavy-laminated sandstone. These facies are deposited through the migration and lateral accretion of fluvial-channel sandstone within a meandering river system (Walker, 1984, 1992; Miall, 1992; Miall, 2006).

Mudstone facies overlie the sandstone-dominate facies and represent a decrease in energy of the fluvial system. No specific stacking pattern exists for mudstone facies other than an overall fining of grain size. Coal commonly overlies the mudstone facies. A mudstone lag is typically present at the base of point bars, presenting a sharp contact with the underlying mudstone plug of the channel.

For the lower Williams Fork Formation, point bars (N=44) compose 67.7% of the architectural elements described and are the dominant gas-bearing reservoirs at Grand Valley Field (Figure 17). Apparent thicknesses of point bars are measured in cored wells and compared to outcrop dimensional data (Pranter et al., 2009; Figure 18). Apparent thickness ranges from a minimum of approximately 3 ft (1 m) and a maximum of 34 ft (10.4 m). The average thickness of point bars in the lower Williams Fork Formation from core is approximately 9 ft (2.7 m) thick. Although thicknesses are measured from core descriptions, the location where the well bore intersected the point bars is not known; therefore the measurement is an apparent thickness value and, in most cases, is likely to be less than the maximum thickness of the deposit.

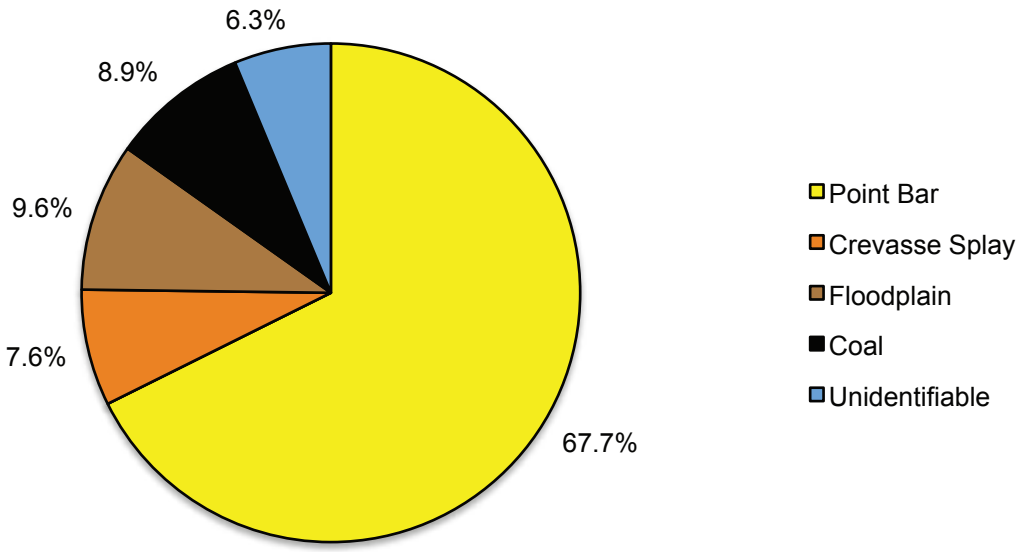

Figure 17: Architectural element percentages for the lower Williams Fork Formation at Grand Valley Field. Architectural elements include point bar, crevasse splay, floodplain, and coal. Facies that did not have a specific assemblage or were isolated were identified as unidentifiable. 14.9% of described core is from the upper Williams Fork Formation and not included in the main architectural elements described.

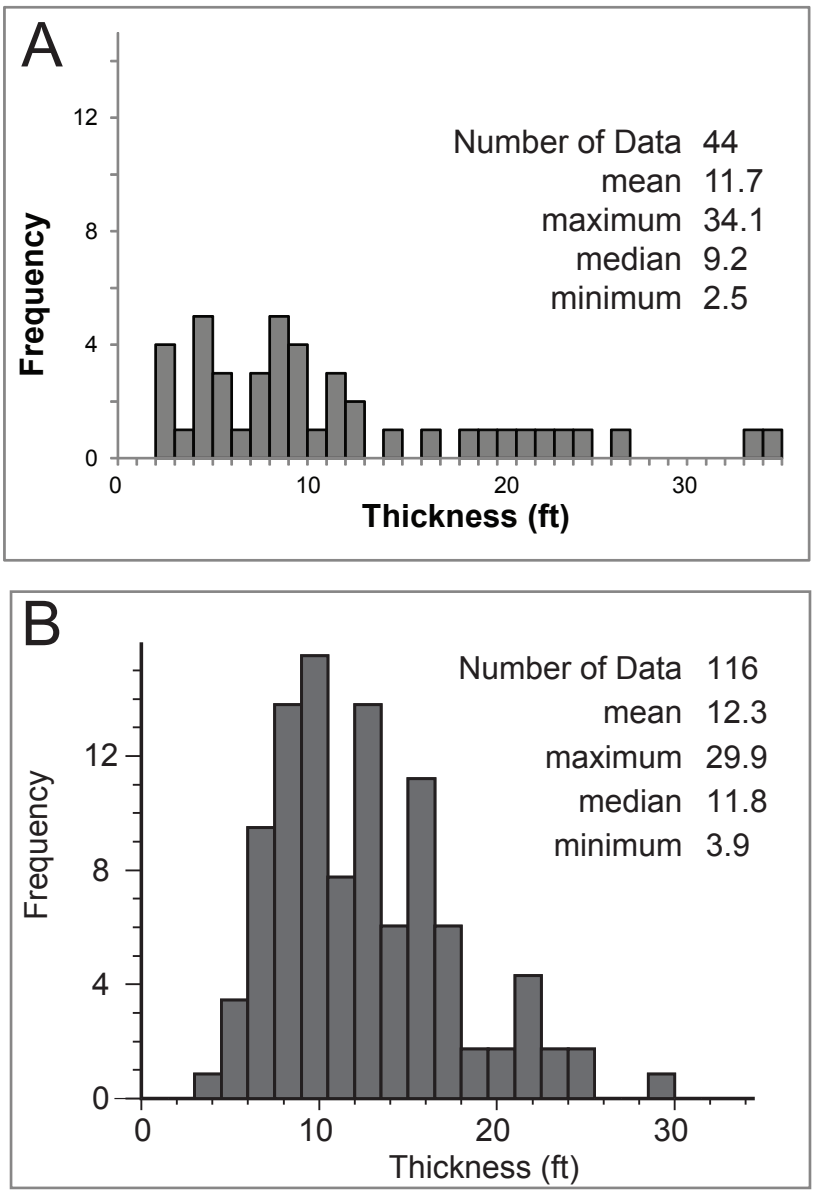

Figure 18: Thickness histograms of point bars from core in comparison to outcrop measurements. (A) Point-bar thickness from lower Williams Fork Formation cores. (B) Point-bar thickness for the lower Williams Fork Formation based on outcrop measurements (Cole and Cumella, 2005; Panjaitan, 2006; Pranter et al., 2009). Outcrop histograms modified from Pranter et al., 2009.

Dimensional data from outcrops located approximately 20 mi (32 km) to the southwest show that point bars (N=116) range in thickness from 3.9-29.9 ft (1.2-9.1 m) and from 44.1-1699.8 ft (13.4-518.1 m) in apparent width (Figure 18, Pranter et al., 2009). Core point bars (N=44) ranged in thickness from 3 - 35 ft (0.9-10.7 m; Figure 18).

Crevasse Splay

Crevasse splays form following break-through of channel banks. Water and sediment travel into the floodplain, and sometimes lake deposits (Figure 12; Bridge and Tye, 2000; Miall, 2006). In a meandering river system, crevasse splays tend to be similar to small deltaic deposits and have a coarsening-upward trend in grain size (Bridge and Tye, 2000; Bridge, 2006). Sedimentary structures from base to top of a typical crevasse splay include organic-rich mudstone at the base, followed by laminated silty mudstone, contorted sandstone from bioturbation, and ripple-laminated sandstone (Figure 16).

Thicknesses of crevasses splays (N=7) were measured and account for 7.6% of the lower Williams Fork Formation (Figure 19). Similar to point bars, there is no way of knowing where the well bores intersected the crevasse splays. Apparent thickness values range from of 3-12 ft (0.9-3.7 m). For comparison, outcrops located approximately 20 mi (32 km) to the southwest at Coal Canyon (Figure 1) show that crevasse splays (N=279) range in thickness from 0.5-15.0 ft (0.2-4.6 m) and from 40.1-843.3 ft (12.2-257.0 m) in apparent width (Figure 19; Pranter et al., 2009).

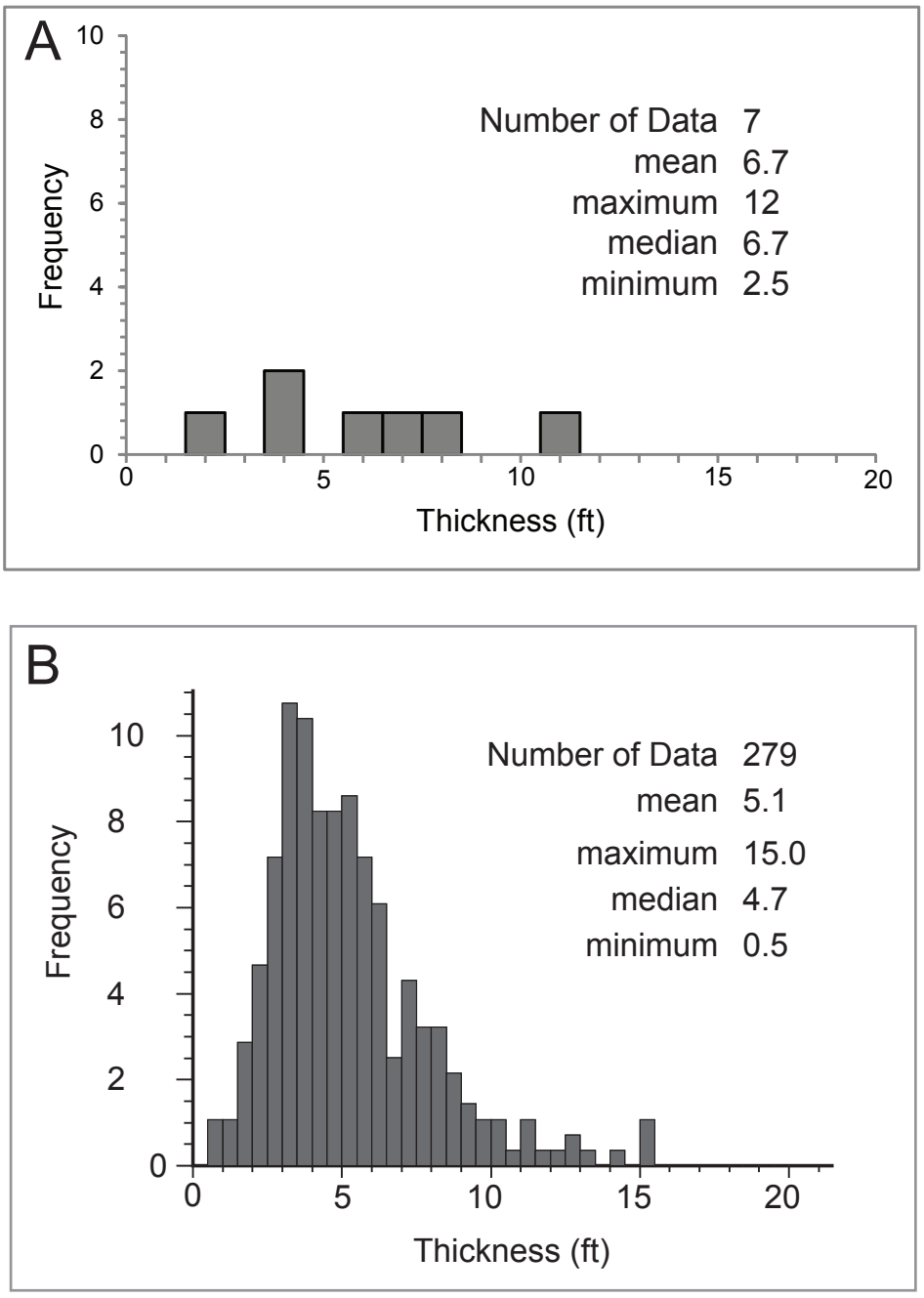

Figure 19: Thickness histograms of crevasse splays from core in comparison to outcrop measurements. (A) Crevasse-splay thickness from lower Williams Fork Formation core. (B) Crevasse-splay apparent thickness for the lower Williams Fork Formation based on outcrop measurements (Cole and Cumella, 2005; Panjaitan, 2006; Pranter et al., 2009). Outcrop histograms modified from Pranter et al., 2009.

Floodplain

The floodplain architectural element dominates the lower Williams Fork Formation and represents a laterally continuous medium surrounding ancient fluvial channels and meander belts, composed of mudstone-rich facies and semi-isolated to isolated, lenticular crevasse splays (Bridge, 2006). Crevasse splays and floodplain were combined as a facies association because they have similar genetic relationships of facies and share the same environment. Floodplain facies are typically laterally continuous throughout a meandering system and act as a medium for crevasse splays (Bridge, 2006). Crevasse splays and floodplain were identified as separate architectural elements because they have different dimensions, internal and external geometries, and bounding surfaces (Miall, 1985). The internal geometry of a floodplain is dominated by mud while crevasse splays are composed of a combination of mud and sand.

Specific facies associated with the mudstone-dominated floodplain include: contorted mudstone, carbonaceous mudstone, silty-laminated mudstone, fissile mudstone, and silty mudstone. Floodplain deposits account for 9.6% of architectural elements in the lower Williams Fork Formation based on core (Figure 17). Although floodplain is prevalent within the lower Williams Fork Formation, it is not commonly found in core. This is due to the high cost of taking whole-core and reservoir intervals being targeted.

Coal

Coal is identified as a key facies, facies association, and architectural element in this study (Table 2, 3; Figure 13). Coal is representative of a marsh or

swamp that is rich in organics and has a characteristic reducing environment (Bridge, 2006). Coal takes on a three dimensionality and an interpretation of environment of deposition can be applied (Allen, 1983; Walker, 1992). Coal beds range in thickness from 0.5 ft (0.2 m) to 12 ft (3.7 m) and account for 8.9% of the total lower Williams Fork Formation core (Figure 17).

Unidentifiable

Throughout the cored intervals described, missing sections and extremely thin intervals were present. Unidentifiable intervals, without any discernable stratigraphic pattern of facies, account for 6.3% of architectural elements (Figure 17).

CORE-TO-LOG COMPARISON

The facies, facies associations, and architectural elements described in core are compared to well-log responses to establish criteria to calculate lithology and manually interpret architectural elements in non-cored wells. Well-log data include 328 V-Clay logs and Coal Flags within the eight square mile study area (Figure 5).

A V-Clay log is the volume of clay calculated by using a cross plot of normalized neutron-porosity and bulk density. V-Clay logs were used rather than gamma-ray logs due to the feldspathic nature of the Williams Fork Formation (Schlumberger Log Interpretation Charts, 1989; M. Connolly, personal communication, 2011). Gamma-ray logs typically show higher API units for sandstone due to the radiogenic feldspars, which increase gamma-ray values in

potassium. Thus, causing arkosic sandstone to look similar to shale/mudstone (Schlumberger Log Interpretation Charts, 1989; M. Connolly, personal communication, 2011). V-Clay and gamma-ray logs were compared prior to using V-Clay logs for manual interpretation of architectural elements (Figure 20). The comparison of a V-Clay and gamma-ray log show the difference between using a V-Clay log versus a gamma-ray log for the calculation of sandstone and mudrock from these well-logs (Figure 20). V-Clay logs consistently show a greater amount of sandstone than gamma-ray logs for the lower Williams Fork Formation.

Gamma-ray logs measure the natural radioactivity of the rock, whereas V-Clay logs estimate the volume of clay present. V-Clay logs are created by applying three data points within the neutron-porosity and bulk-density cross plot to differentiate sand versus clay. Two sand points are plotted to represent the values containing zero percent clay. Data points on the cross plot that have values that are at or higher than the trend of the two sand points are considered to be 0% clay. The third point used is referred to as a clay point. The clay point is plotted to represent data containing 100% clay. To create V-Clay logs, all values on the cross plot are assigned a percentage of clay volume depending on their position on the plot relative to the sand and clay points. (Schlumberger Log Interpretation Charts, 1989; M. Connolly, personal communication, 2011)

V-Clay logs were used to calculate lithology logs using a cut off of 25%. V-Clay values that are ≥ 25% are considered mudrock (Figure 21), and V-Clay values < 25% are sandstone. Coal flags are used to determine where coal is

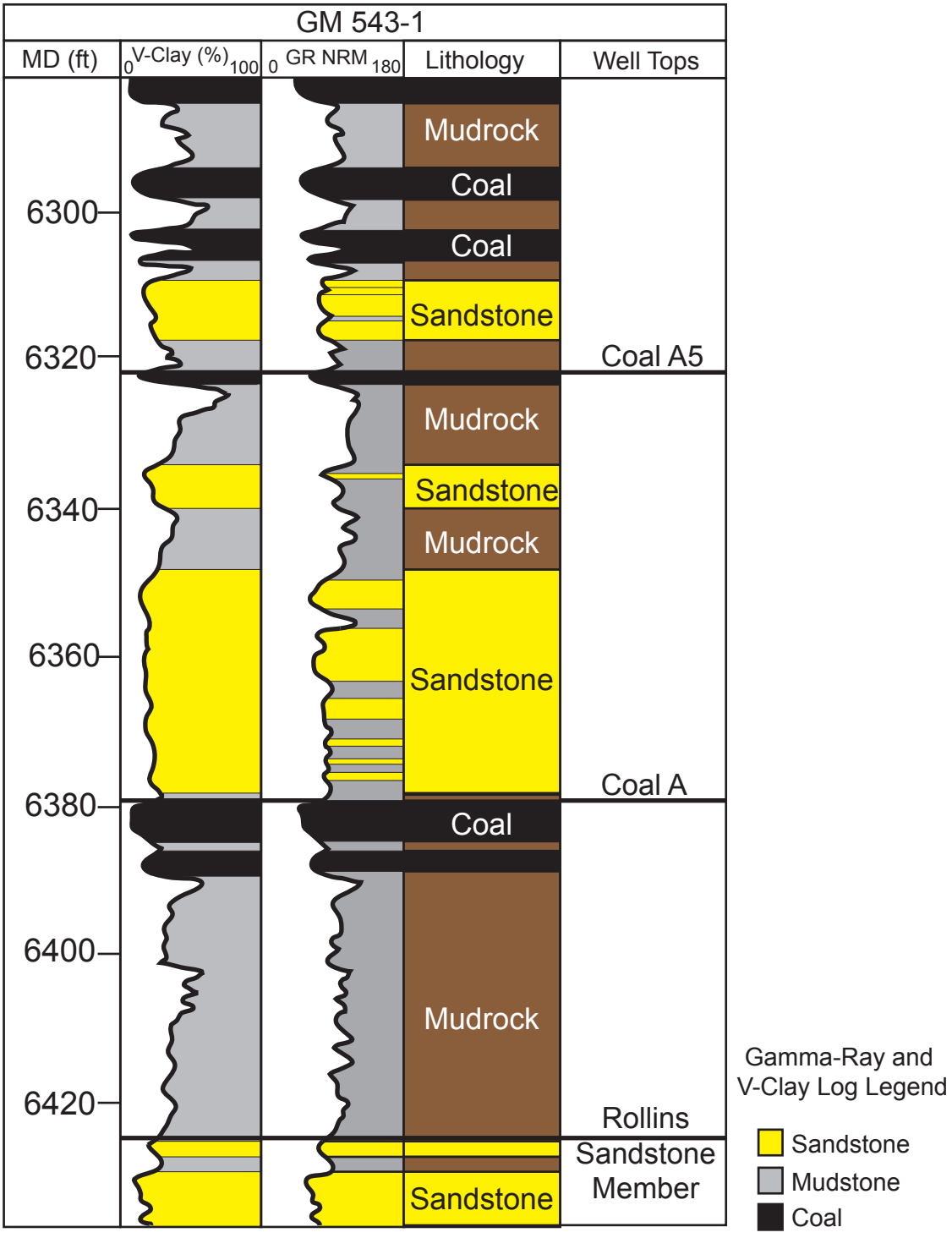

Figure 20: Normalized gamma-ray log compared to v-clay log. The API cut-off used to calculate sandstone versus mudrock is 75 API. The cut-off used to calculate sandstone in the V-Clay log is 25% or less clay is considered sandstone.

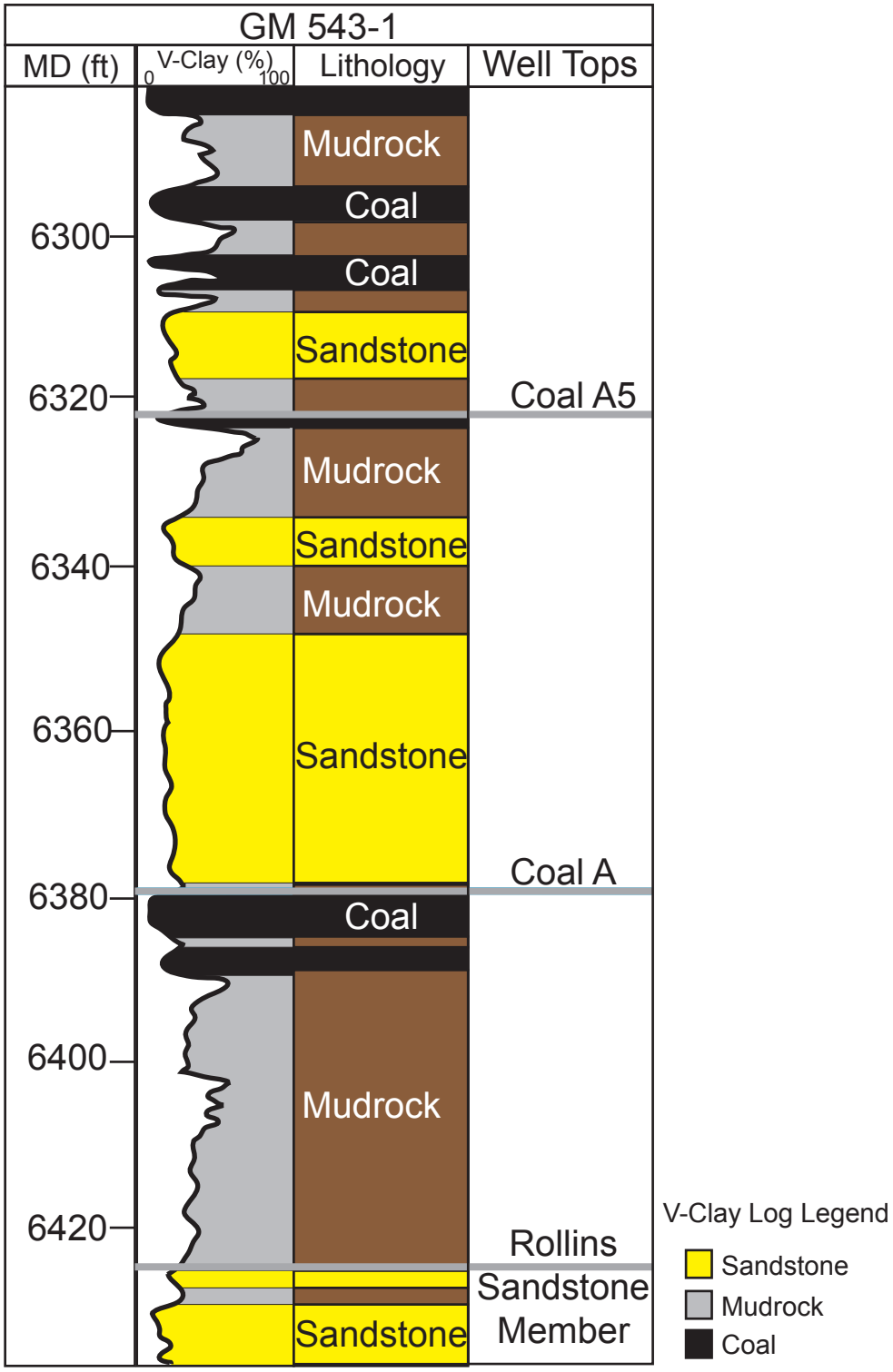

Figure 21: Lithology logs are calculated from a v-clay cutoff. If v-clay is less than 25% (0.25) then lithology is considered to be sandstone. If v-clay is greater than 25% (0.25) then lithology is considered to be mudstone. Coal is identified using the following cut-offs: Gamma-ray < 70 (API), Bulk Density < 2.2 (gm/cm3), and Deep Resistivity > 40 (ohm-m).

present in calculated lithology logs, and interpreted architectural elements. Calculation of the coal-flag log corresponds to the following cut-offs: Normalized gamma-ray < 70 API, normalized bulk-density < 2.2 g/cm^3, deep resistivity (ILD) > 40 OHMM.

To evaluate the stratigraphic variability of fluvial deposits, architectural-element logs were interpreted from the calculated V-Clay logs (Figure 22). Interpreted architectural elements include: point bars and crevasse splays. Floodplain and coal are differentiated in all calculated lithology logs and architectural element logs from cut offs previously described.

Point bars and crevasse splays were interpreted for sandstone intervals using outcrop statistics measured at Coal Canyon (Panjaitan, 2006; Pranter et al., 2009), core description, and typical gamma-ray log responses (Can't, 1992; Figure 23). Interpreted top and base surfaces of point bars and crevasse splays were based on observable inflections, or breaks, in the V-Clay log response. These inflections can occur due to grain-size change, erosional contact, or increase in clay content (Rider, 2002a, 2002b).

SPATIAL VARIABILITY OF FLUVIAL DEPOSITS

Spatial variability of fluvial deposits at Grand Valley Field was analyzed using calculated lithology logs, interpreted architectural-element logs, vertical proportion curves of lithology and architectural-elements, and stratigraphic maps (gross-interval isopachs, sandstone percent, point-bar percent, and crevasse splay percent; Appendix E).

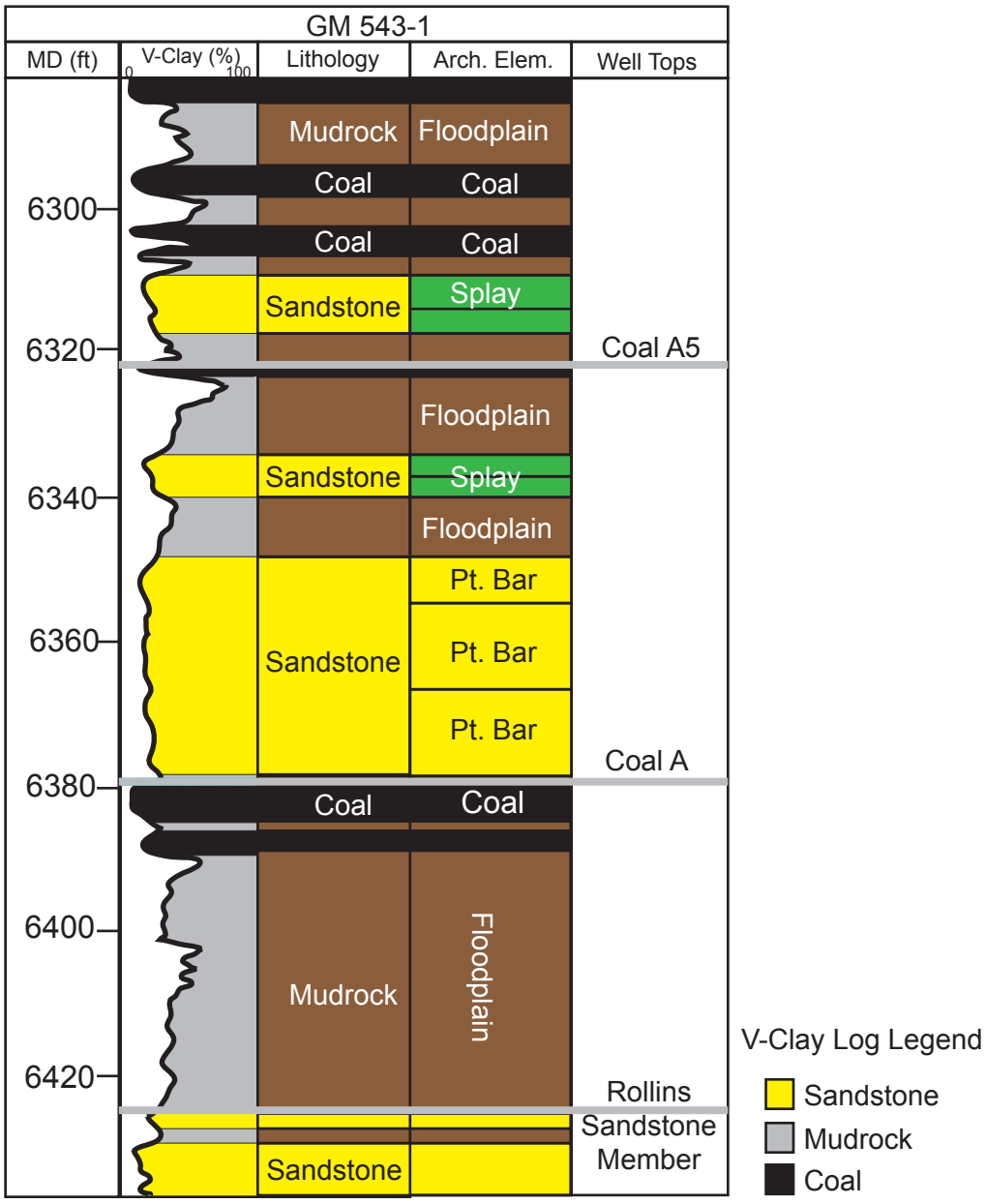

Figure 22: Architectural-element logs were manually interpreted using core and outcrop dimensional data for reference. Point bars commonly show a fining-upward log response and range in thickness from 3 - 30 ft (1 - 9.1 m). Crevasse splays generally coarsen upward and show a thickness range from ~1 - 15 ft (0.3 - 4.6 m). Coal is identified from the coal flag. Floodplain intervals correspond to mudrock intervals based on the v-clay cut-off. Refer to Figure 5 for the well location.

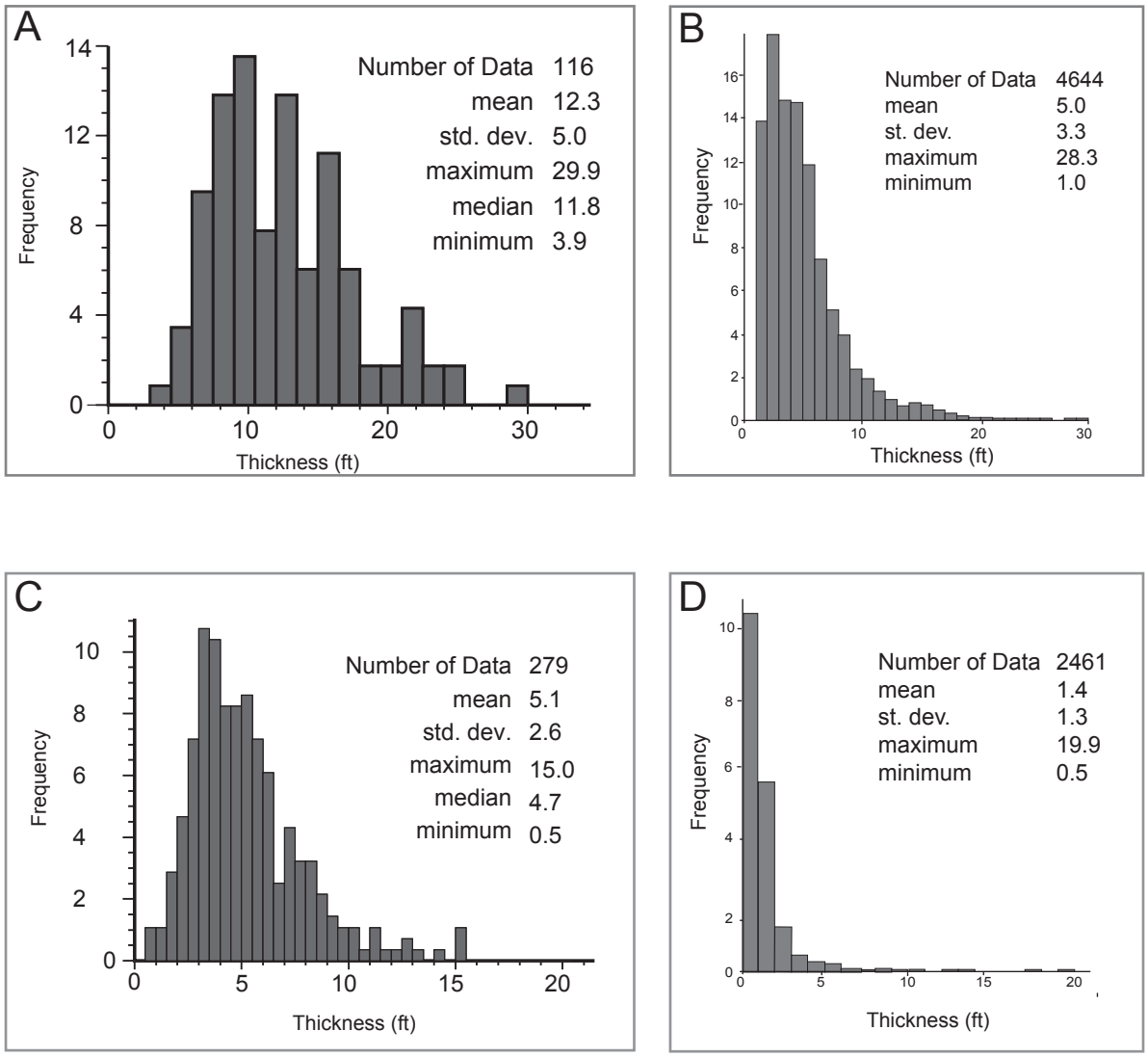

Figure 23: Historgrams showing apparent thickness of (A) point bars in the lower Williams Fork Formation at Coal Canyon (B) interpreted point bars from original architectural element well logs (C) crevasse splays identified in the lower Williams Fork Formation at Coal Canyon in the Piceance Basin, and (D) crevasse splays from original well architectural element well logs. Modified from Pranter et al., 2009.

The stratigraphic framework of the lower Williams Fork Formation at Grand Valley Field was subdivided into 11 intervals based on the interpretation of 12 stratigraphic horizons that were correlated throughout the 8-section study area. V-Clay logs were used to correlate stratigraphic horizons (Figures 24, and 25). The stratigraphic surfaces include: Rollins Sandstone Member, Coal A, Coal A5, Coal B, Coal D, Coal E, Coal F, Middle Sandstone, FS Middle Sandstone, Regressive Marker Cameo, Coal Ridge Coal Zone, and Top lower Williams Fork Formation (Figure 24, 25). In addition to the 12 correlated stratigraphic surfaces, in the model area 9 additional surfaces were defined using the lithology vertical-proportion curve and the changes in the proportion of mudrock and sandstone (Figure 26). Additional stratigraphic surfaces are positioned on specific layers based on identifying 9 major changes in proportion of mudrock and sandstone. These surfaces are identified by layer number and were correlated using the vertical proportion curve (Figure 26). These stratigraphic horizons were used to create zones in the 3-D modeling of fluvial sandstones.

Within the study area, wells were drilled on an irregular 10-ac [4-hectare; 430,600 ft^2 (40,468 m^2)] spacing [330 ft (100 m) north to south and 1,320 ft (402 m) east to west]. Stratigraphic cross-sections that are oriented from west to east and north to south were created to include all wells in the correlation process (Figures 24, and 25). First, west-to-east cross sections are correlated. This is the primary paleocurrent direction of fluvial-channel deposition. Then, cross sections created in the north-to-south direction were analyzed.

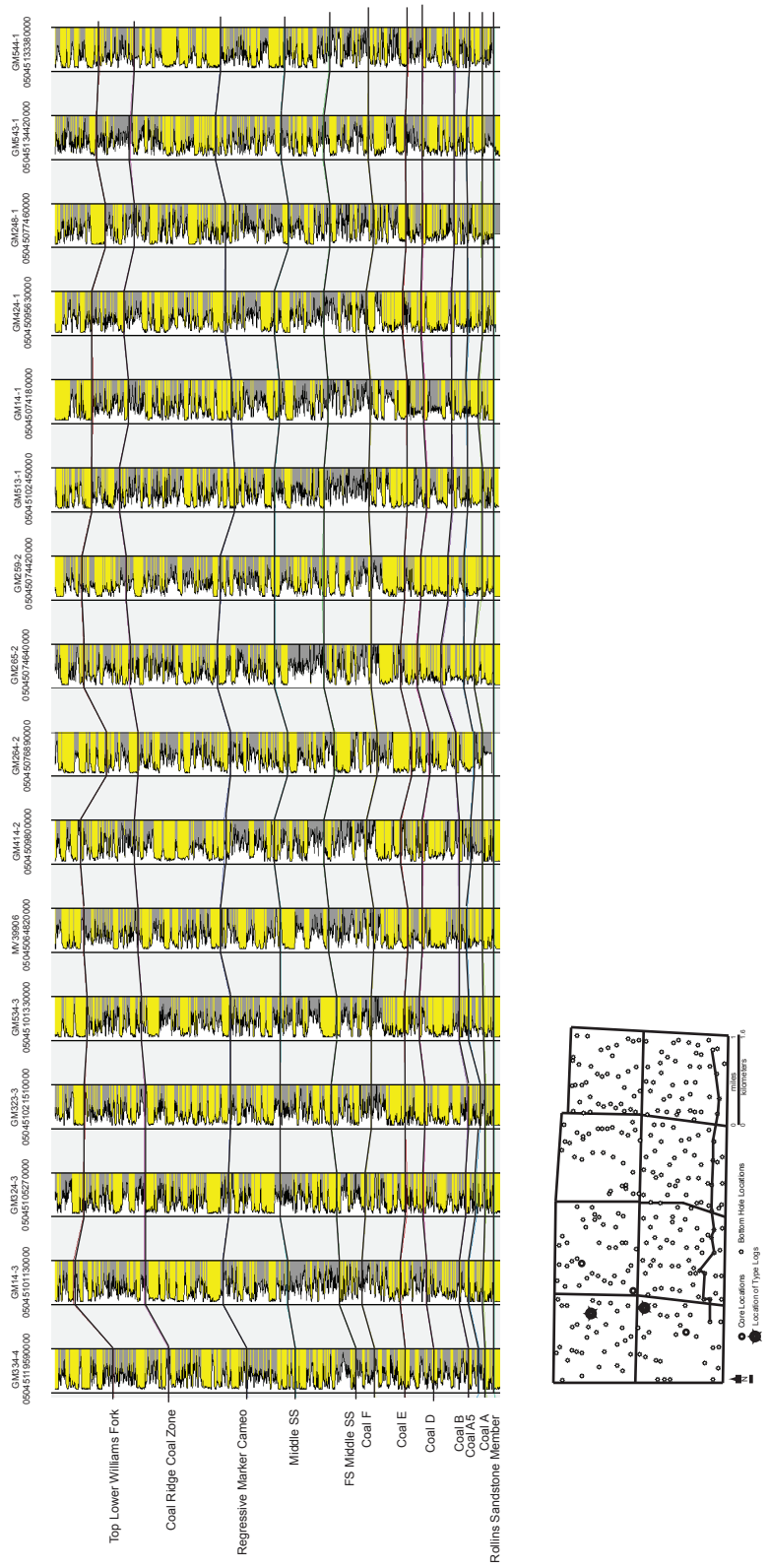

Figure 24: Stratigraphic cross section A-A’ of the lower Williams Fork Formation flattened on the Rollins Sandstone Member.

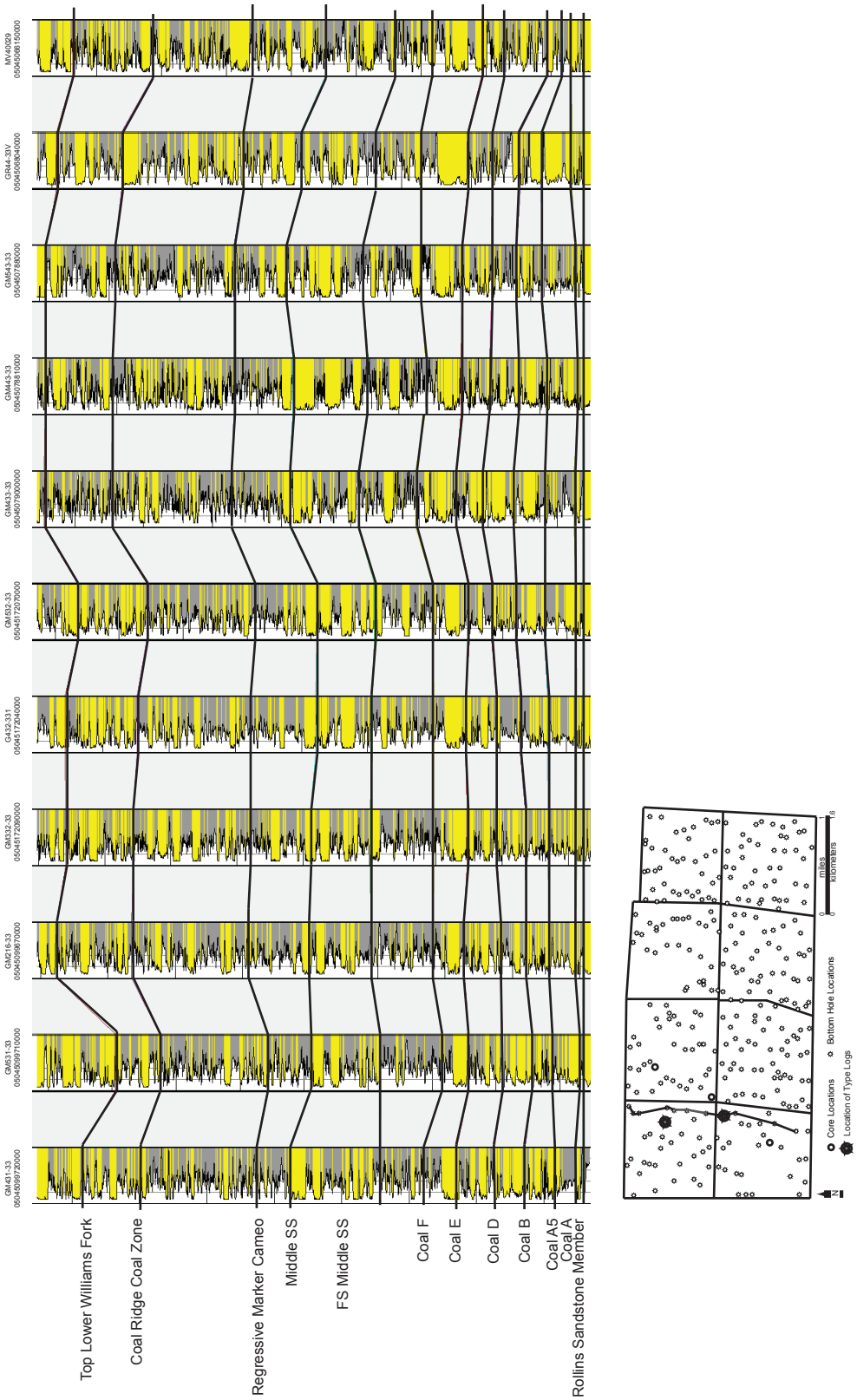

Figure 25: Stratigraphic cross section B-B’ of the lower Williams Fork Formation flattened on the Rollins Sandstone Member.

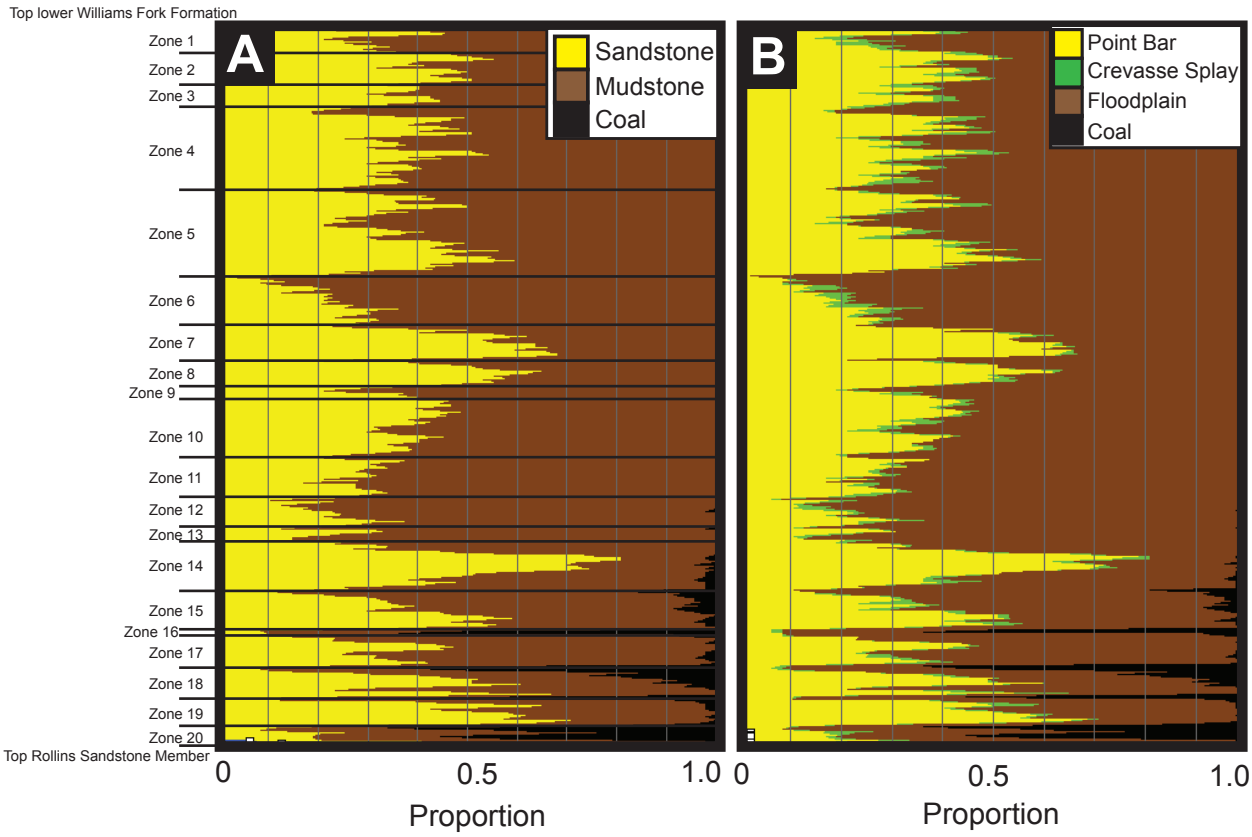

Figure 26: Vertical proportion curves of (A) lithology logs, and (B) architectural-element logs. In addition to the 12 stratigraphic surfaces, 9 additional stratigraphic surfaces were created by using the lithology vertical proportion curve (A) based on major changes in the proportion of sandstone to mudstone within the lower Williams Fork Formation. The stratigraphic intervals between surfaces are referred to as zones.

Within the stratigraphic framework and following the calculation of lithology logs and interpretation of architectural element logs, vertical-proportion curves were created using all wells. Vertical proportion curves show a 1-D trend (values between 0 and 1.0) of the stratigraphic variability in the proportion of lithology and architectural elements. Vertical-proportion curves were calculated at 4-ft (1.2 m) intervals from the Rollins Sandstone Member to the base of the Middle Williams Fork. These curves, created for lithology and architectural elements, show stratigraphic changes of the respective proportions versus depth (Figure 26).

To determine the spatial and stratigraphic variability of sandstone and architectural elements in the lower Williams Fork Formation, maps of sandstone and fluvial-architectural element percent (%) were created for the 8-section study area. For each of the 11 zones, gross-interval isopachs and sandstone percent maps were generated, as well as maps of point-bar and crevasse splay percent. Percentage maps are not created for zones between the 9 surfaces determined from the vertical proportion curve because those specific horizons are only present within the 1 mi^2 (2.6 km^2) modeling area (Figure 26).

Percentage maps were compared to gross-interval isopach maps for each zone (Figures 27, and 28). Three zones, out of eleven, are displayed in Figures 26 and 27 for comparison of low, medium, and high net-to-gross zones. Zones 1, 6, and 10 are shown on percentage maps (Figures 27, and 28). Gross-interval isopach and sandstone percent maps show the thickest interval and percentage of sandstone in zone 1, the top of the lower Williams Fork Formation. Both

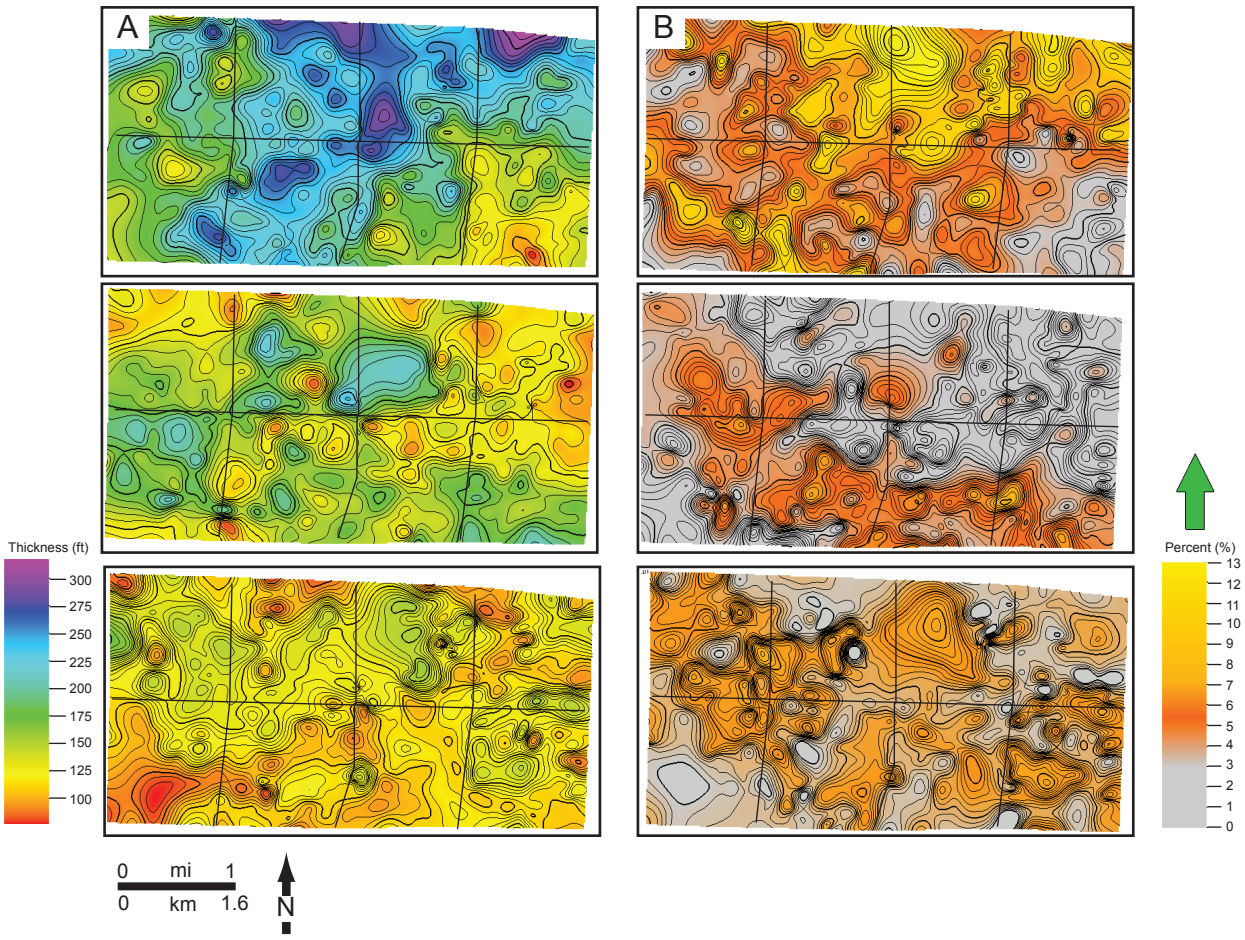

Figure 27: A) Isopach maps of zones 1, 6, and 10 (from top to bottom) showing thickness of each zone. B) Maps of 8-section study area showing sandstone percent.

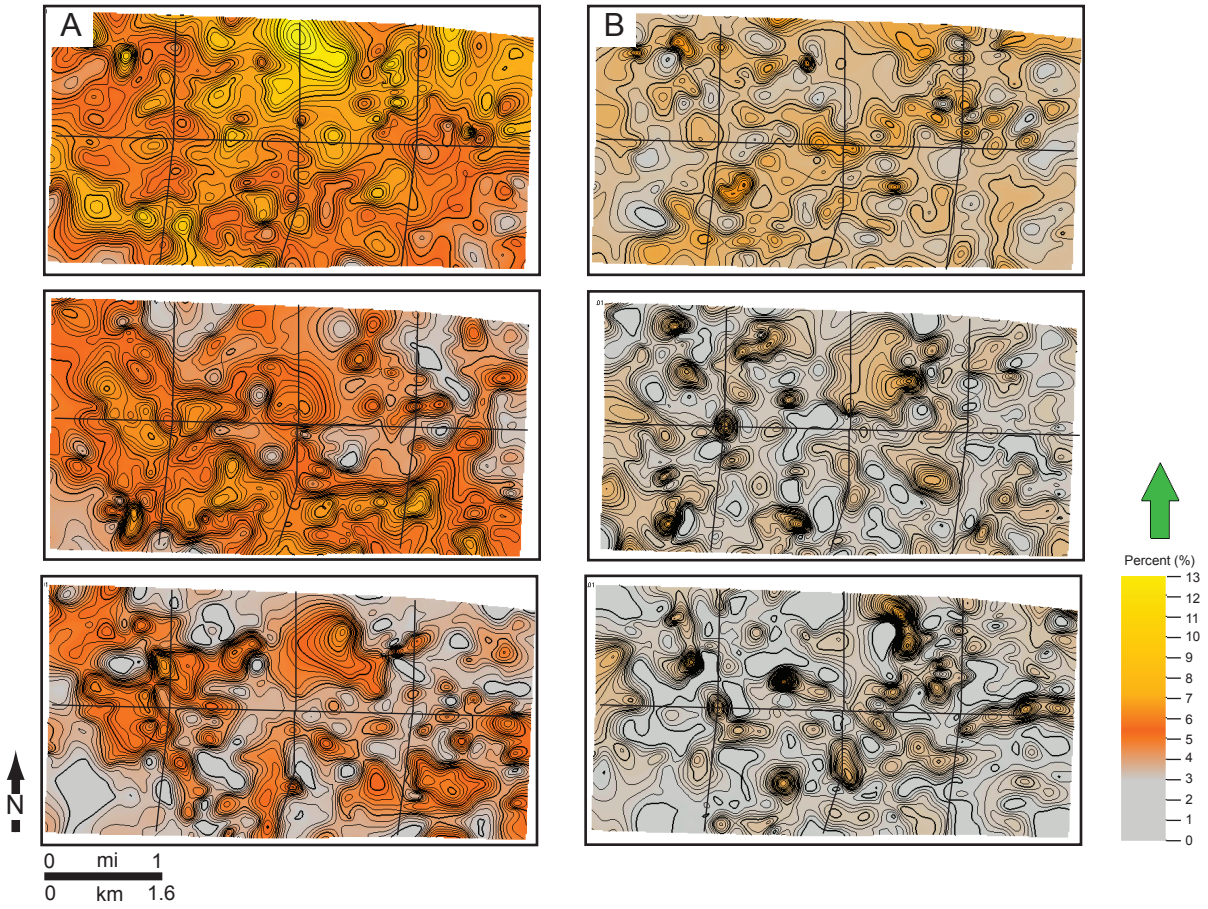

Figure 28: A) Maps showing percent of point bars in zones 1, 6, and 10 (from top to bottom). B) Maps of 8-section study area showing crevasse splay percent.

percent sandstone and gross interval isopach thickness decreases lower in the stratigraphic section. Point-bar and crevasse splay percent decreases lower in the stratigraphic section. The overall decrease in sandstone percent and thickness corresponds to the decrease in thickness and percent of point bars and crevasse splays, due to these architectural elements having been deciphered from sandstone in V-Clay logs.

Percentage maps of architectural elements show a stratigraphic decrease upward throughout the lower Williams Fork Formation in coal from 2% in zone 10 (within the Cameo Coal Zone) to 0% in zone 1. The amount of sandstone increases upward, as does the percentage of point bars. The percentage of sandstone increases from 6% in zone 10 to 8% in zone 6, and 13% in zone 1 (Figure 27). Point bars increase from 6% in zone 10 to 7% in zone 6 to 12% in zone 1 (Figure 28). Crevasse splays do not show a significant increase or decrease between zones 10 and 1. Zone 10 shows 3% splays, with zone 6 and zone 1 showing 2% and 3% respectively (Figure 28).

Lateral distribution of sandstone and architectural-elements throughout the Lower Williams Fork Formation was qualitatively assessed using the stratigraphic maps created. Sandstone and point-bar distribution trend from north-east to south-west throughout the 8-section study area with some variance due to the system meandering throughout deposition. Crevasse splays are sporadically thick adjacent to the thickest point bars.

Evaluation of the percentage and lateral distribution of point bars, crevasse splays, and total sandstone throughout the lower Williams Fork

Formation at Grand Valley Field coincide with previous results that the overall sandstone content, and therefore net-to-gross ratio, increases stratigraphically higher (Cole and Cumella, 2005, Pranter et al., 2009).

RESULTS

Within the lower Williams Fork Formation at Grand Valley Field, twelve facies were identified in cores and include: contorted mudstone, organic-rich (carbonaceous) mudstone, laminated mudstone, fissile mudstone, silty mudstone, coal, ripple-laminated sandstone, planar-laminated sandstone, contorted sandstone, bioturbated sandstone, wavy-laminated sandstone, and structureless sandstone (Table 2; Figures 13, 14). From the twelve facies identified, three facies associations were described: channel sandstone, floodplain and crevasse splay, and coal. Further differentiation into architectural elements includes: point bar, crevasse splay, coal, and floodplain (Table 3).

Apparent thicknesses of point bars in core (N=44) range from 3 - 35 ft (0.9-10.7 m; Figure 18). Point bars in interpreted architectural-element logs (N=4644) range from 2-29.3 ft (0.6-8.9 m). Crevasse splays (N=7) measured account for 7% of core described (Figure 17, 19) with an apparent-thicknesses range of 3-12 ft (0.9-3.7 m). Crevasse splays interpreted in architectural element logs (N=2461) show a range of 1-19.9 ft (0.3-6.1 m).

The stratigraphic framework of the lower Williams Fork Formation at Grand Valley Field was analyzed using 12 key stratigraphic horizons correlated throughout all 328 wells in the 8-section modeling area (Figure 24, 25). V-Clay

logs were used to correlate stratigraphic horizons. 11 zones were differentiated from the stratigraphic horizons showing a range of thicknesses from 39 - 348 ft (12 – 106 m). Nine additional zones were differentiated using the vertical proportion curve, creating 20 total zones.

Stratigraphic mapping is useful as a quantitative and qualitative analysis of the fluvial deposits. Percentage maps of architectural elements showed a stratigraphic decrease upward throughout the lower Williams Fork Formation in coal from 2% in zone 10 (within the Cameo Coal Zone) to 0% in zone 1. The percentage of sandstone increased from 6% in zone 10 to 8% in zone 6, and 13% in zone 1 (Figure 24). Point bars increased from 6% in zone 10 to 7% in zone 6 to 12% in zone 1 (Figure 25). Crevasse splays account for 3% in zone 10, with zone 6 and 1 having 2% and 3% respectively (Figure 25).

DISCUSSION

Dimensional data from outcrop of the lower Williams Fork formation at Coal Canyon show that point bars (N=116) range in thickness from 3.9-29.9 ft (1.2-9.1 m) and crevasse splays (N=279) range in thickness from 0.5-15.0 ft (0.2-4.6 m) in apparent width (Figure 20; Pranter et al., 2009). Outcrop statistics compare to manually interpreted point bars in the architectural-element logs. Apparent thickness of point bars in architectural element logs (N=4644) ranges from 2-29.3 ft (0.6-8.9 m). The thinnest point bar interpreted in architectural elements logs is 1.9 ft (0.6m) thinner than that measured in outcrop. The reason for this difference is the inability to access and interpret these deposits in outcrop,

the resolution of LiDAR, due to scree cover of thin point bar deposits in outcrop, or due to an inaccurate interpretation of architectural element logs. Crevasse splays in core show an apparent-thicknesses range of 3-12 ft (0.9-3.7 m). Crevasse splays interpreted in architectural-element logs (N=2461) show a range of 1-19.9 ft (0.3-6.1 m). The ranges of thickness in interpreted crevasse splays fall within, and slightly above the range of crevasse splays measured in outcrop. Reason for the interpreted maximum thickness difference of 4.9 ft (1.5 m) could be due to the identification of internal heterogeneity in outcrop that was not visible on the manually interpreted V-Clay logs that did not contain core.

Sandstone-body deposits and architectural elements vary throughout the lower Williams Fork Formation and show spatially complex interactions. Results of percentage changes in lithology and architectural elements show an increase in sandstone content, therefore indicating the potential change in fluvial systems upward in the lower Williams Fork formation. This study would need to be coupled with a similar one performed on the upper Williams Fork Formation to analyze the change in lithology and architectural element percentage.

CHAPTER THREE

FLUVIAL RESERVOIR MODELING

Three modeling scenarios were conducted to represent the spatial distribution of the fluvial deposits in the lower Williams Fork Formation. Given the uncertainty of fluvial sandstone-body geometry multiple scenarios were investigated to compare differences in geometries on associated static and dynamic connectivity. Multiple-point geostatistical modeling was used for all modeled scenarios. Multiple-point geostatistical modeling, also referred to as multiple-point geostatistics (Caers and Zhang, 2004) and multiple-point statistics (MPS; Strebelle, 2002, 2006) is herein referred to as MPS modeling.

MPS modeling was the modeling method used for all modeled scenarios in this study. MPS modeling is a pixel-based method of modeling using training images rather than variograms as the primary control (Strebelle, 2000; Strebelle and Journel, 2001; Caers and Zhang, 2004; Strebelle, 2006; Arpat and Caers, 2007). The theoretical framework of multiple-point geostatistical modeling (MPS) is thought to have been developed by Journel and Alabert in 1989 (Strebelle and Journel, 2001). Guardiano and Srivastava (1993) revisited the concept in 1993, but their application was not practical (Strebelle and Zhang, 2004). The idea has been re-visited since this date, (e.g., Guardiano and Srivastava, 1993) and software has been developed by Strebelle (2000). Strebelle (2000) developed the unique modeling algorithm, SNESIM. This algorithm, and the operating techniques needed to conduct MPS modeling, will be discussed. For

mathematical derivations, see Strebelle (2002), Caers and Zhang (2004), and Strebelle (2006).

MODEL FRAMEWORK

An accurate stratigraphic and structural framework is necessary for 3-D reservoir modeling. In this study, the dimensions of the model area are approximately 5648 ft x 4901 ft x 1512 ft (1721.5 m x 1493.8 m x 460.9 m; Figure 29), and include the entire lower Williams Fork Formation. The model area is located within the larger 8-section study area at Grand Valley Field (Figures 5 and 29). The model area was chosen because wells within the approximately 1 mi^2 (1.6 km^2) area are evenly distributed. This even distribution of data eliminates potential error and edge effects.

Twenty zones (Figure 30, Appendix B) and data for 52 deviated wells on an irregular 10-ac [4-hectare; 430,600 ft^2 (40,468 m^2)] spacing were used to create the model framework. Stratigraphic horizons separate the 3-D model grids into 20 zones (Figure 30). Zones are identified by number from bottom to top as: 20 through 1 (Figure 30). Zones 13 through 20 are equivalent to the Cameo Wheeler Coal Zone identified in Coal Canyon (Cole and Cumella, 2005; Pranter et al., 2009). Zones 6, 7, and 8 correlate to the middle sandstone in the eastern portion of the Piceance Basin. The middle sandstone is a marine sandstone that pinches out to the east of Grand Valley Field. The Coal Ridge coal zone incorporates zones 1 through 4. The top of the lower Williams Fork Formation is the top of the model and zone 1. Each layer within all zones is approximately 4 ft

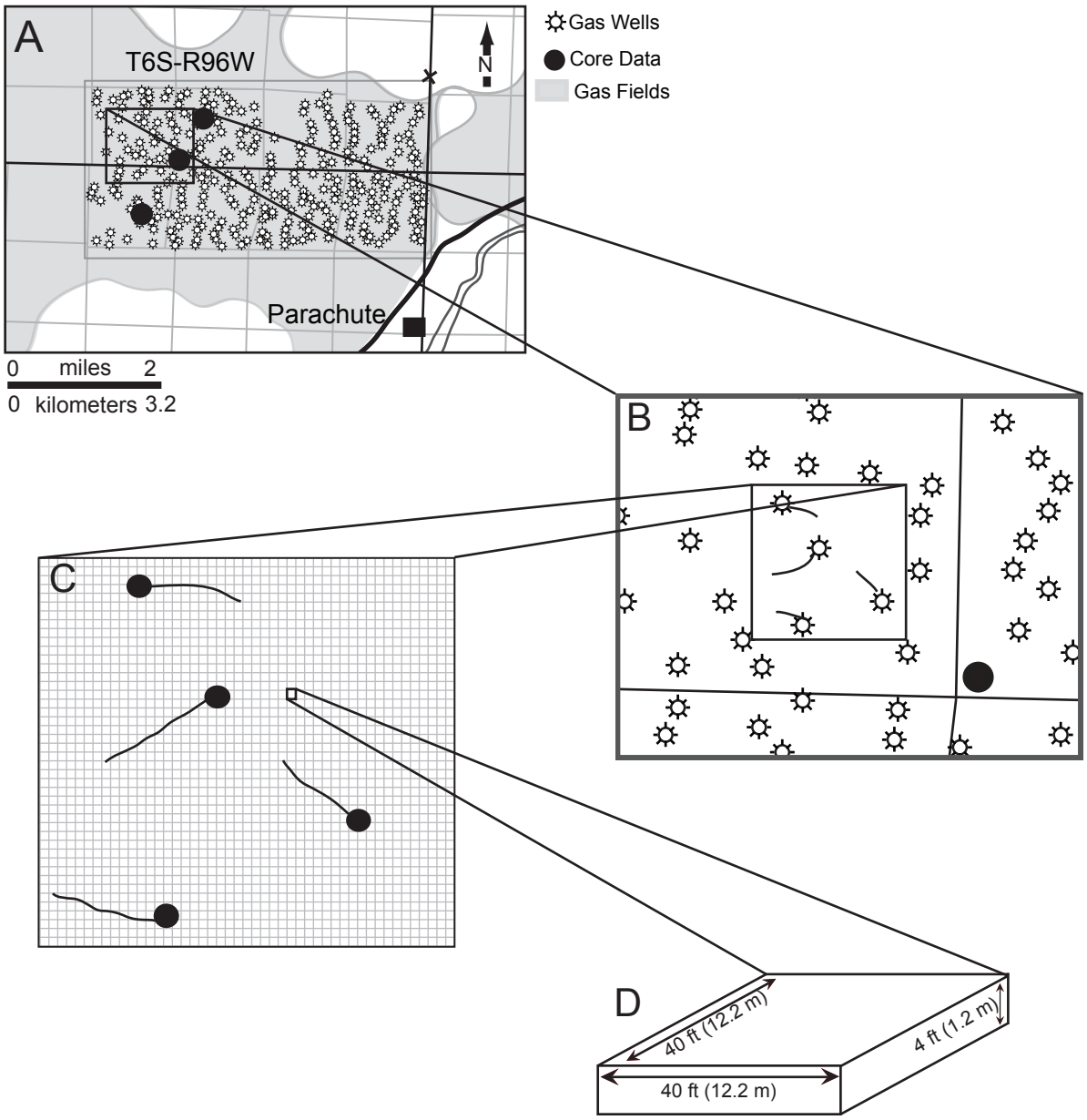

Figure 29: Three-dimensional model framework, showing aerial dimensions of 3-D model grid cells. A) Map view of Grand Valley area. Subsurface data set outlined in gray. Model area is outlined in black. B) Model area. C) 3-D model grid. Black box outlines one grid cell with dimensions of 40 ft x 40 ft (12.2 m x 12.2 m). D) 3-D schematic view of one model cell with dimensions of 40ft x 40 ft x 4 ft (12.2 m x 12.2 m x 1.2 m).

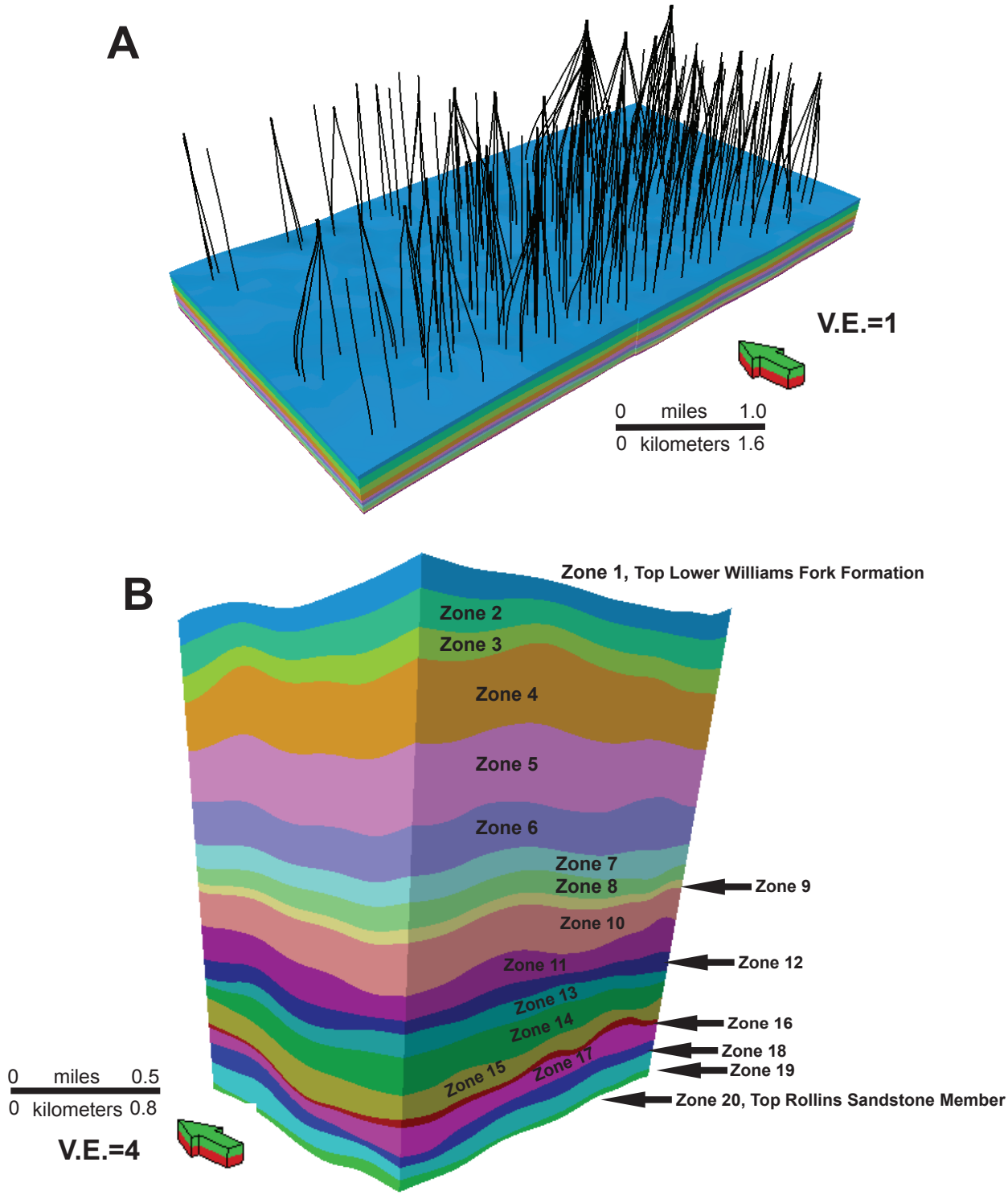

Figure 30: Three-dimensional model framework fof the lower Williams Fork Formation (from the top of Rollins Sandstone Member to top of the Lower Williams Fork Formation). The model consists of 20 zones. A) Location of 328 wells throughout the 8-section area with no vertical exageration. B) Twenty zones in the model area. Model dimensions are approximately 5648 ft x 4901 ft x 1512 ft (1721.5 m x 1493.8 m x 460.9 m).

(1.2 m) thick, and the model contains 378 proportional layers; average thickness of the model is1500 ft (457.2 m) (Table 4).

Model cells should be small enough to represent the smallest geological features of interest. For this study, the cell size is 40 ft (12.19 m) by 40 ft (12.19 m) by 4 ft (1.22 m; Figure 29). Cell size can vary depending on the amount of detail necessary in the model, however, more cells within a model framework will cause computation times to be longer. Calculated lithology logs and manually interpreted architectural-element logs were used to create three modeling scenarios in order to compare and interpret the static connectivity and ultimate dynamic recovery efficiency of the study area.

HIERARCHICAL MODELING APPROACH

To model the fluvial deposits, a hierarchical nested approach was used. With this approach, sandstone, mudrock, and coal lithologies were first modeled as an approximation of the distribution of sandstone fairways that correspond to larger scale meander belts (channel belts) and associated floodplains. Then, within the mapped channel belts and floodplains, smaller scale fluvial deposits (point bars, crevasse splays, mud plugs) were modeled (Figure 31).

Thirty sequential-indicator simulation (SIS) model realizations were created for lithology using a spherical-variogram model with a minor range of 2500 ft (762 m), major range of 2500 (762 m), vertical range of 12 ft (3.7 m), and nugget of zero. Thirty realizations were created to satisfy the central limit theorem (Trotter, 1959; Tye, 2004). Major and minor ranges were arbitrarily

Table 4: Layering scheme by zone

Zone Number and Name		Layering Scheme	Number of Layers
Top	1	Proportional	14
	2	Proportional	17
	3	Proportional	14
	4	Proportional	42
	5	Proportional	45
	6	Proportional	28
	7	Proportional	16
	8	Proportional	14
	9	Proportional	7
	10	Proportional	30
	11	Proportional	23
	12	Proportional	14
	13	Proportional	12
	14	Proportional	21
	15	Proportional	21
	16	Proportional	4
	17	Proportional	15
	18	Proportional	16
	19	Proportional	15
Base	20	Proportional	10

Table 4: Layering scheme by zone within the 3-D model framework. Layers are proportional throughout each zone to create an average of 4-ft (1.2-m)-thick layers.

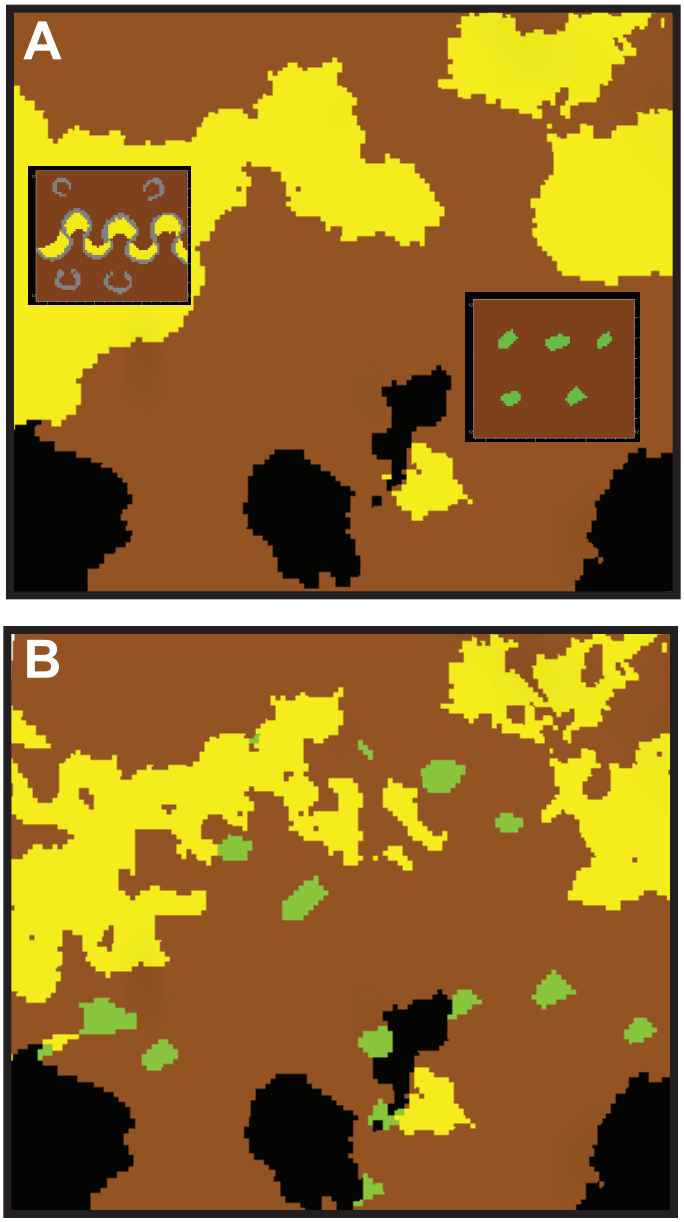

Figure 31: Nested modeling approach. (A) Map view of kriged lithology model with a point-bar training image used within meander belts (yellow reggions) and a crevasse splay training image used within the floodplain region. (B) Map view of MPS model showing heterogeneity and curvilinear features of point bars, crevasse splays, coal, and floodplain.

selected to be approximately one-half the width of the model area (i.e., maximum range would be 5648 ft [1721.5 m] in the I-direction). The vertical range was chosen to incorporate at least 3 layers (4 ft [1.2 m] thick).

The “most-of” option was used with the 30 realizations to create a model that approximates a kriged solution of the distribution of sandstone, mudrock, and coal, herein referred to as the kriged lithology model. The “most of” operation determined which lithology occurs in each cell most of the time and assigns that value to the cell (i.e., if sandstone occurred 15 times, mudrock occurred 10 times, and coal occurred 5 times in one cell, that cell would be assigned as sandstone). The kriged lithology model was used as a constraint for three MPS modeling scenarios. Point bars were only modeled within identified meander belts from the kriged lithology model (i.e. in sandstone regions), crevasse splays were populated within the floodplain areas, and coal as distributed in the kriged lithology model was used directly within all MPS simulations (Figure 31).

MULTIPLE-POINT GEOSTATISTICAL MODELING

MPS modeling uses a training image rather than a variogram as the primary mathematical constraint in 3-D modeling. A training image is a separate 3-D grid that illustrates the spatial relationship between specific architectural elements or environments of deposition (Strebelle and Journel, 2001, Strebelle and Payrazyan, 2002; Caers and Zhang, 2004; Strebelle, 2006; Arpat and Caers, 2007; Roy and Strebelle, 2008). A training image is the main constraint used for MPS modeling. By using a training image, MPS modeling allows the following to

be accounted for: spatial variability, and curvilinear features, of deposits. Training images can be created by using a previously created object-based model, a digitized geologic sketch, or a hand-drawn sketch of the deposits (Strebelle and Journel, 2001, Strebelle and Payrazyan, 2002; Caers and Zhang, 2004; Strebelle, 2006; Arpat and Caers, 2007; Roy and Strebelle, 2008).

MPS modeling is carried out in three broad steps: (1) create a training image using a separate 3-D grid, (2) create a multi-point facies pattern, and (3) run MPS modeling to create output realizations while honoring well data and other constraints.

(1) Creating a Training Image

With MPS modeling, training images are used rather than variograms or objects. Variography does not incorporate the necessary geologic heterogeneity of curvilinear deposits from a mathematical perspective (Strebelle, 2002; Caers and Zhang, 2004). To recreate curvilinear deposits in a 3-D reservoir model, more than two points of spatial correlation are needed, and therefore, a training image is used to replace the well-known variogram. The training image provides a simplified representation of the deposits to be modeled, including their spatial relationship (Caers and Zhang, 2004). Because the training image can be visually evaluated, Caers and Zhang (2004) suggest that training images are thus easier to accept or dismiss based on its simplicity representation, the variogram.

Training images need not be conditioned to hard data, but rather reflect the geologic spatial relationship of, in this case, architectural elements, in a

simplistic manner (Caers and Zhang, 2004; Strebelle, 2006). In this study, geologic features of interest include architectural elements of the lower Williams Fork Formation (point bars, crevasse splays, floodplain, and coal).

Training images can be created in several ways. Training images can be created from an object-based model, a digitized geologic sketch, or hand-drawn. This study uses hand-drawn training images for all models.

The key issues when creating a training image are the size of the 3-D grid being used and the percentage of architectural elements within the training image as compared to the percentage in upscaled well logs. These affect the percentage of architectural elements modeled. The number and size of cells within the model 3-D grid are the key factors in determining the size of the training image. The training image should be large enough to portray the relationships of features (architectural elements) to be modeled, but small enough to run in a reasonable amount of time. A minimum of 50 cells in the I- and J-directions, and 15-to-20 cells in the K-direction are suggested (Schlumberger SIS Support Portal). The size of the training image eventually dictates the reproducibility of the geobodies of interest. If the training image is too small, then the bodies will appear isolated, but if the training image is too large, a better simulation is expected, but long run times result. This study used a training image of 65 cells x 65 cells x 17 cells in the I-, J-, and K-directions, with a cell size of 50 ft x 50 ft x 1 ft (15.2 m x 15.2 m x 0.3 m; Figure 32). When drawing the training image, the percentage of deposits in the training image should be within

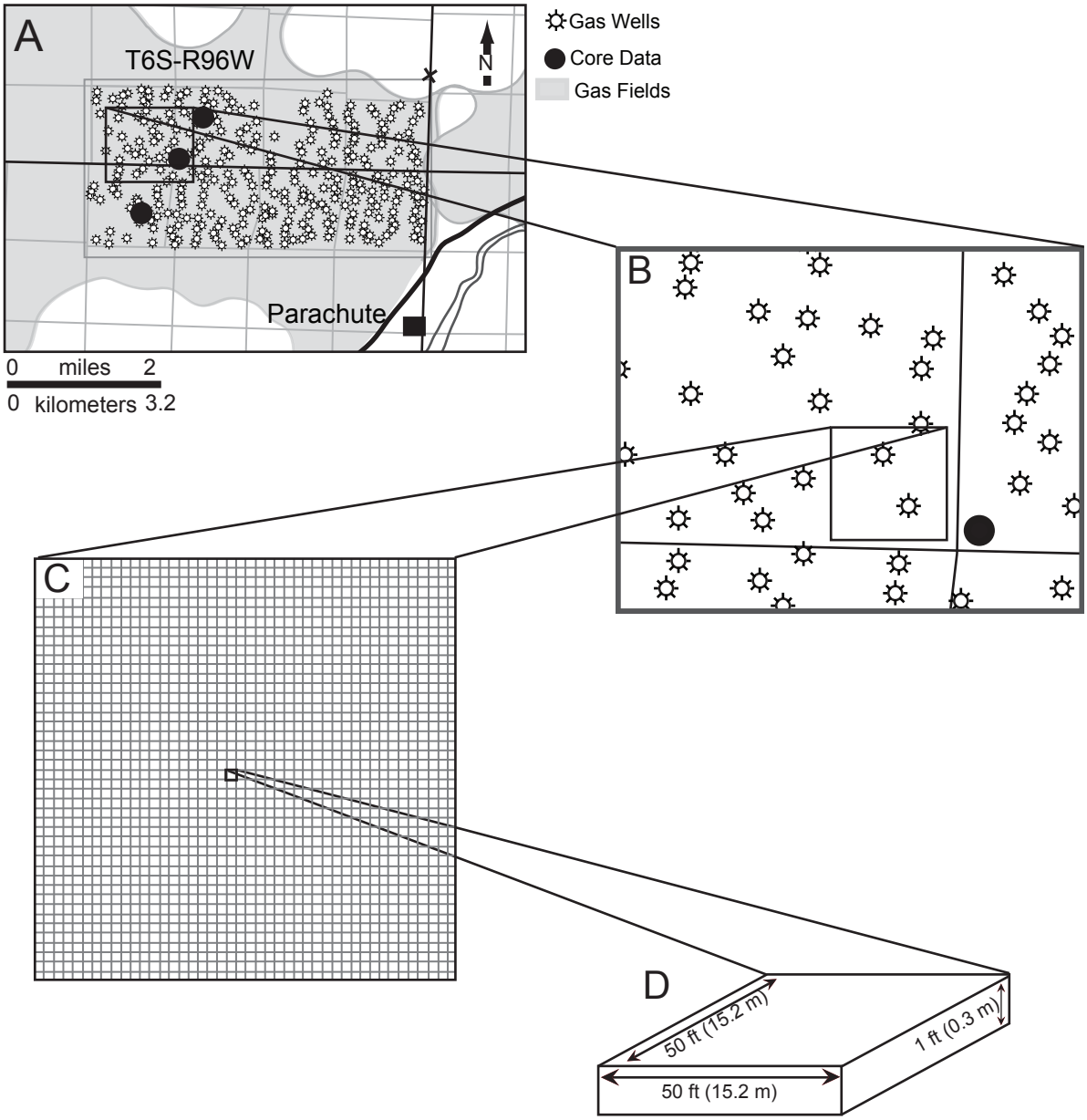

Figure 32: Training images are separate 3-D grids that have different grid and cell sizes than the MPS model. A) Eight-section model area. B) MPS model area. C) Training image grid size of 65 x 56 x 17 cells. D) Each cell has dimensions of 50 (12 m) ft x 50 (12 m) ft x 1 (0.3 m) ft.

+/- 10% of the percentage of deposits in the upscaled well logs or what is desired in the final model.

(2) Making a Multi-Point Facies Pattern (Search Tree)

Prior to running an MPS model, the training image must be analyzed to create a multiple-point facies pattern. A multi-point facies pattern, also known as a search tree, is the probabilities occurrence of specific patterns of deposits that exist within the training image. A search mask is a 3-D volume defined by the user that scans all the cells of a training image. Patterns identified by the search mask, and the probability of these patterns occurring, create the search tree. There is no visible output for this step in Petrel 2010.2; however the process is critical and the SNESIM algorithm running in the background is carrying out a crucial step in the modeling functions.

In Petrel 2010.2, when the MP facies pattern is created from a training image, specific parameters must be set for the number of multi-grids, informed nodes, and search-mask radius. No specific workflow exists to determine the size of the training image in comparison to the size of the model or the input parameters. Therefore a testing procedure was conducted to determine a reasonable cell size, number of cells, appropriate search-mask radius, and number of multi-grids for the modeling that was conducted through this study.

(a) Multi-Grid and Sub-grid Concept

MPS modeling uses multi-grids to achieve a more precise operation of the SNESIM algorithm. A multi-grid is the coarsest grid used to capture large-scale heterogeneity patterns from the training image (Figure 33). The multi-grid

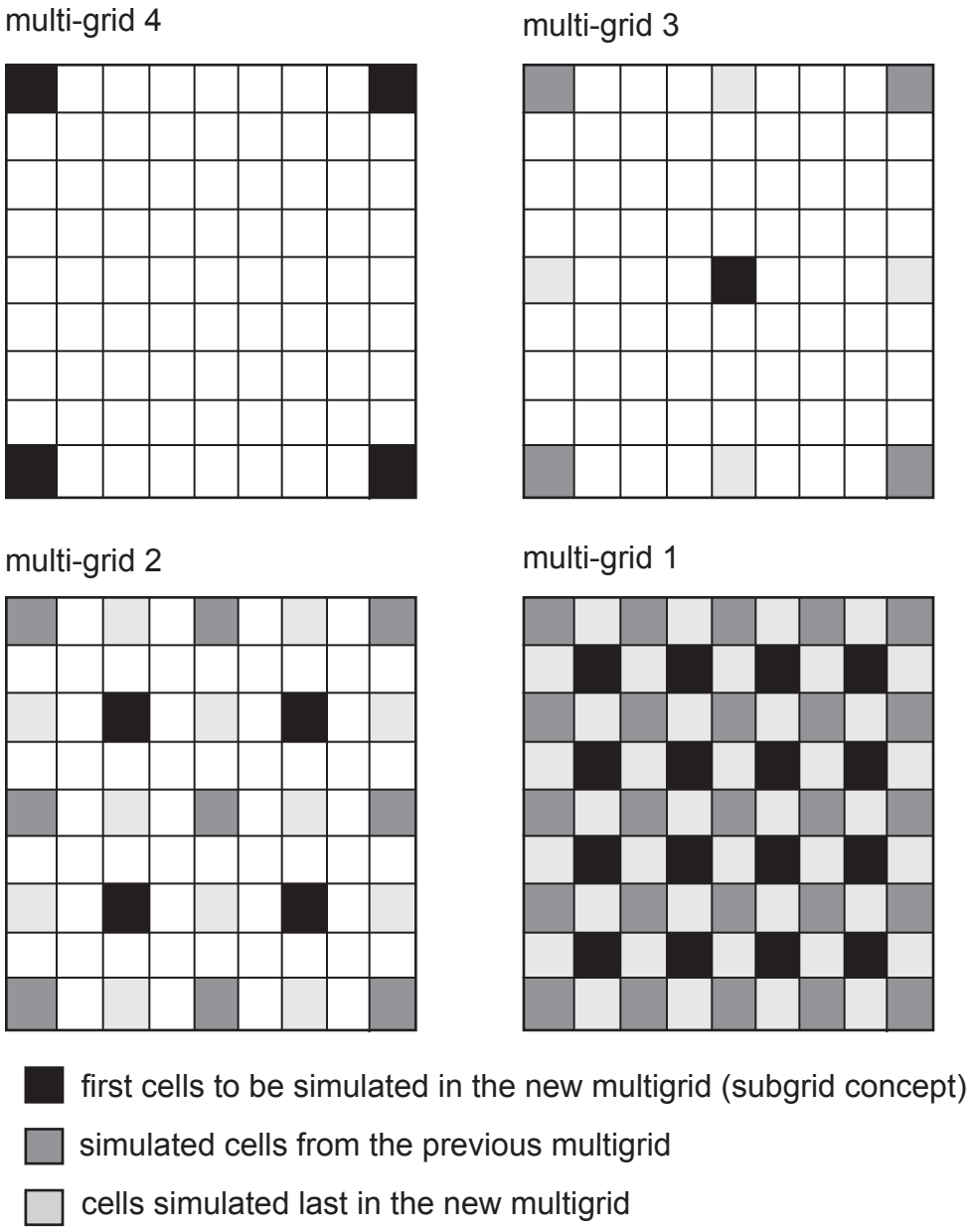

Figure 33: Multigrid and subgrid concept used in MPS modeling to make the SNESIM algorithm run more efficiently. The multigrid used to capture large scale variability from the training image. The coarsest grid sampled is 2^ (m-1) where m is the number of multigrids used. Therefore, if 3 multigrids are used then every 4th cell will be modeled first. The subgrid concept is how the remainder of the grid is filled in. Depending on the choice of multigrid to start with dictates how the subgrids are filled. If 4 multigrids are used, then every 8th cell is simulated and those points become hard data for the next simulation at 3 multigrids (every 4th cell). The number of multigrids, and therefore number of cells modeled, decreases to 1 until all cells are simulated (Schlumberger, SIS portal).

concept attempts to capture longer ranges of features expressed in the training image that will then be used to populate the MPS model. Therefore, multi-grids assist in creating a more curvilinear output and accurate location of features, thus, honoring their relationships in the training image. The parameters for what multi-grid number to use depend on the amount of detail the user wants to see in the model output (Strebelle, 2002).

Multi-grids work in conjunction with sub-grids to populate the coarsest grid first and then get smaller until all unknown cells are assigned a value. A sub-grid is a regular pattern used to fill the specific multi-grid used. The sub-grid allows for a quicker simulation because a specific pattern of previously simulation cells is known. The largest number of multigrids available in MPS modeling is four. The coarsest grid and number of cells between those populated is calculated by using

$$2^{(\text{number of multigrids}-1)} = \text{every } n^{th} \text{ cell gets populated}$$

For example, if 4 multi-grids are used: 2^(4-1)=8 and therefore, every 8^{th} cell will be populated first and then MPS will move to the third multi-grid, and down until every cell is populated (Figure 34; Strebelle, 2002).

The number of multi-grids used depends on user preference and CPU computation time. In this study, two multi-grids were used. Two multi-grids were used because of the need to model every 2 cells in order to capture the small scale heterogeneity of fluvial deposits of the lower Williams Fork Formation.

(b) Informed Nodes

The final input parameter associated with the number of multi-grids is the maximum number of informed nodes. An informed node is a node that is defined

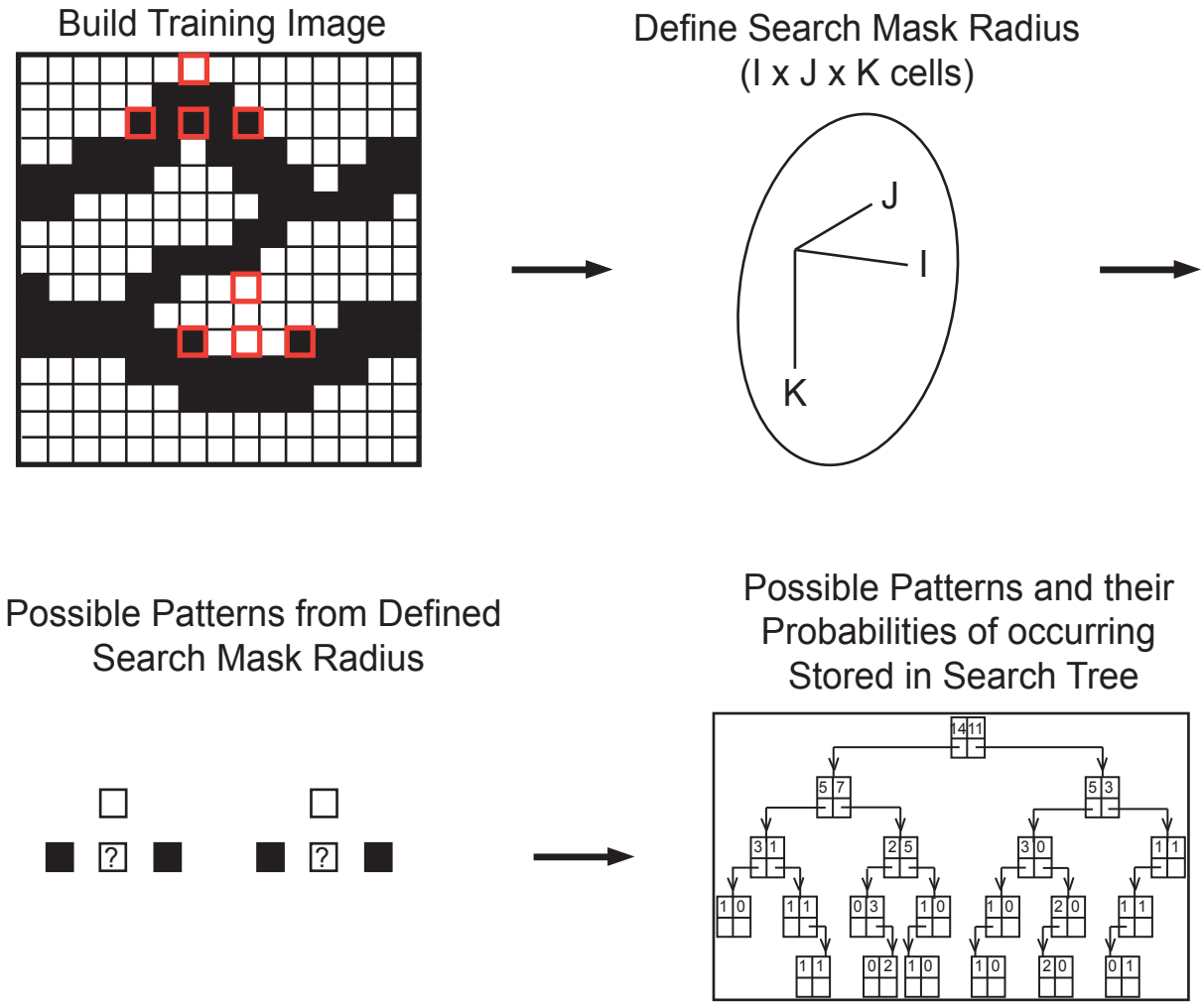

Figure 34: The search mask radius is defined by a specific number of cells in the I, J, and K directions by the user prior to creating a facies pattern used in modeling. First, a training image must be created and the search mask defined. The radius can be defined as an ellipsoid or rectangle. Ellipsoid search masks are used in this study. Next, the search mask scans the training image and determines the possible patterns that can be created and the probability of unknown cells being a specific value. All probabilities are stored in the search tree. The search mask radius and multigrid concept work together in the background to determine the number of cells in the I, J, and K directions that will be scanned when making the MP facies pattern. The search mask radius used in the SNESIM algorithm is similar to the “search radius” used in classical geostatistical modeling (Schlumberger SIS portal).

when working with a sub-grid. Since sub-grids are always used in MPS modeling, the number of informed nodes must always be indicated. The number of informed nodes dictates how many defined nodes are present within the current sub-grid. The sub-grid is based off the number of multi-grids, and therefore, the number of informed nodes will take into consideration previously assigned hard-data points from previous larger sub-grids. Generally speaking, more informed nodes, preserve the best output images (Strebelle, 2002; Schlumberger SIS Support Portal).

(c) Data Template (Search Mask)

The data template (search mask) scans the training image and creates a search tree (Figures 35, and 36). A search tree is the storage of potential patterns and their probability of occurrence from the training image. Although there is no specific search mask size (in terms of number of cells in I-, J-, and K-directions) for a model of “x” size, the user can determine the minimum size of the search mask based on the number of multi-grids used for the model of interest. The number of cells the search-mask radius will cover can be determined by using the following equation (Schlumberger SIS Support Portal, 2011):

$$2^{(m-1)} * (\text{radius in I direction}) * 2 = L$$

Where m is the number of multi-grids used and L is the size, in the J direction, of the architectural element to be modeled from the training image

The search mask should not be too small otherwise the output will be noisy and unrealistic, because the search mask dictates the multiple-point data

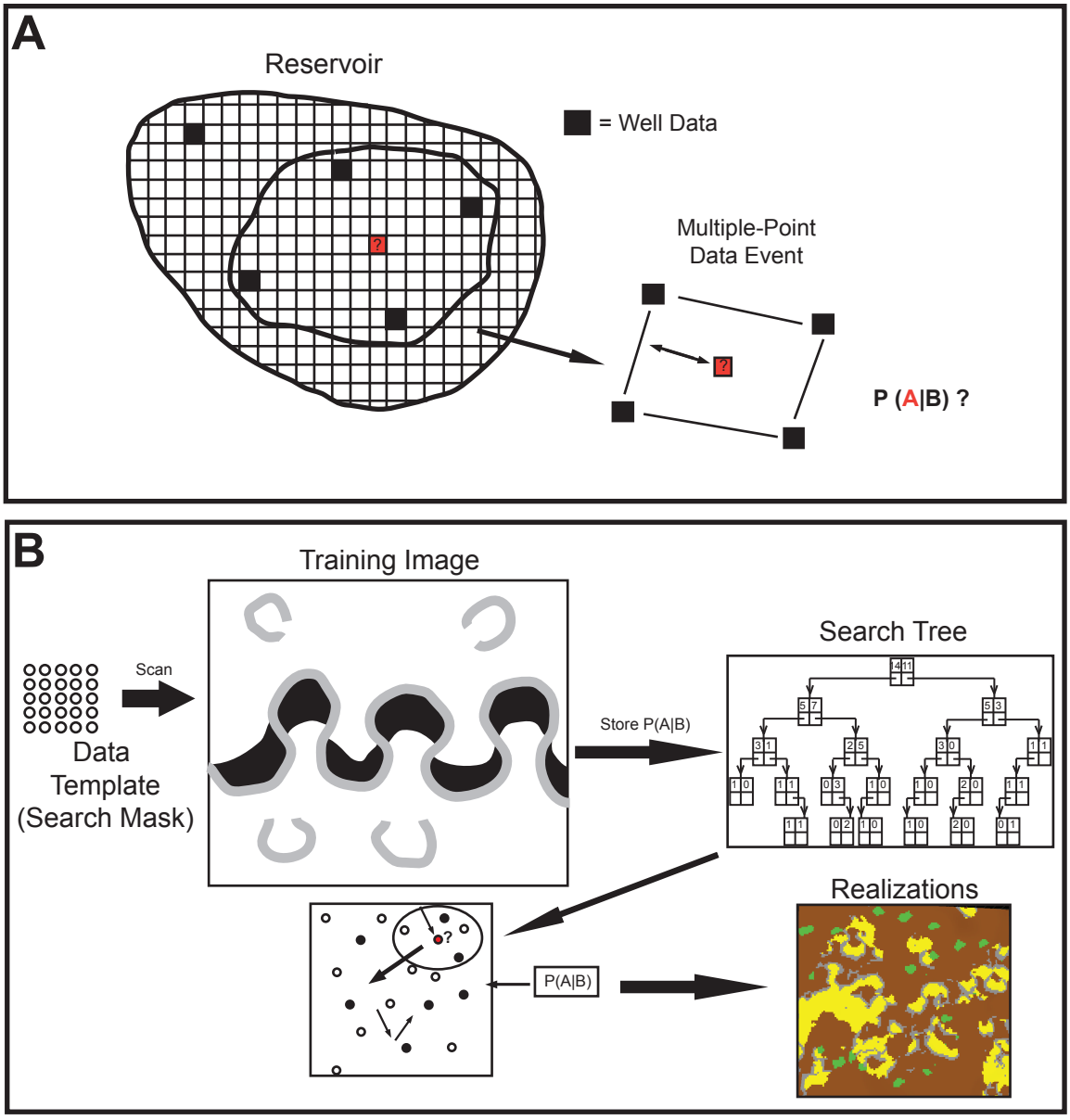

Figure 35: Diagrammatic representation of the SNESIM (single-normal equation simulation) algorithm used for MPS modeling. (A) The SNESIM algorithm uses training images and looks for hard data points (i.e. well data) in three dimensions. (B) Steps of the SNESIM algorithm. A data template (search mask) scans the training image and calculates the probability of specific patterns occurring and storesthem in a search tree. The algorithm then defines a random path of unidentified cells through the model and looks for hard data in 3-D surrounding the unknown cell of interest. Finally, the search tree is referenced to determine the probability of that cell being a certain architectural element and a cpdf (conditional probability distribution function) is used to assign a value to the unknown cell. Output realizations are created when all cells have been assigned a value. (A) modified from Caers (2000). (B) modified from Taskin Akuput, ExxonMobil Research Company; after Strebelle (2000).

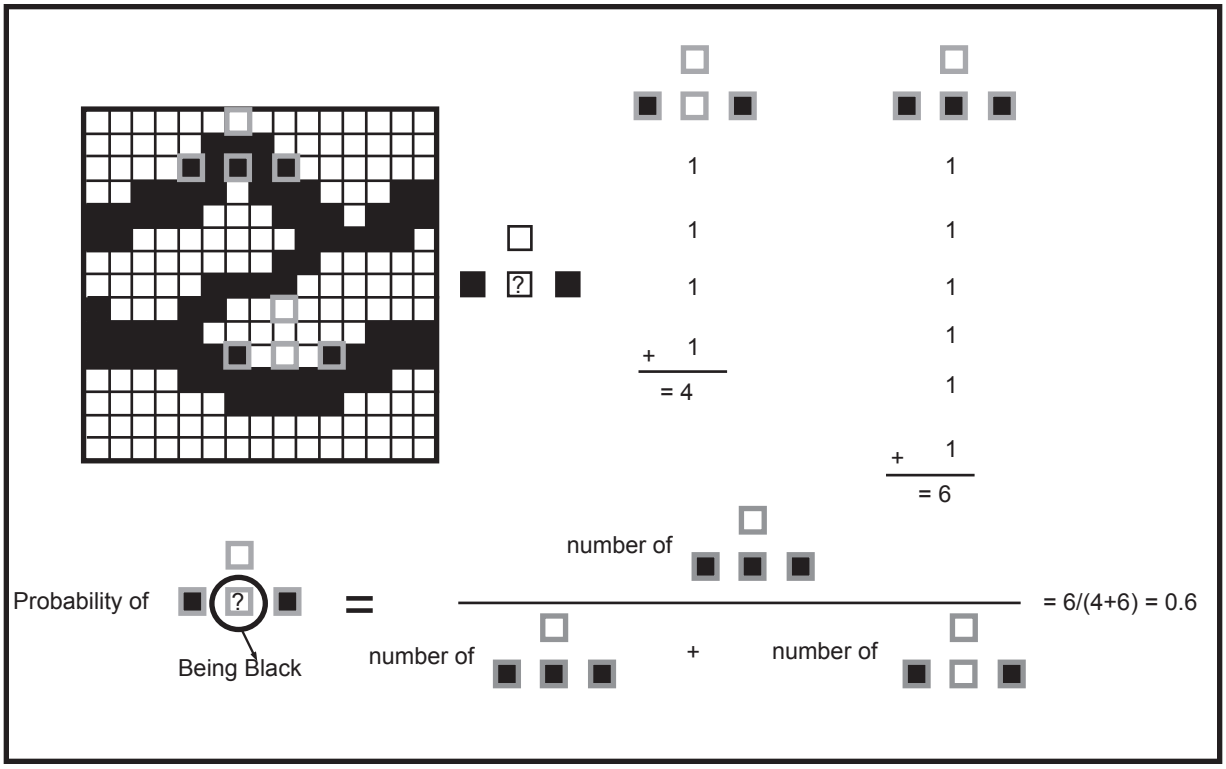

Figure 36: Diagrammatic representation of the SNESIM algorithm scanning the training image and determining the probability of an unknown cell being a speciric architectural element. For the data template created (gray squares) two patterns exist, one with the bottom middle cell being black, one being white. The total number of each pattern within the training image is calculated. Then, to determine what the probability of the cell being black is, the number of patterns with the cell being black is divided by the total number of possible outcomes (i.e. 6/(4+6) = 0.6). For this example, there is a 0.6 (60%) chance of the cell being black. Modified from Taskin Aukput, ExxonMobil Exploration Company.

events that are identified within the training image. Multiple-point data events are the 3-D patterns identified within the training image (Figure 35). The size of the search mask dictates the number, and occurrence, of multiple-point data events present. If the search mask is too large, the output architectural elements might be representative of the training image, but computer run-time will be extensive.

(d) Single-Normal Equation Simulation (SNESIM) Algorithm and MPS Modeling

The algorithm behind MPS is referred to as SNESIM (Strebelle, 2000; Strebelle and Journel, 2001). Specific mathematical derivations of the algorithm can be found in Strebelle (2002). The potential for an algorithm similar to SNESIM began with Journel and Alabert (1989) and has since been reviewed multiple times. Journel and Alabert (1989) developed the original theoretical framework for the SNESIM algorithm, although it was not applicable at that time. Strebelle (2002) solved the first derivations of the algorithm that modern-day CPU's had the ability to run (Strebelle and Zhang, 2004). The SNESIM algorithm has specific steps that repeat for each unknown cell within a 3-D grid until all cells are treated.

A single normal equation is the basis of the SNESIM algorithm used in MPS modeling and uses a three-step process to assign a value to an unknown cell (Caers and Zhang, 2004; Figure 35). (1) The algorithm will search for the nearest well data and for any previously simulated cells that were assigned a value and are now considered hard data, (2) A probability model is constructed based on the findings of step (1) and using any other available soft data constraints (i.e., 3-D seismic), and (3) property value is assigned to the unknown

cell using the probability model created in step (2). Steps (1) through (3) repeat until the entire 3-D grid is populated with property values (Caers and Zhang, 2004; Figure 35, 36).

Within the SNESIM algorithm, a conditional probability distribution function (cpdf) is used to determine “k” possible outcomes of a random variable, each of which is characterized by their specific cpdf (Strebelle and Journel, 2001, 2002; Arapat and Caers, 2004). When Journel and Alabert (1989) first researched MPS the cpdf was recalculated after every cell was assigned a hard value, thus being extremely cumbersome on CPU’s (Strebelle, 2002).

Once an unknown cell was assigned a property, it becomes a hard data point used in conjunction with well data and previously assigned cells. Re-calculating the cpdf after every assignment of a property to a cell was the reason that MPS was not applicable until Strebelle (2002) developed the SNESIM algorithm in which the cpdf runs one time using the training image(s). From the patterns present within the training image, a search tree (pattern template) is used to identify specific patterns occurring in the training image and the probability of those patterns occurring (Figure 35).

(3) MPS modeling

MPS modeling will honor well-log information present within the modeling area. Other possible input parameters include additional soft or hard data, scaling, rotation, and manually controlling the percentages of facies or architectural elements within the training image. Seismic probability volumes are commonly used as an additional constraint. No 3-D seismic was used to

constrain MPS modeling in this study. Scaling and rotation allow for the user to adjust the size and azimuth of the geobodies from the training image to the actual model. If a deposit is isolated and should extend over the entire length of the model (i.e. sinuous channel), then scaling can be used to decrease the amount of isolation of channels throughout the model (Schlumberger SIS Support Portal). No scaling or rotation was used in this study.

ADVANTAGES AND LIMITATIONS OF MPS MODELING

Modeling has advantages and disadvantages. MPS modeling advantages include:

(1) MPS modeling allows for conditioning due to being a pixel-based algorithm.

(2) Models generated using MPS modeling appear like a combination of object-based and sequential indicator simulation patterns.

(3) Three-dimensional conditioning was used for MPS modeling. This allows the user to have greater control over dimensions and include layers of heterogeneity that could be skipped if using a 2-D variogram approach.

(4) MPS modeling is capable of modeling complex facies relationships.

(5) Training images can be produced multiple ways and can be constrained to real-world data (e.g., thickness, height, spatial extent)

(6) MPS modeling can be divided into regions if multiple environments of deposition occur, or if the user wants to isolate specific facies.

The following are limitations and drawbacks of MPS modeling:

(1) Determining the correct size of the training image in comparison to the size of the model output is a difficult and time intensive process. If the training image is too big or too small, the output model realizations will appear pixelated. There is no catalog of training images that is currently publically available.

(2) If the search-mask radius is too small, detail from the training image will be lost and not incorporated into the model output realization. If the search-mask radius is too big, run-time will be excessive.

(3) The training image must be a simplistic, repetitive (stationary) representation of the deposits being modeled. The training image must contain +/- 10% of the rock type desired to be in the final model. Achieving the amount of detail necessary to show the spatial relationship of the deposits can be difficult.

(4) Scaling and rotation (not used in this study) are available parameters to manually set when using MPS. If the user applies a rotation to the training image and again in the MPS modeling input parameters, over rotation can occur in the I, J, or K directions.

(5) Training image generation is time consuming. CPU limitations constrain the model size that can be created in a reasonable amount of time for highly constrained models.

MODELING CONSTRAINTS

This study uses well data and outcrop-based fluvial sandstone-body statistics as geological constraints for the MPS modeling.

Well logs

Well data within the modeling area was used as hard data in the 3-D models. Lithology logs calculated from V-Clay logs were used for SIS modeling of meander belts (channel belts). For MPS modeling, interpreted architectural-element logs provided hard data within the modeling area for the types of fluvial deposits intersected in wells.

Vertical Proportion Curve

The vertical proportion curve was used to constrain architectural-element percentages stratigraphically (Figure 26). Stratigraphic zones were differentiated using stratigraphic horizons and the proportion of mudrock and sandstone within the vertical proportion curve. The final MPS models should contain similar proportions of architectural-elements as the vertical proportion curve.

Outcrop dimensional statistics

Outcrop measurements of sandstone-body apparent width and thickness from the lower Williams Fork Formation at Coal Canyon were used as a constraint in this study (Panjaitan, 2006; Pranter et al., 2009; Appendix A;). Dimensional statistics were used in conjunction with core descriptions to constrain the manual interpretation of architectural-element logs from log response. Average thickness and apparent-width values for single-story

sandstone bodies and crevasse splays were used to constrain the sizes of architectural elements drawn in all training images.

Training Image

For each scenario, one training image was used to model point bars and mudstone plugs within interpreted meander belt (sandstone) trends. Another image was used to model crevasse splays within floodplain identified from the kriged lithology model (Figure 37). Coal deposit distributions were identical in all MPS models, and coal was not incorporated into the training images. Therefore, the only variable that changed between the three scenarios was the distribution and connectivity of point bars and their associated channel mud plug.

Training Image Testing

Twenty-five training images were tested to determine appropriate training-image parameters needed for MPS modeling. Three scenarios are reviewed here. All training images were tested in Petrel 2010.2 by simulating an unconstrained model prior to using hard data as a constraint. For information regarding all trials, see Appendix G.

Trial Scenario 1 (Figure 38): This trial is the first of twenty-five testing scenarios conducted. The parameters used created a discontinuous and noisy model output with a run time of 2.5 hours for the 0.25 mi (0.4 km) modeling area at Grand Valley Field. The grid size used is 79 x 80 x 17 cells with a cell size of 22 ft x 22 ft x 1 ft (6.7 m x 6.7 m x 0.3 m). The data template (search mask) used for this trial is 8 x 3 x 2 cells. Four multi-grids were used with 32 informed nodes.

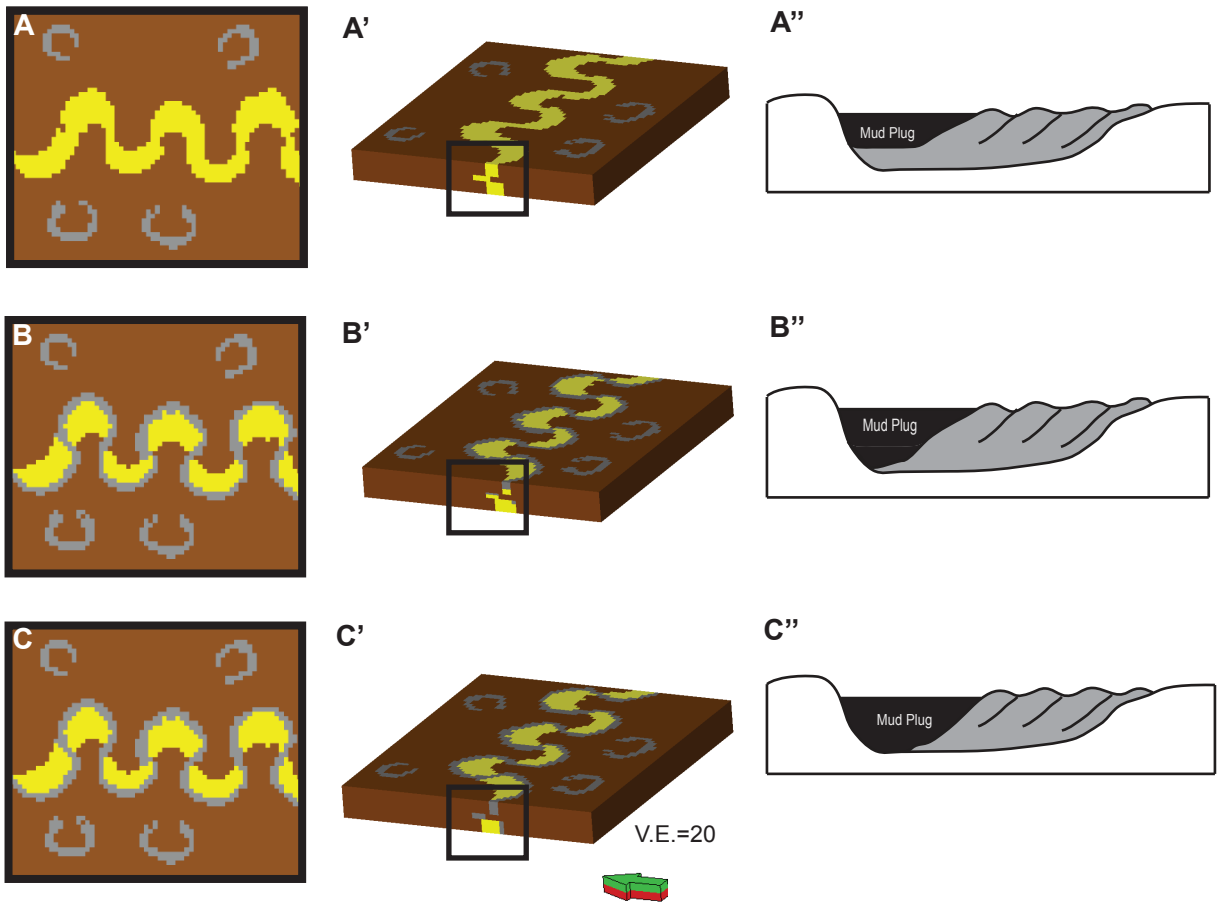

Figure 37: Three training images are used for point bar MPS modeling scenarios. A) String-of-beads, B) partial-mudstone-plug, and C) mudstone-plug. A, B, and C show map views of the training images. A', B', and C' show the 3-D grid and cross sectional view of the training image. The difference is the amount of mudstone plugs present. A', B', and C' have a vertical exageration of 20. A'', B'' and C'' show the cross section (outlined by the black boxes) as a cartoon.

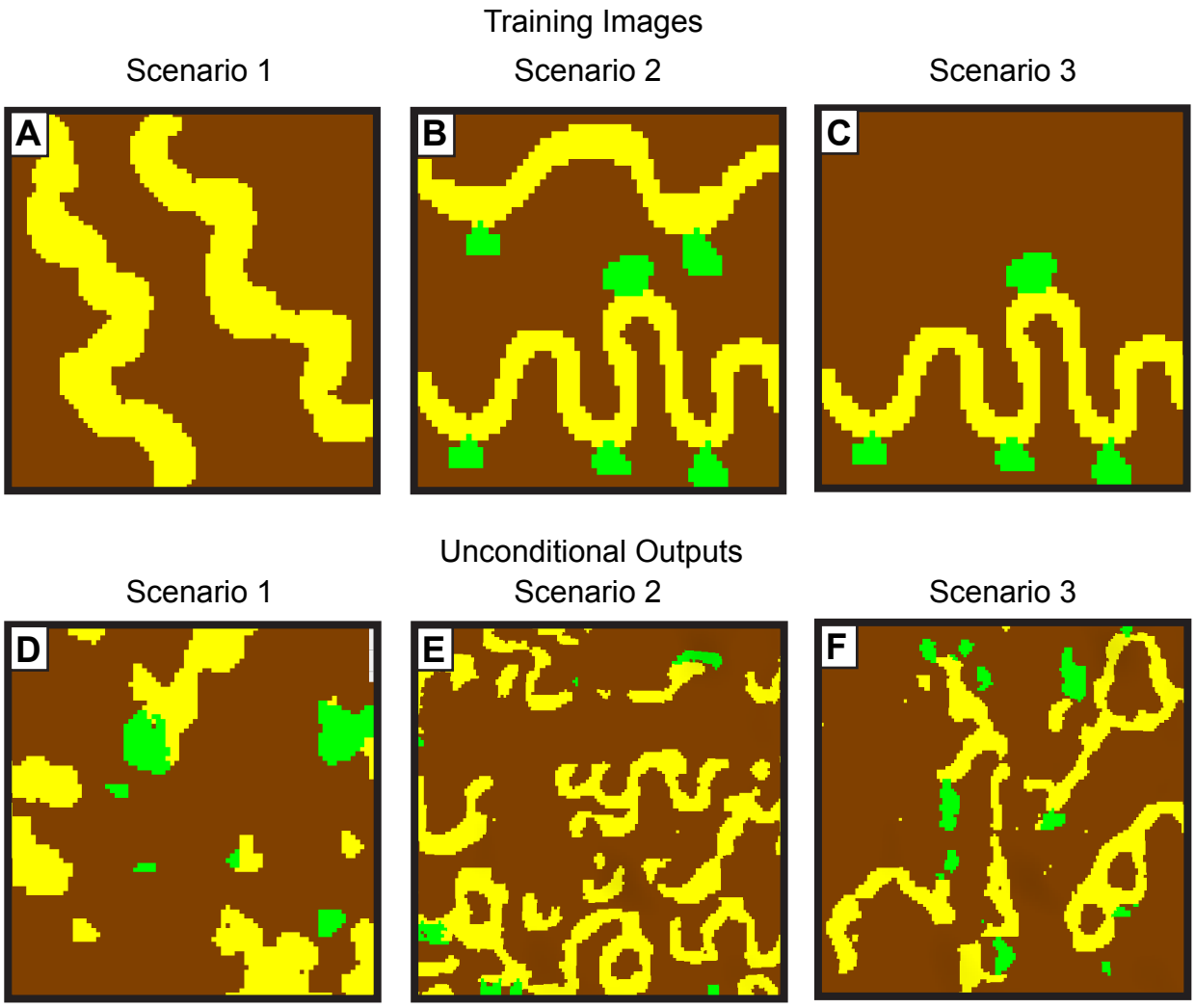

Figure 38: Training image testing scenarios. A, B, and C show a map view of the hand drawn training image. D, E, and F show a map view of the unconditional model output. Trial scenario 1 (A) and (D), scenario 2 (B) and (E), and scenario 3 (C) and (F) show 3 out of the 25 MPS trial scenarios documented prior to creating the training image used for MPS modeling. All training image testing scenarios are in appendix F.

Trial Scenario 2 (Figure 38): Because the first trial was extremely pixilated, a smaller training image with larger cell size was used with a variance in the number of multi-grids, search-mask radius, and informed nodes. The grid size used is 65 x 56 x 17 cells with a cell size of 50 ft x 50 ft x 15 ft (15.2 m x 15.2 m x 4.6 m). A search mask of 8 x 3 x 2 cells is used with three multi-grids and 64 informed nodes. The number of informed nodes used is 64. This provides a cleaner and more representative output; however noise still persisted. It is important to note that 64 informed nodes is the maximum number needed for an accurate simulation. Using 100 informed nodes does not produce a more accurate output and will thus only slow down the run time.

Trial Scenario 3 (Figure 38): The third scenario presented is the largest training image tested. The grid size of 114 x 98 x 17 cells is the size of the entire modeling area. A larger size is tested to attempt to eliminate noise. A cell size of 50 ft x 50 ft x 15 ft (15.2 m x 15.2 m x 4.6 m) is used. The search mask used is 7 x 12 x 2 cells with three multi-grids and 64 informed nodes. This scenario took an extremely long time to run and did not produce accurate enough results for the time taken.

Each of the twenty-five trial scenarios produced different outputs of unconstrained test models. These scenarios are shown to demonstrate the difficulty of creating a training image in the MPS workflow. The main issue with many of the trials, including the three presented above, is that the training image is “over-training” the model and too complicated. The training images used in the final results were drawn as simplistic as possible with no architectural-element

interaction in the K direction and minimal repetition in the I and J directions. Due to having a large amount of dimensional data collected for point bars and crevasse splays, these sandstone bodies were drawn to scale using the outcrop dimensions measured in Coal Canyon (Panjaitan, 2006; Pranter et al., 2009; Table 1) to incorporate outcrop dimensions into the subsurface, assuming these deposits are similar in the lower Williams Fork Formation at Grand Valley Field as they are at the Coal Canyon outcrop location approximately 22 mi (35.4 km) to the west.

Training images are conceptual representations of the geology; however, they are adequately detailed so as to illustrate the spatial relationships of the deposits. If the training image is too complicated, the output model will be pixelated. There is a fine balance between training-image size, architectural-element size, and output model size. In this study, all training images have the same size. The approximate size of the training images is 3250 ft x 2800 ft x 15 ft (990.6 m x 853.4 m x 4.6 m; Figure 32). The number of cells is 65 x 56 x 17 with a cell size of 50 ft (15.2 m) x 50 ft (15.2 m) x 1 ft (.3 m) in the I x J x K directions (Figure 39). An ellipsoid search mask was used with dimensions of 12 x 10 x 2 cells and 2 multi-grids.

Training Images used - This study

Point bars have been documented to have a variety of geometries (Donselaar and Overeem, 2008; Pranter, et al., 2007; Bridge, 2006; Miall, 2006; Ellison, 2004; Cole and Cumella, 2003; Miall, 1985; Gustason, E.R., personal communication). A study by Donselaar and Overeem (2008) suggested variability

of connectivity between point bars in the subsurface and outcrop by a preserved ribbon of sandstone at the base of the channel (“string-of-beads”) versus disconnected deposits separated by a mud plug associated with channel fill after channel avulsion (Figure 39). Conceptually, the presence of mud plugs should decrease both static and dynamic connectivity; but to what degree? Point bars that are connected by a ribbon of sandstone and totally disconnected by a mud plug are the two end member scenarios used for two of the three training images created for MPS modeling. A third scenario, with partially disconnected point bars, was also used to determine the impact that mud plugs have on a system.

Various training images were created that represent different geological scenarios to explore static and dynamic connectivity and ultimate recovery efficiency within the fluvial system at Grand Valley Field. Three different training images were used to simulate differences in point-bar connectivity (Figure 37) herein referred to as: (1) string-of-beads, (2) partial mudstone plugs, (3) mudstone plugs.

The first scenario uses a “string-of-beads” geometry (plan view) in which all point bars are connected by ribbons of sandstone (Figure 37). The second scenario has the channel completely filled with a mud plugs adjacent to the point bars due to abandonment or avulsion. When this happens, the channel fills with mud that separates the point bars (Figure 37; Walker 1984, 1992; Miall, 1996; Bridge, 2006). The third scenario involves a partial mud plug in which the point bars are connected at the bases of the channels by a thin ribbon of sandstone (Figure 37). Because crevasse splays are deposited within the floodplain, one

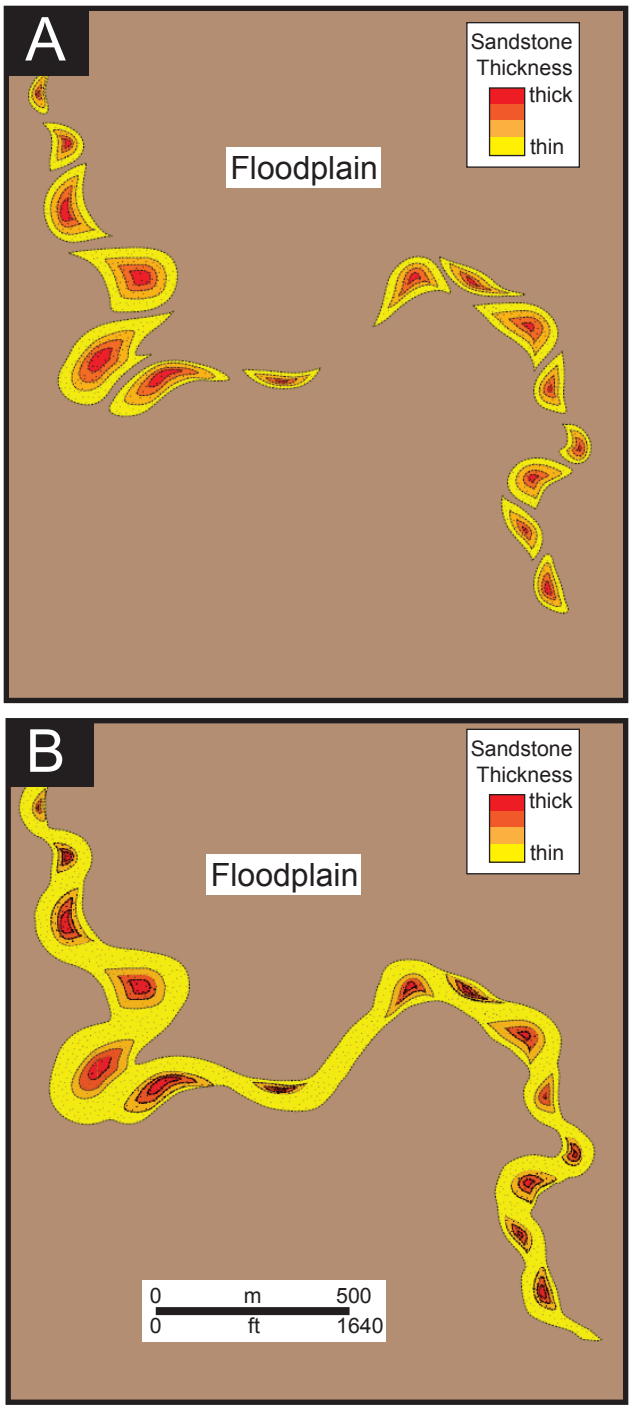

Figure 39: Point bars showing A) disconnected bodies along a meander belt, and B) connected bodies along a meander belt. This study shows two end member scenarios for point bar geometries, and is the basis for the string-of-beads and mudstone-plug MPS training images and models. Modified from Donselaar and Overeem (2008).

training image was used for crevasse splays. The training image for crevasse splays was kept consistent throughout all three scenarios. Coal was not included in the four training images. The location of coal deposits in the models was the same as the distribution of coal in the kriged lithology model.

Architectural-element size within the training images were drawn to scale using outcrop dimensional data from the lower Williams Fork Formation at Coal Canyon (Panjaitan, 2006; Pranter et al., 2009). Mean thickness and apparent-width values were calculated and used to constrain architectural-element size. Mean thickness of point bars (single story channel fill) is 12.3 ft (3.7 m) with an apparent width of 339.5 ft (103.5 m; Table 1). Point bars drawn in training images have an average apparent width of 492 ft (150 m). This is slightly larger than the average measured in outcrop, but significantly less than the maximum apparent width of a point bar in outcrop. The maximum apparent-width value measured at Coal Canyon was 1699.8 ft (518.1 m; Table 1). Thickness of point bars in the training images is 7 ft (2.1 m). No tapering of the base of point bars was used in this study. Average point bar thickness in outcrop is 12.3 ft (3.7 m), with a minimum of 3.9 ft (1.2 m) and a maximum of 29.9 ft (9.1 m). Crevasse splays show an average thickness of 5.1 ft (1.6 m) in outcrop and 5 ft (1.5 m) in the training image. Average apparent-width values in outcrop are 231.1 ft (70.4 m). Crevasse splays were drawn in the training image with an average apparent-width value between 366 ft (111.6 m) and 246 ft (75 m). This range of apparent width falls between the mean and maximum values measured in outcrop of 231.1 ft (70.4 m) and 843 ft (256.9 m).

Based on the maximum search-radius equation for the training-image size, using a search radius of 12 cells in the I-direction and 2 multi-grids, allows for a search radius in the I-direction of 48 cells. Each cell is 50 ft (15.2 m) x 50 ft (15.2 m) x 1 ft (0.3 m). The search-mask incorporates all architectural elements drawn within the training image. In the J-direction, using a search radius of 10 and 2 multi-grids, the search radius is 40 cells. This controls the lateral distribution of point bars and crevasse splays from the training image into the MPS model. Classical geostatistics states that the parameters of the search mask should not be larger than 2/3 of the field of interest (training image; Strebelle and Journel, 2001). The maximum search radius in the I-direction is 49 cells and 42 cells in the J direction, allowing for the search mask used to stay within accepted geostatistical modeling parameters.

NET-TO- GROSS CALCULATION

Net-to-gross ratio was calculated for each zone of the three MPS model scenarios. Total sandstone volume is calculated for each zone, as well as the total rock volume within each zone (Figure 40, Appendix I). Net-to-gross percentages were calculated by using the equation:

N:G = SS Volume\Total Volume (by zone)

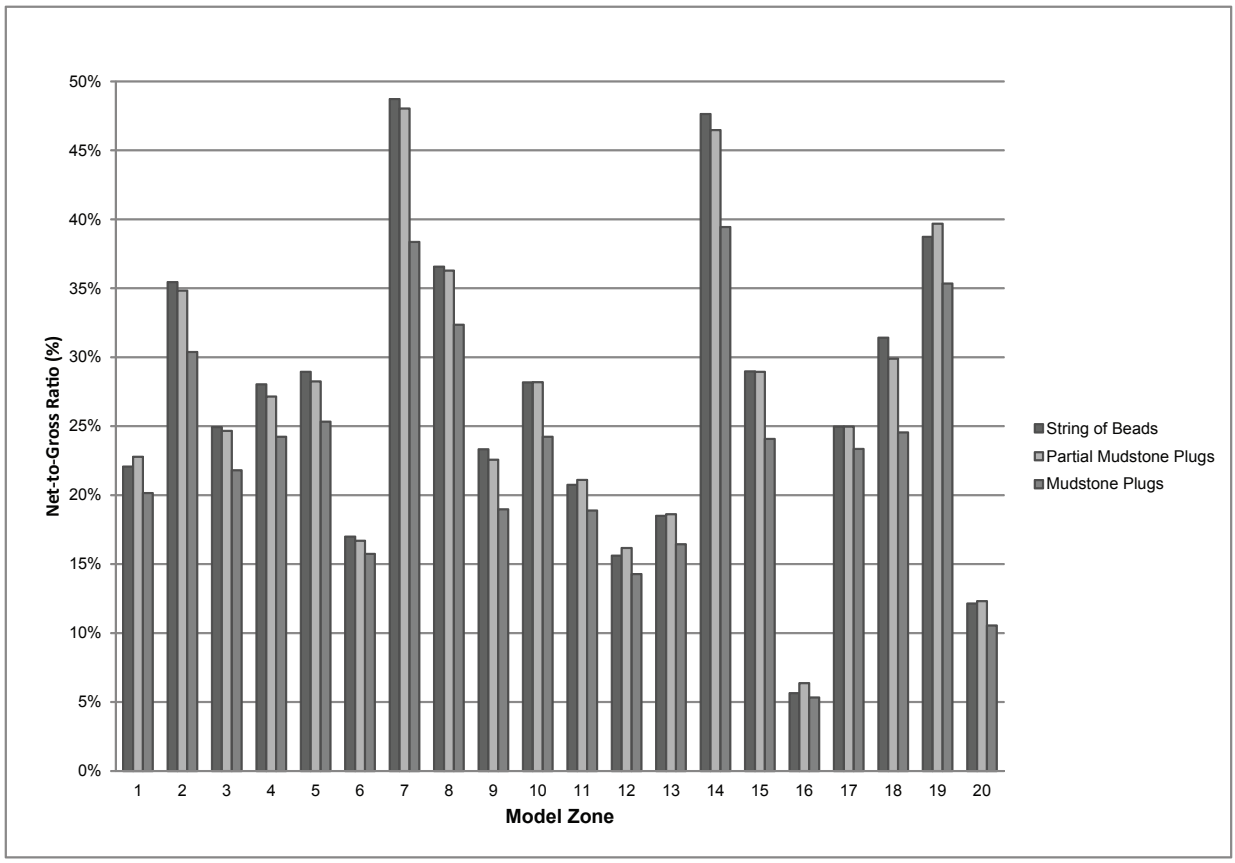

Figure 40: Net-to-gross ratio by zone for MPS modeled scenarios. Zone 1 is stratigraphically highest. Net-to-gross ratio represents the percentage of sandstone associated with point bars and crevasse splays within a zone.

RESULTS

The three MPS modeled scenarios were quantitatively assessed for the percent of architectural elements present in upscaled logs versus the percent in each MPS model scenario. Percentages from upscaled architectural-element logs show values of 34.4% point bars, 3.37% crevasse splays, 59.9% floodplain, and 2.32% coal for the total modeled interval. These values were the main input in MPS modeling, in conjunction with the training images.

Output values for the string-of-beads model show 25.2% point bars, 3.0% crevasse splays, 68.5% floodplain, 2.1% coal, and 1.2% mud plugs. The value difference between the input and outputs are due to mud plugs not being interpreted in architectural-element logs, but being included in the training images. Therefore, the percent of mud plugs in the training images is seen in the model and not in the original upscaled logs. The partial-mud-plug model shows values for architectural elements of 24.9% point bars, 3.01% crevasse splays, 66.8% floodplain, 2.1% coal, and 3.3% mud plugs. The involvement of mud plugs in the training image also accounts for the loss in point-bar percentage in the partial-mudstone-plug model. Finally, the mudstone-plug model displays output architectural elements as 21.3%, 3.0%, 68.8%, 2.1%, and 5.5% for point bars, crevasse spays, floodplain, coal, and mud plugs, respectively.

Net-to-gross ratios range from 5.6% to 48.7% in the string of beads MPS model, 6.4% to 48.0% in the partial mudstone plugs model, and 5.3% to 38.4% in the mudstone plugs model (Figure 40). The highest net-to-gross ratio (48.7%) was calculated in the string of beads model and the lowest net-to-gross ratio

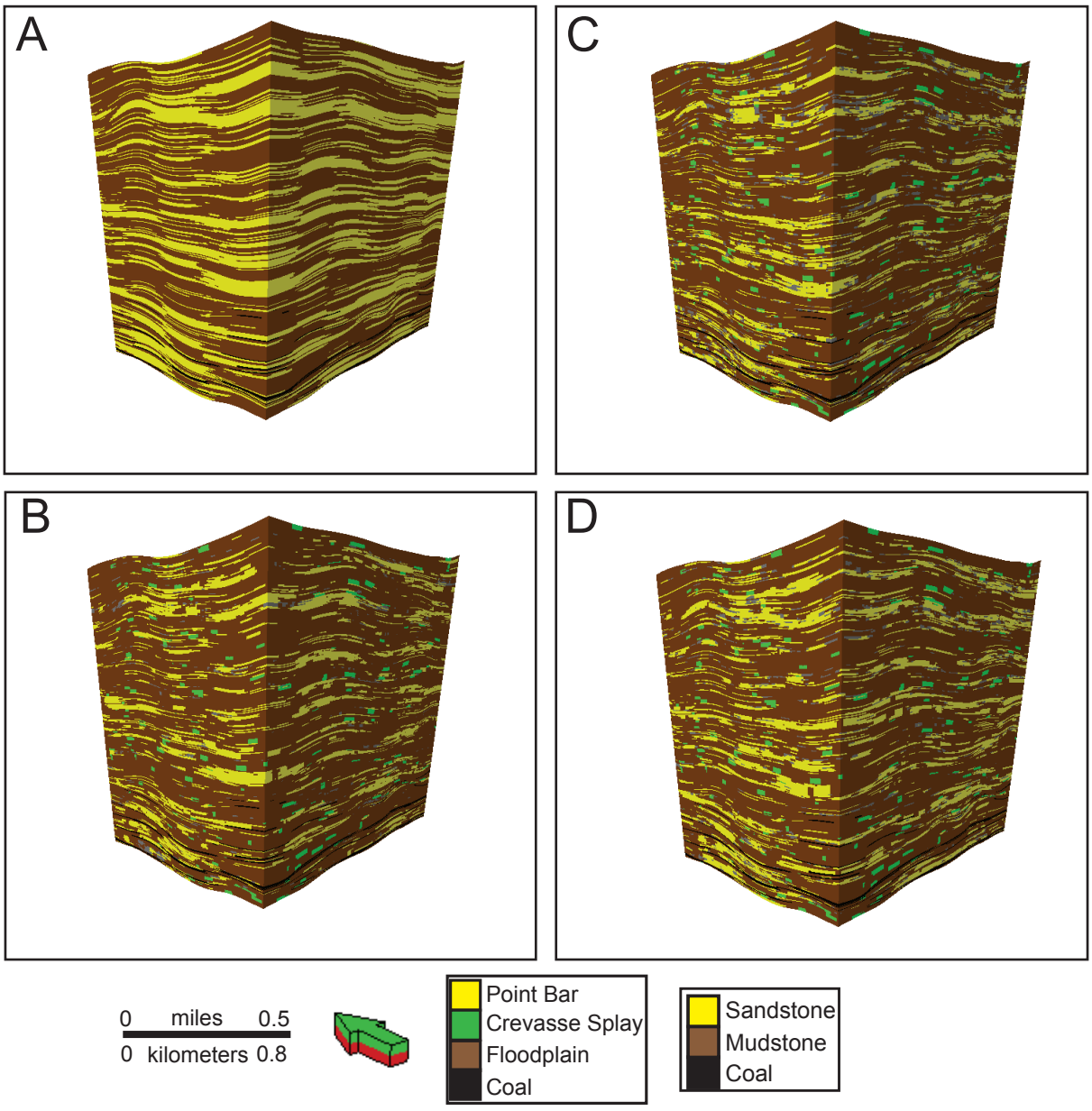

Figure 41: Three-dimensional MPS modeling scenarios using SIS (A) and MPS (B, C, and D). (A) Lithology SIS model. Sandstone, mudstone, and coal are modeled. A vertical proportion curve is used as a constraint in the vertical direction. (B) String-of-Beads MPS model. (C) Mudstone plug MPS model. (D) Partial Mudstone plug MPS model. Point bars, crevasse splays, coal, floodplain, and mudstone plugs are modeled in all MPS models.

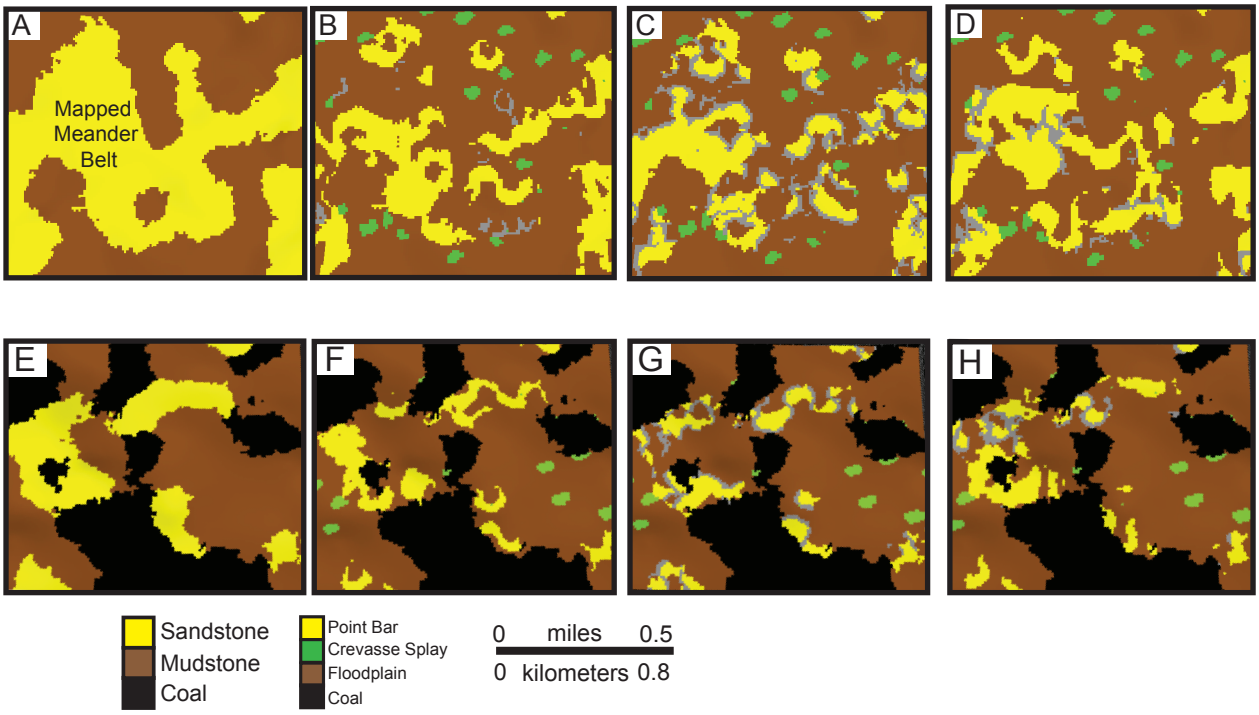

Figure 42: Map view of MPS modeling scenarios. A) Lithology SIS model, B) String-of-beads MPS model, C) mudstone-plug MPS model, D) partial-mudstone-plug MPS model. A through D are map views of layer 58 (wtihin zone 4). E) Lithology SIS model, F) string-of-beads MPS model, G) mudstone-plug MPS model, H) partial-mudstone-plug MPS model. A through D are map views of layer 373 (wtihin zone 20)

occurs in the mudstone plugs model. Overall ratios show a low (less than 50%) net-to-gross ratio for the stratigraphic interval. However, the net-to-gross ratios do not vary by more than 10.4% between models (Figure 40, Appendix I).

PETROPHYSICAL MODELING

In order to evaluate dynamic connectivity of sandstone bodies, petrophysical modeling is conducted to create porosity and permeability models. These property models were inputs into dynamic simulation to evaluate the effect of mud plugs on OGIP, long-term field recovery factor, and dynamic fluid-flow and pressure responses. Strebelle and Journel (2001) state “reproduction of multiple-point continuity in the reservoir model is critical, not so much to produce geologically realistic looking maps, but to provide accurate flow performance predictions.”

Data used for property modeling were downloaded from the Colorado Oil and Gas Conservation Commission (COGCC) website. Of the 52 wells within the modeling area, 12 had neutron-porosity (NPHI), density-porosity (DPHI), and gamma-ray (GR) data (Figure 43; Appendix L). Raster images were digitized for use in 3-D modeling. Petra was used to digitize NPHI and DPHI logs using a half-foot sampling interval. Following the completion of digitizing, log curves were exported and normalized for the interval of interest.

NPHI and DPHI curves used in petrophysical modeling were normalized using PowerLog. Prior to normalization, all logs were calculated to be in fraction, rather than percent, and a coal-flag indicator was used to eliminate values

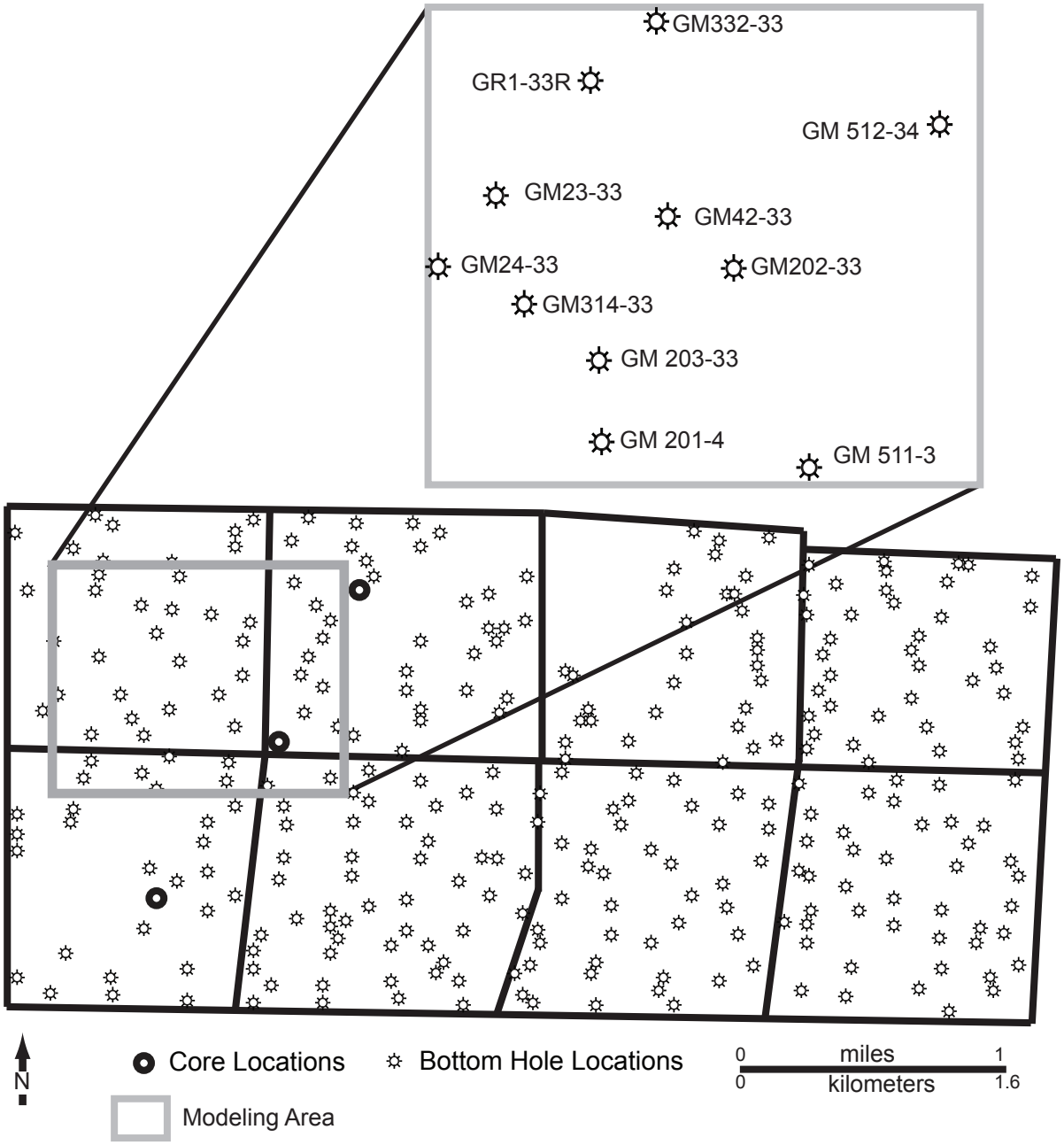

Figure 43: Location of wells within the MPS and property modeling area with available NPHI, DPHI, and GR well logs. NPHI, DPHI, and GR logs are downloaded from the COGCC website, digitized and normalized prior to effective porosity being calculated. Permeability data is taken from available measurements wtihin the ten cores described.

associated with coal. NPHI and DPHI curves were displayed in a multi-well histogram window and the curve with the most normal distribution was manually chosen as the reference curve. All curves were normalized to the reference curve individually using an accordion transform, rather than a bulk-volume shift. Following normalization, NPHI and DPHI curves were exported as LAS files and transferred to Petrel 2010.2 for use in property modeling.

Effective Porosity

Using normalized NPHI, DPHI, and GR logs within the modeling area, total porosity, V-Shale, and effective porosity were calculated as follows: (H. Meng, personal communication, 2011; Figure 44).

Total porosity (PHIT) was calculated using the normalized NPHI and DPHI logs:

$$PHIT=(NPHI+DPHI)/2 \quad (1)$$

Next, a V-shale (Vsh) curve was calculated using normalized gamma-ray (GR_NRM) and gamma-ray API values for clean sandstone (GRclean) and shale (GRshale):

$$Vsh=(GR\_NRM - GRclean) / (GRshale-GRclean) \quad (2)$$

This process was carried out for each well containing NPHI, DPHI, and GR_NRM logs within the modeling area (Figure 43).

Effective porosity (PHIE) was calculated using the values identified in equations (1) and (2), as well as a shale porosity (PHIsh). Shale porosity is a constant taken from available porosity data correlating with core descriptions in the interval of interest. A value of 0.09 (9%) was used to calculate PHIE.

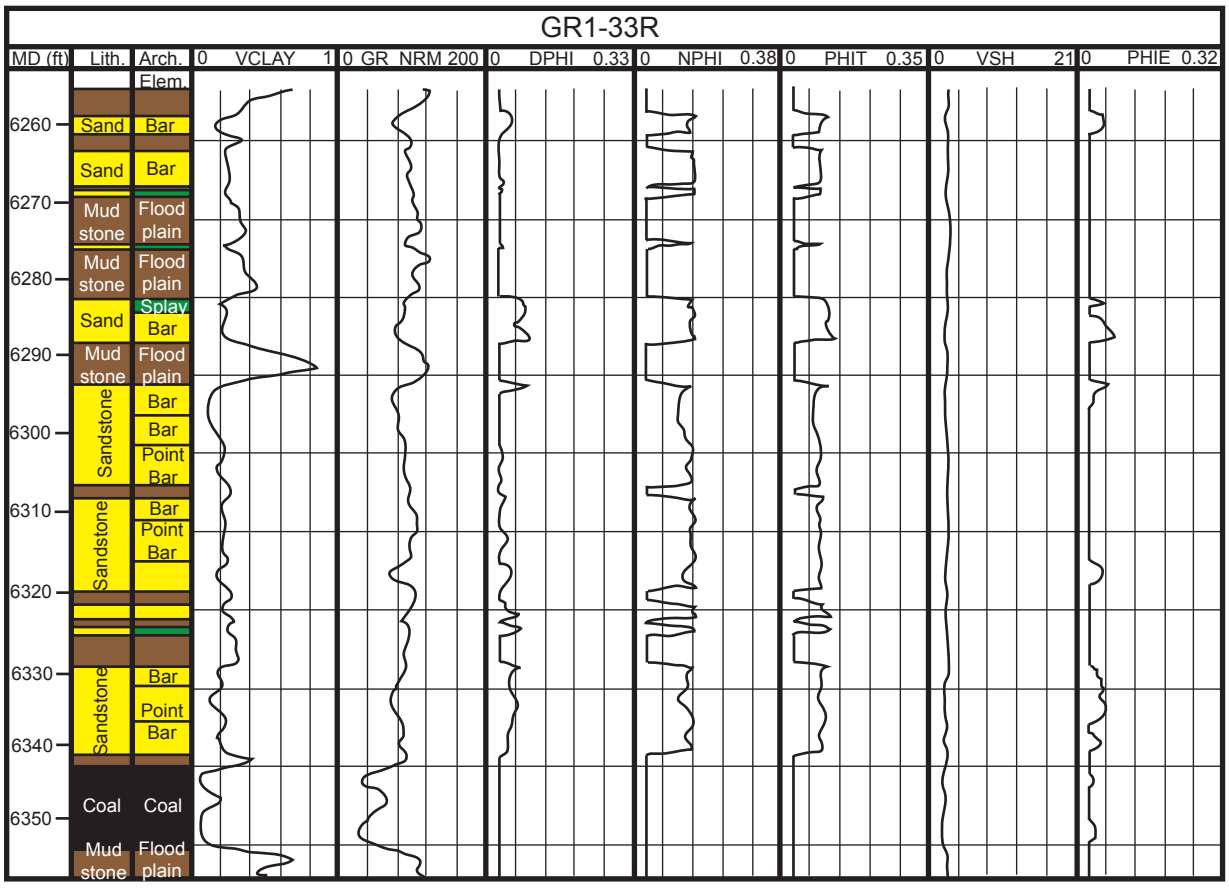

Figure 44: Effective porosity calculation. All logs needed to calculate effective porosity are shown. From left to right: measured depth (ft), calculated lithology, interpreted architectural elements, v-clay (fraction), normalized gamma ray (API), density porosity (fraction), neutron porosity (fraction), calculated total porosity (fraction), calculated v-shale, and calculated effective porosity (fraction). Any lithology and/or architectural element not identified as pay (mudstone/floodplain, and coal) are set to zero values. Effective porosity is only calculated for sandstone (crevasse splays and point bars). Three equations are used to determine effective porosity for the interval. (1) PHIT=(DPHI+NPHI)/2; (2) Vsh=(GR-GRclean)/(GRshale-GRclean); (3) PHIE=PHIT-Vsh*PHIsh where PHIT= Total Porosity, PHIE = Effective Porosity
DPHI = Density Porosity, NPHI = Neutron Porosity, Vsh = Shale Volume, PHIsh = Shale Porosity (% taken from core data), GRshale = Gamma Ray Shale Value, and GRclean = Gamma Ray Clean Sandstone Value.

$$PHIE = PHIT - Vsh * PHIsh \quad (3)$$

To eliminate any erroneous data within the calculation procedure, V-Shale values of greater than 60% were set equal to zero effective porosity, as well as any negative values calculated in PHIE logs.

Porosity Anisotropy

Variogram polar plots were created for sandstone bodies (point bar and crevasse splays) to determine the azimuth of greatest continuity (Figure 45). Variogram polar plots show the variability in 360 degrees, allowing one azimuth direction of least variability to be determined. The azimuths of greatest continuity by zone for point bars and crevasse splays were used in sequential gaussian simulation (SGS) of porosity. SGS input parameters are shown in appendix G. Variogram polar plots for point bars and crevasse splays with associated azimuthal data are shown in appendix H.

Permeability models were created using available porosity and permeability data from cores described in this study. Porosity and permeability data were cross-plotted to show the relationship between the two properties (Figure 46). A cloud transform was used to simulate permeability by architectural element. Due to having a limited amount of porosity data, the cloud transform allowed for a range of permeability values to be calculated from one porosity value. Porosity and permeability models were created for each of the three MPS modeled scenarios (string-of-beads, partial-mudstone-plug, and mudstone-plug; Figure 47).

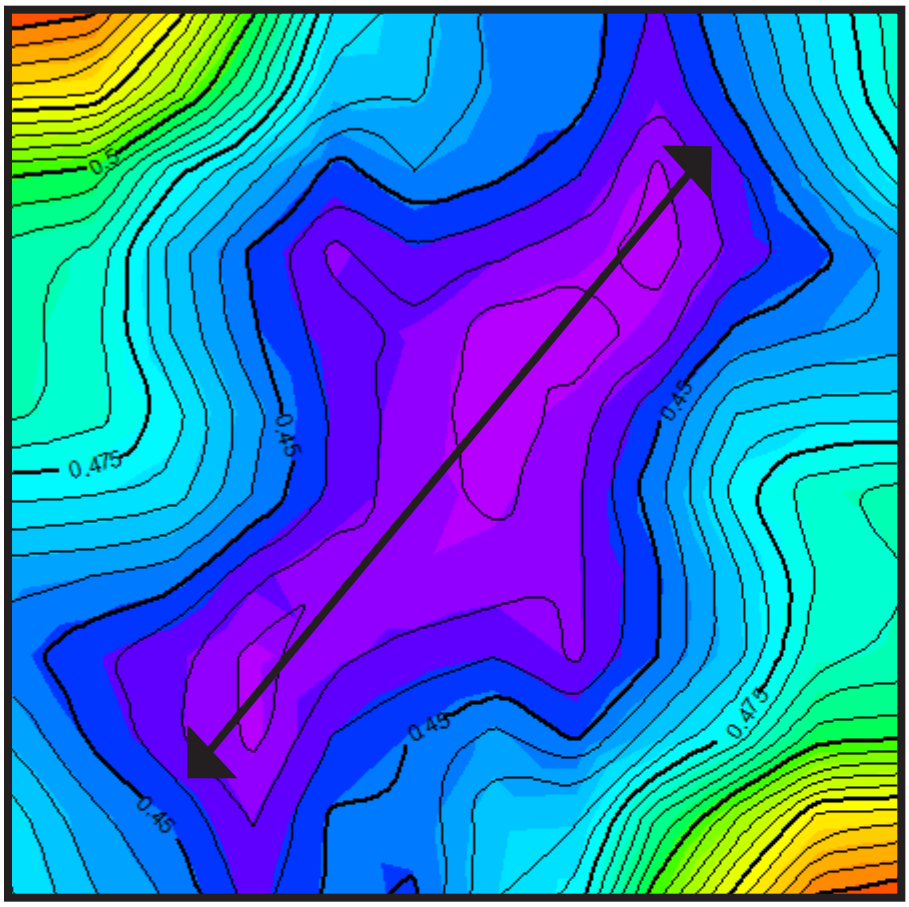

Figure 45: Variogram polar plot of point bars showing the direction of greatest continuity within the specified zone. Azimuth of 25 degrees.

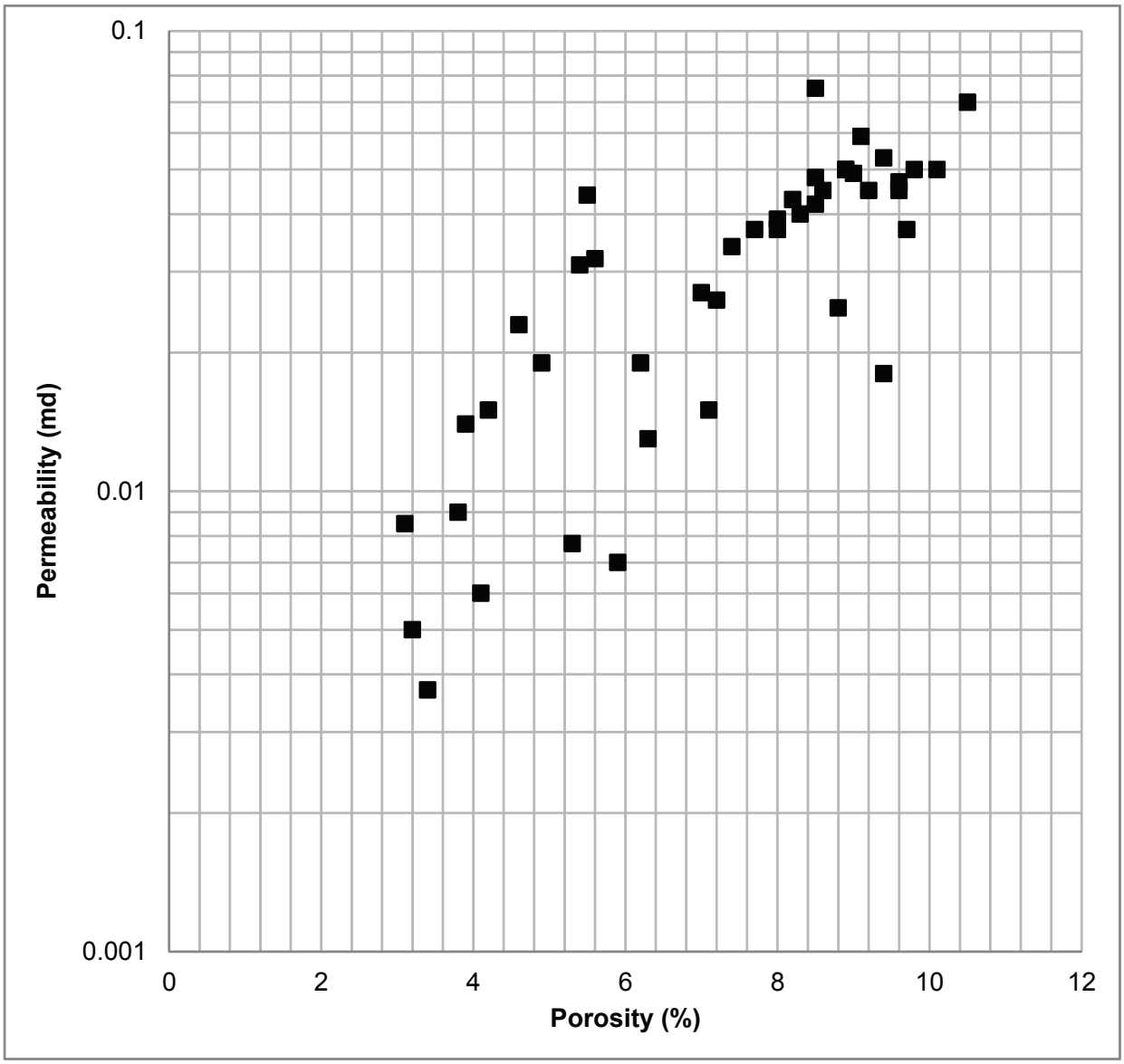

Figure 46: Porosity and permeability cross plot. Porosity and permeability data are obtained the Colorado Oil and Gas Conservation Commission (COGCC) website for the 10 cores described in the study area.

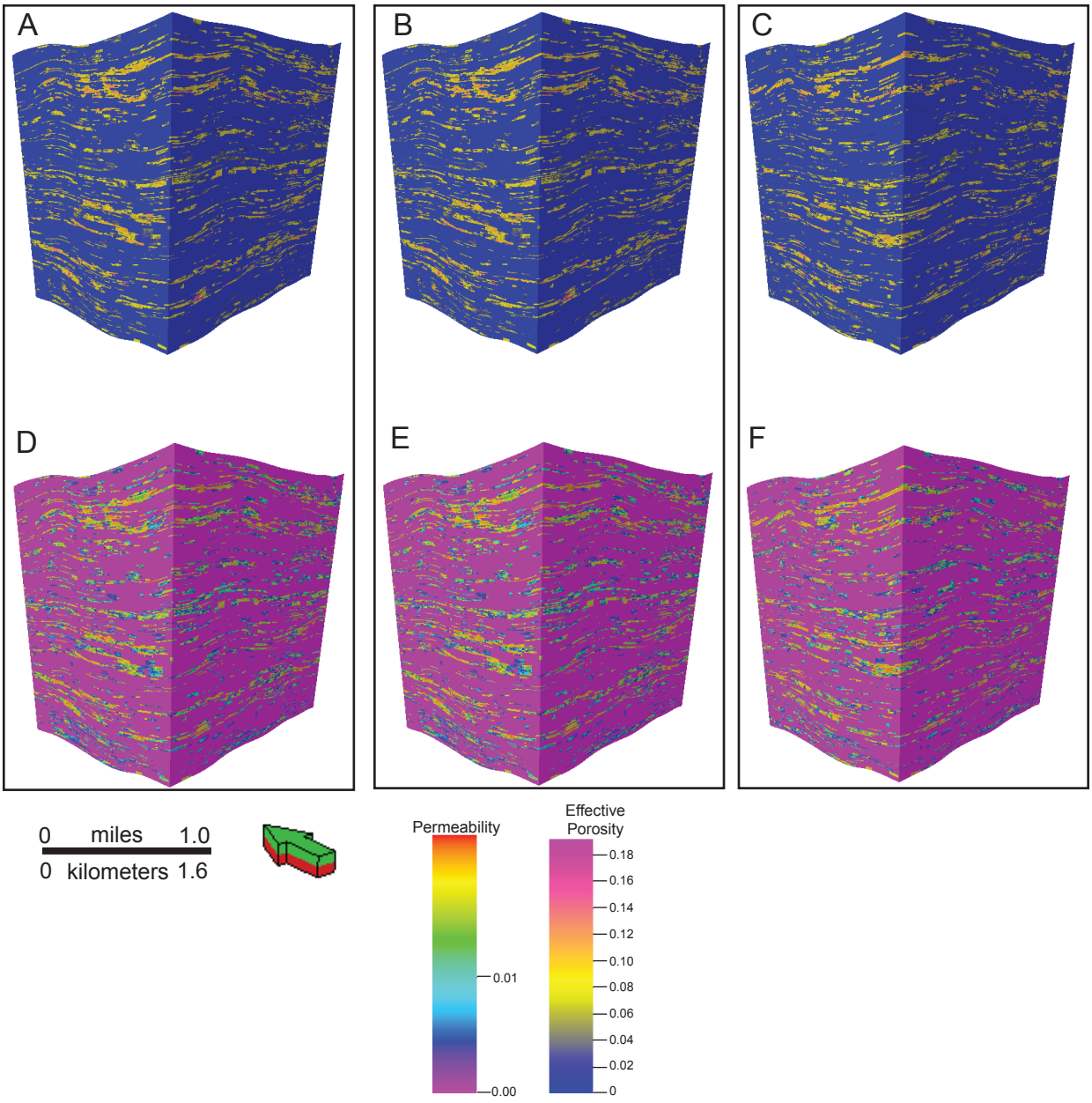

Figure 47: Porosity and permeability models used as input for the dynamic simulation. A) string-of-beads porosity model, D) string-of-beads permeability model, B) partial-mudstone-plug porosity model, E) partial-mudstone-plug permeability model, C) mudstone-plug porosity model, and F) mudstone-plug permeability model.

RESULTS

Six property models were created for input into a dynamic simulation (Figure 47). Petrophysical properties were only modeled in architectural elements identified as pay (e.g. point-bar and crevasse-splay deposits). Petrophysical modeling was carried out using a calculated effective porosity for each of the 12 wells within the modeling area (Figure 43). A cloud transform was used to calculate permeability from a cross-plot of porosity and permeability (Figure 46). In the original calculated effective porosity logs, the range of porosity was from 0% to 28%. Calculated effective porosity logs are upscaled prior to use in property modeling and showed a range from 0% to 19%. All property models showed ranges in porosity from 0-19%. Permeability ranged from 0-0.075 md. All property-model scenarios showed the same range in values of porosity and permeability for their respective MPS model. Therefore, the property models honor the upscaled effective-porosity-log statistics (Figure 47).

DISCUSSION

Results of percentages calculated in upscaled architectural-element logs vary by less than 10% from upscaled architectural-element logs for point bars. Although the statistics calculated in all MPS simulations do not honor exact input values from upscaled well logs, they are within 10% due to mud plugs being modeled in all MPS scenarios and not in manually interpreted architectural-element logs. The presence of mudstone plugs in the training images and not in the upscaled architectural-element logs accounts for the differences in percent

architectural elements between the upscaled logs and the MPS modeling scenarios.

If further studies involve the use of mud plugs to differentiate between point-bar geometries, mud plugs must be identified in core, if possible, and manually interpreted in the original architectural-element logs. By manually interpreting mudstone plugs in the original architectural-element logs, MPS model output statistics of architectural elements would honor the input well log statistics more so than in this study.

Results of net-to-gross ratio calculations ranged from 5.6% to 48.7% in the string of beads MPS model, 6.4% to 48.0% in the partial mudstone plugs model, and 5.3% to 38.4% in the mudstone plugs model. These results indicate the wide range of possible net-to-gross values for individual zone within the model scenarios. The lowest percentage values were calculated from within the thinnest zone. No net-to-gross values were above 50% and therefore correspond with previous literature stating that the lower Williams Fork Formation is a low net-to-gross system.

Results of net-to-gross percentage vary between model scenarios due to the amount of mud plugs included in the training image, and therefore included in the model output. The amount of mud plugs could have been investigated in more detail. For example, additional iterations of MPS models could have been run rather than only three scenarios, two of which show the end-member results.

Property modeling showed similar upscaled log statistics to the output-property models. This is due to having a limited amount of porosity and

permeability data to cross plot, therefore limiting the values calculated from a cloud transform and linear regression. If more porosity and permeability data were available, this would enhance the conceptual dynamic simulation and predication of reservoirs.

CHAPTER FOUR

STATIC AND DYNAMIC CONNECTIVITY OF FLUVIAL SANDSTONES

Depositional connectivity depends upon the following factors: sandstone-to-shale ratios, and sandstone-body depositional architectures (Ainsworth, 2005). This study explores the static and dynamic connectivity associated with meandering fluvial deposits in a low net-to-gross ratio system. Static and dynamic connectivity were conceptually assessed to further understand the behavior and communication of sandstone bodies in the lower Williams Fork Formation at Grand Valley Field. A good understanding of connectivity, both statically and dynamically, of sandstone bodies in the subsurface, can lead to better predictions of hydrocarbon-reservoir location and interaction.

Static and dynamic connectivity were evaluated to identify major changes between the three-modeled MPS scenarios. A conceptual dynamic simulation was conducted to analyze the amount of original gas in place (OGIP) and field recovery efficiency in relation to pressure response. MPS modeling is a useful tool in carrying out more accurate dynamic simulations (Strebelle, 2002).

FLUVIAL STATIC CONNECTIVITY

Each MPS model has different sandstone-body geometries and amounts of mudstone plugs. Static sandstone-body connectivity was calculated by dividing the volume of sandstone connected to wells by the total volume of sandstone in

the model domain (Hovadik and Larue, 2007). This calculation was carried out for each MPS model and performed using Petrel 2010.2.

RESULTS

Results of static connectivity of point bars by zone ranged from 51.1% to 86.4%. The impact of mudstone plugs on static connectivity between the string-of-beads and mudstone-plug models showed a maximum decrease of 26% (Appendix J, Figure 48). Static connectivity decreased approximately 20% between the string-of-beads and partial mudstone-plug models (Appendix J, Figure 48). Zone 7 showed the highest static connectivity of point bars in all three MPS models, showing connectivity of 86.4%, 84.3%, and 78.3% for the string-of-beads, partial-mudstone-plug, and mudstone-plug MPS models, respectively (Figure 48). All model zones are not equal in stratigraphic thickness, however, static connectivity of point bars positively trended with net-to-gross values for each zone (e.g., a higher net-to-gross ratio results in a higher static connectivity value).

Crevasse-splay connectivity was less than 1% for all zones and all models when considered alone. However, crevasse splays made a significant impact on static connectivity when included with point bars. For example, zone 1 showed static connectivity of 69.3% in point bars, with 0.000012% in the splays (Figure 48). However, static connectivity in zone 1, including point bars and crevasse splays, was 93.2%, showing an increase of 23.9% when crevasse splays were included (Figure 48). For comparison, zone 16 had the lowest net-to-gross ratio

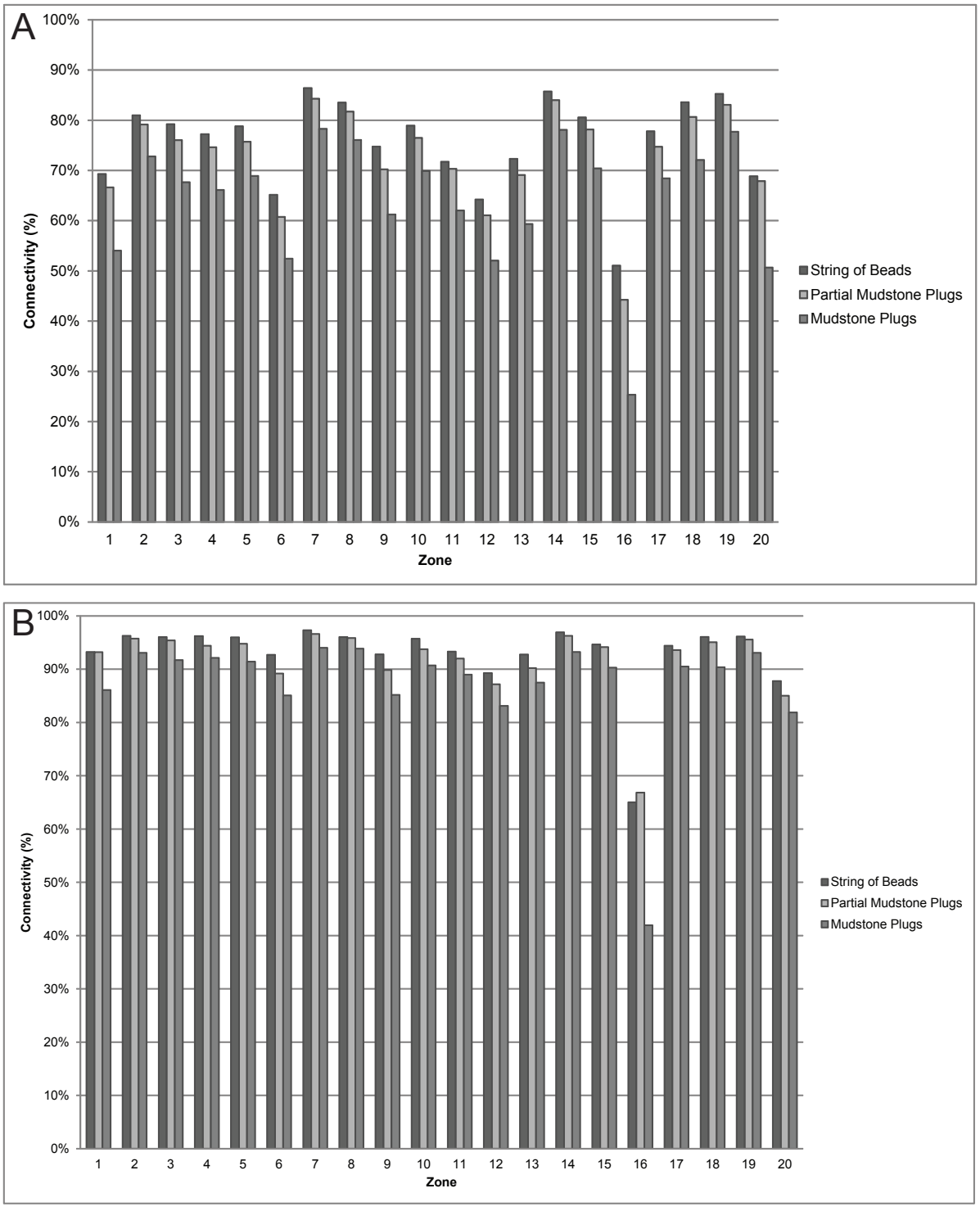

Figure 48: Three-dimensional point bar static connectivity by zone. Static connectivity is calculated by dividing the volume of sandstone connected to well bores by the bulk volume of sandstone in the model area (Hovadik and Larue, 2007). Static connectivity of point bars (A) and total sandstone (B) (point bars and crevasse splays) show the impact crevasse splays have on 3-D connectivity, even though crevasse splays are less than 1% connected when calculated without point bars.

of the 20 model zones, and showed an increase in static connectivity from 51.1% for point bars to 65.0% for total sandstone static connectivity, showing an increase of 13.9% by including crevasse splays (Figure 48). Total sandstone and point bar connectivity were plotted against net-to-gross values for each zone to show the significant difference crevasse splays have on connectivity (Figure 49). Appendix J shows static connectivity results for all stratigraphic zones.

Total sandstone connectivity ranged from 41.94% to 97.34% throughout all MPS model zones, with the string-of-beads MPS model ranging from 65.03% to 97.34%, the partial mudstone-plug MPS model ranging from 66.82% to 96.62%, and the mudstone plug MPS model ranging from 41.94% to 94.02% (Figure 48, Appendix J).

The string-of-beads MPS model showed the highest amount of static connectivity, followed by the partial-mudstone-plugs MPS model, and the mudstone-plugs MPS model. Results of the 3-D connectivity showed overall connectivity range of 65.0% to 97.3% for the MPS string-of-beads MPS model, 66.8% to 96.6% for the partial-mudstone-plugs MPS model, and 41.9% to 94.0% for the mudstone-plug MPS model (Figure 48, Appendix J).

The string-of-beads MPS model was hypothesized to be the most connected, while the mudstone-plug MPS model was thought to be the least connected. This hypothesis is due to presence of mudstone plugs between point bars drawn in the training image used for the mudstone-plug MPS model, and not drawn in the training image used for the string-of-beads model. This

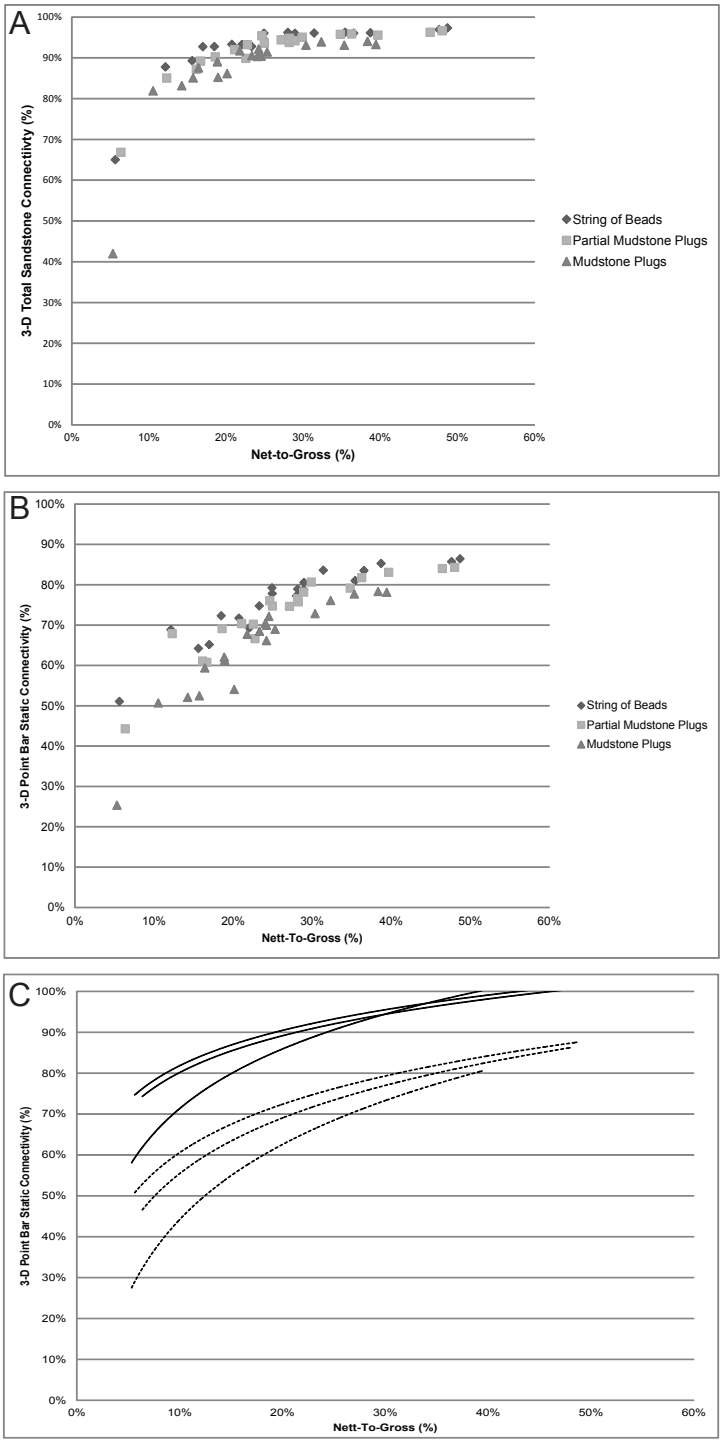

Figure 49: Net-to-gross (%) versus A) total sandstone 3-D static connectivity, B) 3-D point bar connectiivty, and C) best fit curves showing the impact of crevasse splays on static connectivity. Dotted lines show point bar connectivity, solid lines show total sandstone static connectivity.

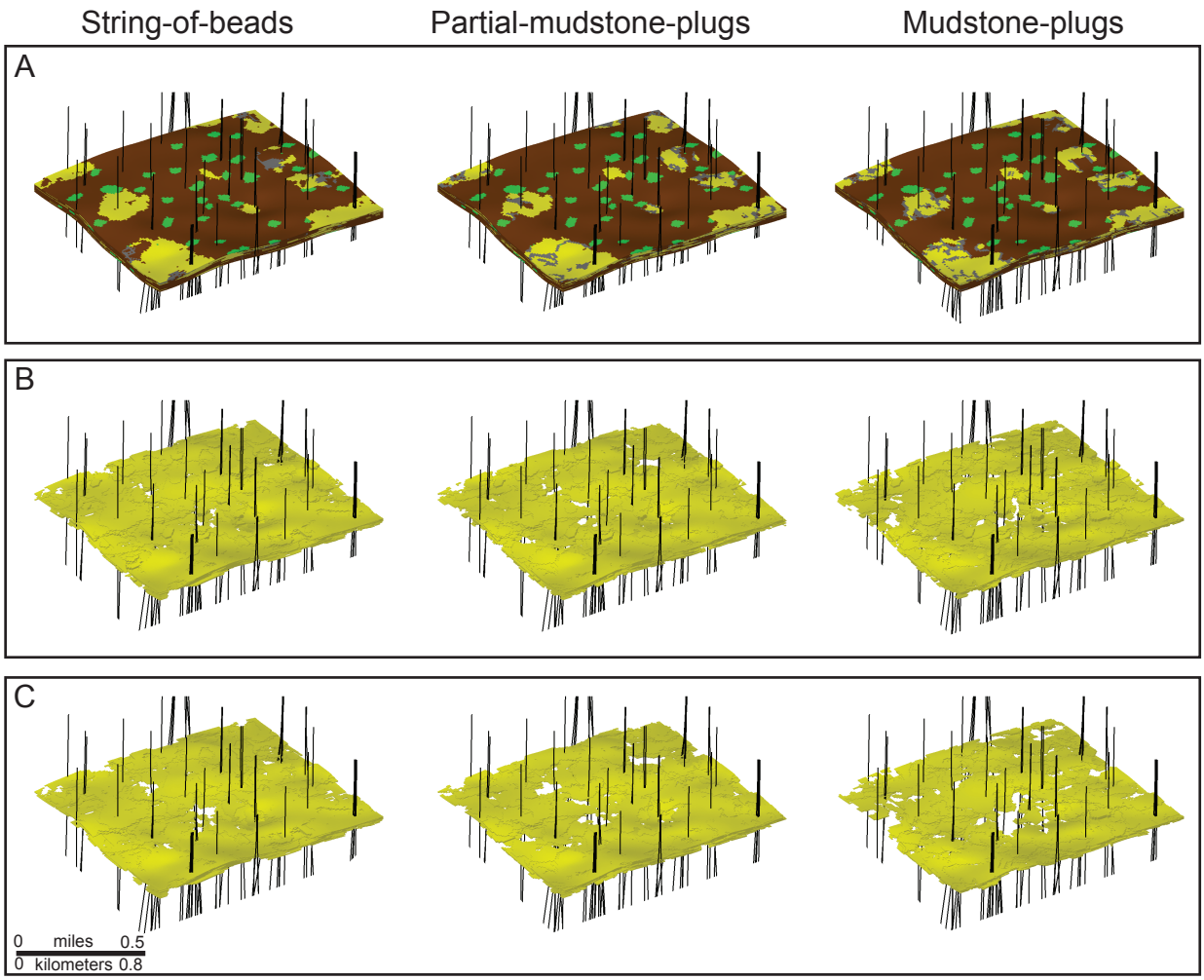

Figure 50: MPS models showing progression from A) original MPS model to B) total sandstone present to C) point bars connected to wells. MPS models show an 84 ft (25.1 m) thick interval wtihin zones 4 and 5. See figure 26 for stratigraphic location of zones.

hypothesis of static connectivity between the three MPS models created is supported by the results discussed and shown in Appendix J.

DYNAMIC CONNECTIVITY AND RECOVERY EFFICIENCY

Quantitative fluid-flow simulations of MPS models explored the 1) original gas in place (OGIP), 2) dynamic fluid-flow and pressure responses, and 3) long-term field recovery factor over a thirty-year time period.

The three detailed architectural-element MPS models and their associated petrophysical models (porosity and permeability), were inputs to flow simulation. For all simulations, water was assumed to be immobile and bulk-volume water has a constant value of 0.02 (dimensionless; T. Schaller, J. Gilman, personal communication, 2011; Gilman, J. R. and Huabing Wang, 2011).

Pressure data were from Mamm Creek Field (~20 mi [32.2 km]) and were applied to the models at Grand Valley Field (Figure 51). Pressure initialization and overburden were calculated prior to fluid-flow simulation. Each stratigraphic zone within the model framework was assigned pressure values at the midpoint of each zone. Therefore, no communication took place between zones, and each stratigraphic zone was in equilibrium. Porosity associated with hydraulic fractures was not included in the calculation of OGIP (T. Schaller and J. Gilman, personal communication, 2011).

Following calculation of OGIP (Figure 52), hydraulic fractures were included within the reservoir simulation using a half-length of approximately 100 ft (30.5 m) and effective conductivity of 250 md-ft (T. Schaller, J. Gilman,

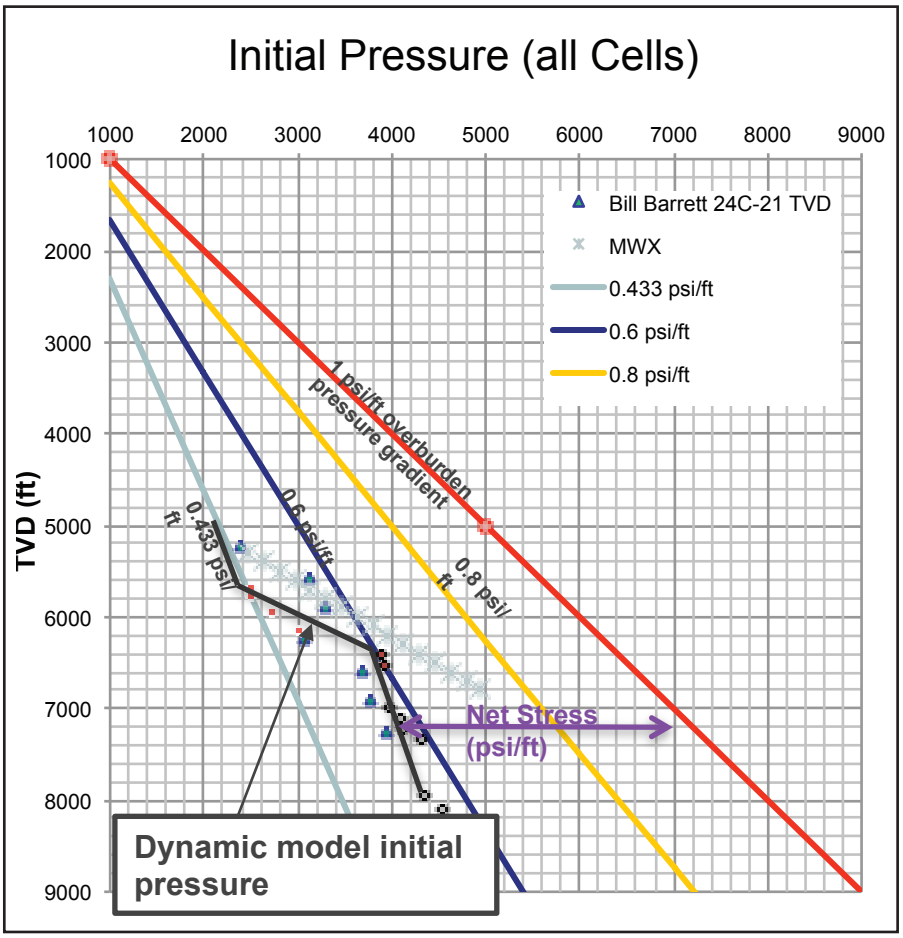

Figure 51: Initial pressure gradient applied to all cells within MPS model scenarios. Data available from Mamm Creek field in the southeastern Piceance Basin taken from Bill Barrett well 24C-21 and MWX well locations. Black line shows the pressure used for all MPS model scenarios. Figure provided by Teresa Schaller, Jim Gilman, and Hai-Ray Meng.

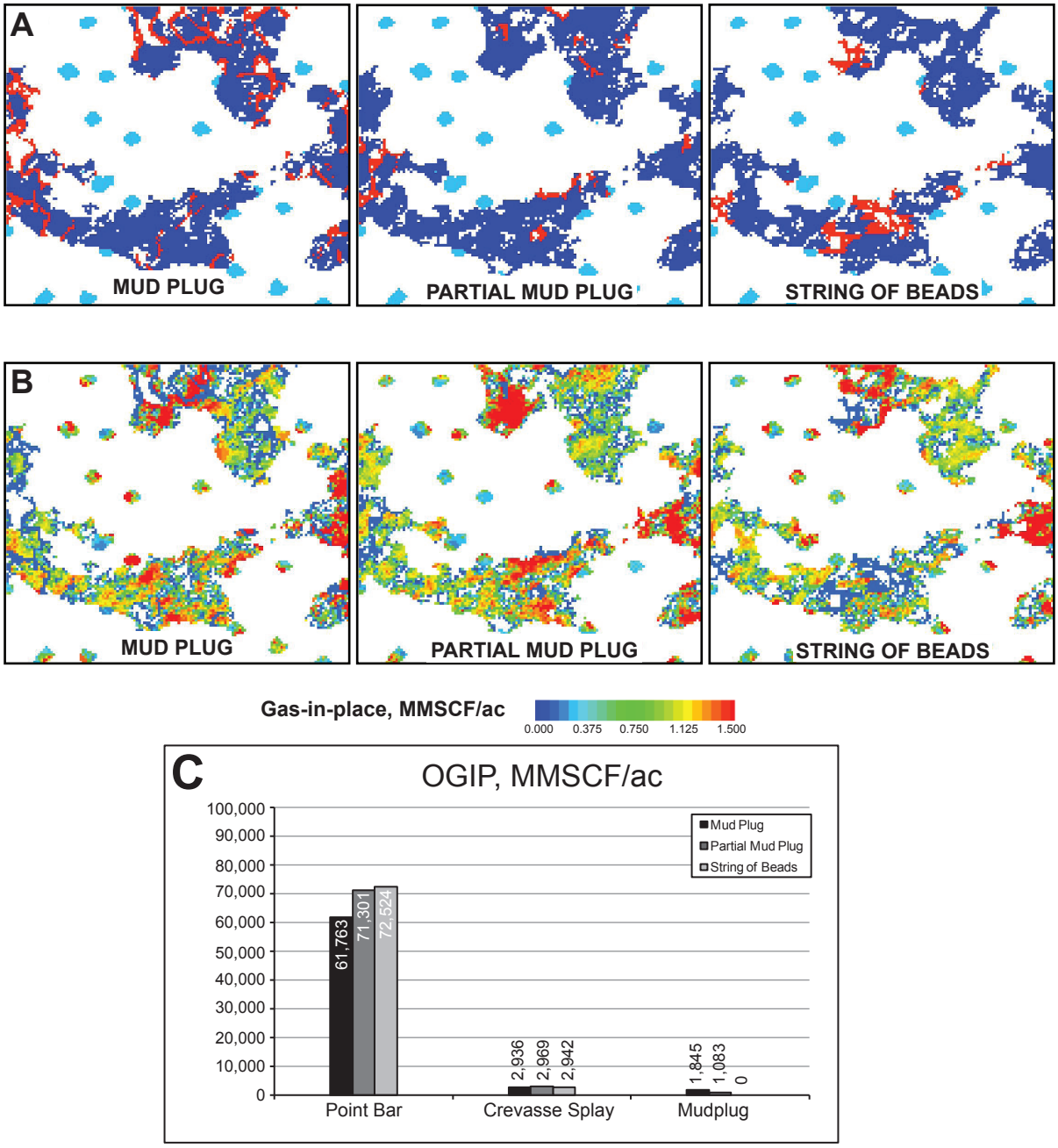

Figure 52: A) Architectural elements identified as pay: point bars-dark blue, crevasse splays-light blue, and mudstone plugs-red. B) Original-gas-in-place (OGIP) for each architectural element model. OGIP. C) OGIP in MMSCF/ac measured by architectural element and model. Figure modified from Teresa Schaller, Jim Gilman, and Hai-Ray Meng personal communication.

personal communication, 2011). Petrophysical constraints and boundary conditions were applied to the wells in order to simulate pressure response over a 30-year period. Wells were constrained to produce a maximum rate of 2.5 MMSCF/D with a limiting bottom-hole pressure of 800 psi.

Long-term field recovery efficiency was evaluated over a 30-year period for all three MPS models and was calculated using 10-ac [4-hectare; 430,600 ft^2 (40,468 m^2)], 20 [8-hectare; 871,200 ft^2 (80,937 m^2)], and 40-ac [16-hectare; 1,742,400 ft^2 (161,874 m^2)] spacing. Sixty-four wells were placed equal-distant apart in the geological model area to simulate 10-ac [4-hectare; 430,600 ft^2 (40,468 m^2)] spacing. When moving to 20-ac [8-hectare; 871,200 ft^2 (80,937 m^2)] and 40-ac [16-hectare; 1,742,400 ft^2 (161,874 m^2)] spacing, every other well was turned off. All wells, at respective spacings, were assigned a fixed bottom-hole pressure (800 psi). Each well was limited to producing a maximum rate of 2.5 MMCF per day.

RESULTS

The range of OGIP was from 35-175 MMSCF/ac for the fluvial sandstone bodies. OGIP for the string-of-beads MPS model was 72,524 MMSCF/ac in point bars, 2942 MMSCF/ac in crevasse splays, and 0 in mudstone plugs, for a total OGIP of 75,466 MMSCF/ac (Figure 52). The partial-mudstone-plug MPS model had OGIP in point bars of 71,301 MMSCF/ac, 2969 MMSCF/ac in crevasse splays, and 1083 MMSCF/ac in mudstone plug deposits for a total OGIP of 75353 MMSCF/ac (Figure 52). The string-of-beads and partial-mudstone-plug

models showed a difference of 113 MMSCF/ac of OGIP. The mudstone plug MPS model had OGIP values of 61,763 MMSCF/ac, 2936 MMSCF/ac, and 1845 MMSCF/ac for point bars, crevasse splays, and mudstone plugs, respectively (Figure 52). The mudstone-plug MPS model had a total of 66,544 MMSCF/ac for the entire model. This differs from the string-of-beads MPS model by 8922 MMSCF/ac and from the partial-mudstone-plug model by 8809 MMSCF/ac. Although OGIP was reported in mudstone plugs for the three MPS models, mudstone plugs were not considered pay, and therefore were not included in static and dynamic connectivity calculations (Figure 52).

Pressure response after 10, 20, and 30 years (Figure 53) showed a maximum drawdown value of -1500 psi from deposits directly connected with wells in the modeling area. Drawdown refers to the decline in pressure over the testing life of the well, in this case 10, 20, and 30 years. Drawdown significantly decreased between wells, especially those that do not have high connectivity with point bars and crevasse splays (Figure 52). Between some wells after 30-years at 20 [8-hectare; 871,200 ft^2 (80,937 m^2)] spacing, the drawdown has remained at 0 psi.

Recovery fraction of the three-modeled scenarios showed an overall range in recovery from 18.7% in the mudstone-plug MPS model at 40-ac [16-hectare; 1,742,400 ft^2 (161,874 m^2)] spacing, to 57.7% in the string-of-beads MPS model at 10-ac [4-hectare; 430,600 ft^2 (40,468 m^2)] spacing (Figure 54). The mudstone-plug MPS model showed differences of 18.7%, 32.7%, and 53.4% recovery at 10-ac [4-hectare; 430,600 ft^2 (40,468 m^2)], 20 [8-hectare; 871,200 ft^2

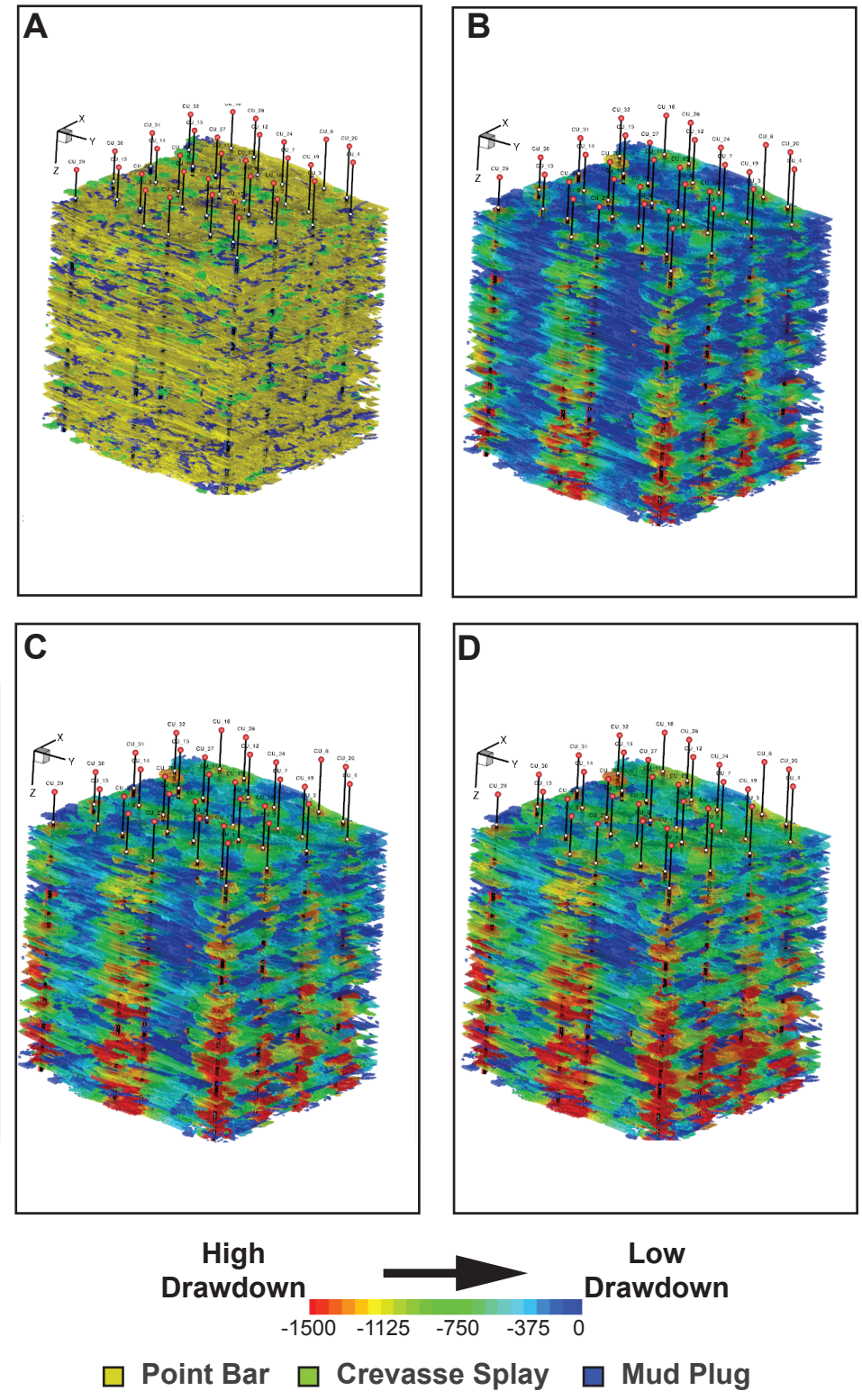

Figure 53: A) Architectural elements and pressure depletion after B) 10, C) 20, and D) 30 years. Figure modified from Teresa Schaller, Jim Gilman, and Hai-Ray Meng.

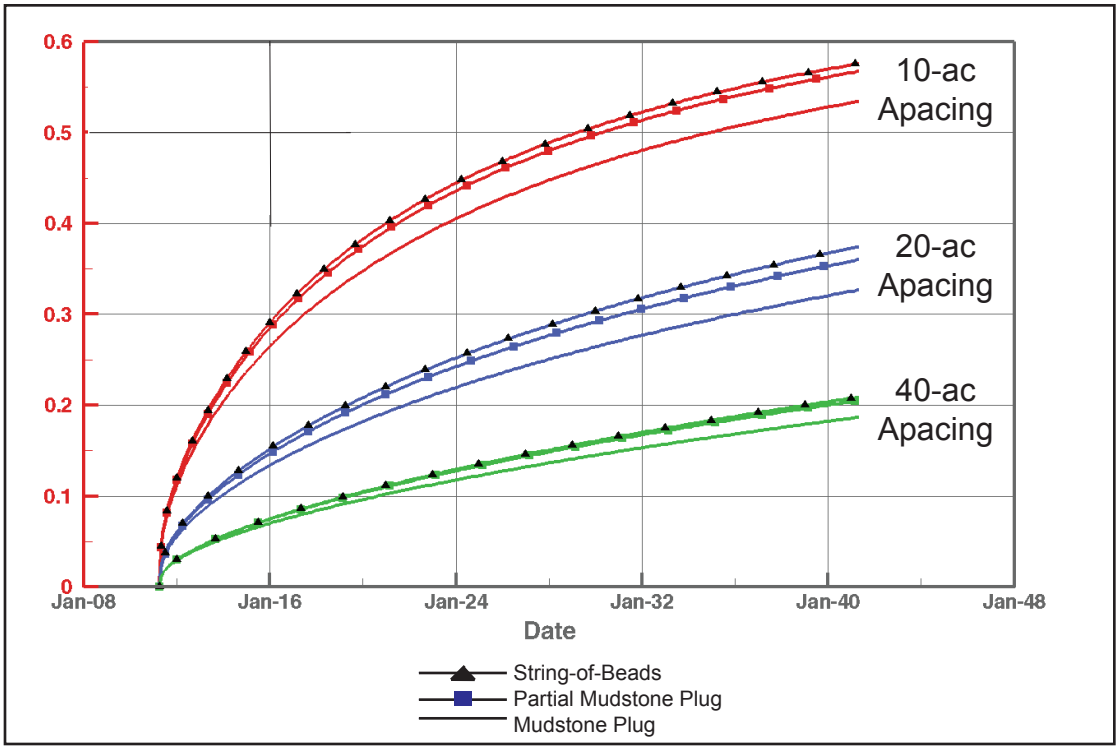

Figure 54: Field recovery efficiency over a 30 year time period for all MPS model scenarios at 10 [4-hectare; 660 ft (201 m)], 20 [8-hectare; 1320 ft (402 m)], and 40-ac [16-hectare; 2640 ft (804 m)], well spacing. Dynamic simulation of field recovery factor over 30 years correlates to overall static connectivity of point bars for the same interval with string-of-beads MPS model showing the most connectivity, partial-mudstone-plug MPS model in the middle, and the mudstone-plug MPS model having the lowest overall static and dynamic connectivity. Figure modified from Teresa Schaller, Jim Gilman, and Hai-Ray Meng.

(80,937 m^2)], and 40-ac [16-hectare; 1,742,400 ft^2 (161,874 m^2)] spacings, respectively. The partial-mudstone-plug model revealed higher values of recovery at the same well spacings, showing 20.5% at 40-ac [16-hectare; 1,742,400 ft^2 (161,874 m^2)], 36.0% at 20 [8-hectare; 871,200 ft^2 (80,937 m^2)], and 56.7% at 10-ac [4-hectare; 430,600 ft^2 (40,468 m^2)] spacings (Figure 54). The string-of-beads MPS model had the highest recovery values after 30-years. Recovery efficiency of the string-of-beads MPS model ranges from 20.9% to 37.5% to 57.7% at 10-ac [4-hectare; 430,600 ft^2 (40,468 m^2)], 20 [8-hectare; 871,200 ft^2 (80,937 m^2)], and 40-ac [16-hectare; 1,742,400 ft^2 (161,874 m^2)] spacings, respectively. The more mudstone-plugs present, the lower the recovery factor (Figure 54).

The results of OGIP calculation and long-term field recovery are consistent with static connectivity results in that the string-of-beads MPS model showed the highest connectivity, and therefore the largest amount of OGIP and recovery efficiency. The mudstone-plug MPS model showed the lowest static connectivity, OGIP, and recovery efficiency. The partial-mudstone-plug model showed values between the two end-member scenarios.

To compare differences in production for all stratigraphic zones to smaller stratigraphic intervals at different net-to-gross ratios, three zones within the mudstone-plug MPS model having low, medium, and high net-to-gross percentages were simulated and produced using 40-foot vertical intervals (Figure 55). These intervals were selected to quantify the difference between a low, medium, and high net-to-gross intervals within the lower Williams Fork Formation.

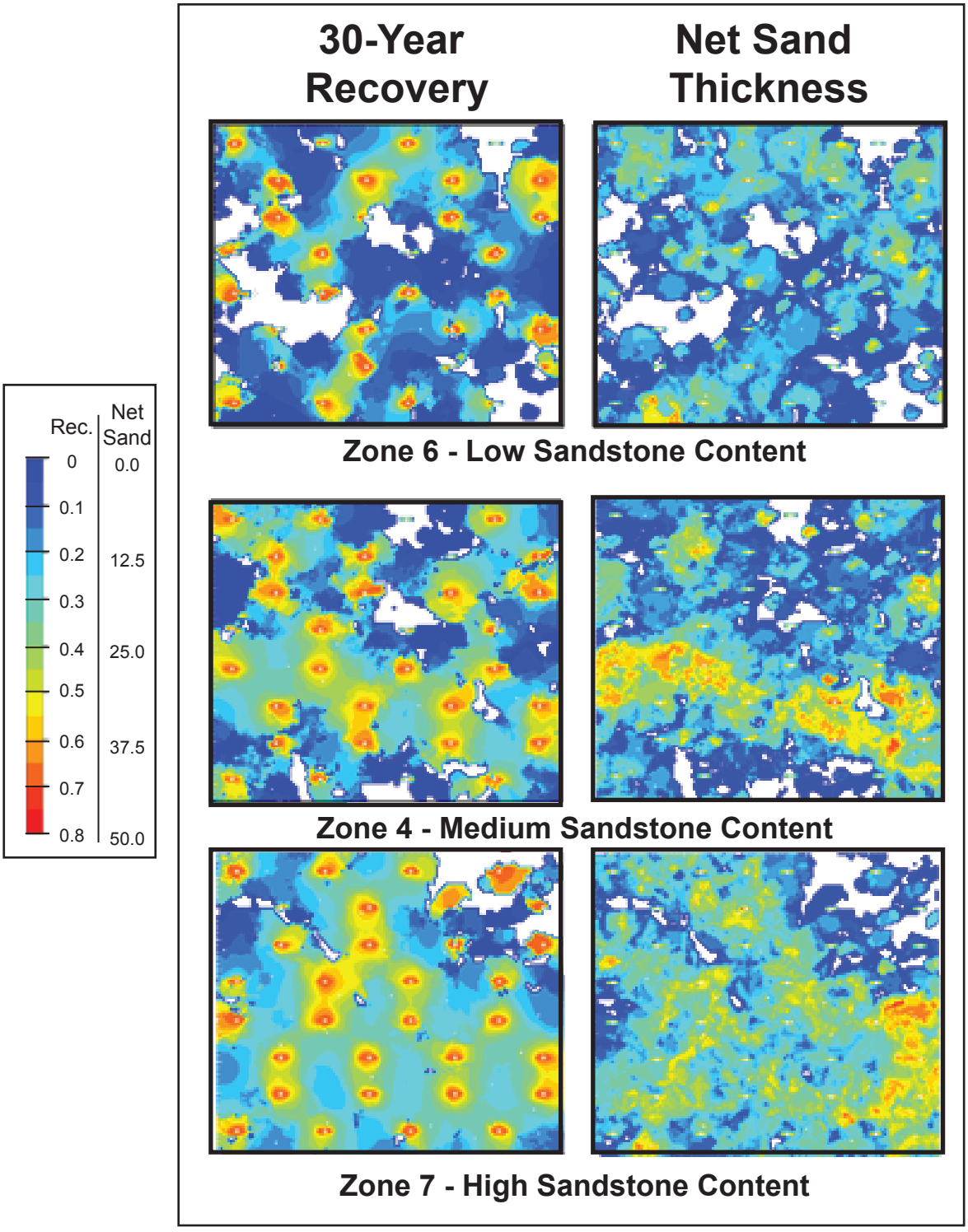

Figure 55: Three zones, each having different net-to-gross ratios, are recovered over 30 years. Each zone is recovered on a 40 foot interval. The net sandstone for each interval shows a high, medium, and low sandstone content for the zones selected. Refer to figure 28 for the location of stratigraphic zones 6, 4, and 7.

Although specific amounts of recovery for each 40-ft (12.2 m) interval were not provided, recovery over 30 years ranged from 1% to approximately 70%. Net-sandstone thickness ranges from 1 to 50 ft (0.3 to 15.2 m; Figure 55).

Comparing cumulative gas recovery from the mudstone-plug and string-of-beads MPS models showed that the presence of mudstone plugs resulted in a total production decrease of 18% (Figure 56). Also, not all wells produced the same amount of gas throughout the model interval, when produced over a 30-year time interval (Figure 57). Identifying the location of wells that did not produce as well throughout the 30-year simulation could be beneficial in well planning within the lower Williams Fork Formation in the future.

Comparison of static to dynamic connectivity for all modeled scenarios showed differences of 35.2%, 35.0%, and 33.8% between static connectivity and dynamic recovery at 10-ac [4-hectare; 430,600 ft^2 (40,468 m^2)] spacing for the string-of-beads, partial-mudstone-plug, and mudstone-plug models, respectively (Figure 58). The string-of-beads MPS model showed dynamic-connectivity values of 57.7%, 37.5%, and 20.9% at 10-ac [4-hectare; 430,600 ft^2 (40,468 m^2)], 20 [8-hectare; 871,200 ft^2 (80,937 m^2)], and 40-ac [16-hectare; 1,742,400 ft^2 (161,874 m^2)] spacings, respectively. The average static connectivity for the string-of-beads MPS model for total sandstone connectivity was 92.9%. The partial-mudstone-plug MPS model showed dynamic connectivity of 56.7% at 10-ac [4-hectare; 430,600 ft^2 (40,468 m^2)], 36.0% at 20 [8-hectare; 871,200 ft^2 (80,937 m^2)], and 20.5% at 40-ac [16-hectare; 1,742,400 ft^2 (161,874 m^2)]. Average static connectivity for total sandstone in the partial-mudstone-plug

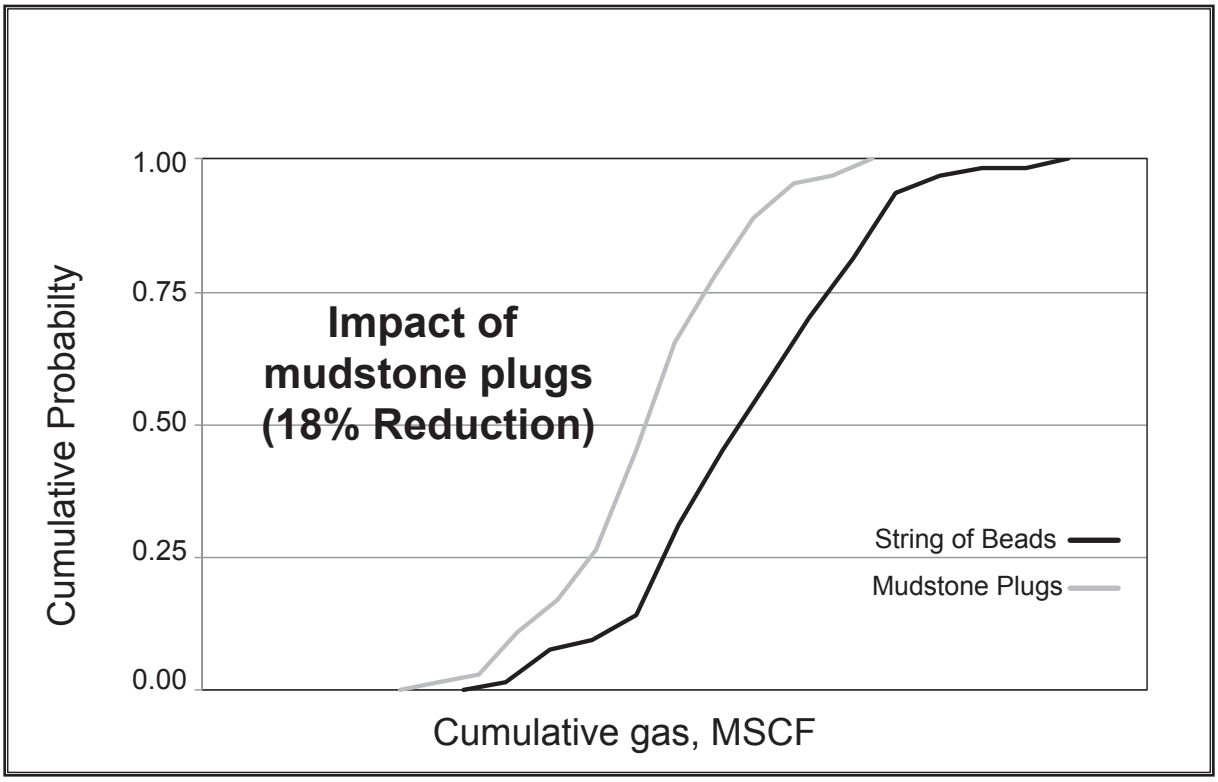

Figure 56: Cumulative production probability comparing the string-of-beads MPS model to the mudstone-plug MPS models at 10-ac (4-hectare, 330 ft) spacing. A difference of 18% production between the two models occurs at 0.50 probability. The 18% difference in production probability occurs due to the presence of mudstone plugs adjacent to point bar deposits and within the floodplian. Figure modified from Teresa Schaller, Jim Gilman, and Hai-Ray Meng.

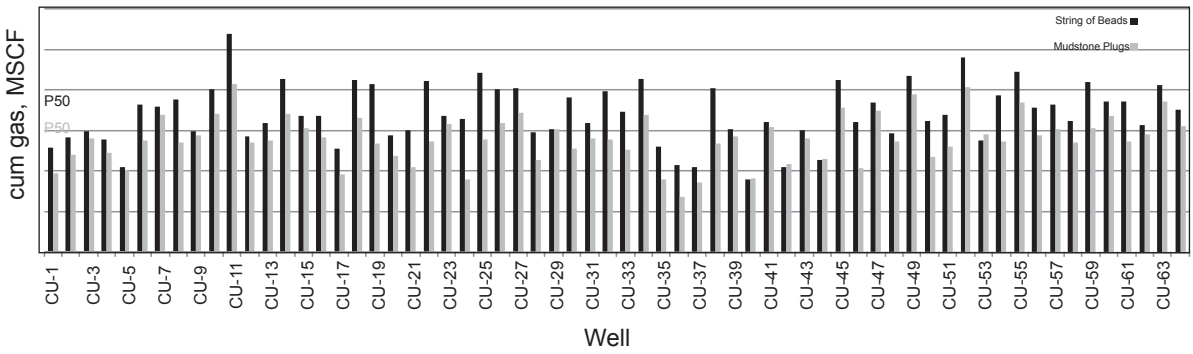

Figure 57: Cumulative gas recovery after 30 years comparing the string-of-beads MPS model with the mudstone-plug MPS model for 64 wells at 10-ac (4-hectare, 330 ft) spacing. P50 lines show the average production for the mudstone-plug and string-of-beads MPS models. This shows that all wells are not producing at the same rate over a 30 year period within the 1 mi^2 (2.6 km^2) MPS modeling area. The string-of-beads MPS model shows the highest recovery over 30-years. The mudstone-plug and string-of-beads MPS models average recovery are shown at lines P50 (black for string-of-beads, gray for mudstone-plug). Figure modified from Teresa Schaller, Jim Gilman, and Hai-Ray Meng.

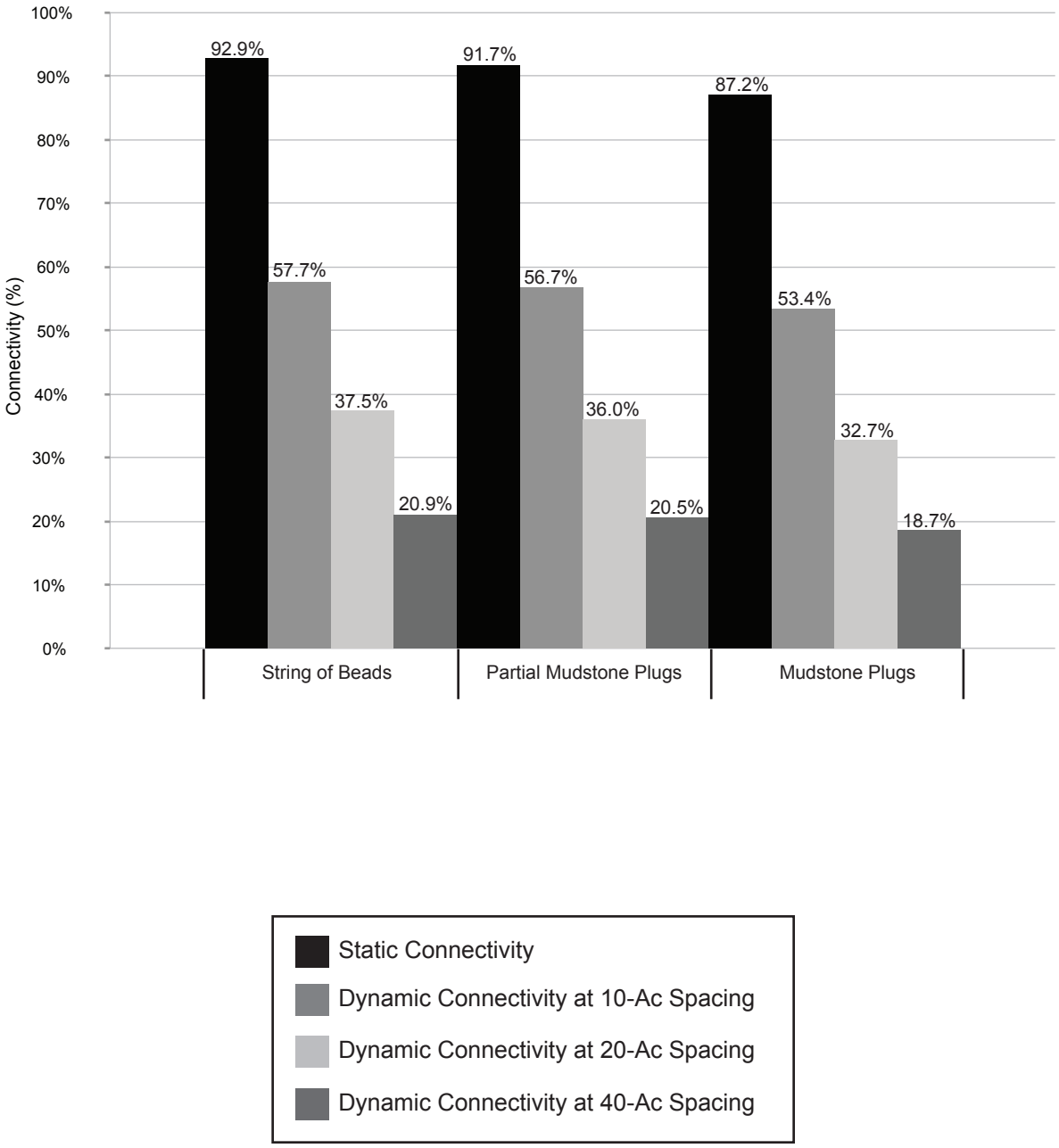

Figure 58: Static versus dynamic connectivity. Average 3-D static connectivity of point bars for each modeled scenario compared to the three different dynamic fluid-flow simulation results. Dynamic connectivity is considered the amount of recovery after 30 years.

model was 91.7% (Figure 58). Finally, the mudstone-plug model dynamic connectivity ranged from 53.4% to 32.7% to 18.7% at 10-ac [4-hectare; 430,600 ft^2 (40,468 m^2)], 20 [8-hectare; 871,200 ft^2 (80,937 m^2)], and 40-ac [16-hectare; 1,742,400 ft^2 (161,874 m^2)] spacings, respectively. This compares to 87.2% static connectivity for all sandstone in the mudstone-plug model (Figure 58).

Results of static and dynamic connectivity show the differences in using both methods for prediction purposes. Static connectivity tends to be optimistic in comparison to dynamic connectivity in which the hydrocarbons are moving through the system, thus representing a potential reservoir. Results of the static connectivity calculation and dynamic simulation support the hypothesis that the string-of-beads model would be the most connected and the mudstone-plug MPS model having the least amount of connectivity.

DISCUSSION

Results of static connectivity and dynamic simulation are useful in the prediction of reservoir response at specific well spacings, and for development. By evaluating three different scenarios involving different amounts of mudstone-plug interaction with point bars, this allows for multiple potential reservoir geometry options. If outcrop statistics are present, and the geologist is able to determine the amount of mudstone plugs present within the system, one of the 3 MPS modeling scenarios could be useful in the evaluation of a meandering river system.

The static connectivity calculation of point bars ranges from 51.1% to 86.4%, while crevasse-splay connectivity was less than 1%. When comparing connectivity percent of point bars and crevasse splays, crevasse splays seem to be insignificant, however, they play an important role. Total sandstone connectivity ranges from 41.94% to 97.34%. The string-of-beads MPS model ranging from 65.03% to 97.34%, the partial mudstone-plug MPS model ranging from 66.82% to 96.62%, and the mudstone plug MPS model ranging from 41.94% to 94.02% (Figure 48, Appendix J). This shows significant increase of 10.2% when crevasse splays are included in the calculation of static connectivity. Therefore, in a meandering system, crevasse splays are important and can increase reservoir performance and connectivity within a system, and should not be discarded as having minimal reservoir potential. The presence of crevasse splays is also important when carrying out a dynamic simulation. The amount of dynamic recovery, although not calculated by individual architectural element, should reveal similar results as the static connectivity.

OGIP in crevasse splays ranged from 2969 MMSCF/640-acre to 2936 MMSCF/640-acre (Figure 52). OGIP of the geologic models ranged from 61,763 to 72,524 MMSCF/acre (for the total 640 ac [1 mi^2] model) in the modeled point bars. Although the highest amount of OGIP is present in point bars, crevasse splays can play an integral role in production of the lower Williams Fork Formation.

The string-of-beads model showed the highest amount of OGIP, while the mudstone-plug model showed the lowest amount of OGIP at 61,763

MMSCF/640-acre. The partial-mudstone-plug model showed a total amount of OGIP at 71,301 MMSCF/6340-acre within point-bar deposits.

Static connectivity results show much higher connectivity than dynamic connectivity due to static connectivity assuming connected sandstone bodies regardless of the size of the interface area that is actually connected between the two bodies. Petrophysical constraints are not taken into account for static connectivity calculations and thus decrease within the dynamic simulation due to small interface areas potentially having very low permeability and not allowing fluids to flow between sandstone bodies. Within the dynamic simulation, hydraulic fractures are also induced which allow for an increase in connectivity, but still less than the average calculated static connectivity.

CHAPTER FIVE

CONCLUSIONS AND RECOMMENDATIONS

CONCLUSIONS

The lower Williams Fork Formation at Grand Valley Field in the Piceance Basin is composed of coal, floodplain, crevasse splays, and point bars. The fluvial sandstone bodies, point bars and crevasse splays, were deposited by meandering fluvial systems during the Late Cretaceous. Core description identified twelve facies, three facies associations, and four architectural elements. The facies within the lower Williams Fork formation at Grand Valley Field, include: (A) contorted mudstone, (B) organic-rich (carbonaceous) mudstone, (C) laminated mudstone, (D) fissile mudstone, (E) silty mudstone, (F) coal, (G) ripple-laminated sandstone, (H) planar-laminated sandstone, (I) contorted sandstone, (J) bioturbated sandstone, (K) wavy-laminated sandstone, (L) structureless sandstone (Table 2; Figures 13, 14). From these twelve facies, three facies associations are identified: (1) coal, (2) floodplain and crevasse splays, (3) and fluvial-channel sandstone deposits. Architectural elements consist of: (1) point bars, (2) crevasse splays, (3) floodplain, and (4) coal (Table 3, Appendix D).

Apparent thicknesses values for point bars in core (N=44) range from 3 - 35 ft (0.9-10.7 m; Figure 18). Point bars in interpreted architectural element logs (N=4644) range in thickness from 2-29.3 ft (0.6-8.9 m). Crevasse splays (N=7) were measured and had an apparent thicknesses range of 3-12 ft (0.9-3.7 m).

Crevasse splays interpreted in architectural-element logs (N=2461) show a thicker range of 1-19.9 ft (0.3-6.1 m).

Net-to-gross ratios ranged from 5.6% to 48.7% in the string-of-beads MPS model, 6.4% to 48.0% in the partial-mudstone-plug model, and 5.3% to 38.36% in the mudstone-plug model (Figure 40). Overall ratios showed a low (less than 50%) net-to-gross ratio for the stratigraphic interval.

MPS modeling allows for the representation of curvilinear features (i.e. point bars and crevasse splays) to be modeled, while incorporating outcrop dimensional data into the subsurface. The following MPS workflow was developed:

1) Perform a detailed stratigraphic analysis to understand the geology of the modeling area.
2) Develop a geological concept model of the modeling area prior to creating training images.
3) Understand the concepts of the SNESIM algorithm, which is used by the MPS modeling.
4) Determine the modeling area of interest, grid size, and cell size.
5) Determine necessary size and percentage of geo-bodies to be represented in the final model and their most simplistic spatial relationship. Also, determine how they appear in today.
6) Create a training image. This can be hand drawn as was done in this study, an object-based model, or a digitized geological sketch of the depositional environment. [In this study, two training images were used

for each model. Point bars were constrained to areas of sandstone identified from a SIS lithology model. Crevasse splays were populated within identified floodplain deposits. Coal was identified from the SIS model and kept consistent throughout all MPS model scenarios.]

7) Test the training image by running an unconditioned model to replicate the pattern created in the training image. This process saves time in the future testing state and allows the user to see if the training image is “over-training” or “under-training” the output model. Creating an unconditioned model also indicates if the search mask, multi-grids, and informed node parameters are sufficient for the model.
8) Create an MP facies pattern to determine maximum search-mask radius, number of multi-grids, and number of informed nodes to use.
9) Test the model output.
10) Evaluate the model in the I, J, and K directions. Note: all layers will not look ideal and therefore, the user must determine what is accurate.
11) If production data is available, carry out history matching for the modeling area.

Results of the 3-D static connectivity show an overall connectivity range of 65.0% to 97.3% for the MPS string-of-beads MPS model, 66.8% to 96.6% for the partial-mudstone-plug MPS model, and 41.9% to 94.0% for the mudstone-plug MPS model (Figure 48, Appendix J). The impact of mudstone plugs on static connectivity between the string-of-beads and mudstone-plug models shows a maximum decrease of 26% for all zones (Appendix J, Figure 48). Static

connectivity decreases approximately 20% between the string-of-beads and partial mudstone-plug models (Appendix J, Figure 48).

Total sandstone connectivity ranges from 41.94% to 97.34% throughout all three MPS models, with the string-of-beads MPS model ranging from 65.03% to 97.34%, the partial mudstone-plug MPS model ranging from 66.82% to 96.62%, and the mudstone plug MPS model ranging from 41.94% to 94.02% (Figure 48, Appendix J). Crevasse-splay connectivity is less than 1% for all zones and all models when considered alone.

Six property models were created for input into a dynamic simulation (Figure 47). The range of OGIP is from 35-175 MMSCF/ac for the fluvial sandstone bodies. OGIP for the string-of-beads MPS model is 72,524 MMSCF/ac in point bars, 2,942 MMSCF/ac in crevasse splays, and 0 in mudstone plugs, for a total OGIP of 75,466 MMSCF/ac (Figure 52). The partial-mudstone-plug MPS model shows an OGIP in point bars of 71,301 MMSCF/ac, 2,969 MMSCF/ac in crevasse splays, and 1,083 MMSCF/ac in mudstone plug deposits for a total OGIP of 75,353 MMSCF/ac (Figure 52). The mudstone plug MPS model shows OGIP values of 61,763 MMSCF/ac, 2,936 MMSCF/ac, and 1845 MMSCF/ac for point bars, crevasse splays, and mudstone plugs respectively (Figure 52). The mudstone-plug MPS model shows a total of 66544 MMSCF/ac for the entire model.

Recovery fraction of the three-modeled scenarios shows a range in recovery from 18.7% in the mudstone-plug MPS model at 40-ac [16-hectare; 2640 ft (804 m)] spacing, to 57.7% in the string-of-beads MPS model at 10-ac [4-

hectare; 660 ft (201 m)] spacing (Figure 54). The more mudstone plug interaction, the lower the recovery factor (Figure 54). Comparing cumulative gas recovery from the mudstone-plug and string-of-beads MPS models shows the presence of mudstone plugs resulted in a total production decrease of 18% (Figure 56).

Comparison of static to dynamic connectivity for all modeled scenarios shows differences of 35.2%, 35.0%, and 33.8% between static connectivity and dynamic recovery at 10-ac [4-hectare; 660 ft (201 m)] spacing for the string-of-beads, partial-mudstone-plug, and mudstone-plug MPS models, respectively (Figure 58). The string-of-beads MPS model shows dynamic connectivity values of 57.7%, 37.5%, and 20.9% at 10 [4-hectare; 660 ft (201 m)], 20 [8-hectare; 1320 ft (402 m)], and 40-ac [16-hectare; 2640 ft (804 m)] spacing, respectively. The average static connectivity for the string-of-beads MPS model for total sandstone connectivity is 92.9%. The partial-mudstone-plug MPS model shows dynamic connectivity of 56.7% at 10-ac [4-hectare; 660 ft (201 m)], 36.0% at 20 [8-hectare; 1320 ft (402 m)], and 20.5% at 40-ac [16-hectare; 2640 ft (804 m)]. Average static connectivity for the total sandstone in the partial-mudstone-plug model is 91.7% (Figure 58). Finally, the mudstone-plug-model dynamic connectivity ranges from 53.4% to 32.7% to 18.7% at 10 [4-hectare; 660 ft (201 m)], 20 [8-hectare; 1320 ft (402 m)], and 40-ac [16-hectare; 2640 ft (804 m)], respectively. This compares to 87.2% static connectivity for all sandstone in the mudstone-plug model (Figure 58).

RECOMMENDATIONS

Research begins and ends with questions. Specific objectives are set from the beginning and other unknowns are unveiled throughout the process. Below is a list of recommendations for items that could be addressed in relation to this study in the future, and further recommendations that were outside the scope of this study.

1) Multiple-point geostatistical modeling (MPS) has the ability to be constrained to both hard and soft data. This study incorporated hard data using dense well control. To have a more constrained MPS modeling scenario, acquiring 3-D seismic to create a 3-D probability cube would assist in the modeling of the distribution of sandstone-body deposits.
2) Although production data in the Piceance Basin is sparse and the ability to tie 3-D models to production history is difficult, if production data was available, history matching of the 3-D MPS sub-surface models to production data would provide a more accurate result.
3) One realization of each MPS scenario was created. Multiple realizations of each MPS scenario could be created to satisfy the central limit theorem (Trotter, 1959; Tye, 2004) and therefore have multiple outputs to test variability of static connectivity and dynamic recovery.
4) In this study, one square mile was modeled. Using MPS to model the entire eight-section area would provide an overview of the larger study area.

5) Additional data can be used in conjunction with core description to assist in interpreting architectural element logs. This data includes: spectral gamma-ray, image logs, and the integration of these with core descriptions.
6) This study was the first MPS modeling work done in the Piceance Basin. Due to the ability of MPS to model curvilinear features (i.e. fluvial channel sandstone-body deposits) and provide accurate dynamic prediction results, it would be beneficial to apply this modeling technique at other locations throughout the Piceance Basin. Using this modeling technique in subsurface locations closer to outcrops of the lower Williams Fork formation (i.e. Coal Canyon, Main Canyon) would allow for better comparison from outcrop to subsurface data in the Piceance Basin.

REFERENCES

Aboktef, A., 2011, Sequence-stratigraphic controls on sandstone diagenesis: An example from the Williams Fork Formation, Piceance Basin, Colorado: Ph.D. Thesis, University of Colorado, Boulder, Colorado, *in progress.*

Allen, J. R. L., 1983, Studies in fluviatile sedimentation: Bars, bar-complexes, and sandstone sheets (low-sinuosity braided streams) in the Brownstones (L. Devonian), Welsh Borders: *Sedimentary Geology*, v. 33, p. 237-293.

Ainsworth, R. B., 2005, Sequence stratigraphic-based analysis of reservoir connectivity: influence of depositional architecture- a case study from a marginal marine depositional setting: Petroleum Geoscience, vol. 11, p. 257-276.

Arpat, G. B., and J. Caers, 2007, Conditional simulation with patterns: Mathematical Geology, v. 39, no. 2.

Baytok, S., 2010, Three-dimensional seismic interpretation and discrete-fracture-network modeling of the Williams Fork Formation, central Mamm Creek Field, Piceance Basin, Colorado: M.S. Thesis, University of Colorado, Boulder, Colorado, 243 p.

Beck, R. A., 1985, Syntectonic sedimentation adjacent to Laramide basement thrusts, Rocky Mountain foreland; timing of deformation: Ames, Iowa, Iowa State University, M.S. thesis, 88 p.

Beck, R. A., C. F. Vondra, J. E. Filkins, and J. D. Olander, 1988, Syntectonic sedimentation and Laramide basement thrusting, Cordilleran foreland; timing of deformation, *in* C. J. Schmidt and W. J. Perry, Jr., eds., Interaction of Rocky Mountain foreland and the Cordilleran Thrust Belt: Geological Society of America Memoir 171 p. 465-487.

Blakey, R. C., 2004, Paleogeography and geologic evolution of North America, http://jan.ucc.nau.edu/~rcb7/namK75.jpg, Accessed January 18, 2011.

Blakey, R. C. and W. Ranney, 2008, Ancient landscapes, 156 p.

Bridge, J.S., 2006, Fluvial facies models: Recent developments, *in* H. W. Posamentier, and R. G. Walker, eds. Facies models revisited: SEPM Special Publication 84, no. 86, p. 85-170.

Bridge, J.S., and R. S. Tye, 2000, Interpreting the dimensions of ancient fluvial channel bars, channels, and channel belts from wireline-logs and cores: AAPG Bulletin, v. 84, no. 8, p. 1205-1228.

Caers, J., and T. Zhang, 2004, Multiple-point geostatistics: A quantitative vehicle for integrating geologic analogs into multiple reservoir models, *in* Integration of outcrop and modern analogs in reservoir modeling: AAPG Memoir 80, p. 383-394.

Cant, J., 1992, Subsurface facies analysis, *in* R.G. Walker and N.P. James, eds., Facies models: Response to sea level change: Geological Association of Canada.

Connolly, Marc, 2011, Personal Communication.

Cole, R. D., and S. P. Cumella, 2003, Stratigrahpic architecture and reservoir characteristics of the Mesaverde Group, southern Piceance Basin, Colorado, *in* K. M. Peterson, T. M. Olson, and D. S. Anderson, eds., Piceance Basin guidebook: Rocky Mountain Association of Geologists, p. 385-442.

Cole, R. D. and S. P. Cumella, 2005, Sand-Body Architecture in the Lower Williams Fork Formation (Upper Cretaceous), Coal Canyon, Colorado, with Comparison to the Piceance Basin Subsurface: The Mountain Geologist, v. 42, no. 3, p. 85-106.

Collins, B. A., 1970, Geology of the coal-bearing Mesaverde Formation (Cretaceous), Coal Basin area, Pitkin County, Colorado: M.S. thesis, Colorado School of Mines, 116 p.

Collins, B. A., 1976, Coal deposits of the Carbondale, Grand Hogback, and Southern Danforth Hills coal fields, eastern Piceance Basin, Colorado: Quarterly of the Colorado School of Mines, v. 71, 138 p.

Collinson, J. D., 1969, The sedimentology of the Grindslow shales and the Kinderscout Grit: A deltaic complex in the Namurian of Northern England: Journal of Sedimentary Petrology, v. 39, n. 1, p. 194-221.

Colorado Oil and Gas Conservation Commission, http://www.cogcc.state.co.us/, Accessed March 15, 2011.

Cumella, S. P., and D. B. Ostby, 2003, Geology of the basin-centered gas accumulation, Piceance Basin, Colorado, *in* K. M. Peterson, T. M. Olson, and D. S. Anderson, eds., Piceance Basin 2003 Guidebook: Rocky Mountain Association of Geologists, Denver, p. 171-193.

Cumella, S. J., J. Scheevel, and L. George, 2005, Geology and mechanics of the basin-centered gas accumulation, Piceance Basin, Colorado: AAPG Search and Discovery.

Cumella, S. P., and J. Scheevel, 2005, The influence of stratigraphy and rock mechanics on Mesaverde gas distribution, Piceance Basin, Colorado, *in* S. P. Cumella, K. W. Shanley, and W. K. Camp, eds., Understanding, exploring, and developing tight-gas sands-2005 Vail Hedberg Conference: AAPG Hedberg Series, no. 3, p. 137-155.

Donselaar, M. E., and I. Overeem, 2008, Connectivity of fluvial point-bar deposits An example from the Miocene Huesca fluvial fan, Ebro Basin, Spain: AAPG Bulletin, v. 92, no. 9, p. 1109-1129.

Elliott, R. E., 1984, Quantification of peat to coal compaction stages, based especially on phenomena in the East Pennine Coalfield, England: Yorkshire Geological Society, v. 45, p. 163-172.

Ellison, A. I., 2004, Numerical modeling of heterogeneity within a fluvial point-bar deposit using outcrop and lidar data: Williams Fork Formation, Piceance Basin, Colorado: M.S. thesis, University of Colorado, Boulder, CO, 234 p.

German, Q. A., Analysis of fluvial sandstone-body characteristics and architecture in a high net-to-gross system: Upper Williams Fork formation, Plateau Creek Canyon, Piceance Basin, Colorado: M.S. thesis, University of Colorado, Boulder, Colorado, 151 p.

Gilman, J., 2011, Personal communication

Gilman, J.R., and Huabing Wang, 2011, Reservoir simulation of detailed object based models of a complex fluvial system, SPE 146037, Denver, CO Oct 31 – Nov. 2, 2011.

Guardiano, F. B., and R. M. Srivastava, 1993, Multivariate geostatistics: Beyond bivariate moments: Quantitative Geology and Geostatistics, v. 5, p. 133-144.

Gustason, E.R., 2011, Personal communication

Hancock, E. T., 1925, Geology and coal resources of the Axial and Monument Butte quadrangles, Moffat County, Colorado: United States Geological Survey Bulletin 757, 134 p.

Hettinger, R. D. and M. A. Kirschbaum, 2002, Stratigraphy of the Upper Cretaceous Mancos Shale (upper part) and Mesaverde Group in the southern part of the Uinta and Piceance basins, Utah and Colorado: USGS Report I-2764, 21 p.

Hettinger, R. D. and M. A. Kirschbaum, 2003, Stratigraphy of the Upper Cretaceous Mancos shale (Upper Part) and Mesaverde Group in the southern part of the of the Uinta and Piceance basins, Utah and Colorado

(Chapter 12), *in* Petroleum systems and geologic assessment of oil and gas in the Uinta-Piceance province, Utah and Colorado: United States Geological Survey Digital Data Series DDS- 69-B, 25 pp.

Hewlett, A. C., 2010, Fluvial architecture and static connectivity of the Williams Fork Formation, central Mamm Creek Field, Piceance basin, Colorado: M.S. thesis, University of Colorado, Boulder, Colorado, 227 p.

Hovadik, J. M., and D. K. Larue, 2007, Static characterizations of reservoirs: refining the concepts of connectivity and continuity: Petroleum Geoscience, v. 13, p. 195-211.

Johnson, R. C., 1989, Geologic history and hydrocarbon potential of Late Cretaceous- age, low-permeability reservoirs, Piceance Basin, western Colorado: United States Geological Survey Bulletin 1787-E, 51 p.

Johnson, R. C., and R. M. Flores, 2003, History of the Piceance Basin from latest Cretaceous through early Eocene and the Characterization of Lower Tertiary sandstone reservoirs, *in* K. M. Paterson, T. M. Olson, and D. S. Anderson, eds., Piceance Basin 2003 guidebook: Rocky Mountain Association of Geologists, p. 21-61.

Johnson, R. C., and S. B. Roberts, 2003, The Mesaverde total petroleum system, Uinta-Piceance province, Utah and Colorado (Chapter 7) *in* Petroleum systems and geologic assessment of oil and gas in the Uinta-Piceance province, Utah and Colorado: United States Geological Survey Digital Data Series DDS-69-B, 68 p.

Lee, W. T., 1909, The Grand Mesa coal field, Colorado: United States Geological Survey Bulletin, v. 341, pt. 2, p. 316-334.

Lopez, S., A. Galli, and I. Cojan, 2001, Fluvial meandering channelized reservoirs: A stochastic and process-based approach: Proceedings of the Annual Conference of the International Association for Mathematical Geology, September 6-12, Cancun, Mexico.

Meng, H. Z., 2011, Personal communication

Miall, A. D., 1985, Architectural-element analysis: A new method of facies analysis applied to fluvial deposits: Earth-Science Reviews, v. 22, p. 261-308.

Miall, A. D., 1992, Alluvial deposits, *in* R. G. Walker and N. P. James, Facies models: Response to sea level change: Geological Society of Canada, p. 119-142.

Miall, A. D., 2006, Fluvial facies models: Recent developments, *in* H. W. Posamentier, and R. G. Walker, eds., Facies Models Revisited, SEPM Special Publication, no. 84, p. 85-170.

Nelson, P. H., 2002, A review of the Multiwell Experiment, Williams Fork and Iles Formations, Garfield County, Colorado (Chapter 15) *in* Petroleum systems and geologic assessment of oil and gas in the Unita-Piceance province, Utah and Colorado: United States Geological Survey Digital Data Series DDS-69-B, 28 p.

Panjaitan, H., 2006, Sand-body dimensions in outcrop and subsurface, lower Williams fork formation, Piceance Basin, Colorado: M.S. thesis, Colorado School of Mines, Colorado, 170 p.

Patterson, P. E., K. Kronmueller, and T. D. Davies, 2003, Sequence Stratigraphy of the Mesaverde Group and Ohio Creek Conglomerate, Northern Piceance Basin, Colorado, *in* K. M. Peterson , T. M. Olson, and D. S. Anderson, eds., Piceance Basin 2003 Guidebook: Rocky Mountain Association of Geologists, Denver, p. 171-193.

Pranter, M. J., A. I. Ellison, R. D. Cole, and P. E. Patterson, 2007, Analysis and modeling of intermediate-scale reservoir heterogeneity based on a fluvial point-bar outcrop analog, Williams Fork Formation, Piceance Basin, Colorado: AAPG Bulletin, v. 81, no. 7, p. 1025-1051.

Pranter, M. J., M. F. Vargas-Lopez, and T. L. Davis, 2008, Characterization and 3D reservoir modelling of fluvial sandstones of the Williams Fork Formation, Rulison Field, Piceance Basin, Colorado, USA: Journal of Geophysics and Engineering, v. 5, p. 158-172.

Pranter, M. J., R. D. Cole, H. Panjaitan, and N. K. Sommer, 2009, Sandstone-body dimensions in a lower coastal-plain depositional setting: Lower Williams Fork Formation, Coal Canyon, Piceance Basin, Colorado: AAPG Bulletin, v. 93, no. 10, p. 1379-1401.

Pranter, M.J., A. D. Hewlett, R. D. Cole, H. Wang, J. Gilman, 2011, Fluvial architecture and connectivity of the Williams Fork Formation: Use of outcrop analogues for stratigraphic characterisation and reservoir modeling: *in press.*

Pranter, M. J., and N. Sommer, 2011, Static connectivity of fluvial sandstones in a lower coastal-plain setting: An example from the Upper Cretaceous lower Williams Fork Formation, Piceance Basin, Colorado: AAPG Bulletin, v. 95, no. 6, p. 899-923.

Preistman, A., 2003, Piceance Basin bibliography, *in* Picenace Basin Guidebook: Rocky Mountain Association of Geologists, p.308-384

Pringle, J. K., A. R. Westerman, J. D. Clark, N. J. Drinkwater, and A. R. Gardiner, 2004, 3-D high-resolution digital models of outcrop analog study sites to constrain reservoir model uncertainty: An example from Alport Castles, Derbyshire, UK: Petroleum Geoscience, v. 10, p. 343-352.

Rider, M. 2002a, Facies, sequences and depositional environments from logs (Chapter 14), *in* M. H. Rider, ed., The Geological Interpretation of Well Logs, 2nd edition: Rider-French Consulting Ltd., p. 226- 238.

Rider, M. 2002b, Sequence stratigraphy and stratigraphy (Chapter 15), *in* M. H. Rider, ed., The Geological Interpretation of Well Logs, 2nd edition: Rider-French Consulting Ltd., p. 239-260.

Roy, P. and S. Strebelle, 2008, Capturing depositional processes using MPS simulation with multiple training images, AAPG Search and Discovery article #40360, Adapted from oral presentation at AAPG Annual Convention 2008.

Schaller, T., 2011, Personal communication.

Schlumberger SIS Support Portal, http://support.slb.com/siskb/preview/previewmain.cfm?caseid=4738833, (accessed February 1, 2011).

Schlumberger IS, 2005, PETREL workflow tools: Introduction course, v. 2004, 2nd ed.: Houston, Texas, Schlumberger Information Solutions, 527 p.

Schlumberger, 1989, Schlumberger Log Interpretation Charts, 152 p.

Shaak, R. V., 2010, Stratigraphic architecture of shallow-marine to coastal-plain parasequences: Lower Williams Fork Formation, southeastern Piceance Basin, Colorado: M.S. thesis, University of Colorado, Boulder, Colorado, 176 p.

Shepherd, M., 2009, Chapter 19: Geostatistical methods, *in* M. Shepherd, ed., Oil field production geology: AAPG Memoir 91, p. 159-174.

Sommer, N. K., 2003, Sandstone-body connectivity in a meandering fluvial system: An example from the Williams Fork Formation, Piceance Basin, Colorado: M.S. thesis, University of Colorado, Boulder, Colorado, 193 p.

Strebelle, S. B., 2002, Conditional simulation of complex geological structures using multiple-point statistics: Mathematical Geology, v. 34, no. 1.

Strebelle, S. B., 2006, Sequential simulation for modeling geological structure from training images, *in* T. C. Coburn, J. M. Yarus, and R. L. Chambers, eds., Stochastic modeling and geostatistics: Principles, methods, and case studies, v. II: AAPG Computer Applications in Geology 5, p. 139-149.

Strebelle, S. B., and A. G., Journel, 2001, Reservoir modeling using multiple point statistics: SPE paper 71324, presented at the Annual Technical Conference and Exhibition, New Orleans, Sept. 30-Oct. 3.

Strebelle, S., and K. Payrazyan, and J. Caers, 2002, Modeling of a deepwater turbidite reservoir conditional to seismic data using multiple-point geostatistics: Society of Petroleum Engineers, SPE 77425, 10 p.

Strebelle, S. and T. Zhang, 2004, Non-stationary multiple-point geostatistical models, *in* O. Leuangthong and C.V. Deutsch, eds., Geostatistics Banff, p. 235-244.

Trotter, H. F., 1959, Elementary proof of the central limit theorem: Arch. Mathematics, v.10, p. 226-234.

Tye, R. S., 2004, Geomorphology: An apprpoach for determining subsurface reservoir dimensions: AAPG Bulletin, v. 88, no. 8, p. 1123-1147.

Tyler, R., W. A. Ambrose, A. R. Scott, and W. R. Kaiser, 1992, Evaluation of the coalbed methane potential in the greater Green River, Piceance, Powder River, and Raton Basins, *in* Wyoming Geological Association Guidebook, p. 269-302.

Vargas, M. R., 2004, Characterization and modeling of fluvial sandstone distribution and static connectivity, Williams Fork Formation, Rulison Field, Piceance Basin, Colorado: M.S. thesis, University of Colorado, Boulder 136 p.

Walker, R. G., 1984, Facies models, 2nd ed., Geoscience Canada reprint series 1:Toronto, Geological Association of Canada 318 p.

Walker, R. G., 1992, Facies, facies models and modern stratigraphic concepts *in* Walker, R.G., and James, N.P., eds., Facies Models: Response to sea level change, Geological Association of Canada, 409 p.

Weijers, L., Y. Kama, J. Shemeta, S. Cumella, 2009, Bigger is better-hydraulic fracturing in the Williams Fork Formation in the Piceance Basin, AAPG Search ad Discovery Article #110092.

Young, R. G., 1955, Sedimentary facies and intertonguing in the Upper Cretaceous of the Book Cliffs, Utah-Colorado: Geological Society of America Bylletin, v. 66, p. 177-202.

Yurewicz, D. A., K. M. Bohacs, J. Kendall, R. E. Klimentidis, K. Kronmueller, M. E. Meurer, T. C. Ryan, and J. D. Yeakel, 2008, Controls on gas and water distribution, Mesaverde basin-centered gas play, Piceance Basin, Colorado, *in* S.P. Cumella, K.W. Shanley, and W.K. Camp, eds., Understanding, exploring, and developing tight-gas sands: 2005 Vail Hedberg Conference: AAPG Hedberg Series, no. 3, p. 105-136.

Appendix A

Lower Williams Fork Sandstone-Body Dimensional Data

Appendix A contains sandstone-body dimensional data collected at Coal Canyon within the lower Williams Fork Formation. Crevasse splay and single story (point bar) sandstone-body data are used to constrain architectural element size in training images used for MPS modeling of the lower Williams Fork Formation at Grand Valley Field.

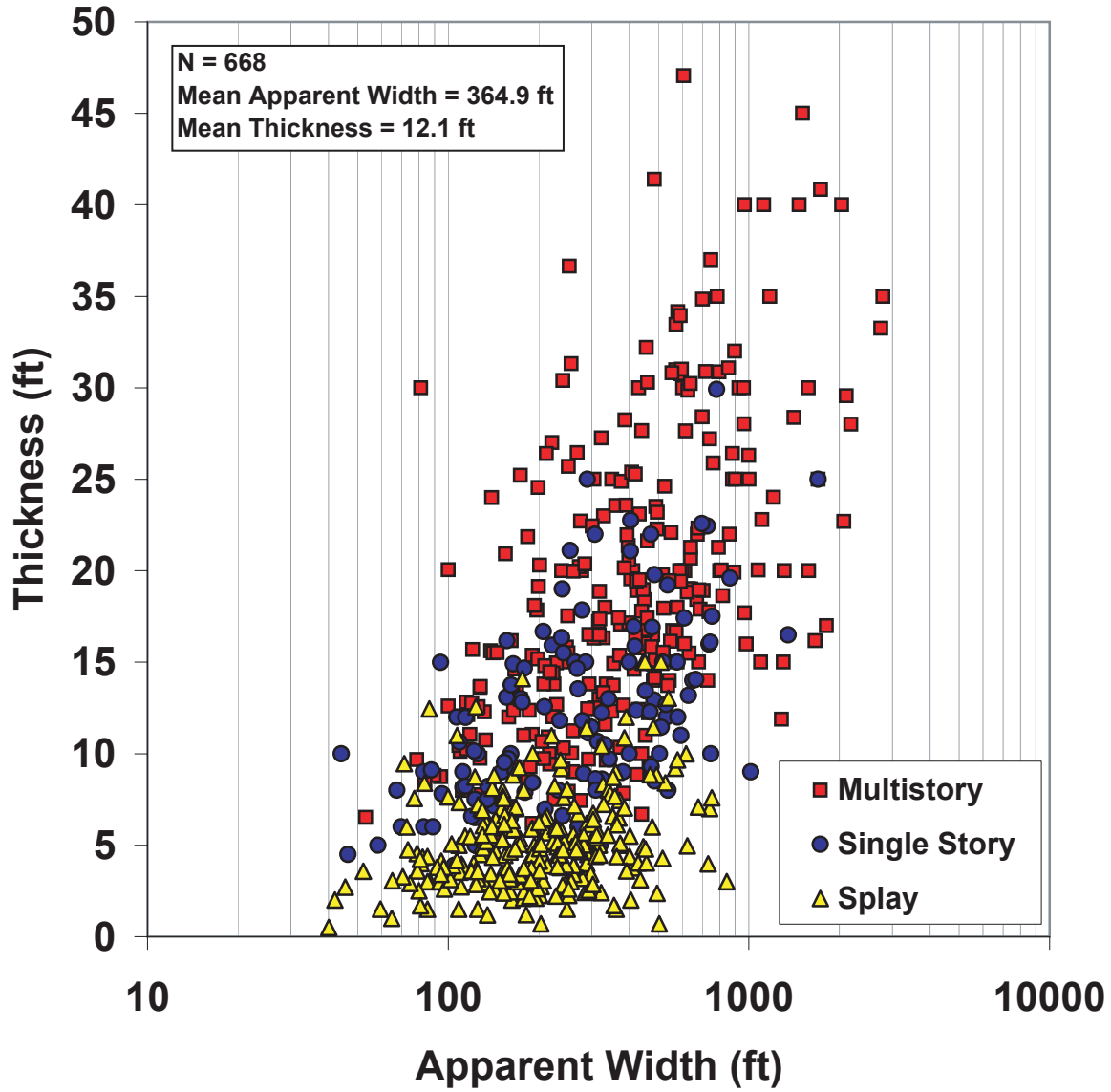

Appendix C. Crossplot of apparent width (ft) versus thickness (ft) for 668 sandstone bodies of the lower Williams Fork Formation.

Appendix B

Stratigraphic Horizon Tops

Appendix B contains the measured depth (ft) of the original 12 stratigraphic horizon tops correlated throughout Grand Valley Field in 328 well logs. Stratigraphic horizons include: Rollins Sandstone Member, Coal A, Coal A5, Coal B, Coal D, Coal E, Coal F, FS Middle Sandstone, Middle Sandstone, Regressive Marker Cameo, Coal Ridge Coal Zone, and top lower Williams Fork Formation.

	Surface Name Measured Depth (ft)											
Well identifier	Rollins Sandstone Member	Coal A	Coal A5	Coal B	Coal D	Coal E	Coal F	FS Middle Sandstone	Middle Sandstone	Regressive Marker Cameo	Coal Ridge Coal Zone	Top Lower Williams Fork
GM543-33	6349.8	6326.0	6234.0	6161.0	6090.0	6005.0	5888.1	5724.0	5506.0	5356.0	5017.0	4820.0
GM543-34	6509.0	6472.8	6401.4	6309.5	6235.9	6146.4	6073.2	5846.0	5665.0	5475.0	5140.0	4908.0
GM543-35	7169.0	7137.1	7081.3	6996.9	6907.9	6852.9	6718.1	6545.0	6348.8	6170.0	5820.3	5616.4
GM544-1	6591.0	6530.7	6482.5	6430.4	6307.9	6251.4	6102.0	5953.0	5785.0	5545.0	5220.0	5088.8
GM544-3	6291.3	6243.4	6200.9	6143.2	6019.0	5966.1	5835.5	5677.0	5474.0	5291.4	4968.0	4758.0
GM544-33	6330.2	6305.0	6229.0	6177.0	6105.0	6028.0	5901.0	5771.0	5551.0	5389.0	5017.0	4825.0
GM544-35	6610.1	6560.4	6503.0	6450.3	6347.1	6259.7	6152.9	5984.0	5781.0	5596.0	5257.0	5084.0
GM614-35	6498.0	6466.8	6394.9	6324.4	6256.9	6179.3	6042.7	5886.0	5689.8	5455.0	5148.0	4888.1
GM643-34	6538.6	6522.7	6452.2	6358.6	6289.3	6222.9	6081.7	5880.0	5724.0	5508.0	5177.0	4931.7
GM643-35	6643.6	6593.8	6540.1	6490.1	6389.5	6293.1	6201.4	6029.0	5858.1	5663.0	5287.0	5105.7
GR1-33R	6383.0	6342.0	6251.0	6161.0	6089.1	6007.0	5897.0	5709.0	5549.0	5347.0	5010.0	4833.1
GR21-3V	6309.5	6282.0	6219.0	6177.0	6091.0	6032.0	5893.0	5681.6	5527.5	5348.7	5008.7	4803.5
GR21-4	6395.2	6368.0	6311.0	6265.0	6176.0	6083.0	5928.8	5795.0	5578.0	5391.0	5071.0	4909.6
GR24-35	6542.0	6493.0	6431.0	6353.0	6275.0	6197.0	6073.0	5922.0	5711.0	5521.2	5195.0	4937.0
GR32-34	6559.4	6535.7	6447.3	6360.7	6294.4	6219.1	6071.3	5956.9	5744.1	5558.6	5200.6	4936.8
GR43-3V	6325.5	6266.4	6204.0	6131.2	6002.0	5968.0	5858.8	5699.4	5496.9	5306.8	4982.0	4773.6
GR44-33V	6319.1	6287.9	6199.0	6140.0	6059.0	5989.0	5858.0	5726.2	5512.8	5348.0	4999.0	4813.6
GV12693	6264.6	6236.0	6163.0	6113.0	6048.0	5993.0	5831.0	5689.7	5463.0	5285.0	4936.0	4729.2
GV19-36	6765.7	6704.0	6654.0	6585.0	6495.0	6405.9	6327.6	6140.0	5965.0	5763.0	5415.7	5203.9
GV21-35	6590.0	6527.0	6476.0	6416.0	6317.0	6216.0	6122.6	5946.0	5759.0	5580.0	5222.0	5068.0
GV23-34	6495.5	6461.8	6394.8	6323.0	6228.6	6167.8	6033.0	5819.0	5659.0	5456.0	5120.0	4858.3
GV24-36	6738.2	6707.5	6638.7	6563.5	6475.1	6339.5	6265.0	6126.4	5962.5	5731.9	5386.4	5172.7
GV40150	6343.4	6312.0	6267.0	6168.0	6093.2	6054.8	5904.6	5743.0	5539.0	5340.0	5021.0	4767.0
MV102-3	6270.7	6241.0	6162.0	6122.0	6037.0	5947.0	5841.0	5682.0	5480.0	5289.0	4950.0	4685.0
MV33-34	6602.9	6539.5	6515.0	6454.0	6358.0	6274.8	6124.8	6002.3	5809.0	5645.0	5288.0	5042.2
MV39-3	6530.4	6506.0	6457.0	6418.0	6263.0	6207.0	6089.0	5942.0	5744.0	5537.0	5212.0	4981.0
MV39906	6376.7	6335.0	6276.0	6243.0	6106.0	6050.3	5923.0	5754.0	5574.0	5344.2	5036.0	4829.6
MV40029	6699.2	6663.0	6636.0	6592.0	6455.3	6387.0	6234.6	6123.0	5906.0	5679.0	5374.0	5127.0
MV40150	6637.7	6591.3	6522.0	6468.0	6362.7	6291.0	6175.4	6025.0	5819.0	5603.9	5265.3	5096.0
MV41-33	6487.3	6449.2	6396.4	6321.6	6228.0	6123.4	6035.4	5877.8	5685.0	5498.2	5172.9	4904.2

	Surface Name Measured Depth (ft)											
Well identifier	Rollins Sandstone Member	Coal A	Coal A5	Coal B	Coal D	Coal E	Coal F	FS Middle Sandstone	Middle Sandstone	Regressive Marker Cameo	Coal Ridge Coal Zone	Top Lower Williams Fork
GM444-36	7232.0	7157.6	7122.7	7030.0	6919.4	6808.8	6735.7	6585.0	6408.0	6168.0	5838.0	5637.0
GM444-4	6698.1	6663.1	6599.6	6573.2	6412.7	6332.3	6222.6	6119.0	5911.3	5697.7	5374.0	5198.7
GM511-1	6730.7	6679.9	6612.8	6547.4	6442.1	6359.6	6253.0	6090.0	5908.0	5720.0	5337.0	5211.0
GM511-2	6313.6	6241.3	6193.0	6121.4	6072.1	5998.0	5888.1	5697.0	5506.0	5301.0	4977.0	4743.0
GM511-3	6378.0	6350.0	6275.0	6225.0	6095.9	6069.0	5946.3	5804.3	5623.4	5367.0	5071.0	4883.0
GM511-33	6587.3	6513.0	6461.9	6400.1	6315.3	6254.5	6165.9	5927.0	5737.5	5564.7	5266.4	5069.0
GM511-36	7032.5	7016.5	6934.4	6882.5	6777.7	6652.4	6579.4	6446.0	6265.0	6064.0	5690.0	5466.4
GM512-1	6867.9	6836.0	6757.3	6714.0	6578.2	6530.5	6375.2	6243.0	6068.0	5868.0	5484.0	5359.0
GM512-3	6582.2	6552.8	6500.5	6454.1	6396.1	6264.4	6178.6	6000.0	5798.0	5588.0	5254.0	5028.0
GM512-34	6488.7	6459.6	6409.2	6287.9	6205.9	6150.0	5975.4	5884.0	5682.0	5510.0	5141.0	4965.0
GM512-4	6489.2	6450.8	6393.9	6356.4	6227.2	6178.8	6029.3	5910.0	5677.0	5495.0	5178.0	5005.3
GM513-1	6322.0	6272.4	6221.5	6167.0	6069.5	5994.1	5850.3	5681.4	5498.0	5345.0	4911.0	4805.0
GM513-2	6196.6	6160.0	6104.0	6033.4	5911.4	5836.9	5715.7	5544.0	5346.0	5164.0	4843.0	4627.9
GM513-3	6598.0	6565.4	6531.1	6484.5	6356.1	6270.2	6119.8	6024.0	5817.0	5609.0	5288.0	5060.0
GM513-36	6938.0	6884.7	6839.5	6773.4	6671.8	6591.9	6463.7	6308.0	6114.0	5921.0	5572.0	5362.0
GM514-2	6236.0	6201.0	6164.0	6111.0	5983.0	5925.0	5776.0	5599.0	5409.0	5241.0	4879.0	4708.6
GM514-3	6693.7	6656.3	6612.0	6586.2	6411.4	6322.1	6231.0	6137.0	5922.0	5688.0	5385.0	5155.6
GM514-35	6460.9	6424.8	6359.4	6288.2	6216.1	6150.6	5996.9	5850.0	5651.6	5424.0	5114.0	4841.5
GM521-1	6588.0	6535.5	6469.7	6404.8	6296.1	6217.4	6116.9	5959.0	5785.0	5568.0	5209.0	5047.1
GM521-36	7290.7	7256.0	7207.3	7127.6	7019.2	6867.7	6783.4	6666.0	6487.0	6266.0	5928.0	5628.0
GM521-4	6403.0	6372.4	6335.7	6293.9	6169.2	6095.6	5929.0	5823.0	5595.0	5420.0	5090.0	4914.0
GM522-3	6464.2	6432.5	6398.9	6340.7	6218.5	6156.4	6043.3	5863.0	5661.0	5467.0	5137.0	4888.2
GM522-33	6516.9	6496.0	6423.0	6330.0	6263.0	6196.0	6097.0	5887.0	5708.0	5525.0	5181.0	4983.0
GM523-3	6445.1	6411.6	6365.4	6317.9	6184.5	6131.7	5971.0	5834.0	5624.0	5434.0	5118.0	4881.3
GM523-36	6732.2	6686.9	6627.9	6564.2	6483.8	6389.5	6289.8	6117.0	5958.2	5769.5	5406.6	5212.8
GM524-1	6419.7	6375.0	6301.0	6239.0	6135.4	6098.9	5939.0	5777.0	5600.0	5400.4	5048.0	4931.0
GM524-2	6168.1	6122.2	6070.6	5999.0	5880.8	5813.8	5697.1	5573.0	5372.0	5172.1	4821.1	4654.0
GM524-3	6545.1	6519.7	6463.2	6425.2	6271.4	6179.0	6083.2	5972.0	5759.0	5575.0	5237.0	5013.6
GM524-35	6583.0	6531.3	6487.1	6411.5	6333.0	6232.9	6135.3	5970.0	5767.0	5564.0	5237.6	4990.0
GM524-4	6644.3	6609.1	6573.7	6535.2	6392.4	6311.7	6217.6	6135.5	5923.4	5684.9	5370.6	5214.6
GM531-33	6471.8	6461.5	6376.6	6311.7	6217.8	6115.0	6031.7	5840.0	5620.9	5486.3	5149.3	5010.6
GM532-2	6393.0	6335.1	6287.9	6216.6	6099.5	6037.3	5928.3	5747.0	5534.0	5358.0	5003.0	4829.0
GM532-3	6639.6	6608.0	6560.0	6481.0	6398.0	6356.0	6196.0	6045.0	5850.0	5647.0	5317.0	5052.0
GM532-33	6850.2	6829.1	6730.7	6639.2	6564.9	6494.4	6378.7	6198.0	6019.0	5824.0	5486.0	5270.0
GM532-34	6632.8	6612.9	6539.5	6446.2	6367.8	6308.4	6138.9	6009.0	5817.0	5642.0	5299.0	5070.0
GM532-4	6610.7	6573.9	6523.8	6488.8	6353.3	6292.9	6158.4	6066.0	5821.0	5652.0	5305.0	5119.0
GM533-33	6349.2	6335.0	6259.0	6166.0	6094.0	6012.0	5879.0	5732.0	5523.0	5371.0	5029.0	4823.9
GM533-4	6413.0	6375.2	6341.2	6300.1	6134.2	6095.0	5958.5	5830.0	5598.6	5430.0	5080.0	4895.0
GM534-2	6210.0	6153.0	6102.4	6026.5	5923.0	5881.8	5738.8	5582.9	5396.0	5198.0	4868.0	4708.0
GM534-3	6518.9	6482.2	6426.2	6385.7	6238.3	6183.0	6057.0	5926.0	5716.0	5525.0	5192.0	4984.8
GM534-33	6530.0	6495.2	6423.3	6377.0	6305.0	6216.0	6083.0	5931.9	5731.0	5569.0	5226.0	5038.1
GM534-34	6334.5	6299.8	6222.5	6167.8	6095.7	6018.7	5912.0	5717.0	5528.0	5337.4	5022.8	4836.0
GM541-3	6279.0	6246.9	6180.6	6106.0	5994.6	5923.1	5818.7	5676.0	5477.0	5275.0	4954.4	4710.0
GM541-35	7462.0	7439.6	7361.8	7318.1	7216.7	7121.6	7006.4	6839.0	6643.0	6447.3	6117.0	5864.2
GM541-36	7607.6	7563.8	7480.5	7433.1	7352.5	7221.7	7154.2	7003.0	6832.0	6579.3	6252.6	6007.0
GM542-1	6541.0	6479.9	6452.3	6396.6	6259.8	6171.8	6073.1	5915.5	5757.0	5505.0	5166.0	5037.0
GM542-2	6636.6	6597.5	6542.7	6490.3	6403.7	6286.5	6207.8	6042.0	5850.8	5651.0	5289.0	5119.0
GM542-34	6893.1	6839.2	6761.5	6692.1	6619.7	6541.9	6390.4	6242.0	6057.0	5836.0	5499.0	5274.0
GM542-4	6568.4	6545.6	6479.5	6435.6	6302.2	6227.9	6087.6	5966.0	5743.0	5572.0	5233.0	5043.2
GM543-1	6424.0	6377.4	6321.0	6275.3	6151.8	6088.4	5949.1	5779.0	5621.0	5375.0	5055.0	4924.0

	Surface Name Measured Depth (ft)											
Well identifier	Rollins Sandstone Member	Coal A	Coal A5	Coal B	Coal D	Coal E	Coal F	FS Middle Sandstone	Middle Sandstone	Regressive Marker Cameo	Coal Ridge Coal Zone	Top Lower Williams Fork
GM431-36	7685.4	7652.5	7571.1	7501.3	7388.3	7267.5	7179.5	7052.0	6856.0	6643.0	6290.8	6019.8
GM431-4	6383.9	6364.4	6279.3	6231.0	6159.6	6087.0	5917.3	5784.0	5561.0	5407.0	5066.0	4886.0
GM43-2	6283.6	6234.0	6176.0	6113.0	6005.0	5949.0	5811.0	5619.0	5436.0	5242.0	4894.0	4709.0
GM432-2	6310.8	6270.2	6202.8	6118.9	6019.6	5936.4	5828.0	5671.0	5462.0	5272.0	4944.0	4738.8
GM432-3	6505.8	6469.0	6426.0	6339.0	6251.0	6197.0	6065.2	5886.0	5695.0	5499.0	5179.0	4949.8
GM432-33	6651.0	6632.9	6542.6	6461.2	6388.7	6297.2	6198.7	6013.0	5844.0	5647.0	5302.0	5086.0
GM432-34	6599.4	6589.2	6497.1	6432.3	6362.5	6271.4	6164.6	5965.0	5800.0	5592.5	5252.0	5011.0
GM432-35	7215.6	7201.1	7100.8	7014.0	6944.2	6903.4	6748.4	6590.4	6383.0	6191.0	5850.0	5629.0
GM432-36	7522.0	7489.0	7423.0	7374.3	7254.3	7144.6	7056.6	6915.0	6739.0	6511.0	6153.0	5952.0
GM432-4	6285.0	6249.1	6183.9	6132.3	6003.4	5957.5	5819.8	5687.0	5461.0	5299.0	4941.0	4767.0
GM43-33	6322.7	6301.0	6203.0	6124.0	6054.0	5986.0	5870.0	5705.0	5502.0	5320.0	4969.0	4823.0
GM433-3	6469.8	6436.3	6374.6	6325.3	6194.4	6129.2	5973.3	5860.0	5645.0	5468.0	5146.0	4914.0
GM433-33	6475.0	6448.0	6365.0	6274.0	6185.0	6109.0	5990.0	5823.0	5625.0	5457.0	5109.0	4911.9
GM433-35	7178.5	7152.6	7065.5	6985.1	6925.3	6863.8	6688.2	6556.0	6351.0	6159.0	5820.0	5592.5
GM433-36	7060.3	7002.9	6955.7	6905.6	6785.7	6681.0	6586.4	6447.0	6278.0	6038.0	5695.0	5462.0
GM433-4	6532.6	6508.2	6492.7	6441.2	6309.4	6256.2	6082.6	5986.7	5758.0	5560.1	5241.0	5045.4
GM43-35	7121.8	7055.0	7021.6	6873.0	6808.2	6744.3	6671.7	6509.7	6298.3	6075.8	5775.9	5537.2
GM43-36	7196.0	7139.0	7090.4	7036.3	6913.7	6765.5	6717.7	6564.7	6396.0	6158.0	5822.0	5611.0
GM434-1	6609.2	6560.0	6503.0	6452.0	6346.0	6283.0	6141.0	5977.0	5827.0	5574.0	5251.0	5137.0
GM434-2	6170.2	6134.8	6088.5	6020.6	5910.1	5838.8	5746.7	5569.0	5387.0	5186.7	4838.0	4684.6
GM434-3	6458.3	6422.8	6376.0	6327.9	6177.1	6119.3	5993.8	5857.0	5650.6	5458.0	5148.0	4904.0
GM434-33	6640.4	6619.0	6532.0	6483.0	6399.0	6311.0	6178.0	6050.6	5811.0	5651.0	5332.0	5140.0
GM434-34	6306.0	6274.5	6203.0	6153.3	6085.6	5985.1	5849.0	5693.0	5541.1	5332.3	4996.0	4764.0
GM434-36	6736.6	6725.2	6628.9	6572.2	6481.0	6362.7	6280.0	6118.0	5956.0	5742.0	5388.0	5206.0
GM434-4	6680.1	6640.2	6622.1	6593.9	6436.4	6339.7	6241.1	6136.6	5937.5	5717.6	5405.0	5225.8
GM441-1	6623.4	6563.0	6514.4	6454.8	6332.6	6232.8	6159.5	6009.0	5837.0	5593.0	5252.0	5098.0
GM441-2	6650.2	6604.7	6553.4	6495.8	6402.6	6289.1	6199.3	6018.0	5831.0	5638.0	5300.0	5103.4
GM441-3	6341.0	6290.7	6246.0	6163.2	6053.7	5981.9	5880.2	5714.0	5554.0	5352.7	5027.0	4766.0
GM441-33	6636.7	6599.3	6552.7	6474.6	6385.1	6206.6	6128.4	6028.0	5786.0	5665.0	5300.0	5100.6
GM441-36	7729.4	7670.7	7624.8	7547.9	7462.5	7332.7	7229.6	7105.3	6960.0	6690.1	6354.4	6133.6
GM441-4	6538.5	6513.2	6433.6	6374.0	6289.0	6222.4	6064.7	5956.0	5727.0	5564.0	5203.0	5031.0
GM44-2	6166.6	6099.0	6046.0	5975.0	5875.0	5801.0	5683.0	5515.0	5336.0	5143.0	4775.0	4621.0
GM442-1	6512.2	6456.2	6404.6	6346.8	6216.1	6132.3	6051.9	5881.6	5718.4	5475.0	5126.0	5006.3
GM442-2	6633.1	6588.0	6533.7	6497.9	6377.6	6288.2	6161.9	5999.0	5820.0	5639.0	5296.0	5083.0
GM442-33	6634.0	6610.3	6521.9	6435.3	6348.7	6285.4	6166.7	5995.0	5810.0	5631.0	5269.0	5114.0
GM442-34	7019.8	7000.7	6943.3	6845.2	6768.7	6662.1	6530.6	6391.5	6208.4	6000.8	5662.0	5388.5
GM442-35	7144.7	7106.3	7028.4	6976.9	6895.4	6803.3	6696.5	6539.0	6350.0	6159.0	5815.0	5552.5
GM442-36	7464.5	7434.5	7371.3	7307.8	7211.6	7093.0	6995.0	6851.0	6669.0	6428.0	6088.0	5904.2
GM442-4	6564.5	6543.3	6469.2	6431.0	6282.7	6261.9	6090.4	6003.0	5770.0	5591.9	5230.2	5070.0
GM44-3	6298.4	6260.0	6209.0	6158.0	6035.0	5974.0	5848.0	5691.0	5488.0	5284.0	4969.0	4750.2
GM443-1	6520.0	6464.9	6403.9	6379.0	6252.6	6174.1	6060.2	5898.0	5737.0	5487.0	5149.0	5021.5
GM443-3	6290.0	6239.9	6182.9	6146.7	5990.6	5934.5	5828.0	5658.0	5461.0	5276.0	4942.3	4762.0
GM443-33	6322.3	6308.0	6222.0	6138.0	6056.0	5976.0	5874.0	5713.0	5499.0	5332.0	4987.0	4797.5
GM443-34	6523.0	6488.2	6420.3	6372.0	6319.8	6212.2	6046.0	5880.0	5686.0	5488.0	5141.0	4901.4
GM443-35	7148.0	7117.8	7038.9	6962.2	6879.7	6824.1	6687.9	6517.0	6350.0	6149.0	5787.6	5571.8
GM443-4	6743.0	6702.5	6672.6	6626.9	6467.7	6410.1	6254.7	6169.0	5922.0	5753.0	5415.0	5164.0
GM44-36	7158.7	7103.5	7036.5	6955.8	6839.7	6711.2	6643.5	6503.0	6325.0	6092.0	5759.0	5557.0
GM444-1	6592.8	6528.5	6483.2	6426.3	6308.7	6243.0	6105.0	5948.0	5785.0	5533.0	5209.0	5087.0
GM444-3	6310.5	6251.2	6206.1	6159.1	6023.2	5970.2	5842.5	5689.4	5480.0	5286.0	4967.0	4773.0
GM444-33	6306.0	6278.0	6194.0	6143.0	6062.0	5983.0	5868.0	5738.2	5501.0	5343.0	4982.0	4792.4

	Surface Name Measured Depth (ft)											
Well identifier	Rollins Sandstone Member	Coal A	Coal A5	Coal B	Coal D	Coal E	Coal F	FS Middle Sandstone	Middle Sandstone	Regressive Marker Cameo	Coal Ridge Coal Zone	Top Lower Williams Fork
GM411-1	6767.0	6722.5	6662.0	6576.2	6486.2	6413.2	6316.2	6136.0	5961.0	5759.0	5387.0	5252.0
GM411-2	6339.2	6266.5	6229.9	6158.1	6092.0	6015.9	5930.9	5753.0	5549.0	5327.0	5038.0	4761.0
GM411-3	6401.3	6378.6	6300.5	6248.6	6143.5	6079.2	5958.0	5821.0	5635.8	5419.0	5082.0	4912.6
GM411-33	6598.2	6512.9	6486.4	6432.0	6326.3	6249.8	6149.3	5920.1	5725.3	5549.7	5258.1	5085.7
GM411-34	6760.6	6745.3	6682.8	6614.2	6511.9	6337.9	6250.4	6165.0	5963.0	5831.6	5443.0	5214.5
GM411-36	7095.3	7055.2	7024.7	6918.7	6817.8	6656.8	6581.0	6457.0	6295.0	6084.0	5717.0	5470.8
GM412-3	6578.5	6550.2	6494.3	6435.7	6367.8	6258.3	6171.5	5995.0	5789.0	5579.0	5251.0	4999.1
GM412-34	6529.8	6500.4	6452.3	6341.9	6253.2	6156.6	6007.1	5926.0	5727.0	5557.0	5182.0	5003.0
GM412-36	6902.0	6865.2	6802.9	6756.6	6648.2	6517.2	6437.0	6315.0	6127.0	5944.0	5575.1	5341.7
GM412-4	6447.0	6419.0	6367.4	6327.8	6200.4	6113.7	5993.0	5860.7	5639.9	5447.0	5137.0	4969.4
GM41-3	6221.7	6166.0	6117.0	6045.0	5986.0	5890.0	5809.0	5588.0	5412.0	5199.0	4885.0	4647.7
GM413-1	6349.0	6310.2	6238.9	6188.8	6092.5	6040.5	5878.3	5726.0	5530.0	5365.0	4958.1	4833.7
GM413-2	6256.8	6212.2	6134.0	6067.1	5967.9	5906.8	5763.8	5605.5	5417.0	5235.0	4917.0	4692.3
GM413-3	6552.0	6505.5	6480.3	6408.0	6345.6	6208.9	6108.0	5946.0	5747.0	5537.0	5187.0	4983.0
GM413-34	6429.9	6407.8	6333.7	6232.0	6147.9	6088.1	5936.0	5839.0	5618.0	5458.0	5090.0	4916.0
GM413-36	7052.4	6981.2	6931.1	6875.6	6793.0	6690.3	6607.1	6427.0	6267.0	6069.0	5702.0	5483.5
GM41-35	7248.8	7202.6	7169.6	7058.3	6976.4	6842.4	6710.1	6617.0	6422.0	6226.0	5868.0	5629.0
GM41-4	6252.0	6229.0	6151.0	6086.1	6022.9	5938.3	5791.9	5682.0	5467.0	5287.0	4929.0	4741.0
GM414-2	6276.8	6236.0	6189.0	6142.0	6009.0	5927.0	5795.0	5634.0	5447.0	5260.0	4921.0	4718.0
GM414-3	6626.0	6592.8	6540.7	6513.7	6317.0	6239.2	6185.1	6079.0	5858.0	5628.0	5320.0	5066.0
GM414-35	6513.3	6417.0	6356.3	6273.1	6212.2	6143.5	5968.5	5861.3	5661.0	5420.1	5095.3	4850.4
GM42-1	6471.9	6408.0	6367.0	6323.0	6193.0	6108.0	6001.1	5838.0	5678.0	5435.0	5081.4	4959.0
GM421-1	6629.4	6607.6	6534.3	6475.4	6348.3	6263.8	6169.8	6003.0	5838.0	5618.0	5266.0	5114.3
GM421-2	6389.0	6343.7	6289.0	6193.1	6127.5	6053.8	5959.4	5780.0	5599.0	5407.0	5061.0	4822.6
GM421-34	6689.5	6661.1	6639.4	6571.0	6450.6	6309.2	6242.3	6122.3	5936.6	5746.7	5404.2	5123.7
GM421-36	7051.0	7022.1	6966.3	6916.6	6802.8	6680.1	6584.9	6466.0	6302.0	6060.0	5713.9	5456.0
GM421-4	6402.9	6359.6	6313.2	6290.6	6209.3	6122.2	5949.0	5851.0	5631.0	5461.0	5122.0	4934.0
GM422-2	6211.2	6142.0	6103.7	6028.5	5942.8	5852.5	5742.4	5587.0	5415.0	5212.0	4885.0	4686.0
GM422-3	6422.0	6390.4	6332.4	6266.1	6166.0	6091.5	5995.9	5817.0	5611.0	5416.0	5089.0	4831.0
GM422-33	6569.1	6541.0	6457.0	6371.3	6311.0	6229.0	6137.0	5957.0	5763.0	5577.5	5237.0	5023.0
GM422-34	6613.0	6577.4	6523.1	6456.2	6358.1	6269.7	6081.7	6017.0	5813.0	5648.0	5293.0	5069.1
GM422-36	7099.0	7060.0	7026.8	6960.5	6854.9	6739.5	6653.5	6520.8	6328.0	6111.0	5772.6	5546.3
GM42-3	6210.0	6156.0	6110.0	6042.0	5951.0	5881.0	5746.0	5583.0	5393.0	5200.0	4871.0	4678.3
GM423-1	6661.0	6629.0	6535.5	6491.4	6385.3	6332.7	6183.4	6036.0	5863.0	5653.0	5293.0	5135.2
GM423-2	6256.6	6195.5	6160.4	6080.8	5957.3	5911.5	5763.3	5626.0	5450.0	5257.0	4907.0	4747.0
GM42-33	6385.4	6354.0	6261.0	6177.0	6101.0	6009.0	5911.0	5755.0	5564.0	5376.0	5015.0	4814.0
GM423-3	6443.0	6413.8	6361.8	6322.7	6172.2	6114.7	5990.5	5824.0	5622.0	5438.0	5117.0	4907.4
GM423-36	6959.0	6908.9	6863.8	6811.7	6705.2	6633.0	6528.3	6364.0	6208.0	5980.0	5629.0	5427.0
GM42-34	6660.7	6648.7	6556.0	6495.0	6417.1	6325.0	6215.2	6020.0	5856.0	5640.0	5307.0	5086.0
GM42-35	7163.7	7148.8	7068.0	7005.0	6908.0	6821.4	6717.0	6569.0	6364.7	6169.5	5816.0	5556.6
GM42-4	6531.7	6510.0	6442.0	6406.0	6294.0	6222.0	6082.0	5971.0	5725.0	5561.0	5209.0	5024.0
GM424-1	6284.6	6241.0	6189.0	6122.0	6013.0	5943.6	5803.0	5642.0	5459.0	5271.0	4890.0	4770.0
GM424-2	6188.3	6113.5	6082.3	5994.6	5883.0	5811.7	5698.3	5549.0	5355.0	5151.0	4806.0	4667.2
GM424-3	6536.0	6503.9	6453.5	6418.4	6247.1	6166.9	6061.9	5961.0	5757.0	5567.0	5224.0	5005.2
GM424-33	6691.8	6658.3	6586.0	6539.0	6477.4	6394.8	6242.4	6062.0	5870.0	5714.0	5366.0	5192.0
GM424-35	6673.2	6643.9	6544.6	6499.4	6419.8	6368.4	6206.9	6027.0	5844.4	5630.0	5308.2	5067.0
GM424-36	6763.7	6708.7	6662.8	6591.1	6488.1	6420.1	6300.7	6139.0	5960.0	5754.5	5400.0	5230.0
GM43-1	6410.0	6366.0	6294.0	6255.0	6134.8	6072.0	5926.0	5757.0	5605.0	5365.0	5033.0	4886.0
GM431-33	6516.0	6496.3	6433.1	6343.9	6252.6	6141.2	6045.1	5914.4	5645.3	5547.7	5200.4	5029.1
GM431-34	6877.2	6798.7	6768.0	6702.6	6633.0	6524.6	6397.2	6250.7	6052.0	5876.0	5526.0	5264.2

	Surface Name Measured Depth (ft)											
Well identifier	Rollins Sandstone Member	Coal A	Coal A5	Coal B	Coal D	Coal E	Coal F	FS Middle Sandstone	Middle Sandstone	Regressive Marker Cameo	Coal Ridge Coal Zone	Top Lower Williams Fork
GM323-36	6993.2	6956.1	6889.5	6858.4	6757.8	6637.4	6543.8	6417.0	6249.0	6026.0	5676.0	5473.7
GM32-4	6223.2	6203.0	6142.0	6100.0	6015.0	5944.0	5775.0	5631.0	5403.0	5235.7	4873.0	4744.0
GM324-1	6265.9	6241.8	6193.0	6133.0	6031.0	5964.0	5832.0	5664.7	5496.0	5287.0	4921.0	4814.0
GM324-3	6597.4	6565.0	6532.0	6490.1	6332.9	6268.3	6114.6	6005.0	5790.8	5597.0	5279.0	5052.0
GM324-33	6691.7	6649.5	6567.9	6522.0	6450.2	6367.1	6229.6	6070.6	5868.1	5688.0	5360.3	5190.0
GM324-35	6592.8	6545.1	6484.7	6402.8	6329.6	6272.7	6122.9	5966.0	5774.8	5562.4	5246.0	4969.0
GM33-1	6553.5	6512.0	6438.0	6397.0	6276.0	6212.0	6083.0	5927.0	5769.0	5528.0	5190.0	5063.0
GM331-35	7523.7	7512.0	7410.4	7355.0	7258.4	7170.1	7081.7	6887.3	6701.9	6529.0	6193.0	5947.0
GM331-36	7679.7	7635.0	7570.8	7480.8	7377.3	7244.3	7152.9	6999.3	6831.0	6609.0	6258.1	6008.5
GM33-2	6181.1	6131.0	6084.0	6015.0	5908.0	5846.0	5721.0	5550.0	5360.0	5164.0	4821.0	4644.5
GM332-1	6576.0	6530.6	6488.0	6436.3	6319.0	6230.2	6121.8	5971.0	5794.0	5570.0	5225.0	5088.1
GM332-33	6644.0	6626.0	6539.7	6470.2	6385.6	6293.8	6192.2	6002.0	5823.2	5639.0	5288.0	5082.6
GM332-34	6608.1	6594.5	6534.0	6478.0	6399.0	6311.6	6192.0	5998.0	5821.0	5625.0	5290.0	5049.0
GM332-35	7213.0	7193.1	7119.7	7044.2	6958.7	6872.0	6782.3	6602.0	6401.6	6200.0	5875.0	5603.9
GM33-3	6375.6	6345.0	6287.0	6247.0	6128.0	6055.0	5931.0	5758.0	5562.0	5366.0	5049.0	4812.8
GM333-3	6387.0	6356.3	6294.9	6246.6	6108.6	6051.8	5893.8	5764.0	5552.0	5377.0	5061.0	4833.0
GM333-35	7259.8	7229.7	7123.4	7078.9	7013.9	6962.8	6798.7	6626.0	6443.0	6252.0	5908.0	5714.3
GM333-36	6830.0	6778.9	6731.0	6674.0	6569.0	6460.0	6374.0	6223.0	6052.0	5813.0	5481.0	5281.0
GM33-34	6486.1	6456.0	6373.0	6287.0	6206.0	6135.0	6007.6	5821.0	5653.0	5458.0	5116.0	4900.8
GM333-4	6604.0	6561.7	6516.6	6451.9	6335.8	6282.9	6133.4	6039.9	5806.0	5629.0	5289.0	5095.4
GM33-35	7125.1	7076.1	7015.8	6875.5	N/A	6748.5	6672.0	6506.6	6297.6	6070.4	5777.5	5527.1
GM33-4	6510.9	6483.0	6459.0	6419.0	6249.7	6219.2	6083.7	5943.8	5706.0	5515.0	5199.4	5015.0
GM334-1	6618.0	6563.0	6511.0	6413.0	6315.0	6258.2	6094.0	5953.0	5770.0	5562.7	5214.7	5134.6
GM334-3	6429.7	6390.5	6340.6	6297.2	6146.8	6087.9	5951.2	5836.0	5622.0	5426.0	5116.0	4880.0
GM334-4	6736.6	6702.2	6676.6	6631.1	6493.8	6379.7	6259.0	6182.0	5942.0	5746.3	5432.0	5211.4
GM34-1	6573.0	6529.0	6472.1	6404.0	6303.0	6240.0	6116.0	5959.0	5779.0	5551.0	5213.0	5110.0
GM341-1	6768.7	6725.0	6633.0	6591.0	6493.0	6393.0	6308.0	6141.0	5974.0	5736.0	5408.0	5225.1
GM341-36	7886.0	7813.2	7766.3	7697.7	7616.9	7494.8	7399.2	7280.7	7119.0	6870.2	6515.8	6300.3
GM34-2	6134.0	6077.0	6034.0	5963.0	5854.0	5795.0	5683.0	5503.0	5329.0	5113.0	4779.0	4627.0
GM342-33	6695.2	6675.5	6593.9	6507.5	6424.5	6339.3	6230.3	6056.0	5874.0	5687.0	5336.0	5142.0
GM342-34	6625.0	6598.1	6524.0	6445.9	6382.5	6297.0	6172.4	5986.0	5833.0	5611.0	5269.0	5021.0
GM342-35	7280.1	7245.3	7193.2	7117.4	7009.0	6926.5	6824.6	6645.0	6441.0	6255.8	5912.0	5666.9
GM342-36	7527.9	7470.8	7418.2	7367.8	7242.7	7141.8	7043.8	6901.3	6722.0	6492.3	6161.0	5940.0
GM342-4	6610.5	6579.2	6525.4	6458.8	6329.1	6286.2	6128.7	6031.3	5800.0	5622.0	5269.0	5115.0
GM34-3	6399.6	6365.0	6335.0	6301.0	6136.0	6093.0	5963.7	5822.0	5607.0	5431.1	5112.0	4867.3
GM343-3	6350.9	6315.0	6261.5	6207.4	6046.2	6003.5	5859.1	5722.0	5531.0	5364.5	5013.0	4813.1
GM343-35	7127.0	7099.0	7038.1	6954.6	6878.9	6809.0	6684.9	6506.0	6342.0	6139.9	5790.0	5547.1
GM34-34	6302.0	6269.0	6194.0	6124.3	6048.0	5987.0	5836.0	5674.3	5510.8	5308.6	4968.0	4762.0
GM343-4	6870.0	6836.2	6802.3	6770.6	6678.5	6544.8	6436.6	6309.0	6053.0	5888.0	5547.0	5326.0
GM34-35	6611.7	6555.7	6478.5	6437.6	6361.3	6277.6	6144.2	5971.0	5785.0	5605.0	5256.0	5057.4
GM34-4	6567.0	6549.7	6511.3	6475.0	6368.5	6248.8	6130.0	6028.0	5791.0	5594.4	5275.0	5061.6
GM344-1	6706.9	6660.2	6604.3	6554.4	6436.6	6375.9	6236.7	6073.0	5918.0	5665.0	5339.0	5200.5
GM344-2	6255.1	6199.0	6139.0	6088.0	5982.0	5921.0	5797.0	5631.7	5432.0	5246.0	4880.0	4716.0
GM344-3	6332.0	6286.5	6242.8	6192.4	6063.2	5975.9	5871.8	5720.0	5529.0	5325.0	5002.0	4800.2
GM344-36	6917.2	6868.7	6777.2	6744.0	6616.1	6526.5	6458.9	6301.0	6114.0	5890.0	5557.0	5357.3
GM40118	6714.0	6690.0	6607.6	6548.0	6446.0	6366.0	6263.0	6092.0	5922.0	5717.0	5346.0	5218.0
GM40119	6310.0	6233.0	6199.0	6122.0	6086.0	5994.0	5866.0	5711.0	5500.0	5307.3	4994.0	4736.8
GM40148	6676.0	6637.5	6557.0	6516.0	6408.4	6324.0	6216.8	6056.0	5870.0	5677.0	5314.0	5164.0
GM40151	6339.2	6311.0	6265.0	6225.0	6107.1	6049.0	5893.0	5754.4	5538.0	5338.0	5019.0	4865.0
GM41-1	6733.4	6708.8	6651.0	6598.0	6485.0	6393.0	6311.0	6130.0	5974.0	5744.0	5400.0	5228.0

	Surface Name Measured Depth (ft)											
Well identifier	Rollins Sandstone Member	Coal A	Coal A5	Coal B	Coal D	Coal E	Coal F	FS Middle Sandstone	Middle Sandstone	Regressive Marker Cameo	Coal Ridge Coal Zone	Top Lower Williams Fork
GM24-1	6217.0	6169.0	6106.7	6043.8	5952.9	5889.0	5743.0	5580.0	5402.0	5201.0	4832.0	4719.9
GM241-1	6578.3	6525.0	6437.0	6388.0	6271.0	6185.0	6093.0	5941.0	5760.0	5545.0	5184.0	5045.8
GM243-1	6680.0	6632.0	6573.0	6527.0	6394.0	6337.0	6190.0	6031.0	5830.0	5657.0	5283.0	5139.3
GM24-33	6678.3	6632.0	6539.0	6496.0	6432.5	6333.8	6201.8	6028.0	5838.7	5667.0	5333.0	5177.5
GM24-34	6254.9	6227.0	6147.0	6092.0	6029.0	5960.0	5794.0	5660.0	5450.0	5269.0	4919.0	4688.6
GM24-36	6721.8	6655.0	6603.0	6546.0	6448.0	6388.1	6272.1	6101.0	5916.0	5717.2	5368.1	5205.0
GM244-1	6776.0	6731.0	6676.0	6621.0	6489.0	6411.0	6300.0	6140.0	5963.0	5760.0	5392.0	5245.0
GM245-1	6479.0	6436.0	6367.0	6331.0	6201.0	6131.0	6030.0	5874.0	5719.0	5459.0	5132.0	4982.0
GM246-1	6513.5	6462.0	6398.0	6350.0	6227.0	6130.0	6055.0	5887.0	5711.0	5479.0	5144.0	4997.0
GM248-1	6509.0	6461.0	6409.0	6359.0	6241.0	6178.0	6052.0	5888.0	5736.0	5496.0	5155.0	5046.0
GM249-1	6601.3	6572.0	6494.0	6434.0	6342.0	6284.0	6153.0	5995.0	5818.0	5586.0	5246.0	5137.0
GM250-1	6371.5	6320.0	6267.0	6198.0	6097.0	6038.0	5891.0	5727.0	5533.0	5349.0	4974.0	4805.2
GM251-2	6628.0	6583.0	6525.0	6472.0	6392.0	6306.0	6193.0	6028.0	5818.0	5642.0	5286.0	5088.3
GM253-2	6464.4	6415.8	6357.4	6287.8	6212.0	6124.4	6033.8	5865.0	5671.8	5478.2	5144.0	4896.0
GM254-2	6212.5	6154.0	6123.0	6054.0	5996.0	5925.0	5796.0	5619.0	5432.0	5232.0	4930.0	4708.6
GM255-2	6215.0	6161.0	6107.6	6045.0	5944.0	5879.0	5745.0	5567.0	5376.0	5187.0	4851.0	4657.0
GM256-2	6203.9	6159.0	6110.0	6043.0	5986.0	5921.0	5791.0	5588.0	5433.0	5216.0	4876.0	4699.5
GM257-2	6326.8	6298.2	6239.0	6157.0	6081.0	5981.0	5906.0	5735.0	5543.0	5344.0	4998.0	4819.0
GM258-2	6350.0	6310.0	6252.9	6183.0	6072.0	6013.0	5880.0	5687.0	5507.0	5335.0	5001.0	4806.7
GM259-2	6241.7	6193.0	6134.0	6070.0	5965.0	5905.0	5776.0	5594.8	5419.0	5212.0	4853.5	4688.0
GM260-2	6135.0	6072.0	6029.0	5967.0	5846.0	5780.0	5671.0	5507.0	5329.0	5094.0	4772.0	4619.0
GM261-2	6188.0	6113.0	6064.0	6002.0	5898.0	5842.0	5701.0	5534.0	5359.0	5168.0	4819.0	4655.0
GM263-2	6249.0	6220.0	6177.0	6115.0	5998.0	5937.0	5804.0	5615.0	5419.0	5248.0	4892.6	4703.4
GM264-2	6115.0	6023.5	5988.1	5922.0	5820.0	5753.2	5622.3	5465.0	5288.0	5070.0	4726.0	4607.0
GM265-2	6148.3	6075.1	6031.5	5953.0	5857.0	5797.2	5683.0	5507.0	5324.0	5106.0	4776.0	4602.0
GM266-3	6205.9	6164.0	6115.0	6043.0	5951.0	5869.0	5754.5	5589.0	5403.0	5224.0	4904.0	4668.0
GM267-3	6212.0	6143.0	6108.0	6046.0	5959.0	5893.0	5787.0	5632.0	5430.0	5226.0	4913.0	4639.0
GM269-3	6371.0	6336.0	6281.0	6222.0	6119.0	6052.0	5911.0	5747.6	5563.0	5367.0	5044.0	4815.4
GM31-1	6620.1	6582.0	6512.5	6458.6	6351.0	6250.0	6155.0	5997.0	5843.0	5600.0	5270.0	5127.0
GM311-3	6360.7	6328.7	6257.9	6221.6	6112.6	6049.2	5913.8	5762.0	5567.0	5391.0	5026.0	4820.0
GM311-36	7074.2	7058.5	7025.5	6947.7	6822.5	6674.3	6610.9	6480.0	6303.0	6100.0	5740.0	5492.5
GM312-34	6696.0	6673.7	6613.4	6528.0	6426.4	6314.7	6197.1	6098.0	5901.0	5739.0	5362.0	5192.0
GM312-36	6977.5	6963.8	6892.2	6823.2	6732.4	6607.8	6531.5	6385.1	6201.0	6000.0	5640.5	5427.4
GM312-4	6461.0	6415.4	6352.1	6332.7	6205.9	6132.3	6000.9	5878.0	5667.0	5473.0	5148.0	4974.0
GM31-3	6243.2	6210.0	6149.0	6064.0	5967.0	5900.0	5802.0	5665.0	5475.0	5274.6	4949.1	4727.0
GM313-3	6545.5	6513.3	6482.7	6437.6	6348.6	6215.2	6132.2	5945.0	5743.0	5535.0	5207.0	4994.0
GM31-34	6763.0	6693.7	6647.6	6591.6	6473.2	6315.3	6231.8	6136.4	5957.8	5754.4	5411.3	5141.4
GM31-35	7739.0	7709.2	7677.5	7568.4	7478.0	7311.2	7231.8	7107.0	6890.3	6724.5	6338.1	6121.6
GM314-1	6397.0	6345.5	6287.0	6228.2	6134.5	6073.9	5908.6	5774.0	5595.0	5401.0	5032.0	4902.0
GM314-3	6674.0	6637.6	6586.0	6550.5	6388.9	6266.0	6206.7	6108.0	5904.0	5639.0	5359.0	5107.6
GM314-33	6789.2	6759.6	6697.6	6643.8	6595.0	6488.1	6350.5	6178.0	5962.0	5794.0	5454.3	5292.0
GM32-1	6616.0	6572.0	6506.0	6466.0	6342.0	6260.0	6157.0	6013.5	5839.0	5590.0	5284.7	5107.0
GM321-3	6383.8	6352.3	6277.1	6222.4	6141.8	6042.6	5963.1	5795.0	5586.0	5404.0	5073.0	4867.0
GM321-34	6601.3	6580.5	6536.4	6483.0	6392.9	6300.8	6166.2	6015.9	5831.8	5680.1	5315.2	5071.6
GM321-36	7281.1	7269.1	7240.5	7180.6	7023.0	6903.2	6815.7	6698.0	6525.0	6298.0	5963.0	5673.3
GM321-4	6442.8	6412.6	6355.5	6333.2	6252.6	6162.8	6004.9	5890.0	5671.0	5488.0	5187.5	4981.0
GM32-2	6290.9	6217.8	6159.0	6087.0	5995.0	5912.6	5826.5	5634.0	5440.0	5251.0	4914.0	4727.2
GM322-3	6494.8	6465.6	6385.4	6338.2	6250.2	6160.8	6062.7	5920.0	5699.0	5512.0	5168.0	4907.0
GM322-4	6371.9	6325.7	6285.1	6221.4	6099.1	6036.0	5896.9	5797.0	5568.0	5391.0	5060.0	4875.0
GM323-3	6467.5	6434.8	6412.2	6366.6	6208.4	6133.4	6004.5	5855.0	5660.2	5472.0	5149.0	4927.0

	Surface Name Measured Depth (ft)											
Well identifier	Rollins Sandstone Member	Coal A	Coal A5	Coal B	Coal D	Coal E	Coal F	FS Middle Sandstone	Middle Sandstone	Regressive Marker Cameo	Coal Ridge Coal Zone	Top Lower Williams Fork
05045110000000	6908.0	6856.6	6802.3	6748.7	6653.8	6547.9	6456.0	6309.7	6125.2	5953.9	5611.9	5376.7
DOE2-M-36	7457.4	7410.7	7334.7	7287.5	7195.0	7082.5	6976.0	6863.6	6634.9	6403.0	6079.0	5877.5
GM12359	6432.3	6356.8	6338.9	6256.5	6156.6	6093.8	5987.8	5751.6	5560.3	5390.9	5098.3	4929.0
GM12389	6609.7	6589.2	6490.0	6417.4	6347.7	6240.8	6165.7	5987.7	5795.1	5573.1	5308.1	5078.5
GM12724	6715.0	6702.8	6642.4	6569.0	6469.8	6347.0	6253.4	6121.4	5968.3	5803.6	5372.1	5164.6
GM12754	6491.2	6469.0	6406.0	6341.0	6236.0	6151.1	6074.9	5900.0	5698.0	5526.0	5170.0	4995.7
GM13-1	6628.8	6586.0	6504.0	6446.0	6350.0	6295.0	6142.0	5987.0	5797.0	5612.0	5235.0	5103.0
GM13-2	6198.8	6143.8	6058.9	6007.1	5913.8	5843.0	5712.0	5534.3	5322.8	5160.0	4834.9	4613.8
GM13-33	6600.0	6580.0	6484.0	6409.0	6360.2	6273.4	6138.0	5979.3	5780.0	5589.9	5239.0	5088.7
GM13-34	6371.7	6345.0	6257.0	6177.0	6097.0	6037.0	5924.8	5787.3	5570.6	5378.0	5014.0	4812.0
GM13455	7071.5	7039.9	7002.3	6940.6	6805.6	6676.9	6553.0	6443.0	6268.0	6057.0	5708.4	5458.0
GM14-1	6311.0	6257.0	6208.0	6150.0	6048.0	5982.0	5847.0	5687.0	5499.0	5323.0	4933.0	4800.0
GM14-3	6718.5	6680.0	6625.7	6587.6	6462.3	6367.6	6221.0	6135.0	5937.0	5697.0	5401.0	5136.0
GM14-35	6522.0	6432.0	6357.0	6284.5	6203.1	6157.9	5965.0	5862.7	5669.2	5432.0	5091.0	4863.9
GM14-4	6332.4	6298.0	6274.6	6224.5	6100.4	6013.7	5918.5	5834.2	5623.0	5380.0	5067.3	4920.2
GM201-4	6440.0	6420.0	6342.0	6293.0	6211.0	6135.0	5956.0	5815.0	5611.0	5437.0	5098.0	4947.0
GM202-33	6306.7	6272.0	6191.0	6133.0	6049.0	5968.0	5840.0	5686.0	5482.0	5322.0	4977.0	4794.8
GM203-33	6588.0	6557.0	6484.0	6425.0	6342.0	6246.0	6100.0	5972.0	5758.0	5600.0	5257.0	5091.8
GM21-1	6665.0	6620.0	6549.0	6484.0	6372.0	6280.0	6198.0	6033.0	5859.0	5653.0	5285.0	5139.0
GM21-2	6326.0	6258.0	6204.0	6132.0	6066.0	5989.0	5894.0	5718.0	5547.0	5348.0	4999.0	4774.9
GM21-36	7279.9	7226.2	7183.6	7084.4	6999.3	6844.5	6759.1	6648.0	6472.0	6248.0	5907.4	5607.0
GM216-33	6409.9	6387.4	6310.8	6241.4	6164.7	6057.5	5965.2	5780.3	5597.3	5416.1	5069.4	4847.9
GM218-33	6507.3	6467.0	6393.5	6296.2	6220.1	6156.0	6048.0	5864.0	5678.0	5497.0	5135.0	4990.9
GM22-1	6638.0	6603.0	6528.0	6468.0	6352.0	6283.0	6172.0	6018.0	5841.0	5627.0	5261.0	5113.0
GM22-2	6209.0	6139.0	6091.0	6014.0	5922.0	5844.7	5737.0	5566.0	5390.0	5191.0	4840.0	4688.0
GM22-3	6401.8	6355.4	6293.5	6199.8	6115.2	6060.3	5937.9	5773.6	5568.5	5370.2	5033.9	4777.8
GM22-33	6391.9	6356.0	6276.0	6206.0	6130.0	6036.0	5953.1	5770.7	5565.0	5380.8	5045.0	4846.0
GM223-33	6281.8	6260.0	6171.0	6118.0	6038.0	5959.0	5843.0	5686.0	5480.0	5317.0	4971.0	4779.0
GM22-34	6575.0	6544.5	6485.0	6405.0	6324.0	6262.0	6108.9	5976.0	5769.0	5617.7	5258.0	5036.2
GM22-35R	7486.2	7461.7	7373.5	7272.9	7220.9	7114.4	6992.1	6833.9	6646.9	6425.9	6136.1	5877.6
GM22-36	7114.9	7071.9	7012.2	6976.4	6873.8	6756.7	6645.6	6536.0	6348.0	6131.2	5781.8	5563.6
GM224-34	6727.6	6712.8	6646.8	6588.2	6483.9	6345.8	6278.8	6134.1	5948.8	5779.4	5397.9	5226.3
GM225-36	6905.0	6852.2	6787.3	6726.8	6618.9	6537.5	6432.3	6265.0	6081.0	5894.0	5526.0	5347.0
GM227-35	6586.0	6538.4	6480.7	6416.6	6340.3	6228.7	6131.9	5969.0	5789.0	5609.4	5226.7	5075.0
GM228-34	6647.0	6594.7	6570.4	6493.1	6399.6	6299.8	6132.6	6053.0	5845.0	5685.0	5333.6	5079.8
GM230-34	6304.6	6267.3	6206.0	6150.0	6080.0	6010.0	5865.0	5765.0	5548.0	5346.9	5008.3	4781.8
GM231-34	6310.8	6286.0	6205.0	6163.0	6103.0	6039.0	5884.0	5744.0	5525.0	5358.0	4988.0	4796.3
GM232-34	6341.7	6309.3	6262.0	6186.0	6122.9	6060.1	5902.0	5774.8	5568.1	5377.9	5015.5	4795.8
GM23-33	6549.3	6519.7	6483.0	6388.0	6339.4	6247.0	6113.4	5967.0	5749.7	5599.0	5240.0	5099.3
GM233-34	6315.0	6282.2	6210.7	6149.7	6077.2	6007.1	5860.1	5692.4	5512.6	5324.2	4986.8	4792.6
GM23-34	6402.0	6363.0	6291.0	6192.0	6119.9	6047.0	5907.0	5752.0	5556.0	5361.0	5035.0	4800.2
GM23-35	6724.0	6696.4	6608.3	6556.2	6474.0	6431.4	6259.1	6092.0	5886.0	5691.0	5360.0	5130.0
GM23-36	6891.9	6850.0	6812.0	6762.2	6660.0	6555.0	6479.2	6310.0	6134.0	5919.0	5571.0	5373.0
GM234-34	6537.6	6526.0	6451.7	6412.5	6351.8	6261.4	6076.5	5910.0	5724.0	5526.0	5175.0	4944.7
GM235-34	6488.0	6463.2	6396.0	6307.9	6228.0	6158.0	6037.0	5817.0	5655.0	5457.0	5124.0	4881.0
GM237-36	6693.4	6658.0	6585.7	6527.0	6419.0	6327.0	6245.0	6073.0	5910.0	5692.0	5342.0	5176.0
GM238-36	6732.8	6707.1	6639.7	6573.6	6480.3	6369.7	6269.2	6120.7	N/A	5731.9	5391.3	5193.9
GM239-36	6962.2	6911.3	6870.2	6811.4	6719.1	6627.7	6535.1	6380.0	6194.0	6010.7	5634.5	5407.0

Appendix C

Available Well Logs

Appendix C displays the available well logs for 328 wells within the 8-section area at Grand Valley Field. NPHI, DPHI, and GR logs were downloaded from the Colorado Oil and Gas Conservation Commission website. Lithology logs were creating using specific cut-offs from the v-clay and coal flag logs. Architectural element logs were manually interpreted using outcrop and core dimensional data collected from the lower Williams Fork Formation and ten cores described in this study.

VCL2: V-Clay log

COAL_FLAG: Coal flag indicator

LITHOLOGY: Calculated lithology from V-CLAY log

ARCH_ELE: Manually interpreted architectural element log

GR_NRM: Normalized Gamma Ray

DPHI: Normalized density porosity

NPHI: Normalized neutron porosity

PHIT: Calculated total porosity

VSH: Calculated V-Shale

PHIE: Calculated effective porosity

Well Name	Well UWI	Available Logs									
		VCL2	COAL_FLAG	Lithology	Arch_Elem	GR_NRM	DPHI	NPHI	PHIT	VSH	PHIE
MV39906	05045064820000	X	X	X	X						
MV40150	05045065220000	X	X	X	X						
MV33-34	05045065710000	X	X	X	X						
MV40029	05045066150000	X	X	X	X						
GV19-36	05045066200000	X	X	X	X						
GV12693	05045066230000	X	X	X	X						
GV40150	05045066250000	X	X	X	X						
GV24-36	05045066310000	X	X	X	X						
GV23-34	05045066400000	X	X	X	X						
GV21-35	05045066480000	X	X	X	X						
MV39-3	05045067850000	X	X	X	X						
GR43-3V	05045068010000	X	X	X	X						
GR21-3V	05045068020000	X	X	X	X						
GR44-33V	05045068040000	X	X	X	X						
MV41-33	05045068090000	X	X	X	X						
GR32-34	05045068130000	X	X	X	X						
GM12389	05045068270000	X	X	X	X						
GR24-35	05045068380000	X	X	X	X						
GR21-4	05045068530000	X	X	X	X						
DOE2-M-36	05045068630000	X	X	X	X						
GM13-33	05045068920000	X	X	X	X						
GM41-4	05045068980000	X	X	X	X						
GM34-2	05045070500000	X	X	X	X						
GM13-1	05045070560000	X	X	X	X						
GM21-2	05045070580000	X	X	X	X						
GM44-2	05045070610000	X	X	X	X						
GM43-33	05045070620000	X	X	X	X						
GM14-35	05045070920000	X	X	X	X						
GM42-3	05045071020000	X	X	X	X						
GM24-33	05045071040000	X	X	X	X	X	X	X	X	X	X
GM12359	05045071050000	X	X	X	X						
GM31-3	05045071130000	X	X	X	X						
GM13-2	05045071150000	X	X	X	X						

Well Name	Well UWI	Available Logs									
		VCL2	COAL_FLAG	Lithology	Arch_Elem	GR_NRM	DPHI	NPHI	PHIT	VSH	PHIE
GM40119	05045071160000	X	X	X	X						
GM201-4	05045071190000	X	X	X	X	X	X	X	X	X	X
GM203-33	05045071200000	X	X	X	X	X	X	X	X	X	X
GM202-33	05045071250000	X	X	X	X	X	X	X	X	X	X
GM22-2	05045071270000	X	X	X	X						
GM33-2	05045071280000	X	X	X	X						
GM43-2	05045071290000	X	X	X	X						
GM41-3	05045071300000	X	X	X	X						
GM42-4	05045071310000	X	X	X	X						
GM42-33	05045071320000	X	X	X	X	X	X	X	X	X	X
GM13-34	05045071330000	X	X	X	X						
GM22-1	05045071470000	X	X	X	X						
MV102-3	05045071720000	X	X	X	X						
GM22-3	05045071730000	X	X	X	X						
GR1-33R	05045071890000	X	X	X	X	X	X	X	X	X	X
GM34-3	05045071900000	X	X	X	X						
GM44-3	05045071910000	X	X	X	X						
GM33-3	05045071920000	X	X	X	X						
GM24-34	05045072220000	X	X	X	X						
GM32-2	05045072380000	X	X	X	X						
GM24-1	05045072590000	X	X	X	X						
GM40118	05045072710000	X	X	X	X						
GM40148	05045072720000	X	X	X	X						
GM231-34	05045073080000	X	X	X	X						
GM33-4	05045073150000	X	X	X	X						
GM32-4	05045073160000	X	X	X	X						
GM42-1	05045073700000	X	X	X	X						
GM33-1	05045073710000	X	X	X	X						
GM43-1	05045073720000	X	X	X	X						
GM32-1	05045073730000	X	X	X	X						
GM269-3	05045073950000	X	X	X	X						
GM33-34	05045073980000	X	X	X	X						
GM14-4	05045074110000	X	X	X	X						
GM14-1	05045074180000	X	X	X	X						
GM12724	05045074190000	X	X	X	X						

Well Name	Well UWI	Available Logs									
		VCL2	COAL_FLAG	Lithology	Arch_Elem	GR_NRM	DPHI	NPHI	PHIT	VSH	PHIE
GM259-2	05045074420000	X	X	X	X						
GM250-1	05045074430000	X	X	X	X						
GM31-1	05045074440000	X	X	X	X						
GM265-2	05045074640000	X	X	X	X						
GM255-2	05045074680000	X	X	X	X						
GM263-2	05045074730000	X	X	X	X						
GM243-1	05045074890000	X	X	X	X						
GM244-1	05045074900000	X	X	X	X						
GM22-33	05045074990000	X	X	X	X						
GM22-34	05045075000000	X	X	X	X						
GM24-36	05045075020000	X	X	X	X						
GM223-33	05045075030000	X	X	X	X						
GM34-1	05045075080000	X	X	X	X						
GM258-2	05045075230000	X	X	X	X						
GM260-2	05045075310000	X	X	X	X						
GM235-34	05045075430000	X	X	X	X						
GM34-4	05045075490000	X	X	X	X						
GM42-35	05045075700000	X	X	X	X						
GM21-1	05045075760000	X	X	X	X						
GM23-33	05045075770000	X	X	X	X	X	X	X	X	X	X
GM267-3	05045075960000	X	X	X	X						
GM23-36	05045076080000	X	X	X	X						
GM34-34	05045076350000	X	X	X	X						
GM261-2	05045076870000	X	X	X	X						
GM230-34	05045076880000	X	X	X	X						
GM264-2	05045076890000	X	X	X	X						
GM23-34	05045077110000	X	X	X	X						
GM232-34	05045077140000	X	X	X	X						
GM237-36	05045077300000	X	X	X	X						
GM241-1	05045077310000	X	X	X	X						
GM266-3	05045077320000	X	X	X	X						
GM246-1	05045077420000	X	X	X	X						
GM251-2	05045077430000	X	X	X	X						
GM249-1	05045077450000	X	X	X	X						
GM248-1	05045077460000	X	X	X	X						

Well Name	Well UWI	Available Logs									
		VCL2	COAL_FLAG	Lithology	Arch_Elem	GR_NRM	DPHI	NPHI	PHIT	VSH	PHIE
GM245-1	05045077480000	X	X	X	X						
GM31-34	05045077560000	X	X	X	X						
GM324-1	05045077800000	X	X	X	X						
GM40151	05045078310000	X	X	X	X						
GM33-35	05045078510000	X	X	X	X						
GM43-35	05045078550000	X	X	X	X						
GM543-33	05045078800000	X	X	X	X						
GM443-33	05045078810000	X	X	X	X						
GM434-33	05045078840000	X	X	X	X						
GM544-33	05045078860000	X	X	X	X						
GM444-33	05045078880000	X	X	X	X						
GM433-33	05045079000000	X	X	X	X						
GM534-33	05045079020000	X	X	X	X						
GM533-33	05045079040000	X	X	X	X						
GM238-36	05045079180000	X	X	X	X						
GM333-36	05045079190000	X	X	X	X						
GM254-2	05045079610000	X	X	X	X						
GM257-2	05045079780000	X	X	X	X						
GM256-2	05045079910000	X	X	X	X						
GM12754	05045080070000	X	X	X	X						
GM218-33	05045080090000	X	X	X	X						
GM224-34	05045080280000	X	X	X	X						
GM332-34	05045081020000	X	X	X	X						
GM42-34	05045081030000	X	X	X	X						
GM342-34	05045081040000	X	X	X	X						
GM41-1	05045082040000	X	X	X	X						
GM341-1	05045082050000	X	X	X	X						
GM344-2	05045093860000	X	X	X	X						
GM434-1	05045094220000	X	X	X	X						
GM334-1	05045094230000	X	X	X	X						

Well Name	Well UWI	Available Logs									
		VCL2	COAL_FLAG	Lithology	Arch_Elem	GR_NRM	DPHI	NPHI	PHIT	VSH	PHIE
GM321-34	05045094720000	X	X	X	X						
GM421-34	05045094790000	X		X	X						
GM431-34	05045094800000	X		X	X						
GM314-1	05045095000000	X		X	X						
GM422-33	05045095550000	X		X	X						
GM245-2	05045092453210	X	X	X	X						
GM31-35	05045092983277	X	X	X	X						
GM524-1	05045095770000	X		X	X						
GM414-2	05045098000000	X		X	X						
GM514-2	05045098010000	X		X	X						
GM432-3	05045098740000	X		X	X						
GM532-3	05045098750000	X		X	X						
GM443-3	05045099390000	X		X	X						
GM343-3	05045099400000	X		X	X						
GM216-33	05045099670000	X	X	X	X						
GM544-3	05045099700000	X		X	X						
GM531-33	05045099710000	X	X	X	X						
GM431-33	05045099720000	X	X	X	X						
GM344-3	05045099730000	X		X	X						
GM444-3	05045099740000	X		X	X						
GM511-3	05045099750000	X	X	X	X	X	X	X	X	X	X
GM311-3	05045099760000	X		X	X						
GM411-3	05045099770000	X		X	X						
GM512-3	05045100050000	X		X	X						
GM412-3	05045100070000	X		X	X						
GM424-2	05045100100000	X		X	X						
GM524-2	05045100200000	X		X	X						
GM14-3	05045101130000	X	X	X	X						
GM414-3	05045101160000	X		X	X						
GM314-3	05045101190000	X		X	X						
GM514-3	05045101200000	X	X	X	X						
GM334-3	05045101250000	X		X	X						
GM434-3	05045101320000	X	X	X	X						
GM534-3	05045101330000	X		X	X						
GM532-4	05045101760000	X		X	X						

Well Name	Well UWI	Available Logs									
		VCL2	COAL_FLAG	Lithology	Arch_Elem	GR_NRM	DPHI	NPHI	PHIT	VSH	PHIE
GM433-4	05045101810000	X		X	X						
GM333-4	05045101820000	X		X	X						
GM542-4	05045102060000	X		X	X						
GM442-4	05045102070000	X		X	X						
GM342-4	05045102090000	X		X	X						
GM434-2	05045102130000	X		X	X						
GM534-2	05045102140000	X		X	X						
GM323-3	05045102150000	X		X	X						
GM423-3	05045102160000	X	X	X	X						
GM523-3	05045102170000	X		X	X						
GM522-3	05045102210000	X		X	X						
GM422-3	05045102220000	X		X	X						
GM322-3	05045102230000	X		X	X						
GM413-1	05045102440000	X	X	X	X						
GM513-1	05045102450000	X	X	X	X						
GM443-34	05045103740000	X		X	X						
GM543-34	05045103750000	X		X	X						
GM234-34	05045103760000	X	X	X	X						
GM643-34	05045103770000	X	X	X	X						
GM421-1	05045103800000	X	X	X	X						
GM332-1	05045103810000	X	X	X	X						
GM521-1	05045103820000	X	X	X	X						
GM233-34	05045104650000	X		X	X						
GM434-34	05045104660000	X		X	X						
GM534-34	05045104670000	X		X	X						
GM511-1	05045104840000	X	X	X	X						
GM324-3	05045105270000	X		X	X						
GM424-3	05045105280000	X		X	X						
GM524-3	05045105290000	X		X	X						
GM41-35	05045106350000	X		X	X						
GM13455	05045106380000	X		X	X						
GM311-36	05045106390000	X		X	X						
GM513-3	05045106400000	X	X	X	X						
GM413-3	05045106410000	X		X	X						
GM313-3	05045106420000	X		X	X						

Well Name	Well UWI	Available Logs									
		VCL2	COAL_FLAG	Lithology	Arch_Elem	GR_NRM	DPHI	NPHI	PHIT	VSH	PHIE
GM421-4	05045108590000	X		X	X						
GM521-4	05045108600000	X		X	X						
GM321-4	05045108610000	X		X	X						
GM321-3	05045108680000	X		X	X						
GM22-36	05045108710000	X	X	X	X						
GM312-36	05045108720000	X		X	X						
GM524-4	05045109170000	X	X	X	X						
GM442-34	05045109210000	X	X	X	X						
GM542-34	05045109220000	X	X	X	X						
GM532-34	05045109230000	X	X	X	X						
GM432-34	05045109240000	X	X	X	X						
GM413-34	05045113620000	X	X	X	X						
GM312-34	05045113630000	X	X	X	X						
GM512-34	05045113640000	X	X	X	X	X	X	X	X	X	X
GM412-34	05045113650000	X	X	X	X						
GM511-36	05045113960000	X	X	X	X						
GM422-36	05045113970000	X	X	X	X						
GM412-36	05045113990000	X	X	X	X						
GM421-36	05045114000000	X	X	X	X						
GM614-35	05045114250000	X	X	X	X						
GM414-35	05045114260000	X		X	X						
GM514-35	05045114270000	X		X	X						
GM253-2	05045115020000	X	X	X	X						
GM421-2	05045115030000	X		X	X						
GM411-2	05045115050000	X		X	X						
GM511-2	05045115060000	X		X	X						
GM333-35	05045115980000	X		X	X						
GM332-35	05045115990000	X		X	X						
GM433-35	05045116000000	X	X	X	X						
GM543-35	05045116010000	X	X	X	X						
GM343-35	05045116020000	X		X	X						
GM443-35	05045116030000	X	X	X	X						
GM442-35	05045116040000	X	X	X	X						
GM331-35	05045116050000	X		X	X						
GM432-35	05045116090000	X	X	X	X						

Well Name	Well UWI	Available Logs									
		VCL2	COAL_FLAG	Lithology	Arch_Elem	GR_NRM	DPHI	NPHI	PHIT	VSH	PHIE
GM22-35R	05045116100001	X	X	X	X						
GM342-35	05045116110000	X		X	X						
GM441-3	05045116950000	X	X	X	X						
GM541-3	05045116960000	X		X	X						
GM433-3	05045119190000	X		X	X						
GM333-3	05045119240000	X	X	X	X						
GM432-4	05045119370000	X		X	X						
GM533-4	05045119390000	X		X	X						
GM343-4	05045119570000	X		X	X						
GM443-4	05045119580000	X		X	X						
GM334-4	05045119590000	X		X	X						
GM513-2	05045120150000	X		X	X						
GM413-2	05045120160000	X		X	X						
GM422-2	05045120780000	X		X	X						
GM423-2	05045120790000	X		X	X						
GM524-35	05045121330000	X	X	X	X						
GM424-35	05045121340000	X	X	X	X						
GM324-35	05045121350000	X		X	X						
GM23-35	05045121360000	X	X	X	X						
GM322-4	05045122630000	X		X	X						
GM312-4	05045122640000	X		X	X						
GM512-4	05045122650000	X	X	X	X						
GM412-4	05045122660000	X		X	X						
GM532-2	05045124860000	X		X	X						
GM432-2	05045124870000	X		X	X						
GM542-2	05045124880000	X		X	X						
GM442-2	05045124890000	X		X	X						
GM441-2	05045124900000	X		X	X						
GM444-4	05045124940000	X	X	X	X						
GM434-4	05045124950000	X	X	X	X						
GM643-35	05045126620000	X	X	X	X						
GM227-35	05045126630000	X		X	X						
GM34-35	05045126640000	X		X	X						
GM544-35	05045126660000	X	X	X	X						
GM441-4	05045127830000	X		X	X						

Well Name	Well UWI	Available Logs									
		VCL2	COAL_FLAG	Lithology	Arch_Elem	GR_NRM	DPHI	NPHI	PHIT	VSH	PHIE
GM431-4	05045127840000	X		X	X						
GM314-33	05045128270000	X		X	X	X	X	X	X	X	X
GM324-33	05045128280000	X		X	X						
GM424-33	05045128290000	X	X	X	X						
GM411-33	05045128300000	X	X	X	X						
GM511-33	05045128320000	X	X	X	X						
GM21-36	05045130480000	X		X	X						
GM521-36	05045130490000	X	X	X	X						
GM321-36	05045130500000	X		X	X						
GM541-35	05045130520000	X	X	X	X						
GM541-36	05045130660000	X		X	X						
GM442-36	05045130670000	X	X	X	X						
GM431-36	05045130690000	X	X	X	X						
GM342-36	05045130700000	X		X	X						
GM432-36	05045130710000	X	X	X	X						
GM341-36	05045130720000	X		X	X						
GM441-36	05045130730000	X	X	X	X						
GM31-35	05045130860000	X		X	X						
GM411-36	05045130870000	X	X	X	X						
GM331-36	05045130880000	X		X	X						
GM444-1	05045133360000	X		X	X						
GM344-1	05045133370000	X	X	X	X						
GM544-1	05045133380000	X		X	X						
GM443-1	05045134410000	X	X	X	X						
GM543-1	05045134420000	X	X	X	X						
GM442-1	05045134740000	X	X	X	X						
GM542-1	05045134750000	X	X	X	X						
GM228-34	05045135480000	X	X	X	X						
GM422-34	05045135490000	X	X	X	X						
GM523-36	05045139790000	X	X	X	X						
GM424-36	05045139800000	X	X	X	X						
GM225-36	05045139810000	X		X	X						
GM513-36	05045139820000	X	X	X	X						
GM44-36	05045141330000	X		X	X						
GM433-36	05045141340000	X	X	X	X						

Well Name	Well UWI	Available Logs									
		VCL2	COAL_FLAG	Lithology	Arch_Elem	GR_NRM	DPHI	NPHI	PHIT	VSH	PHIE
GM43-36	05045141350000	X	X	X	X						
GM444-36	05045141360000	X	X	X	X						
GM434-36	05045141370000	X	X	X	X						
GM441-1	05045142610000	X	X	X	X						
GM344-36	05045142620000	X		X	X						
GM411-1	05045144670000	X	X	X	X						
GM512-1	05045144680000	X	X	X	X						
GM423-1	05045144690000	X	X	X	X						
GM423-36	05045146910000	X	X	X	X						
GM323-36	05045146920000	X		X	X						
GM239-36	05045146930000	X	X	X	X						
GM413-36	05045146940000	X	X	X	X						
GM432-33	05045172040000	X	X	X	X						
GM442-33	05045172050000	X	X	X	X						
GM441-33	05045172060000	X	X	X	X						
GM532-33	05045172070000	X	X	X	X						
GM342-33	05045172080000	X	X	X	X						
GM332-33	05045172090000	X	X	X	X	X	X	X	X	X	X
GM411-34	05045172100000	X	X	X	X						

Appendix D

Diagrammatic Illustrations of Core Descriptions

Appendix D shows nine out of ten cores described within and surrounding Grand Valley Field to interpret facies, facies associations, and architectural elements associated with the lower Williams Fork Formation. No description is included for Oxy Core 679-20-26. All core descriptions are displayed as diagrammatic illustrations with sedimentary structures, grain size, and bioturbation shown. A legend can be found in figure 11.

Order of core descriptions:

1-7 LW Getty
Grand Valley #2 Federal
MV8-4
MV24-20
MV29-27
MV33-34
Orchard Unit
PA424-34
GM231-34

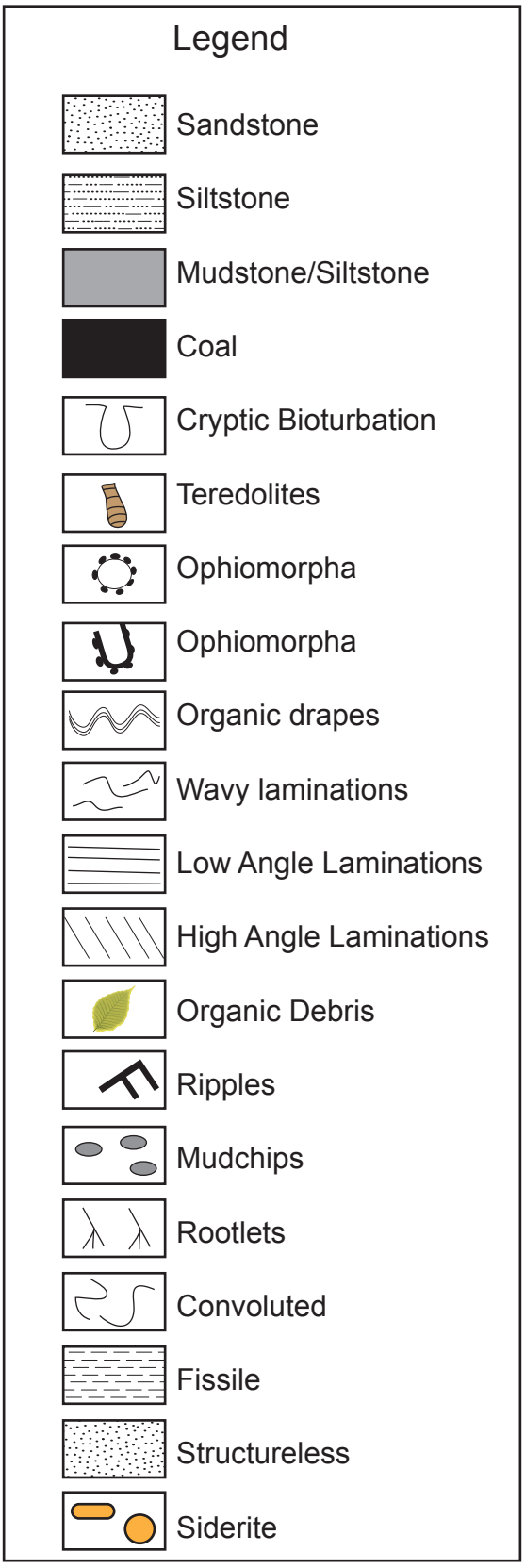
Legend
Sandstone
Siltstone
Mudstone/Siltstone
Coal
Cryptic Bioturbation
Teredolites
Ophiomorpha
Ophiomorpha
Organic drapes
Wavy laminations
Low Angle Laminations
High Angle Laminations
Organic Debris
Ripples
Mudchips
Rootlets
Convoluted
Fissile
Structureless
Siderite

1-7 LW Getty Core Description

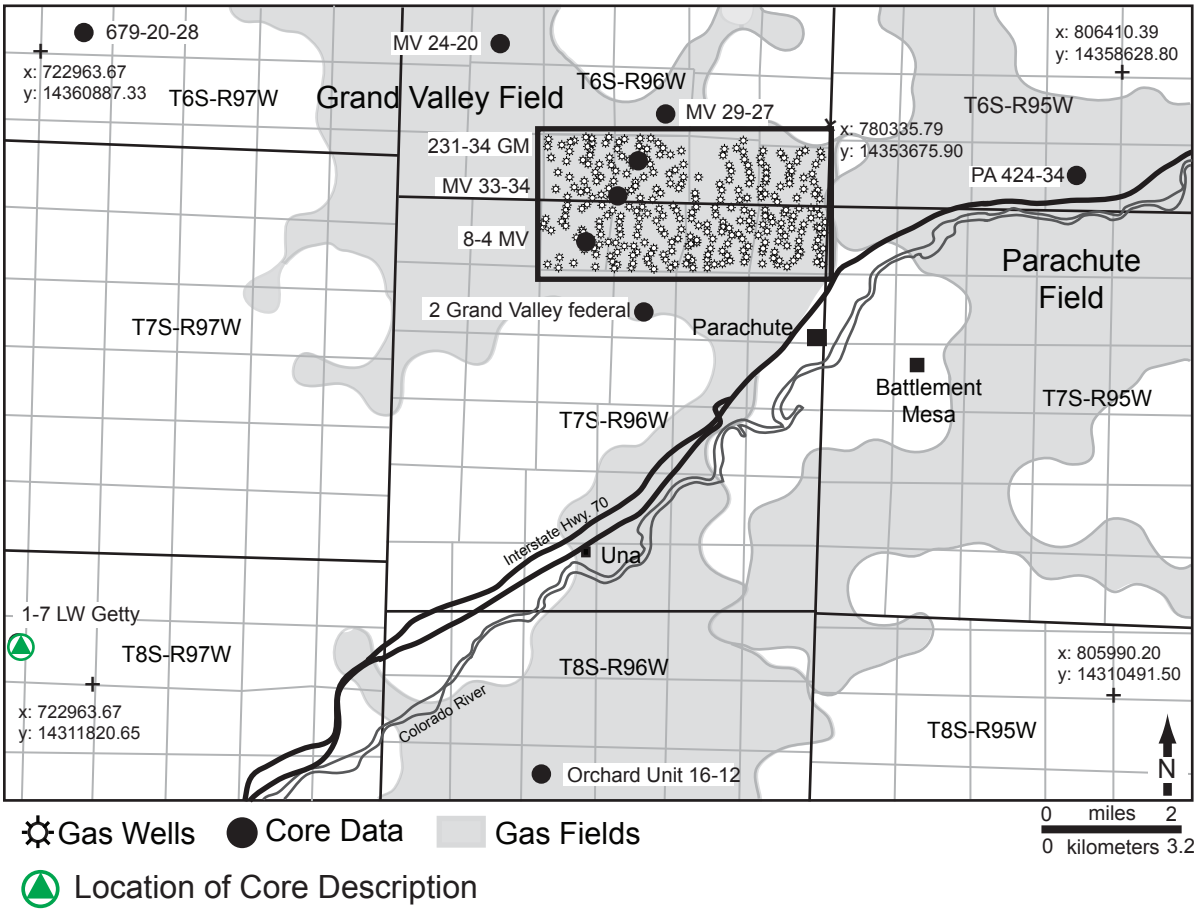

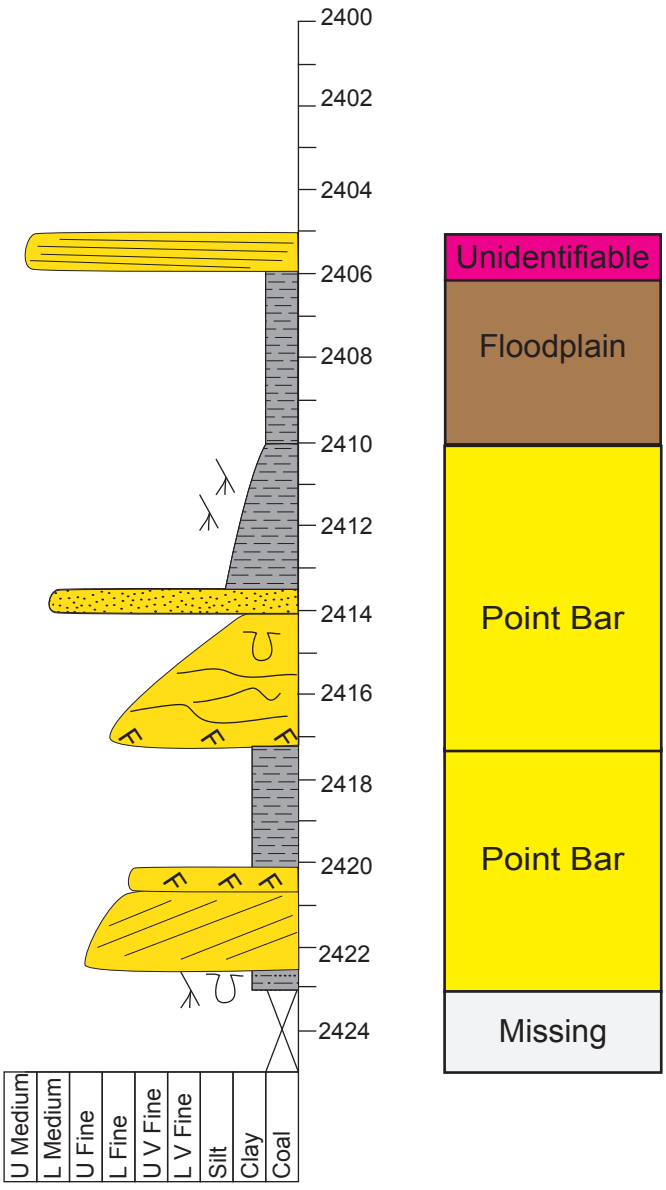
Core Description (ft)
Interpretation
2400
2402
2404
2406
2408
2410
2412
2414
2416
2418
2420
2422
2424
Unidentifiable
Floodplain
Point Bar
Point Bar
Missing
U Medium
L Medium
U Fine
L Fine
U V Fine
L V Fine
Silt
Clay
Coal

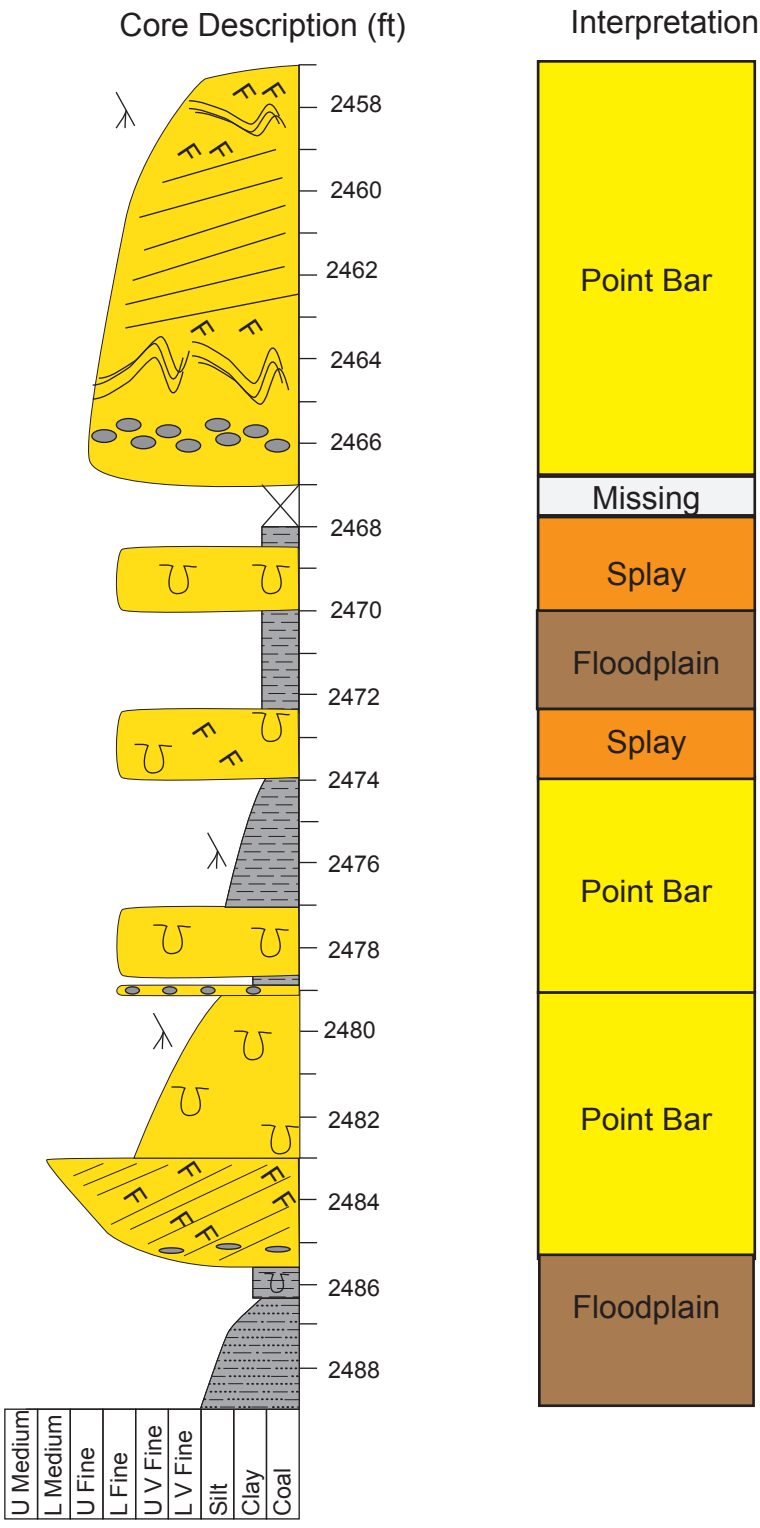
Core Description (ft)
Interpretation
2458
2460
2462
2464
2466
2468
2470
2472
2474
2476
2478
2480
2482
2484
2486
2488
Point Bar
Missing
Splay
Floodplain
Splay
Point Bar
Point Bar
Floodplain
U Medium
L Medium
U Fine
L Fine
U V Fine
L V Fine
Silt
Clay
Coal

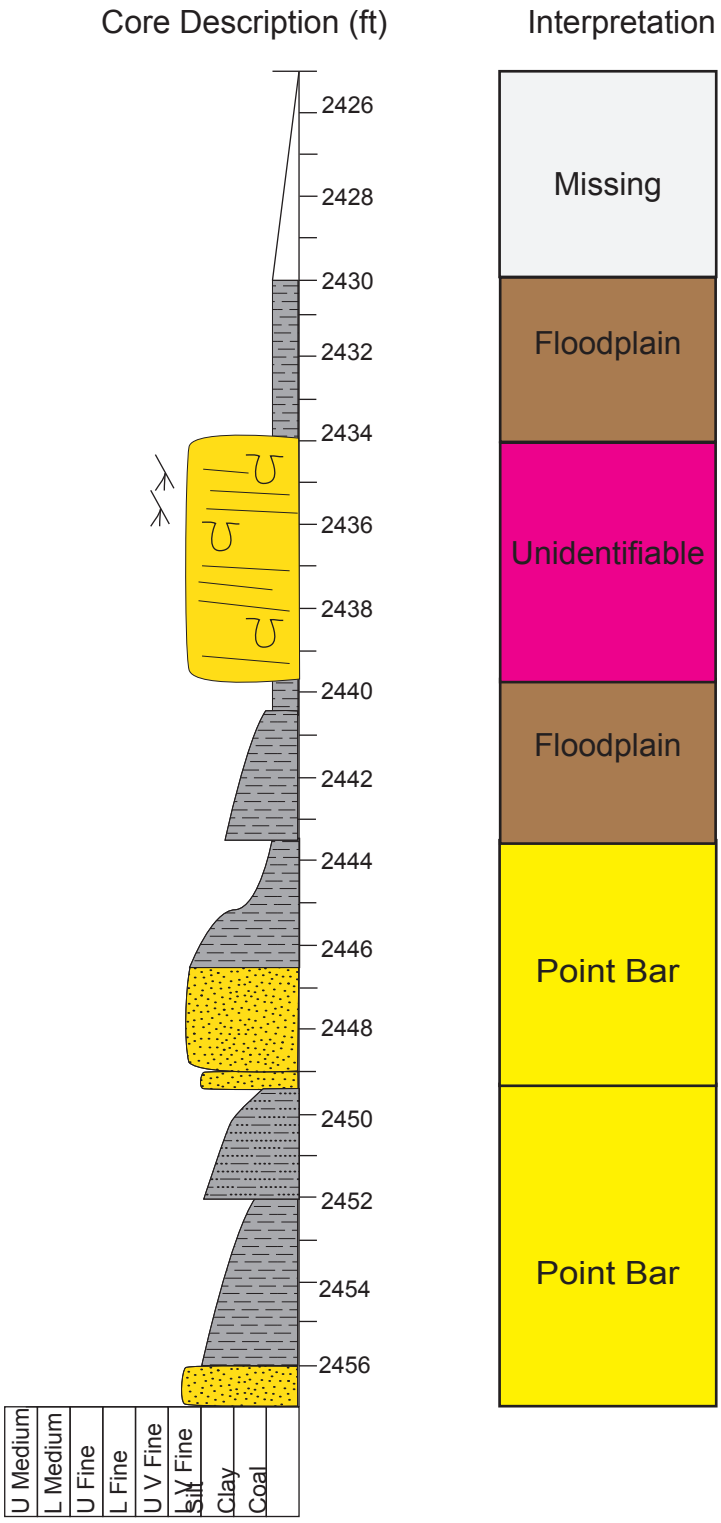
Core Description (ft)
Interpretation
2426
2428
2430
2432
2434
2436
2438
2440
2442
2444
2446
2448
2450
2452
2454
2456
U Medium
L Medium
U Fine
L Fine
U V Fine
L V Fine
Silt
Clay
Coal
Missing
Floodplain
Unidentifiable
Floodplain
Point Bar
Point Bar

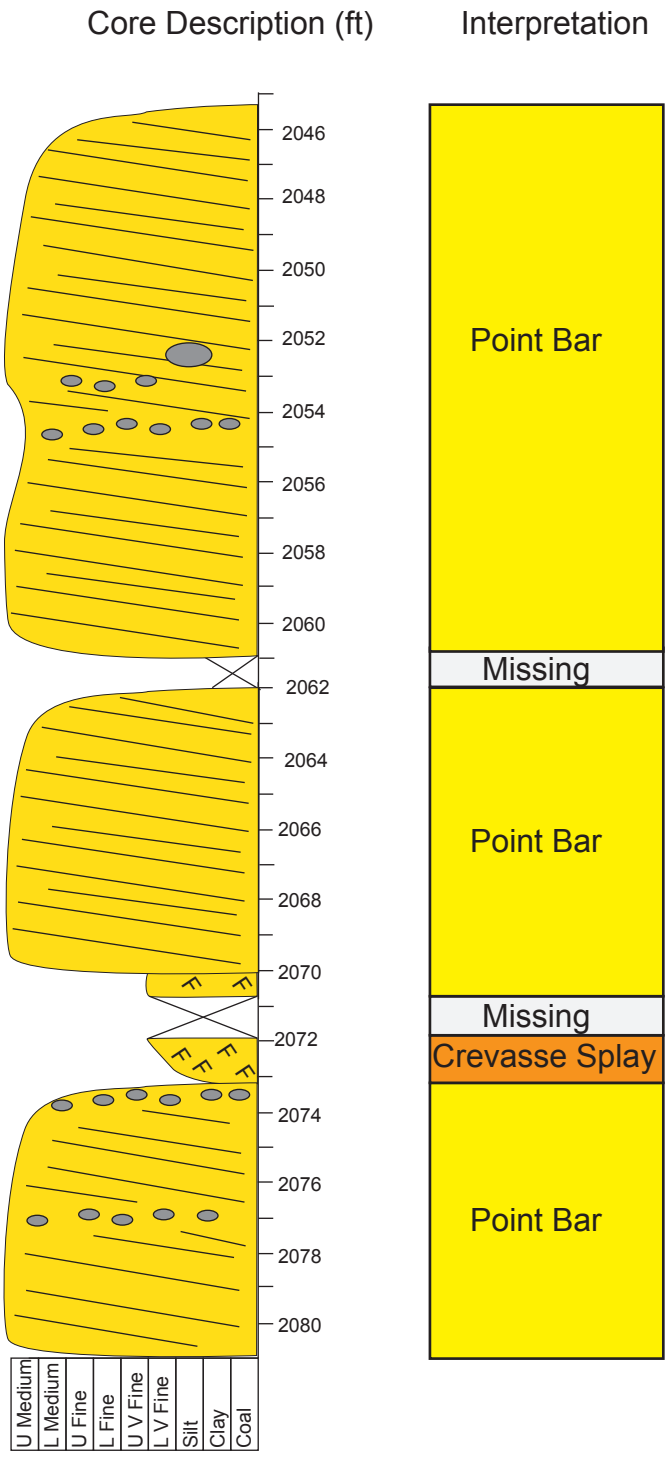
Core Description (ft)
Interpretation
2046
2048
2050
2052
2054
2056
2058
2060
2062
2064
2066
2068
2070
2072
2074
2076
2078
2080
F
F
F
F
F
F
Point Bar
Missing
Point Bar
Missing
Crevasse Splay
Point Bar
U Medium
L Medium
U Fine
L Fine
U V Fine
L V Fine
Silt
Clay
Coal

GM 231-34 Core Description

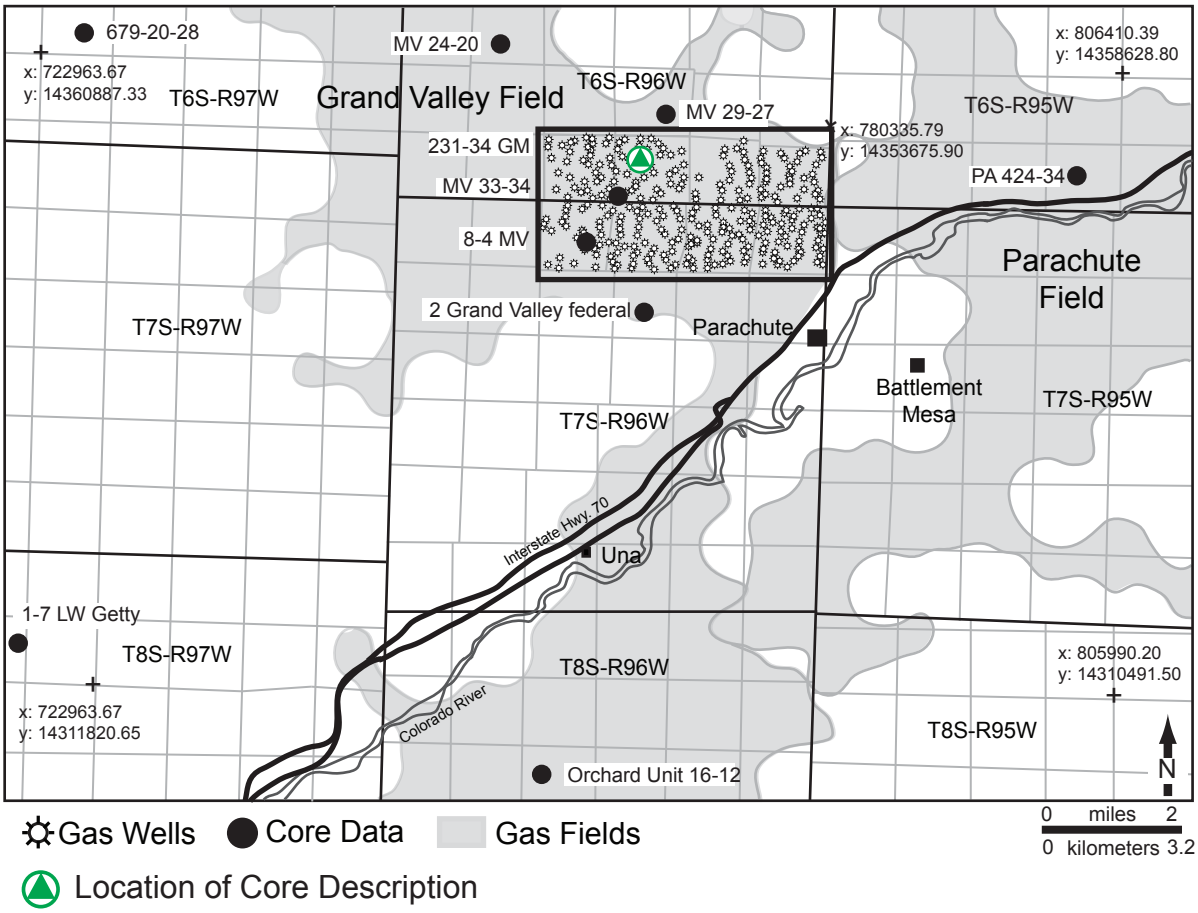

Core Description (ft)

Interpretation

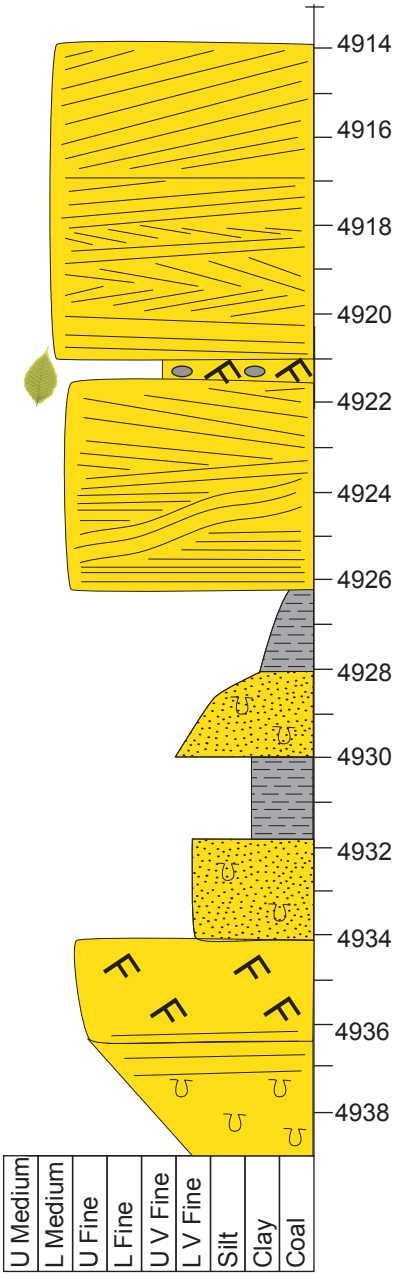

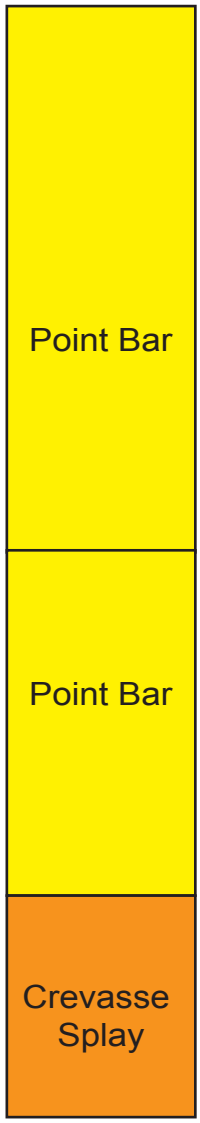

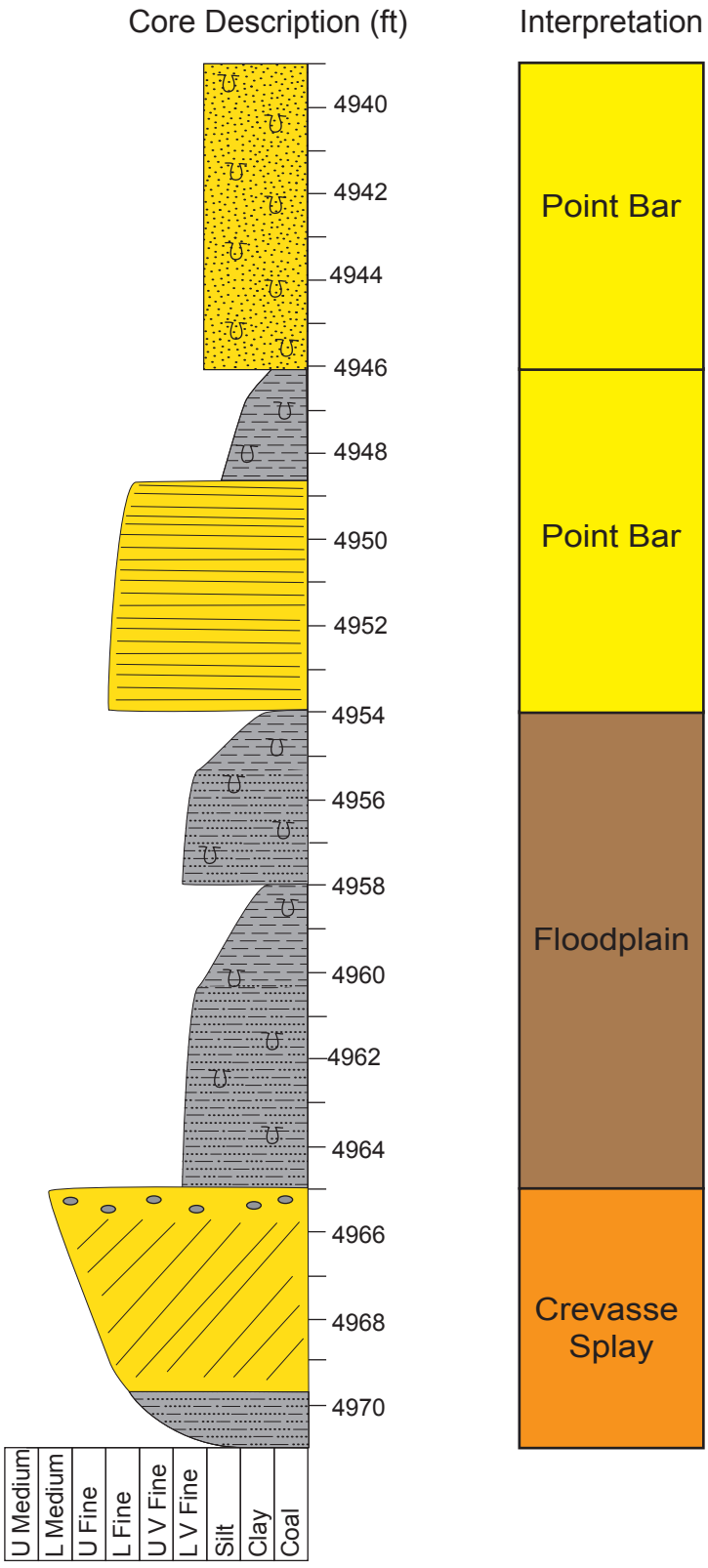
Core Description (ft)
Interpretation
4940
4942
4944
4946
4948
4950
4952
4954
4956
4958
4960
4962
4964
4966
4968
4970
Point Bar
Point Bar
Floodplain
Crevasse Splay
U Medium
L Medium
U Fine
L Fine
U V Fine
L V Fine
Silt
Clay
Coal

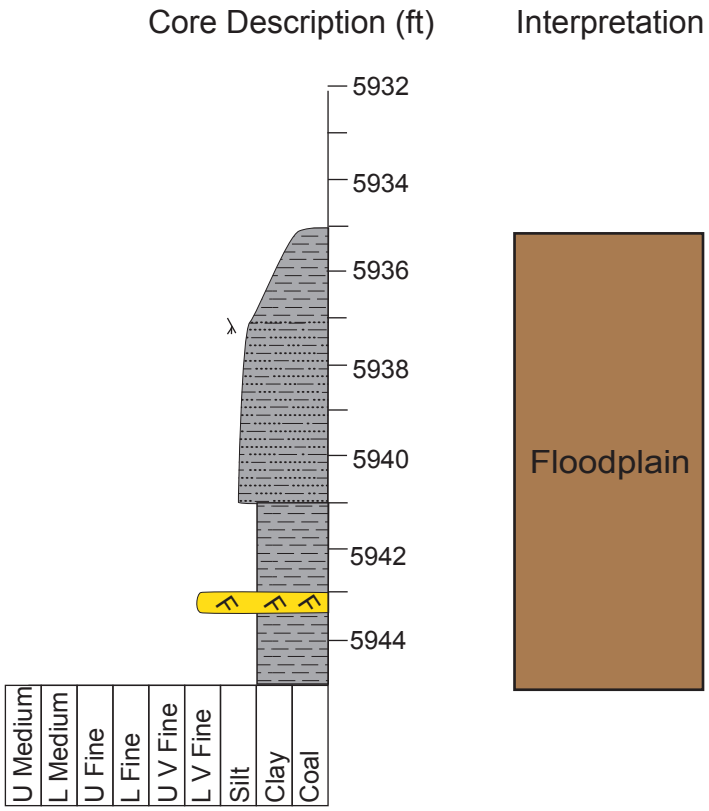
Core Description (ft)
Interpretation
5932
5934
5936
5938
5940
5942
5944
Floodplain
U Medium
L Medium
U Fine
L Fine
U V Fine
L V Fine
Silt
Clay
Coal

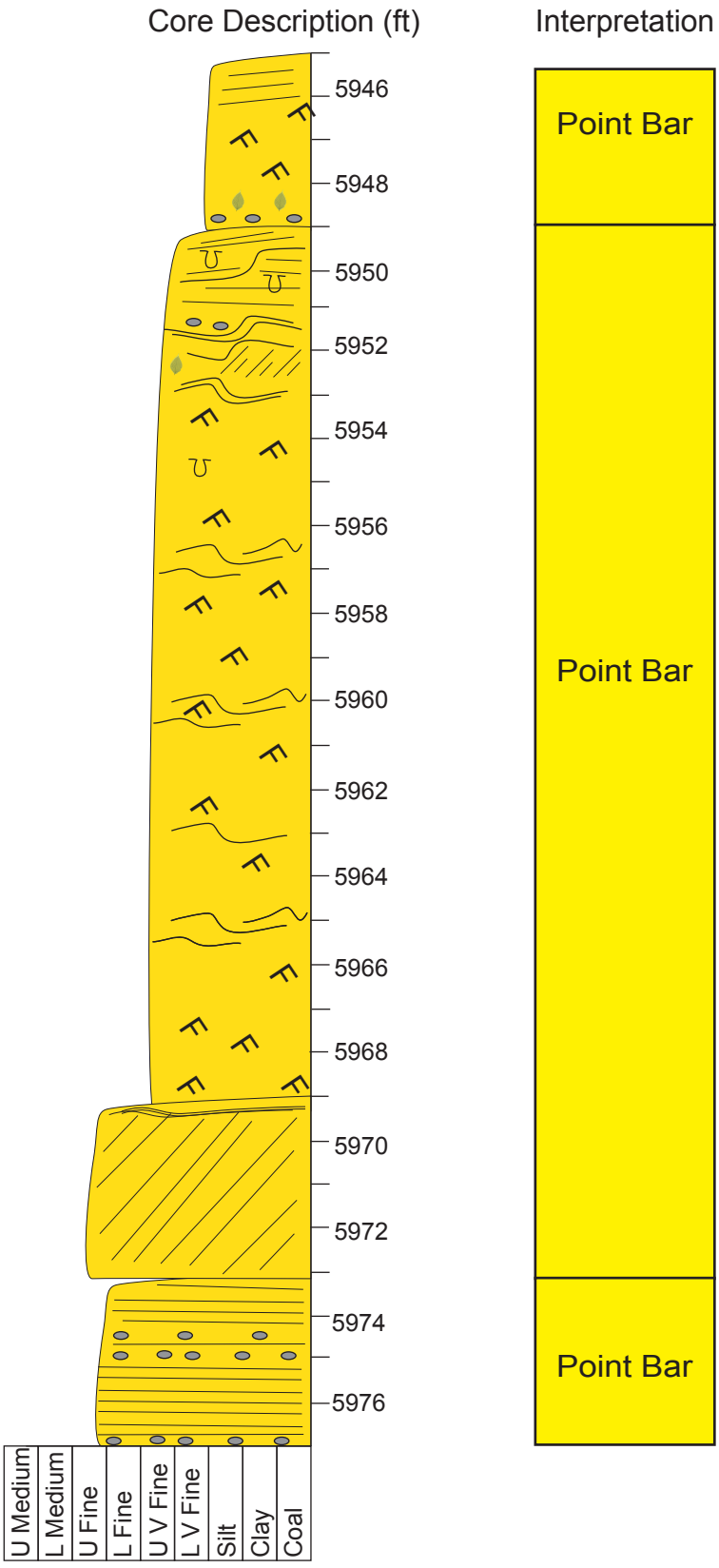
Core Description (ft)
Interpretation
5946
5948
5950
5952
5954
5956
5958
5960
5962
5964
5966
5968
5970
5972
5974
5976
Point Bar
Point Bar
Point Bar
U Medium
L Medium
U Fine
L Fine
U V Fine
L V Fine
Silt
Clay
Coal

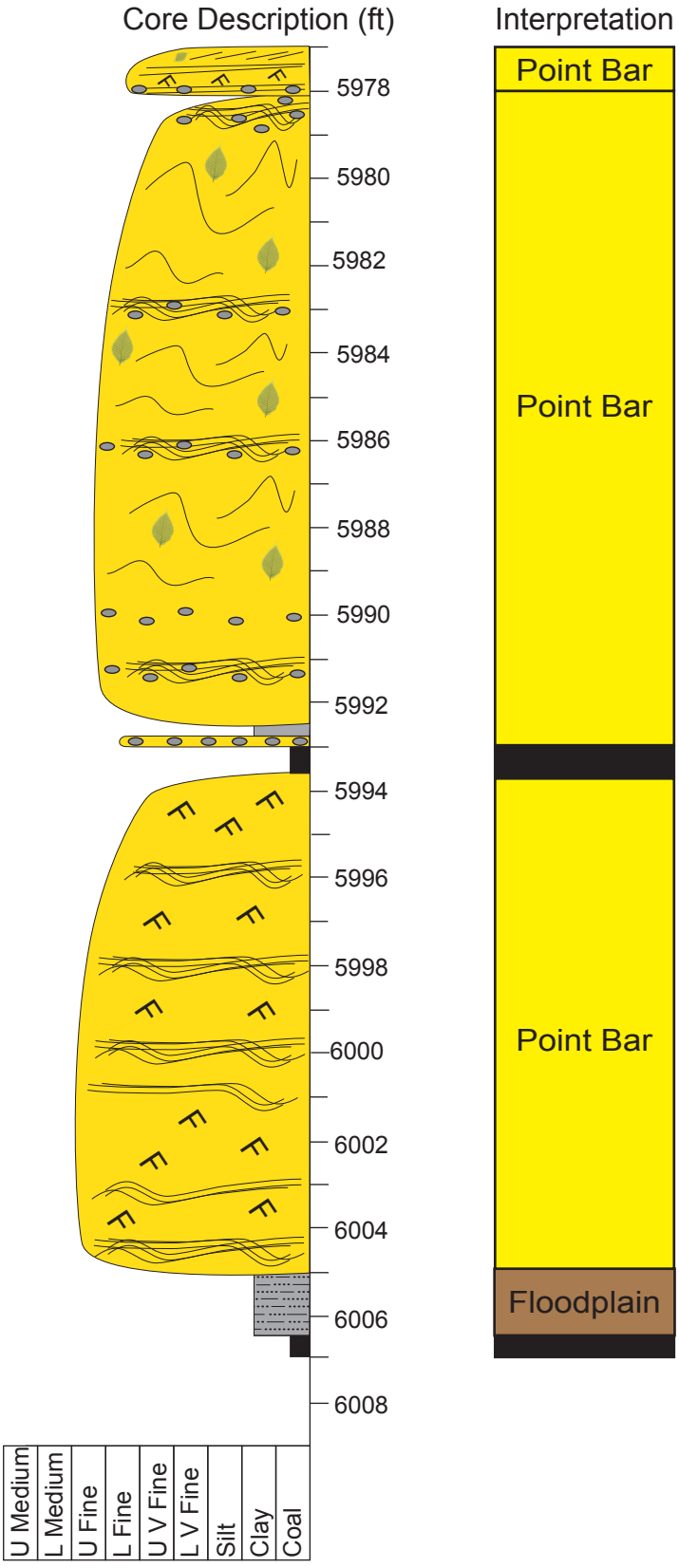
Core Description (ft)
Interpretation
5978
5980
5982
5984
5986
5988
5990
5992
5994
5996
5998
6000
6002
6004
6006
6008
Point Bar
Point Bar
Point Bar
Floodplain
U Medium
L Medium
U Fine
L Fine
U V Fine
L V Fine
Silt
Clay
Coal

2 Grand Valley Federal Core Description

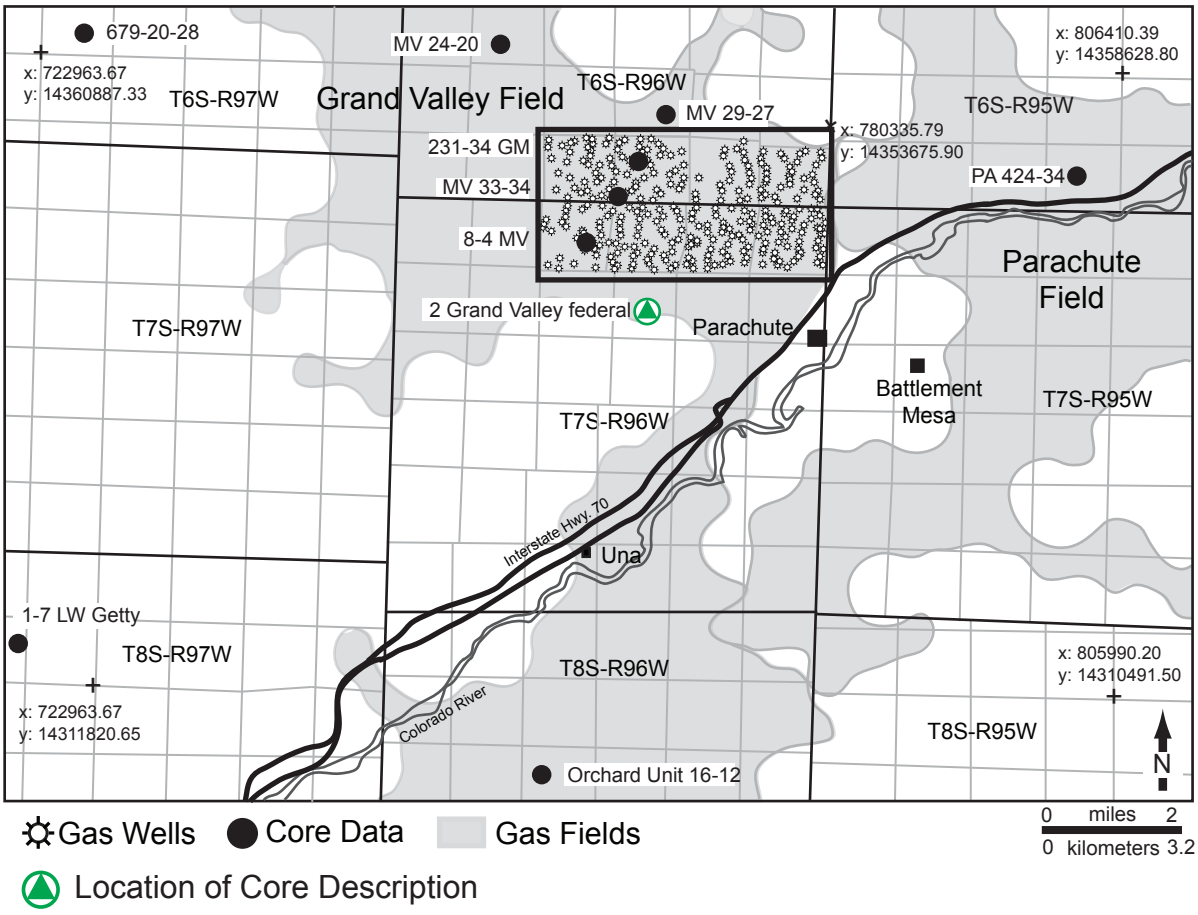

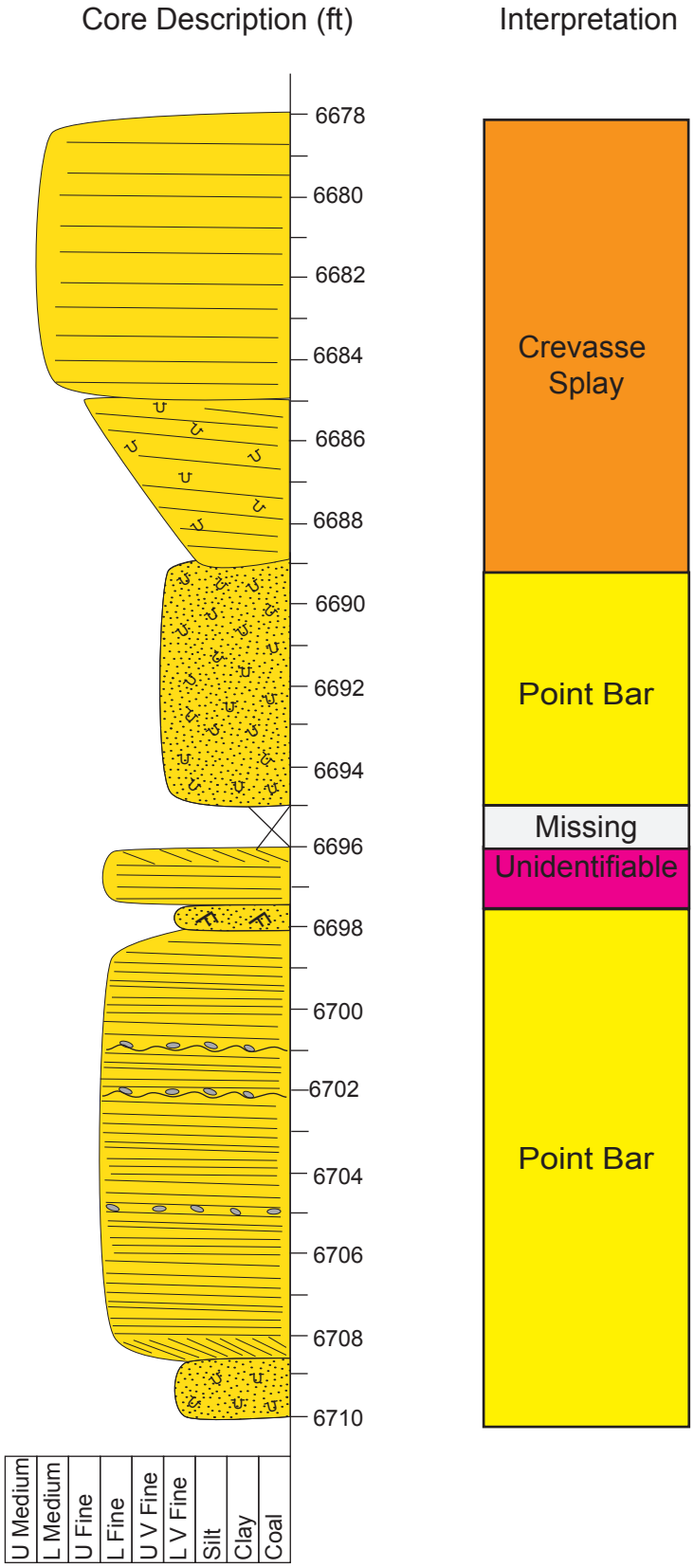
Core Description (ft)
Interpretation
6678
6680
6682
6684
6686
6688
6690
6692
6694
6696
6698
6700
6702
6704
6706
6708
6710
Crevasse Splay
Point Bar
Missing
Unidentifiable
Point Bar
U Medium
L Medium
U Fine
L Fine
U V Fine
L V Fine
Silt
Clay
Coal

8-4 MV Core Description

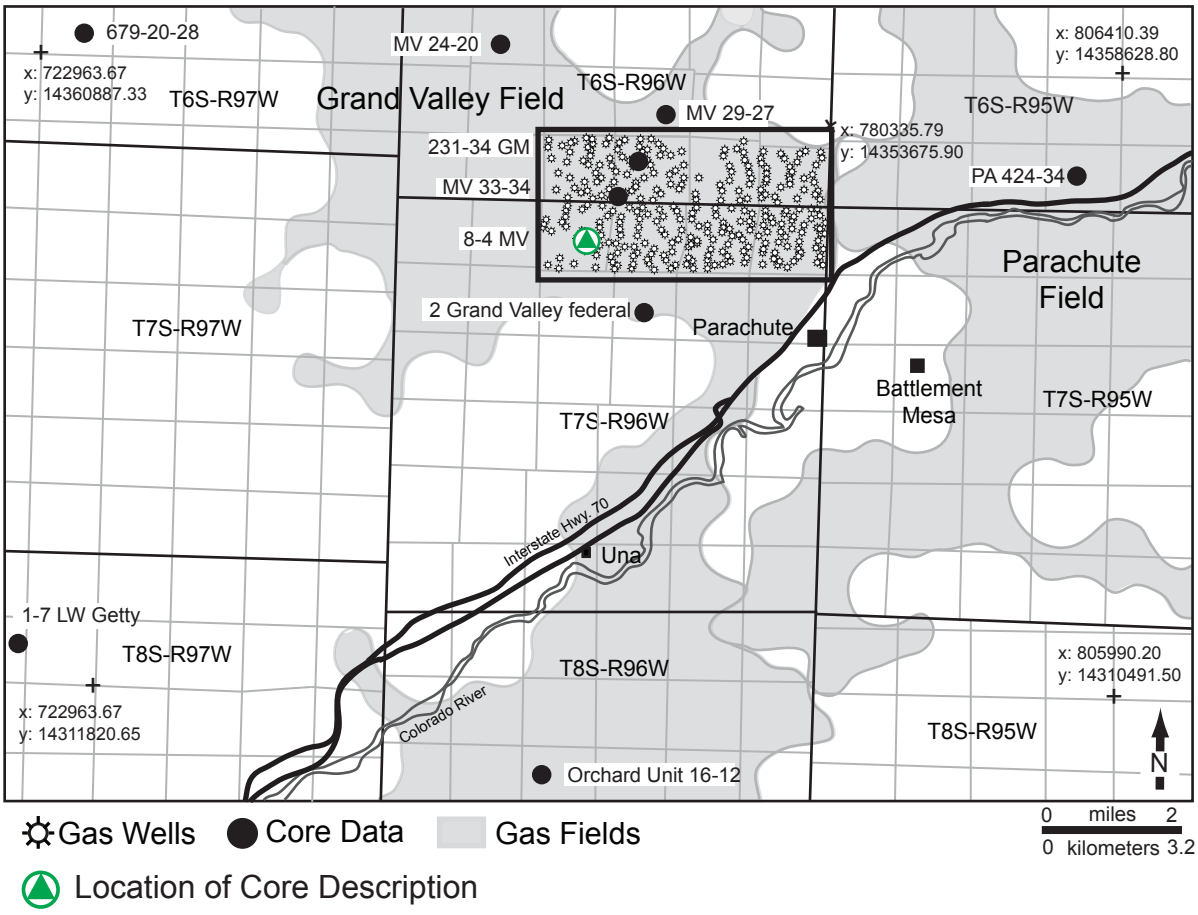

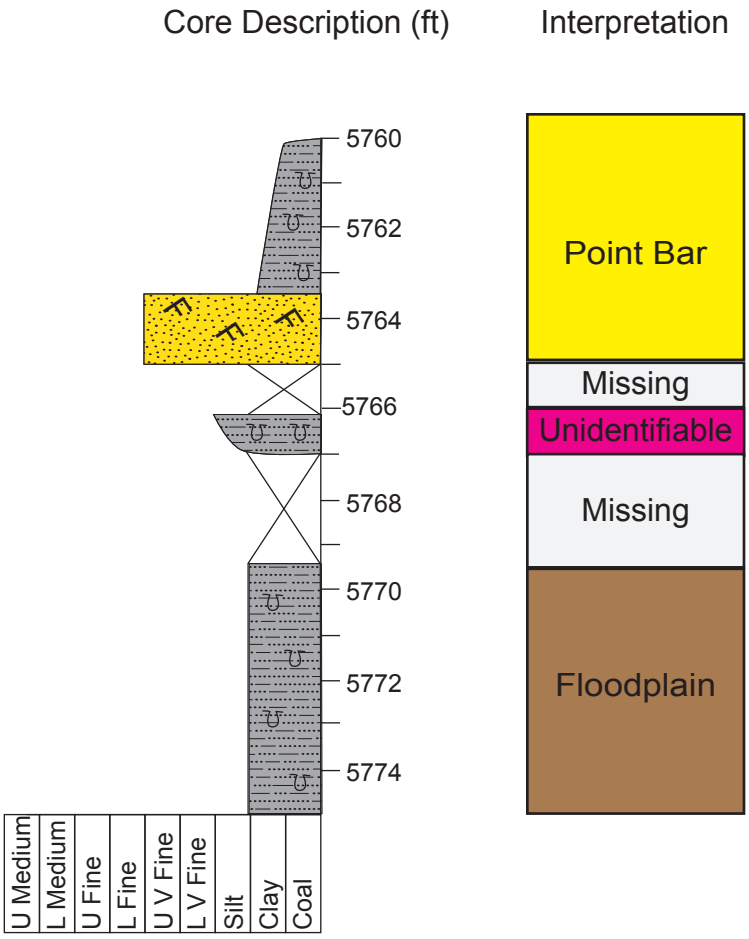
Core Description (ft)
Interpretation
5760
5762
5764
5766
5768
5770
5772
5774
Point Bar
Missing
Unidentifiable
Missing
Floodplain
U Medium
L Medium
U Fine
L Fine
U V Fine
L V Fine
Silt
Clay
Coal

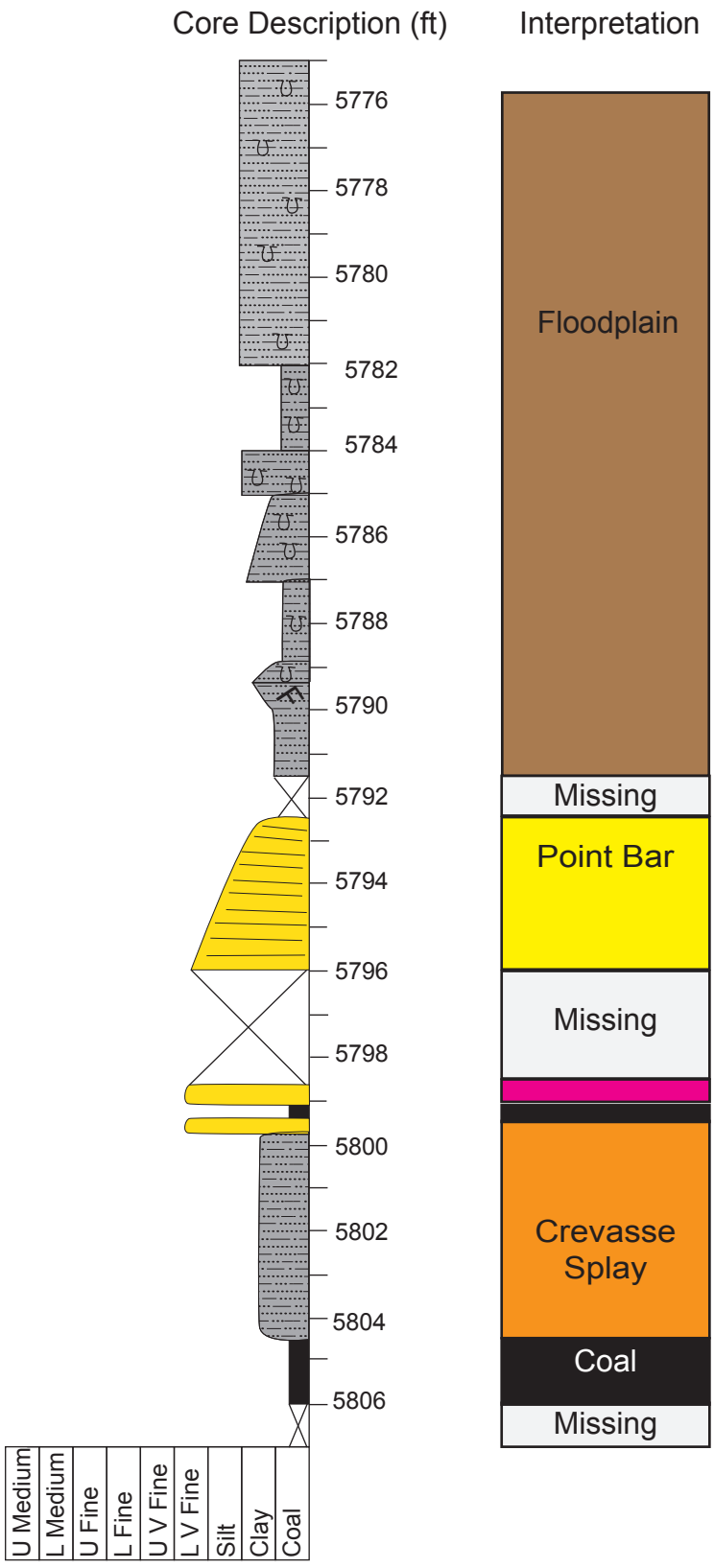
Core Description (ft)
Interpretation
5776
5778
5780
5782
5784
5786
5788
5790
5792
5794
5796
5798
5800
5802
5804
5806
Floodplain
Missing
Point Bar
Missing
Crevasse Splay
Coal
Missing
U Medium
L Medium
U Fine
L Fine
U V Fine
L V Fine
Silt
Clay
Coal

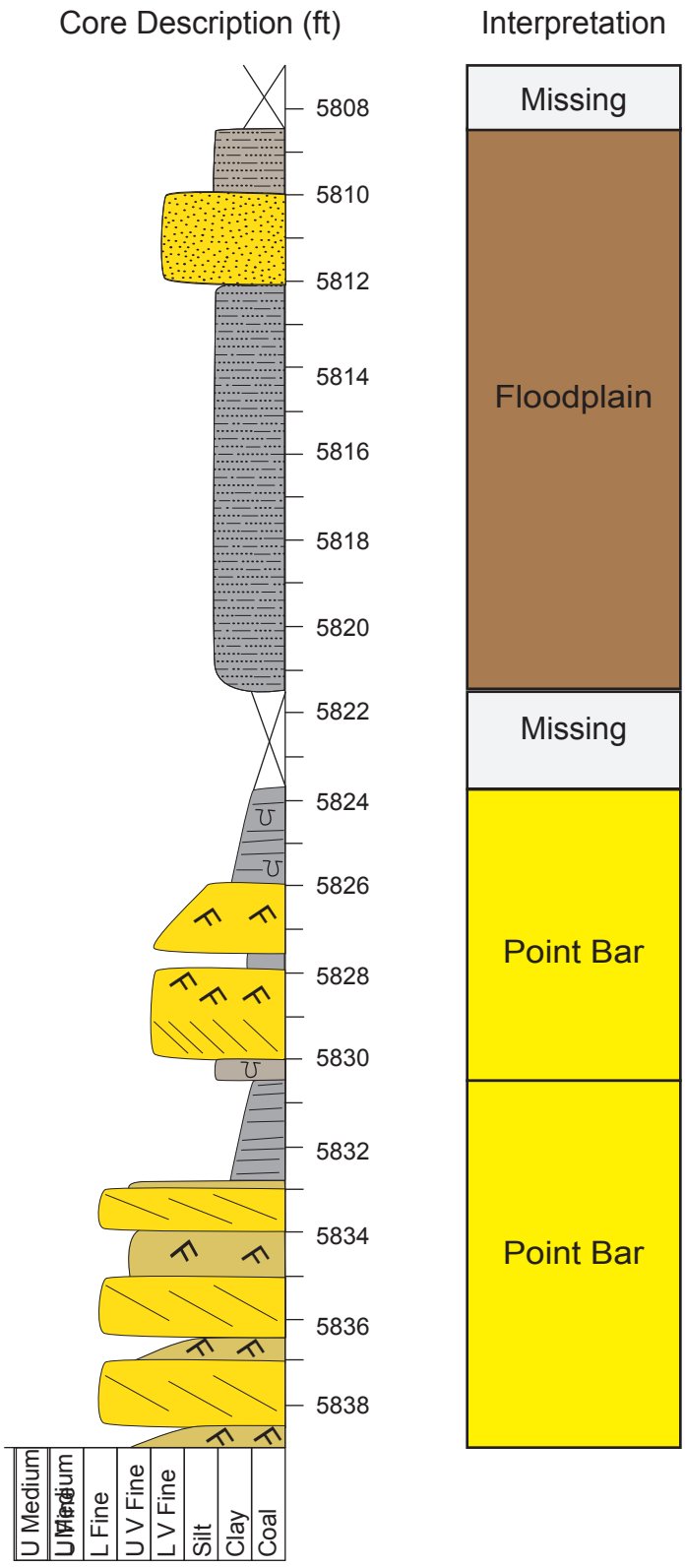
Core Description (ft)
Interpretation
5808
5810
5812
5814
5816
5818
5820
5822
5824
5826
5828
5830
5832
5834
5836
5838
Missing
Floodplain
Missing
Point Bar
Point Bar
U Medium
L Fine
U V Fine
L V Fine
Silt
Clay
Coal

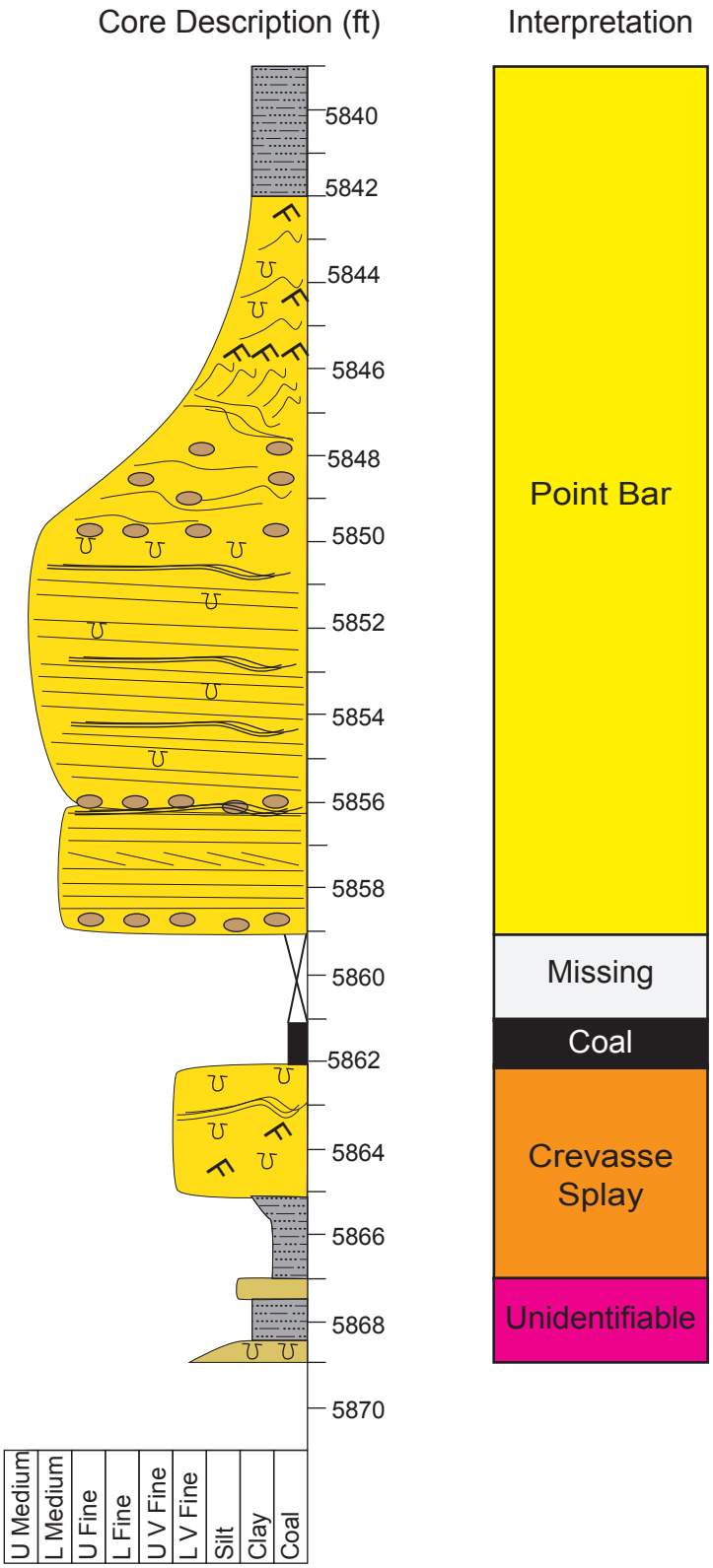
Core Description (ft)
Interpretation
5840
5842
5844
5846
5848
5850
5852
5854
5856
5858
5860
5862
5864
5866
5868
5870
Point Bar
Missing
Coal
Crevasse Splay
Unidentifiable
U Medium
L Medium
U Fine
L Fine
U V Fine
L V Fine
Silt
Clay
Coal

MV 24-20 Core Description

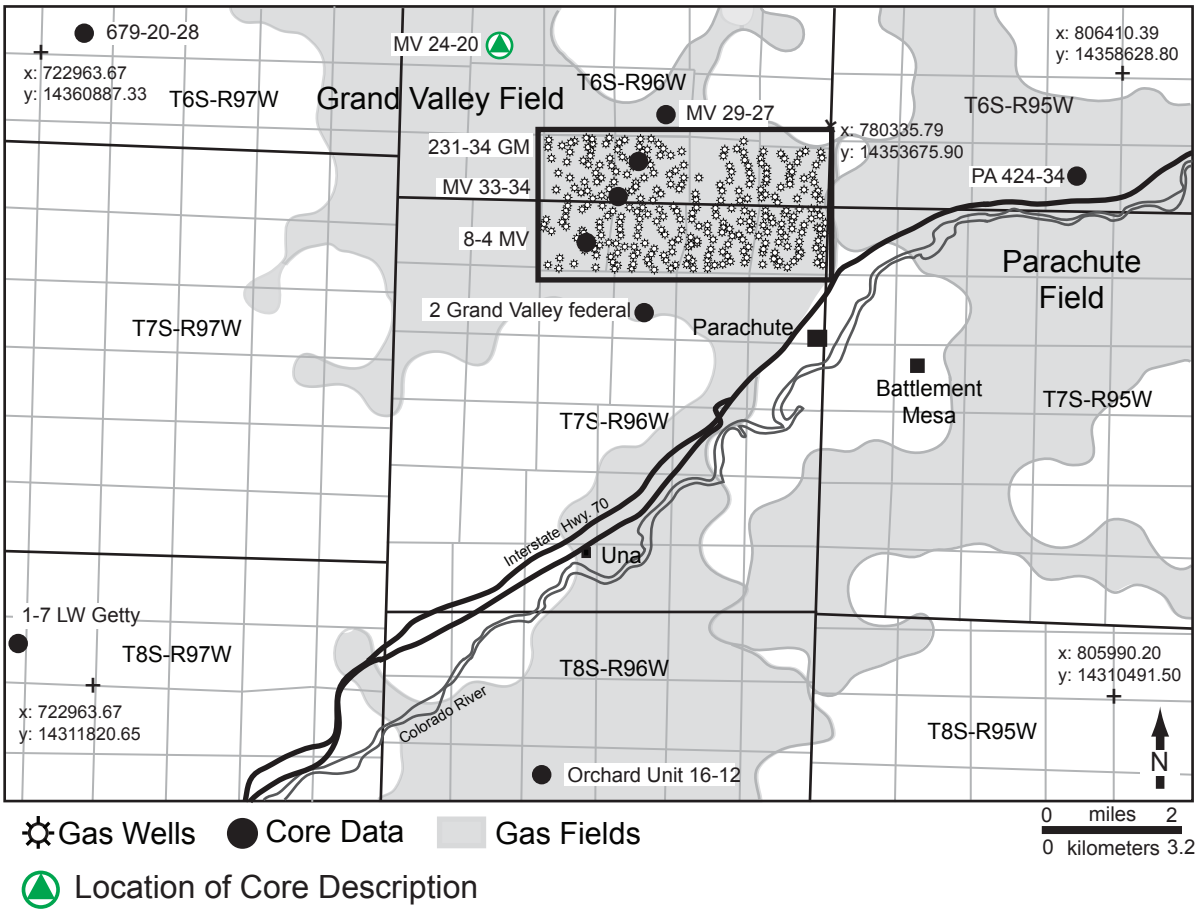

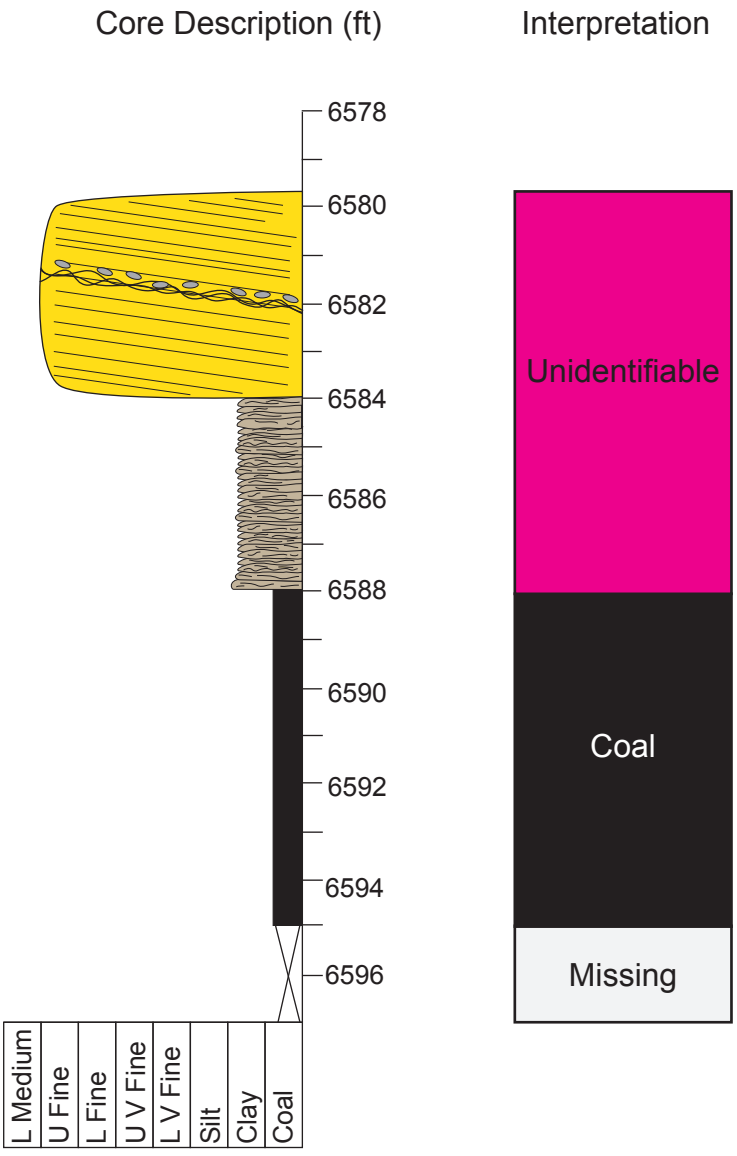
Core Description (ft)
Interpretation
6578
6580
6582
6584
6586
6588
6590
6592
6594
6596
Unidentifiable
Coal
Missing
L Medium
U Fine
L Fine
U V Fine
L V Fine
Silt
Clay
Coal

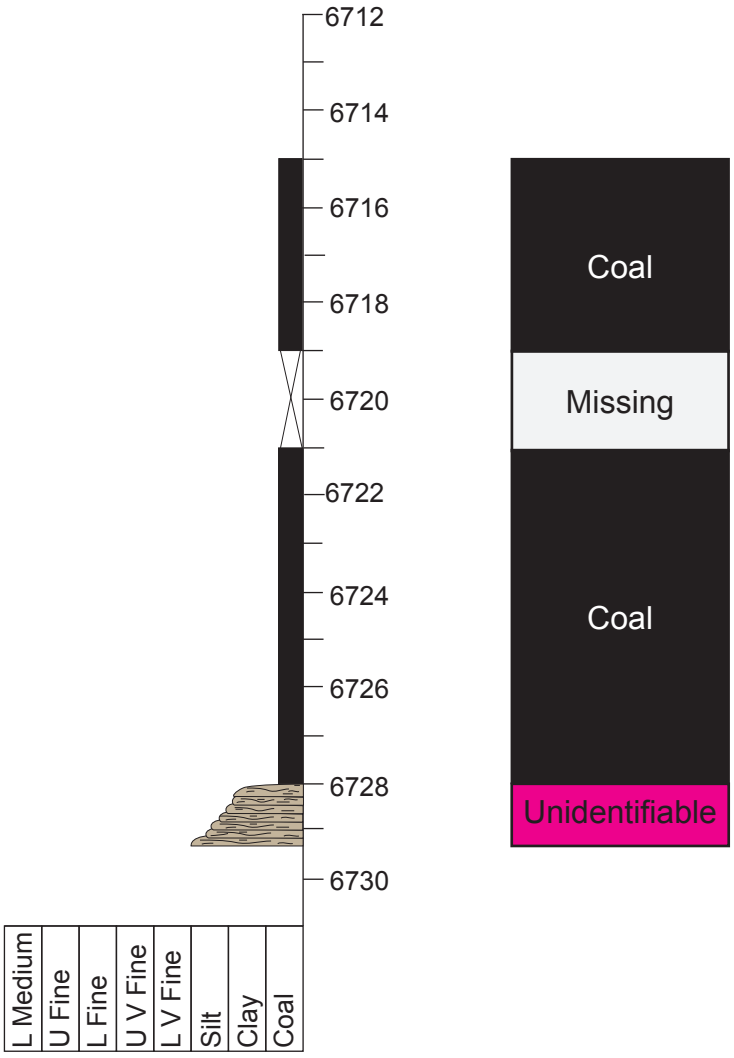
Core Description (ft)
Interpretation
6712
6714
6716
6718
6720
6722
6724
6726
6728
6730
Coal
Missing
Coal
Unidentifiable
L Medium
U Fine
L Fine
U V Fine
L V Fine
Silt
Clay
Coal

MV 29-27 Core Description

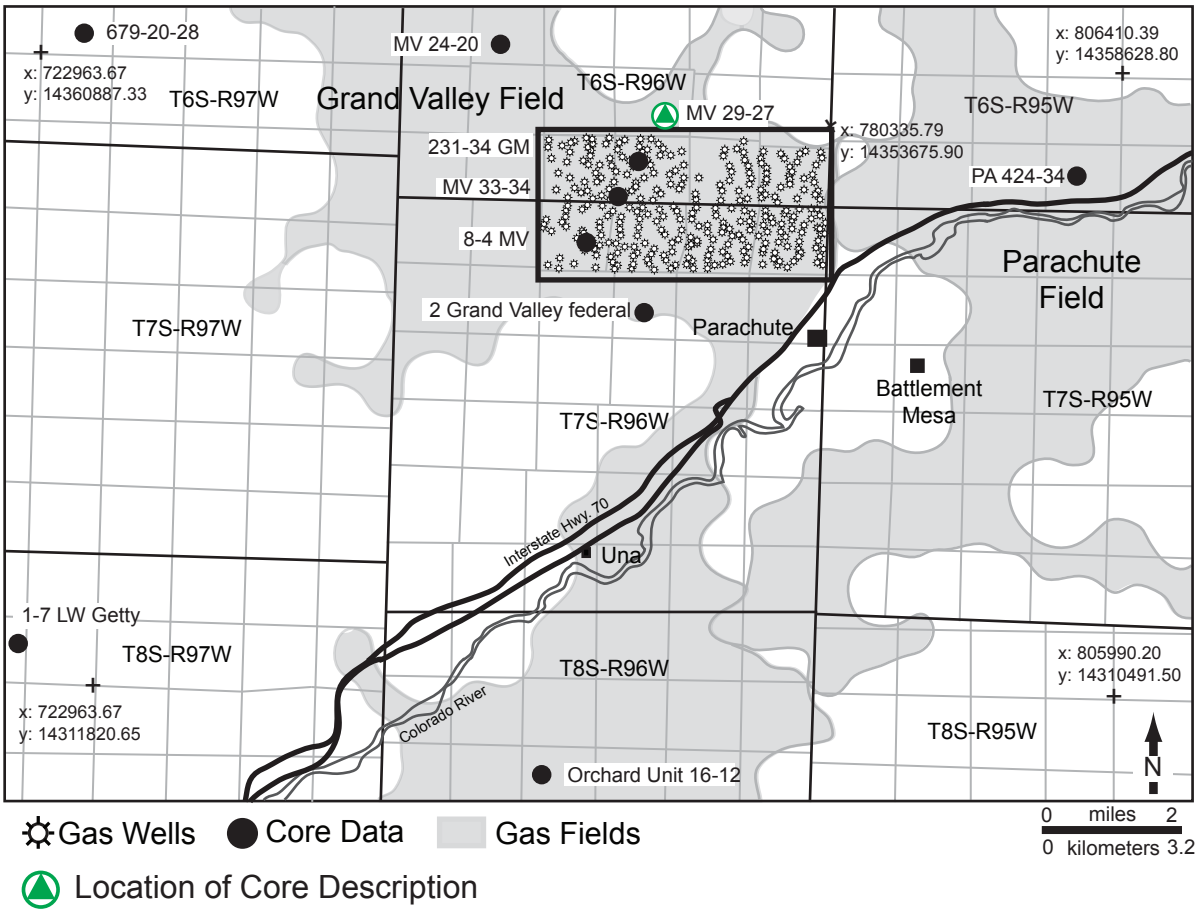

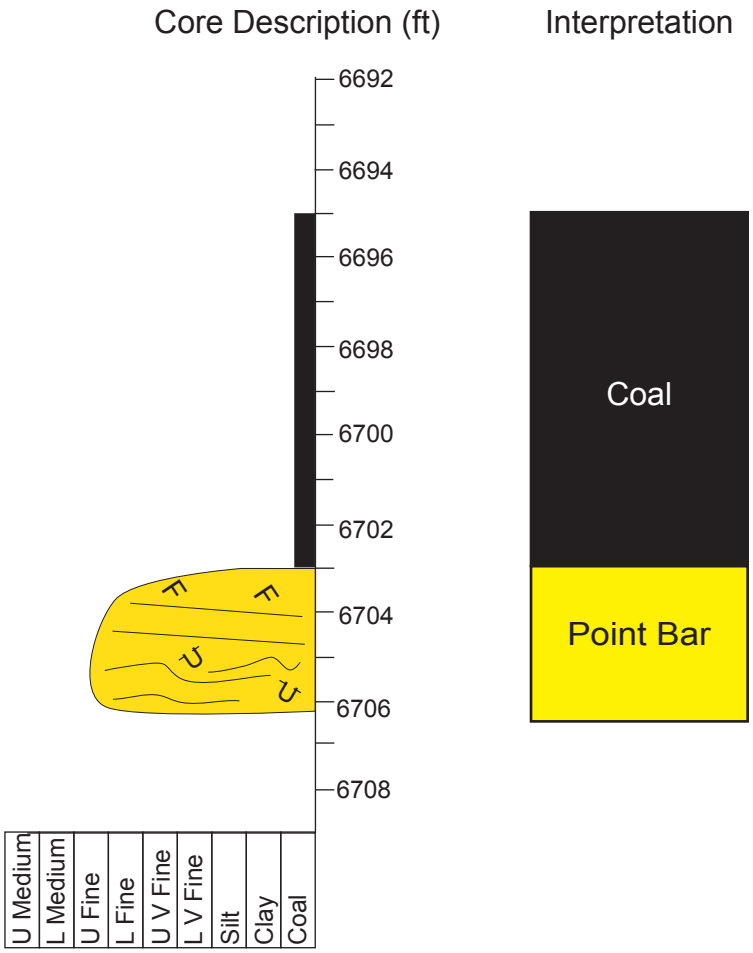
Core Description (ft)
Interpretation
6692
6694
6696
6698
6700
6702
6704
6706
6708
F
F
U
U
Coal
Point Bar
U Medium
L Medium
U Fine
L Fine
U V Fine
L V Fine
Silt
Clay
Coal

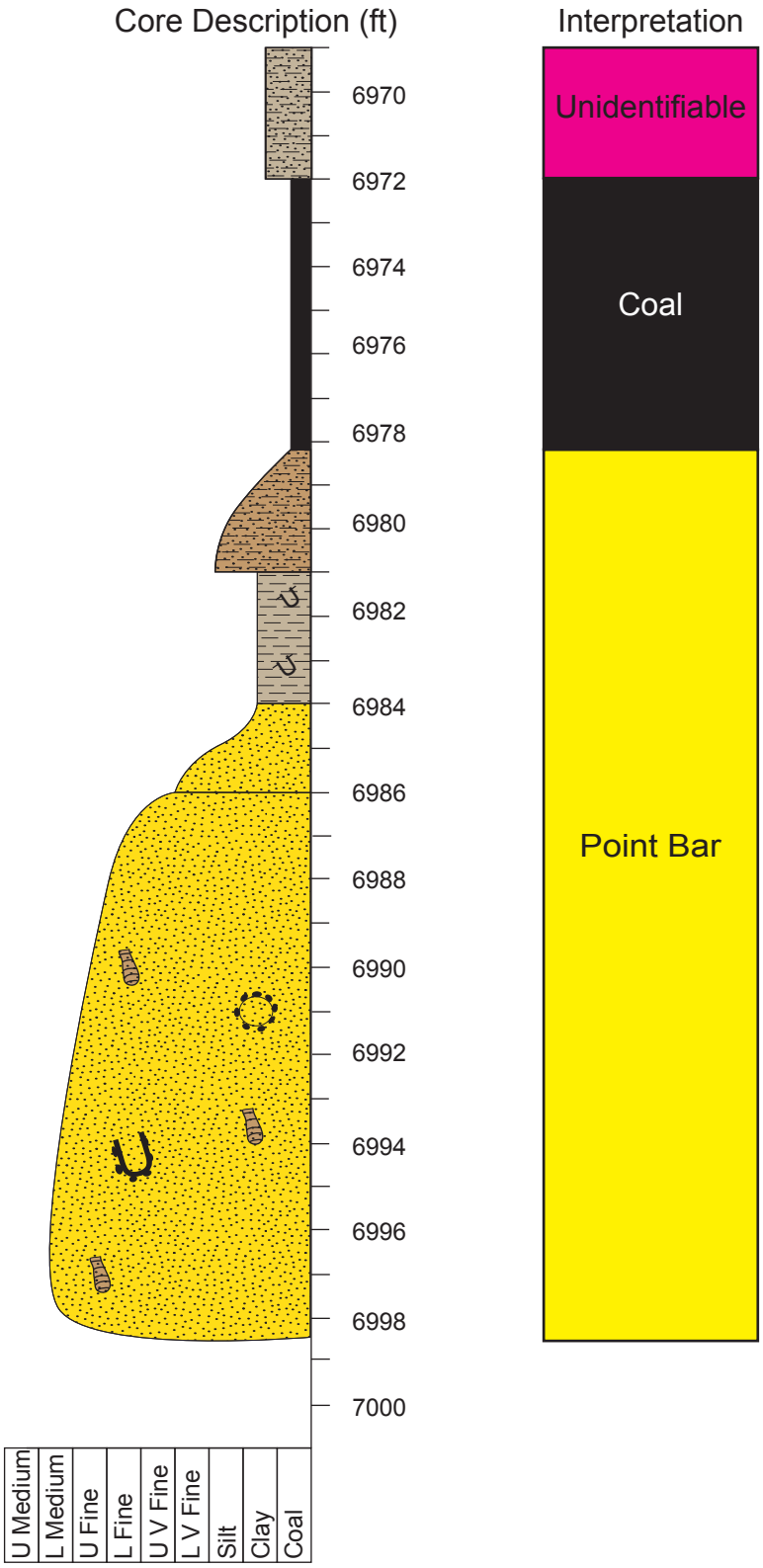
Core Description (ft)
Interpretation
6970
6972
6974
6976
6978
6980
6982
6984
6986
6988
6990
6992
6994
6996
6998
7000
Unidentifiable
Coal
Point Bar
U Medium
L Medium
U Fine
L Fine
U V Fine
L V Fine
Silt
Clay
Coal

MV 33-34 Core Description

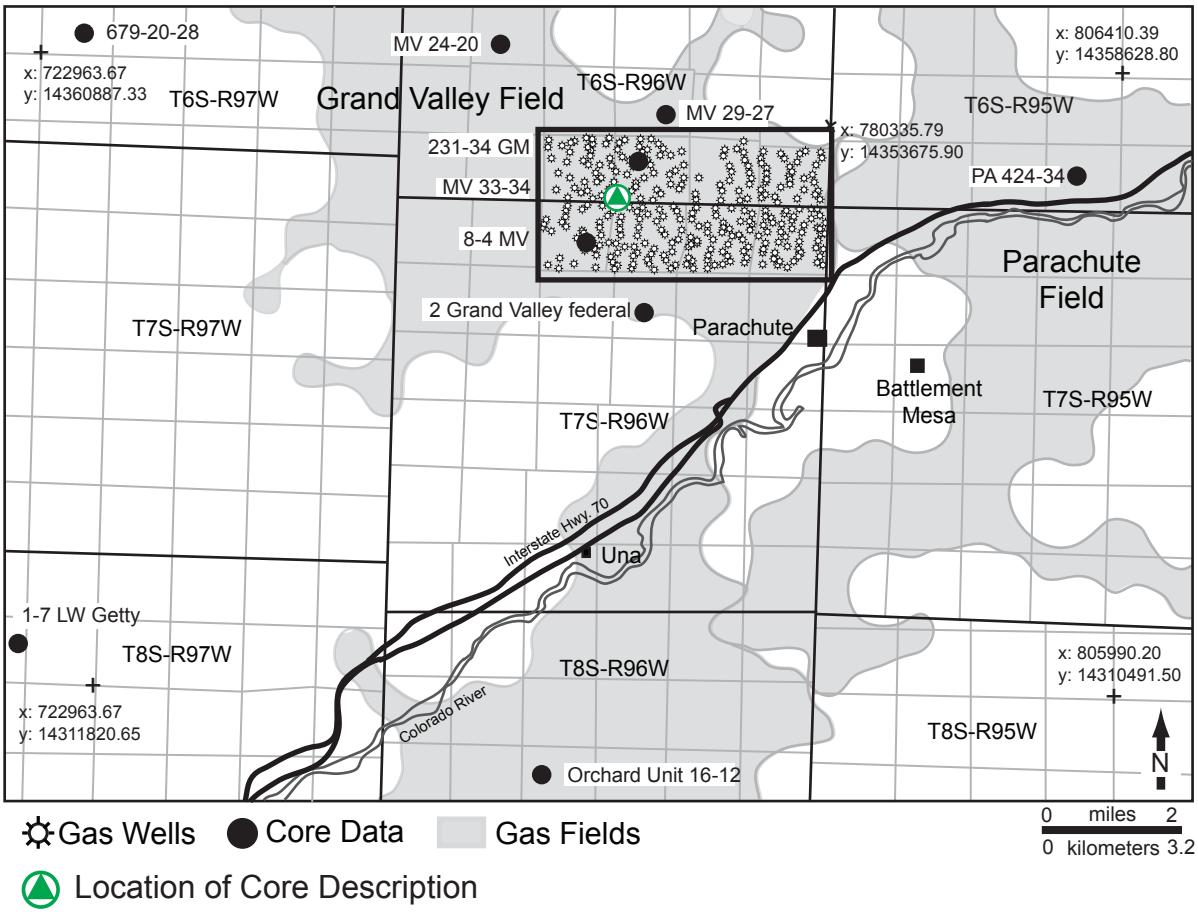

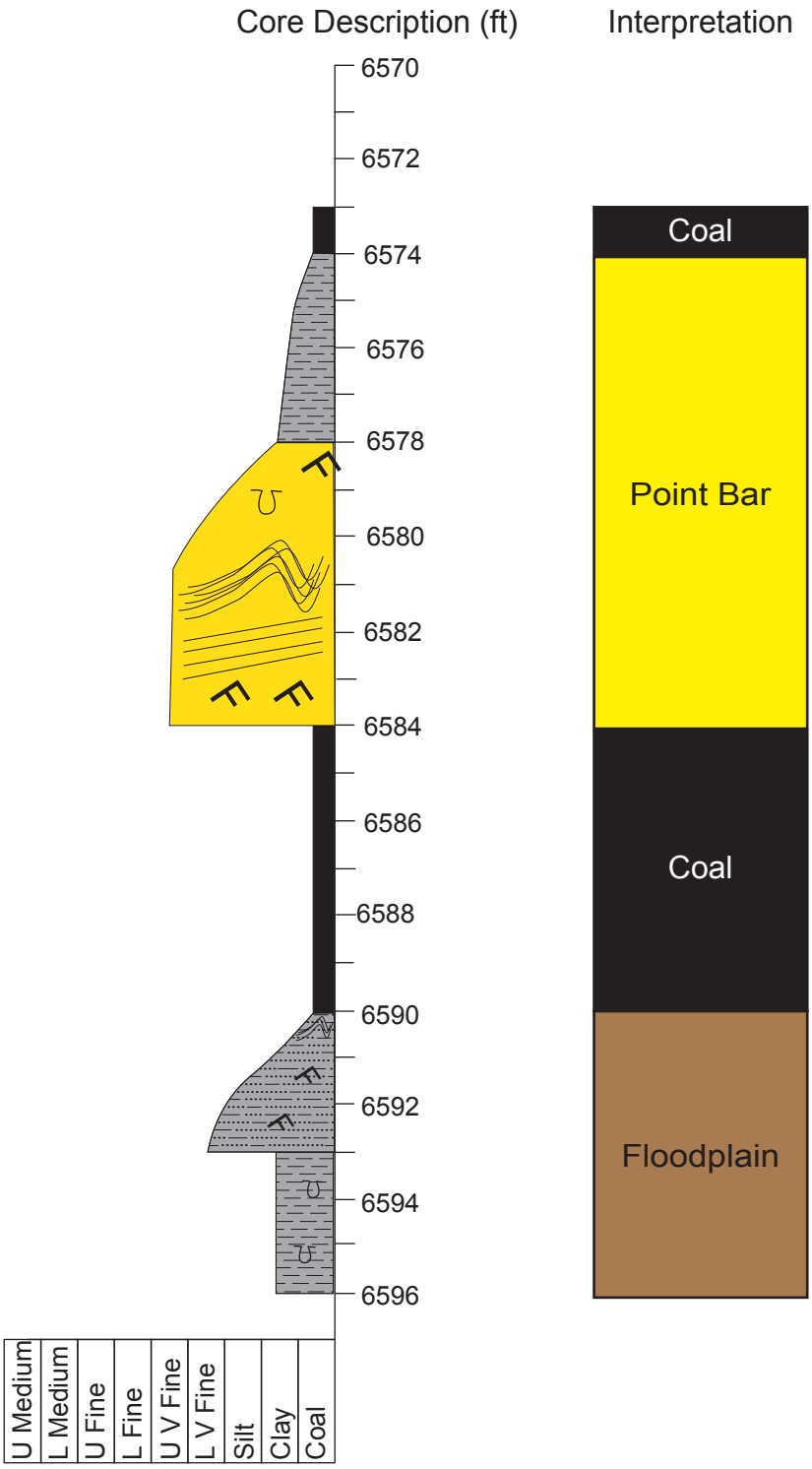
Core Description (ft)
Interpretation
6570
6572
6574
6576
6578
6580
6582
6584
6586
6588
6590
6592
6594
6596
U
F
F
F
F
F
P
P
Coal
Point Bar
Coal
Floodplain
U Medium
L Medium
U Fine
L Fine
U V Fine
L V Fine
Silt
Clay
Coal

Orchard Unit 16-12 Core Description

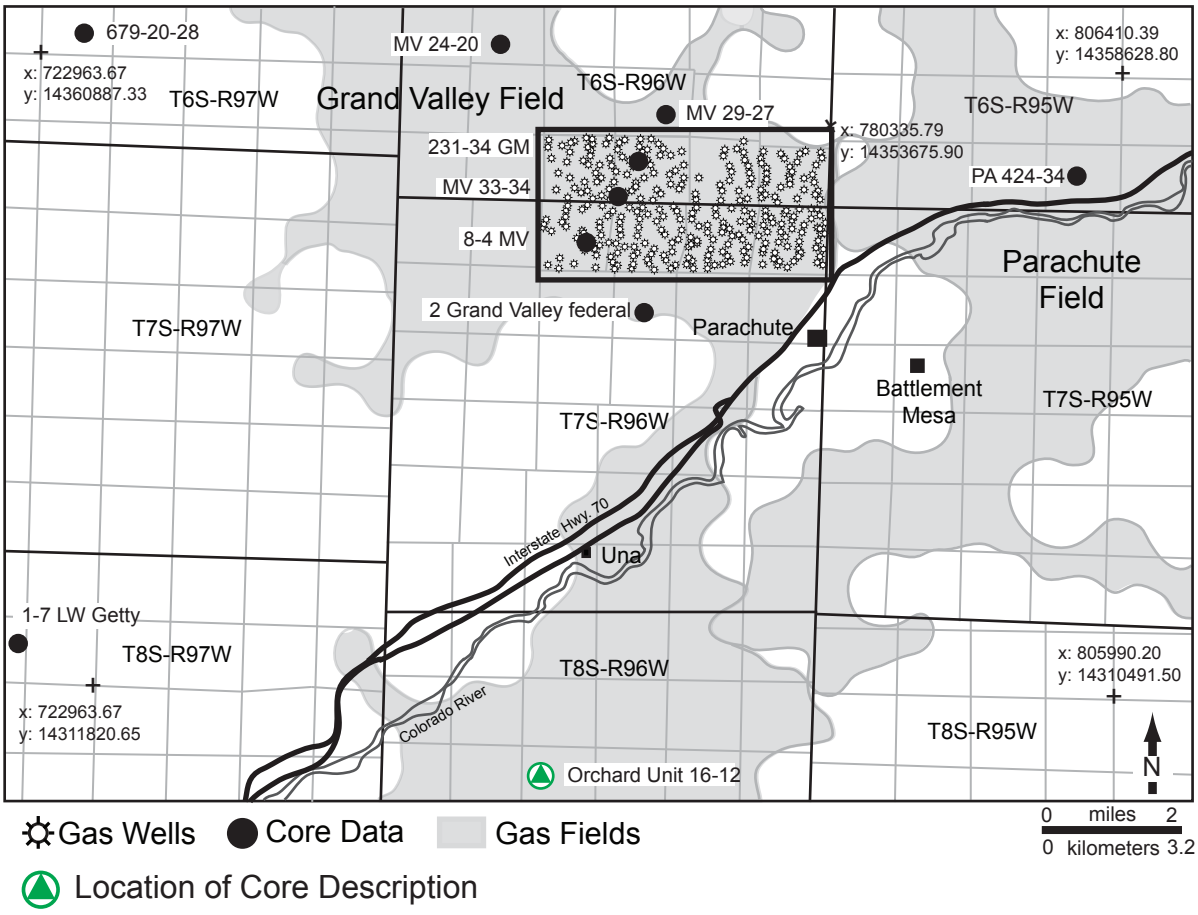

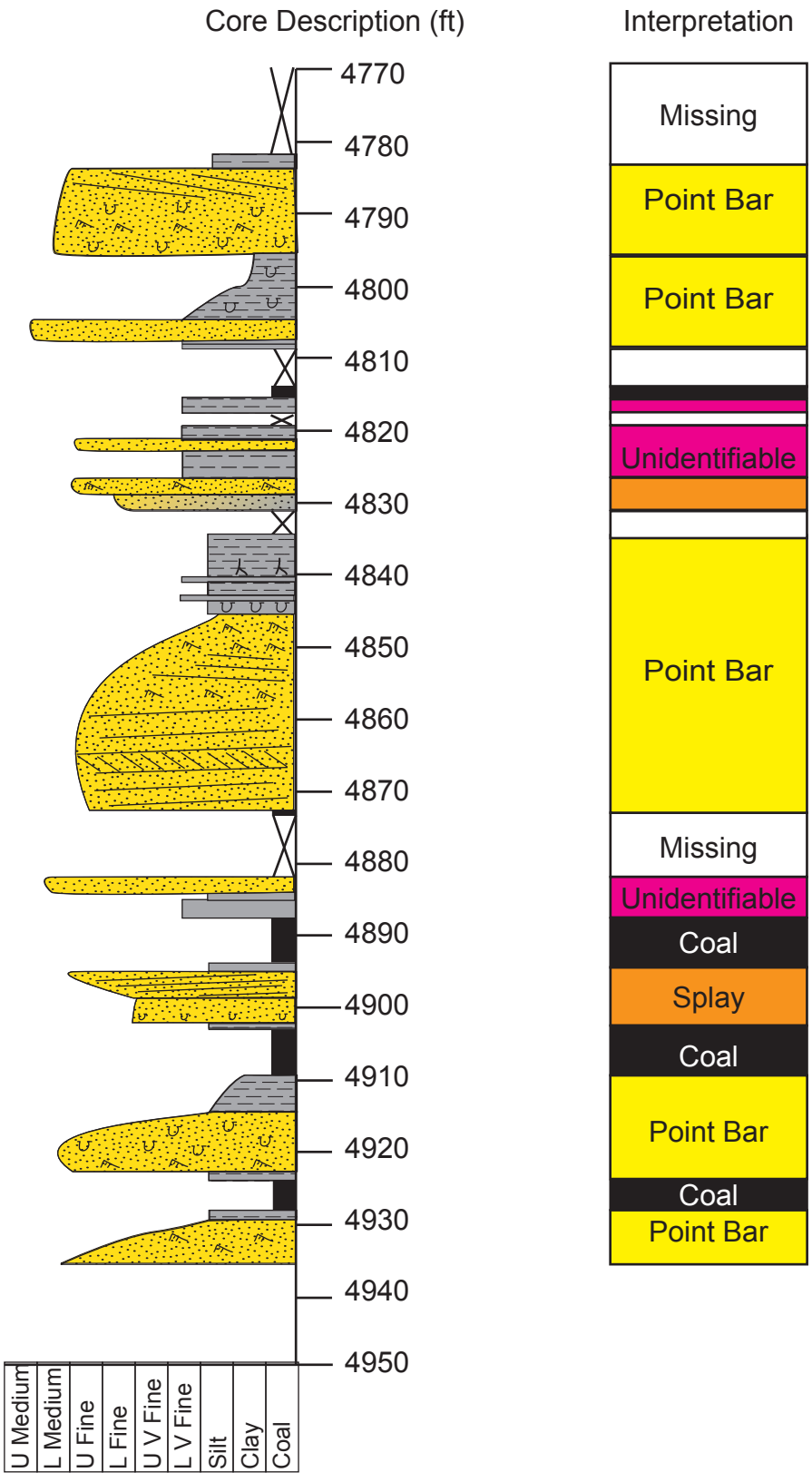
Core Description (ft)
Interpretation
4770
4780
4790
4800
4810
4820
4830
4840
4850
4860
4870
4880
4890
4900
4910
4920
4930
4940
4950
Missing
Point Bar
Point Bar
Unidentifiable
Point Bar
Missing
Unidentifiable
Coal
Splay
Coal
Point Bar
Coal
Point Bar
U Medium
L Medium
U Fine
L Fine
U V Fine
L V Fine
Silt
Clay
Coal

PA 424-34 Core Description

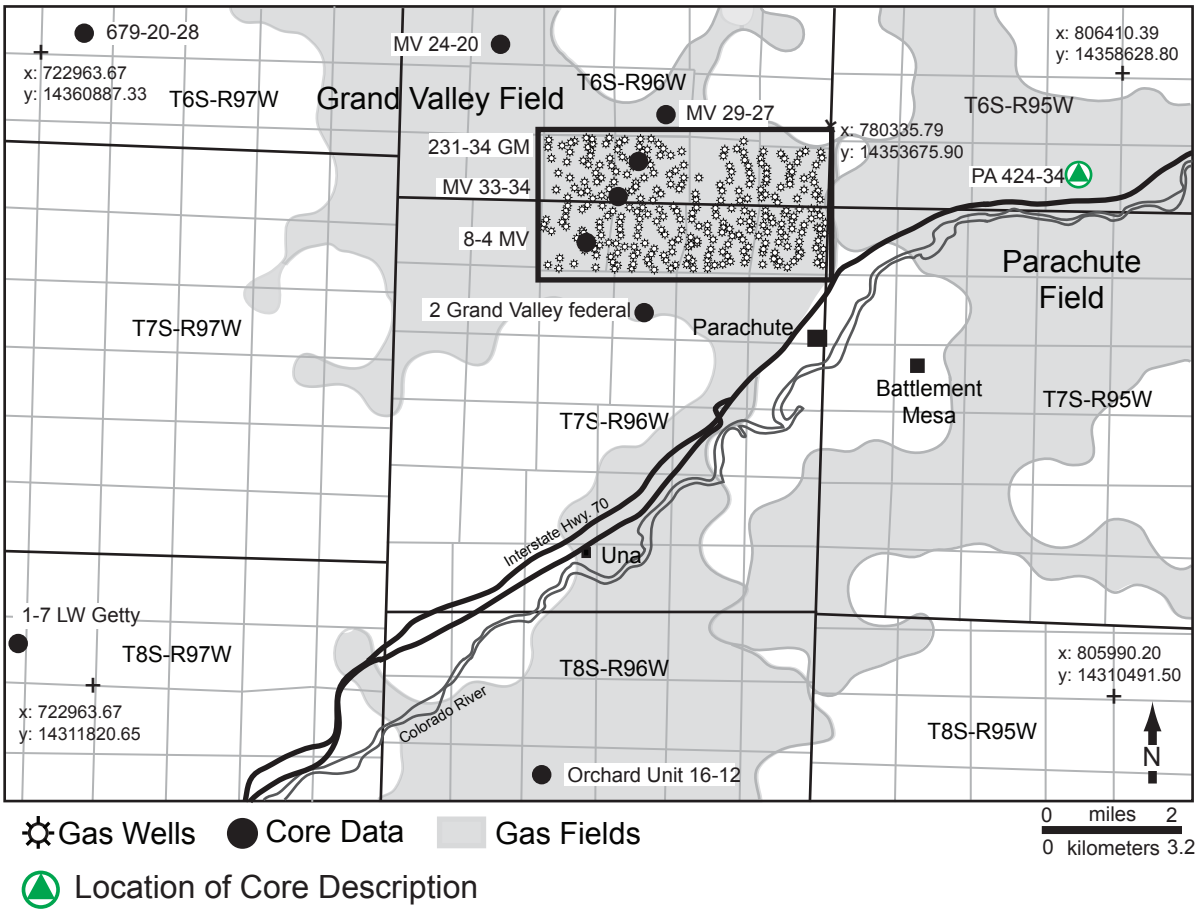

Core Description (ft) Interpretation

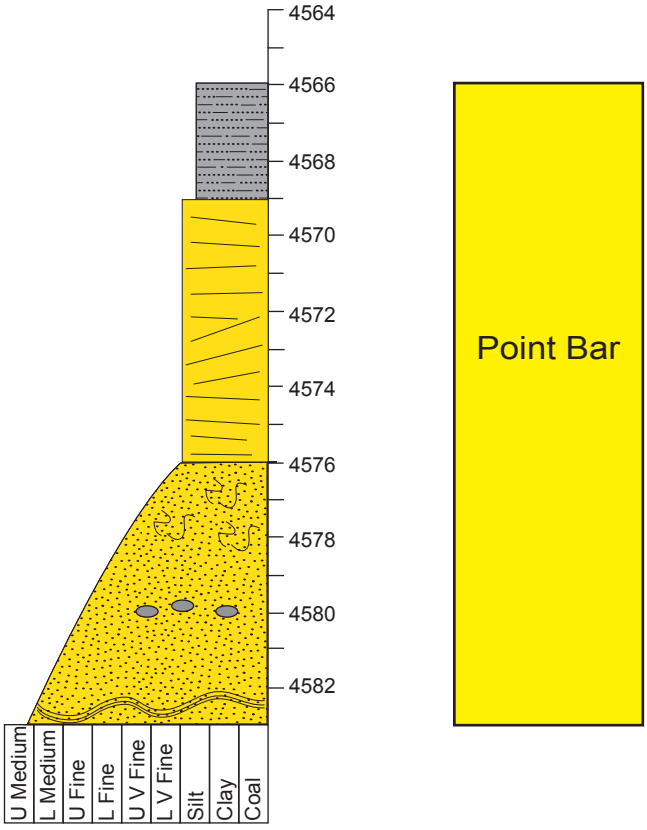

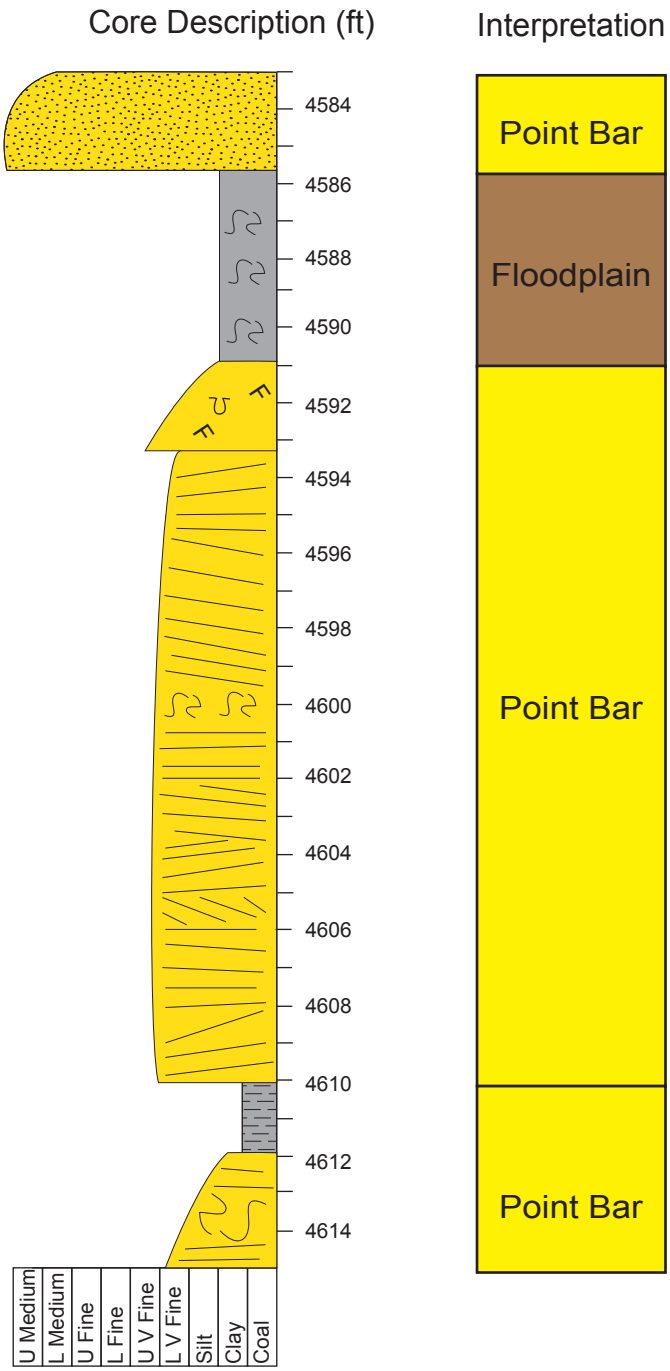
Core Description (ft)
Interpretation
4584
4586
4588
4590
4592
4594
4596
4598
4600
4602
4604
4606
4608
4610
4612
4614
Point Bar
Floodplain
Point Bar
Point Bar
U Medium
L Medium
U Fine
L Fine
U V Fine
L V Fine
Silt
Clay
Coal

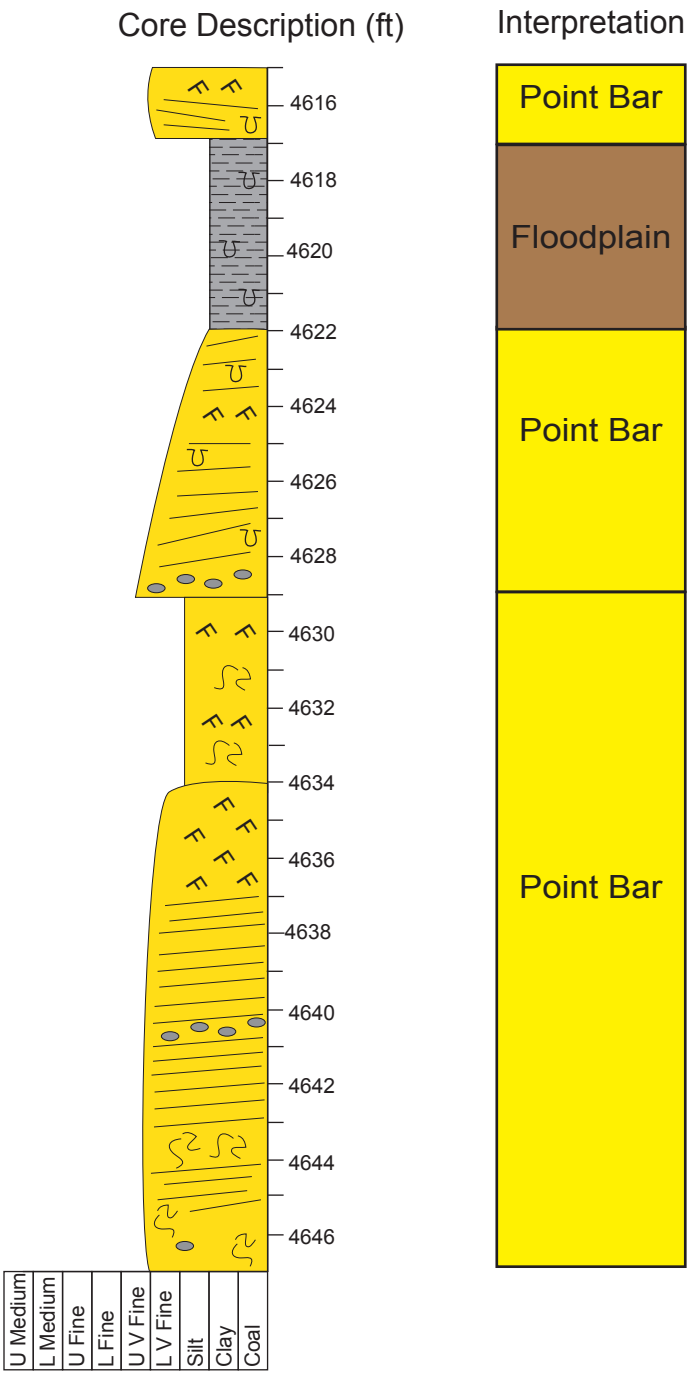
Core Description (ft)
Interpretation
4616
4618
4620
4622
4624
4626
4628
4630
4632
4634
4636
4638
4640
4642
4644
4646
Point Bar
Floodplain
Point Bar
Point Bar
U Medium
L Medium
U Fine
L Fine
U V Fine
L V Fine
Silt
Clay
Coal

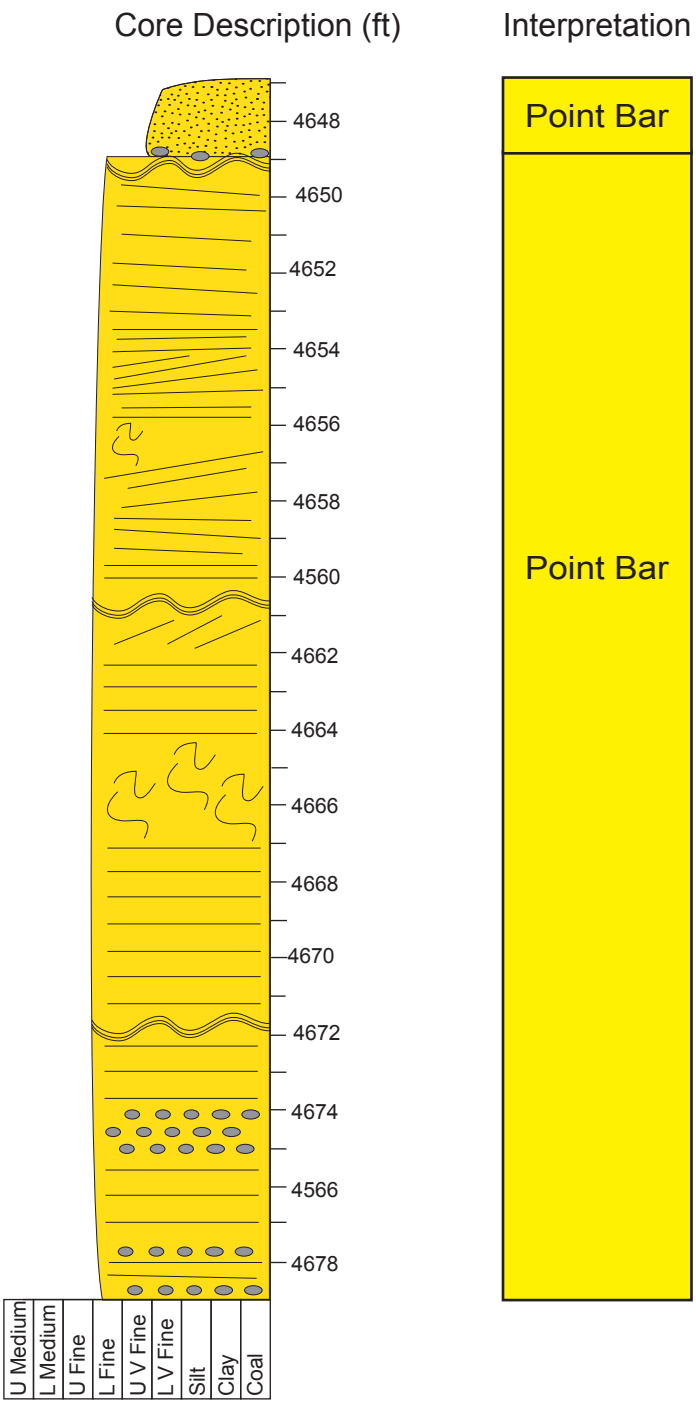
Core Description (ft)
Interpretation
4648
4650
4652
4654
4656
4658
4560
4662
4664
4666
4668
4670
4672
4674
4566
4678
U Medium
L Medium
U Fine
L Fine
U V Fine
L V Fine
Silt
Clay
Coal
Point Bar
Point Bar

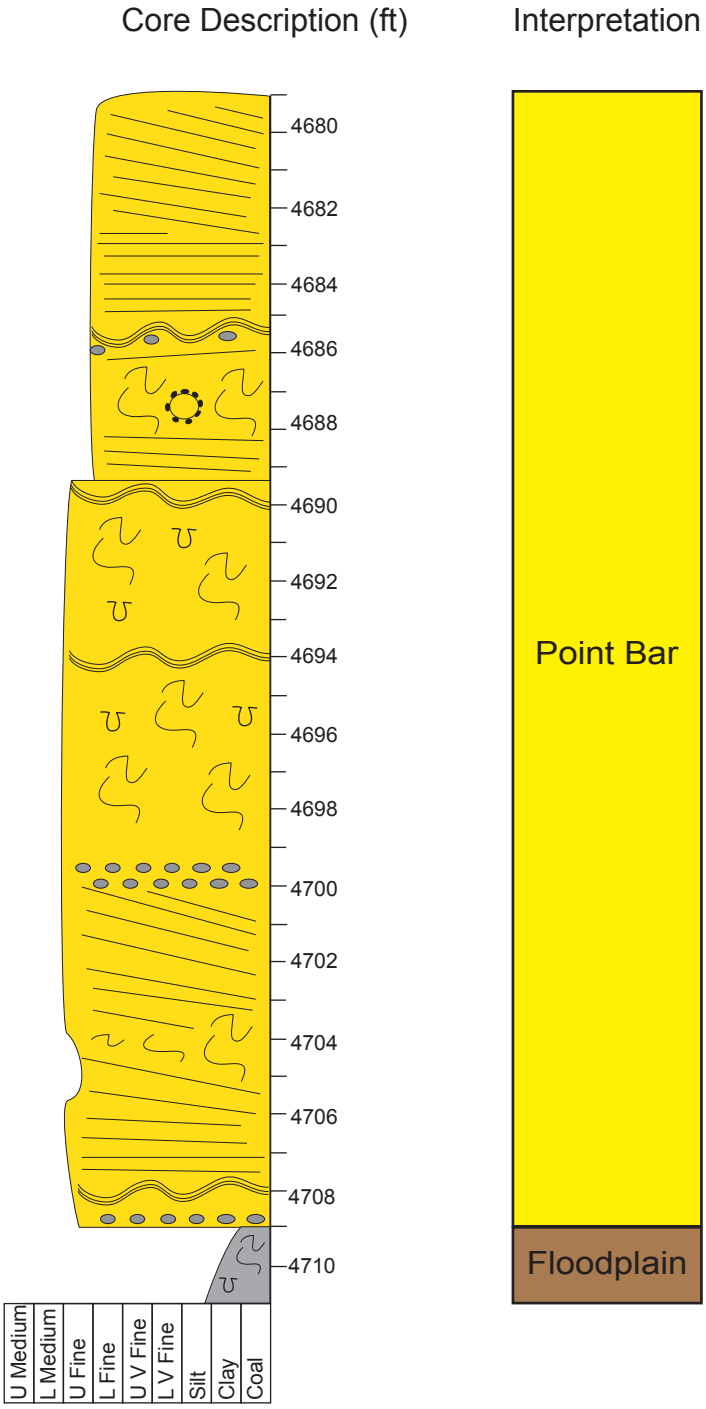
Core Description (ft)
Interpretation
4680
4682
4684
4686
4688
4690
4692
4694
4696
4698
4700
4702
4704
4706
4708
4710
Point Bar
Floodplain
U Medium
L Medium
U Fine
L Fine
U V Fine
L V Fine
Silt
Clay
Coal

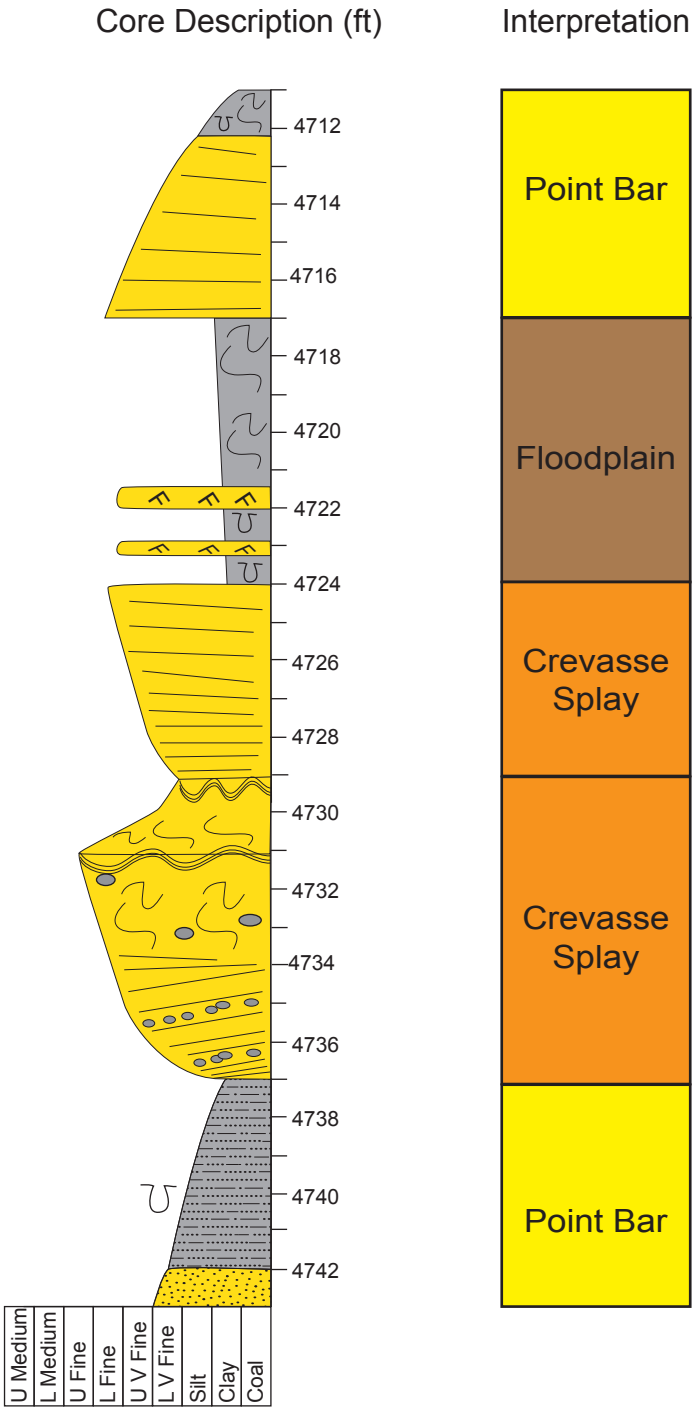
Core Description (ft)
Interpretation
4712
4714
4716
4718
4720
4722
4724
4726
4728
4730
4732
4734
4736
4738
4740
4742
Point Bar
Floodplain
Crevasse Splay
Crevasse Splay
Point Bar
U Medium
L Medium
U Fine
L Fine
U V Fine
L V Fine
Silt
Clay
Coal

Core Description (ft)

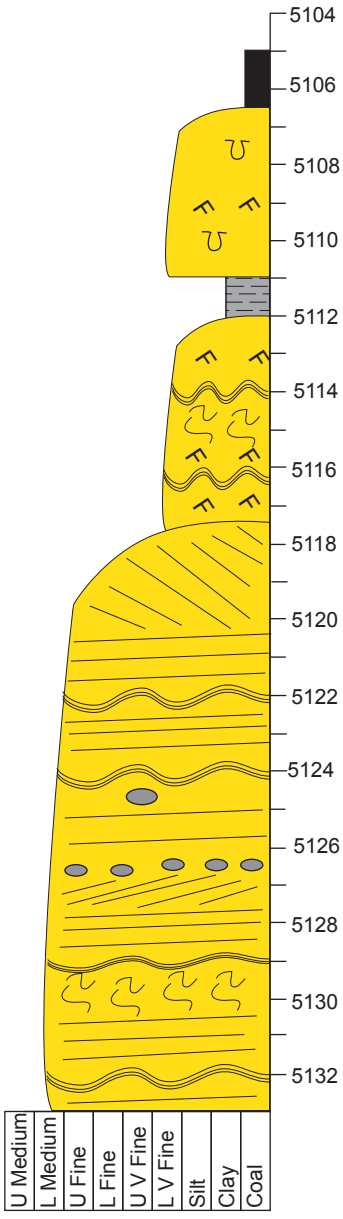

Interpretation

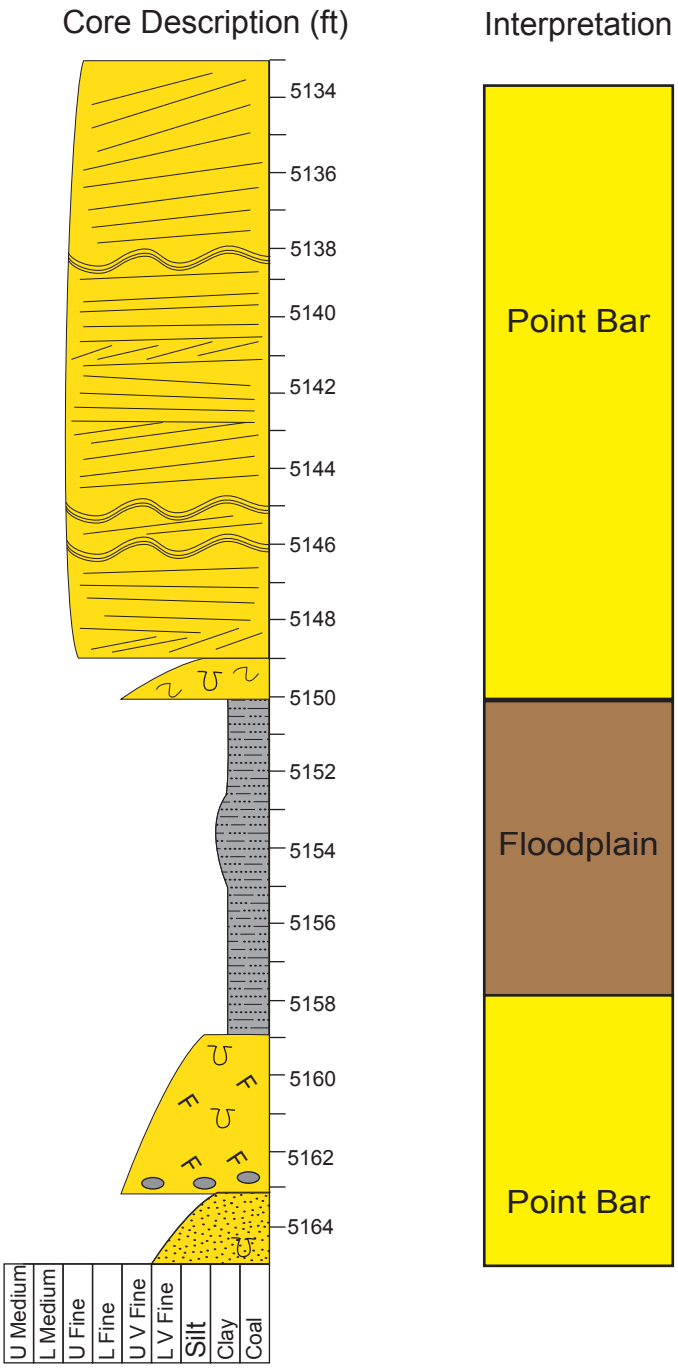
Core Description (ft)
Interpretation
5134
5136
5138
5140
5142
5144
5146
5148
5150
5152
5154
5156
5158
5160
5162
5164
Point Bar
Floodplain
Point Bar
U Medium
L Medium
U Fine
L Fine
U V Fine
L V Fine
Silt
Clay
Coal

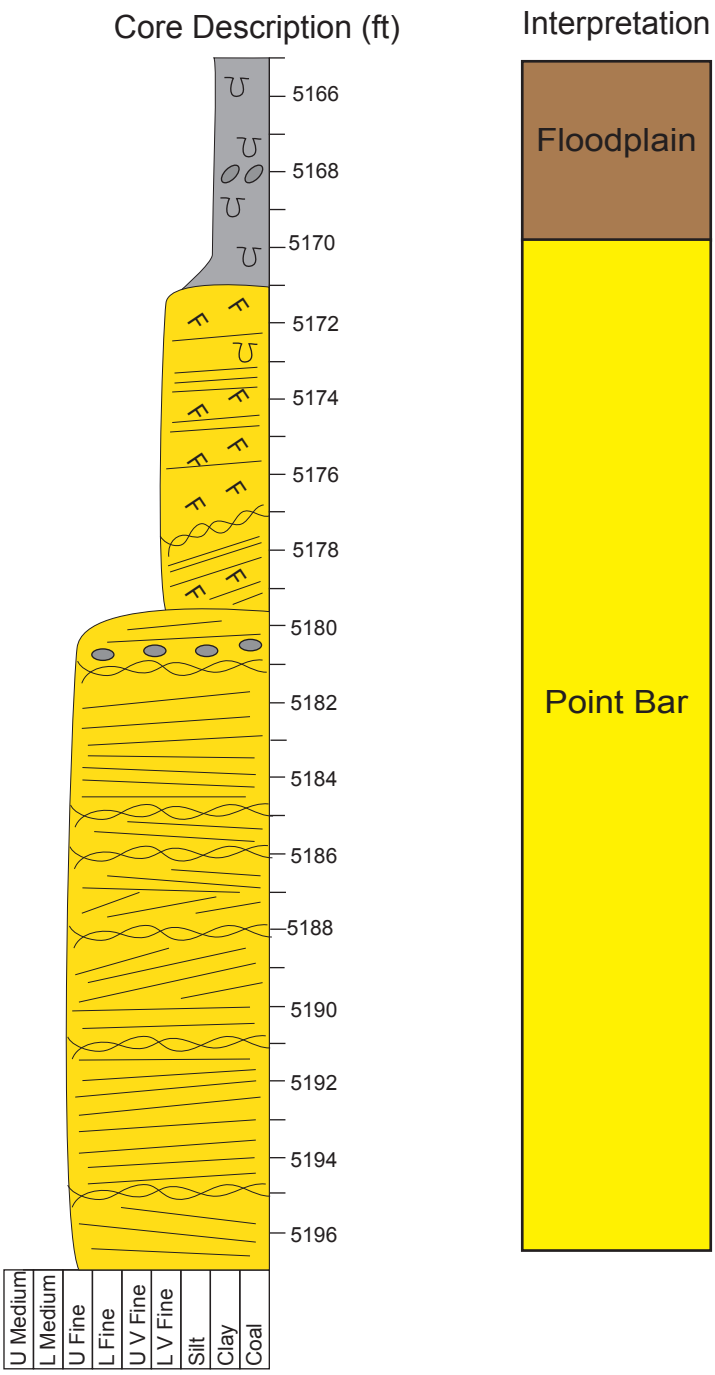
Core Description (ft)
Interpretation
5166
5168
5170
5172
5174
5176
5178
5180
5182
5184
5186
5188
5190
5192
5194
5196
Floodplain
Point Bar
U Medium
L Medium
U Fine
L Fine
U V Fine
L V Fine
Silt
Clay
Coal

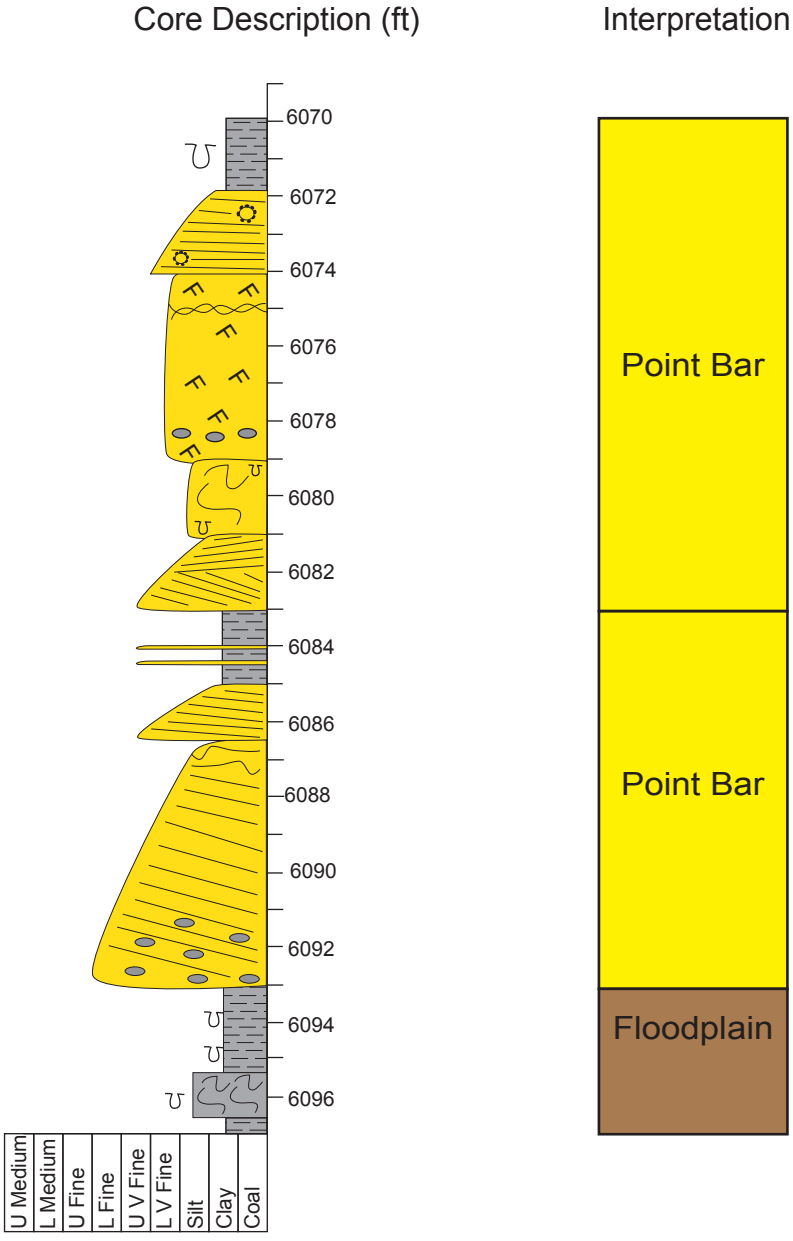
Core Description (ft)
Interpretation
6070
6072
6074
6076
6078
6080
6082
6084
6086
6088
6090
6092
6094
6096
Point Bar
Point Bar
Floodplain
U Medium
L Medium
U Fine
L Fine
U V Fine
L V Fine
Silt
Clay
Coal

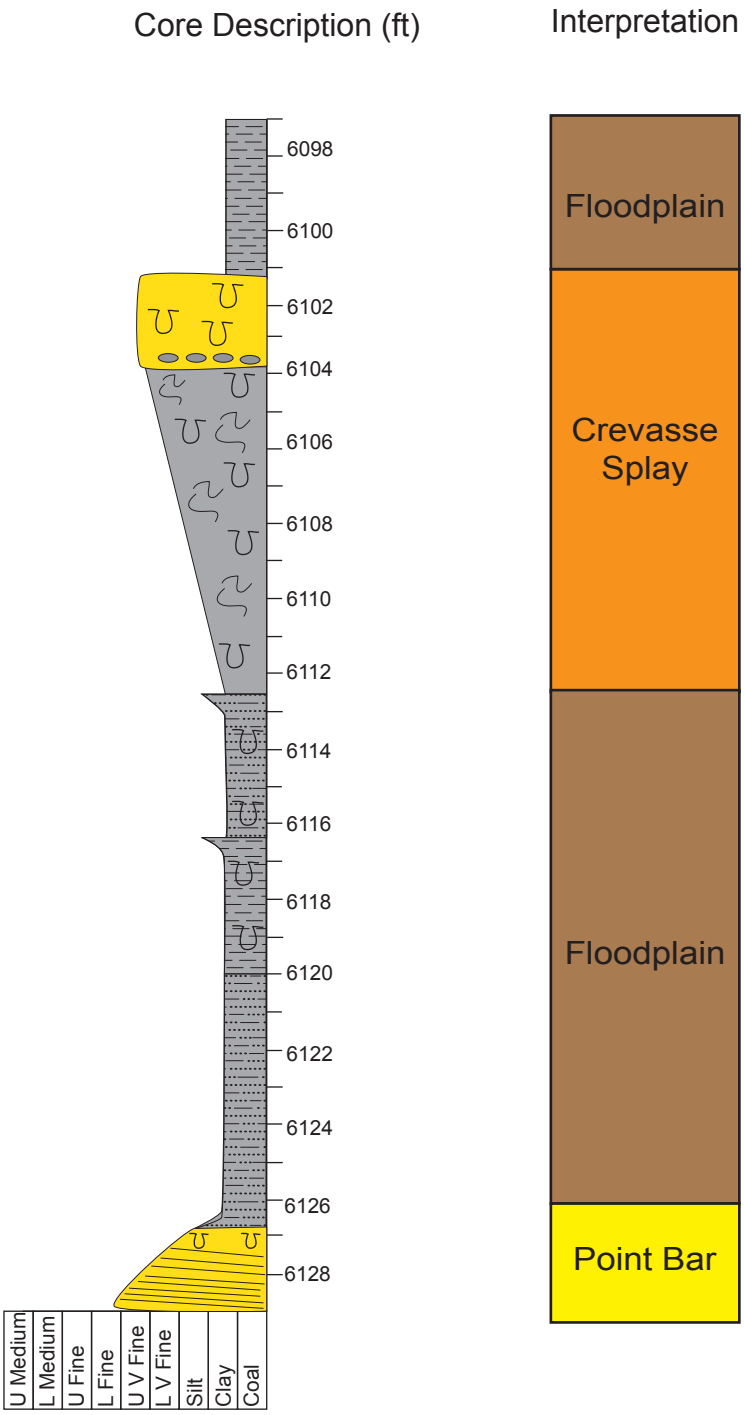
Core Description (ft)
Interpretation
6098
6100
6102
6104
6106
6108
6110
6112
6114
6116
6118
6120
6122
6124
6126
6128
U Medium
L Medium
U Fine
L Fine
U V Fine
L V Fine
Silt
Clay
Coal
Floodplain
Crevasse Splay
Floodplain
Point Bar

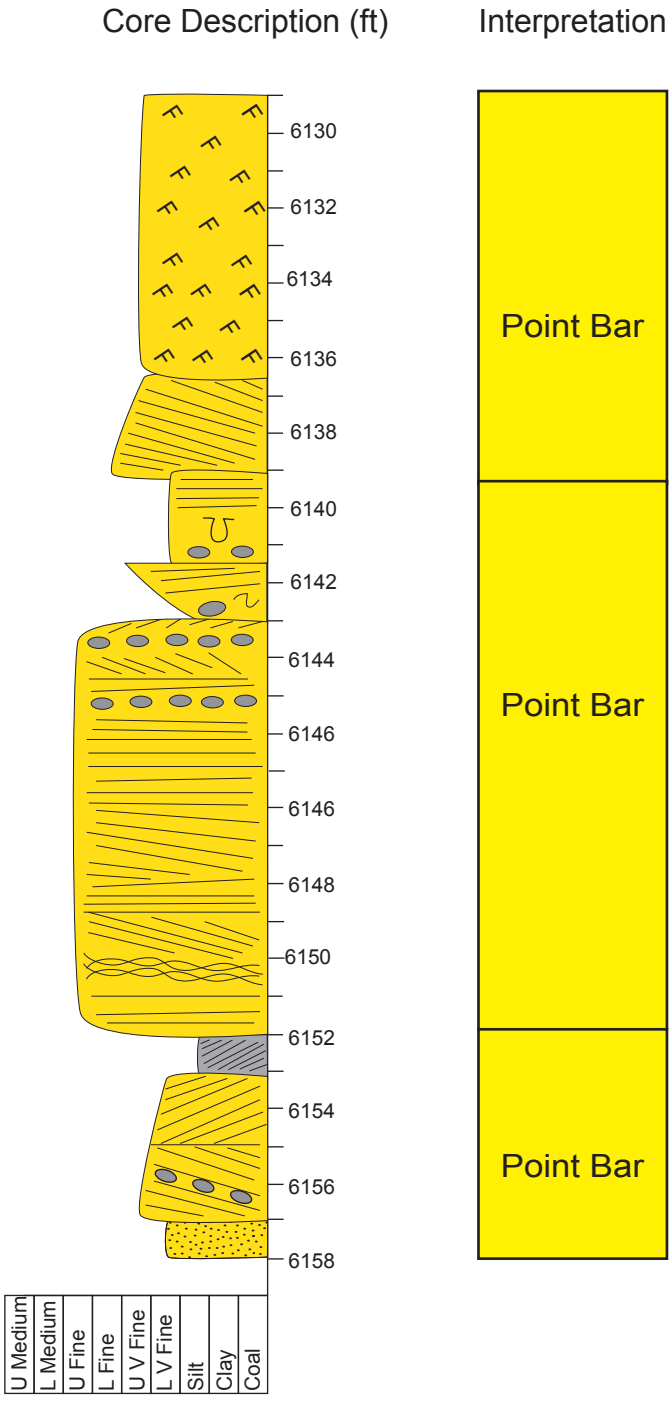
Core Description (ft)
Interpretation
6130
6132
6134
6136
6138
6140
6142
6144
6146
6146
6148
6150
6152
6154
6156
6158
Point Bar
Point Bar
Point Bar
U Medium
L Medium
U Fine
L Fine
U V Fine
L V Fine
Silt
Clay
Coal

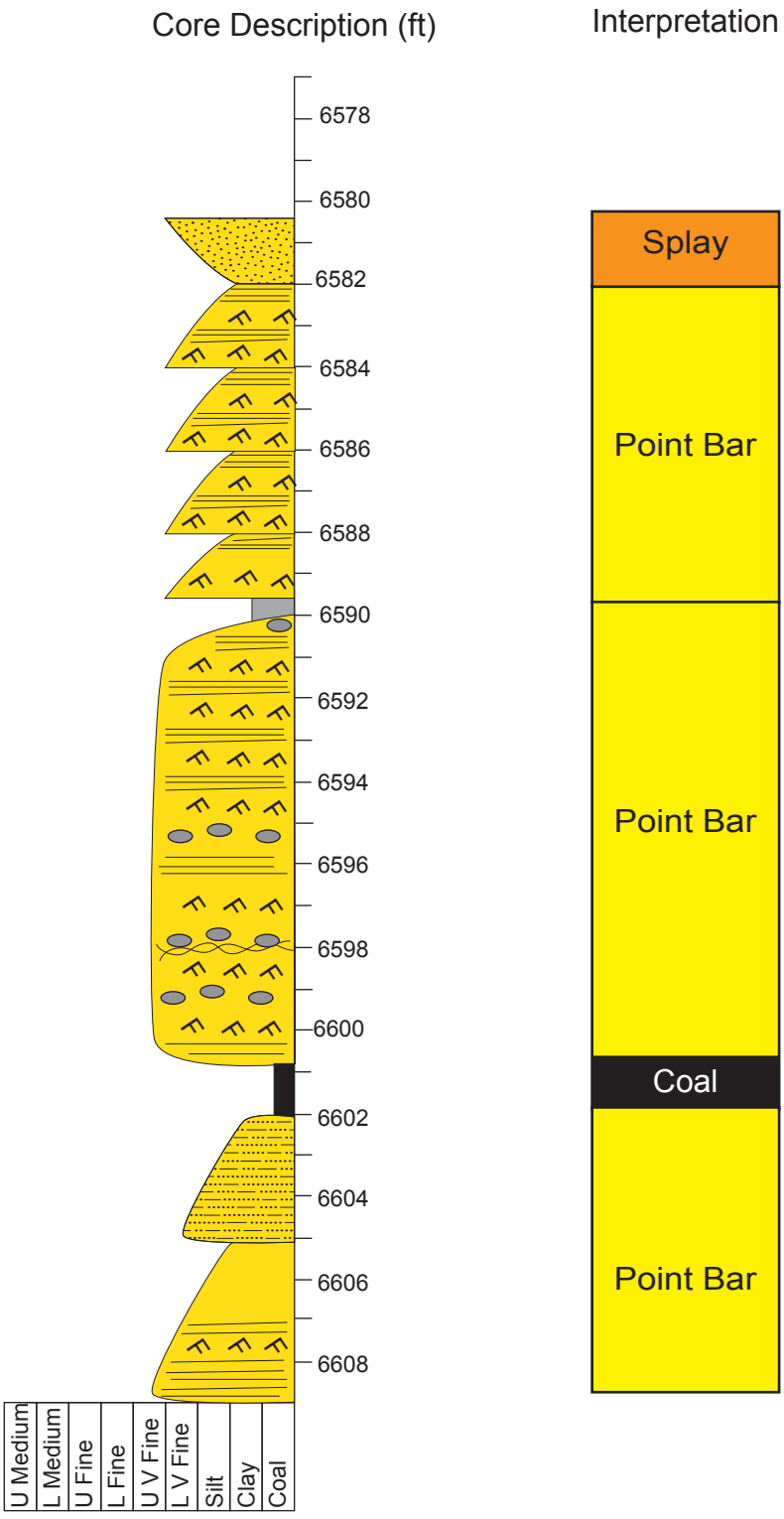
Core Description (ft)
Interpretation
6578
6580
6582
6584
6586
6588
6590
6592
6594
6596
6598
6600
6602
6604
6606
6608
U Medium
L Medium
U Fine
L Fine
U V Fine
L V Fine
Silt
Clay
Coal
Splay
Point Bar
Point Bar
Coal
Point Bar

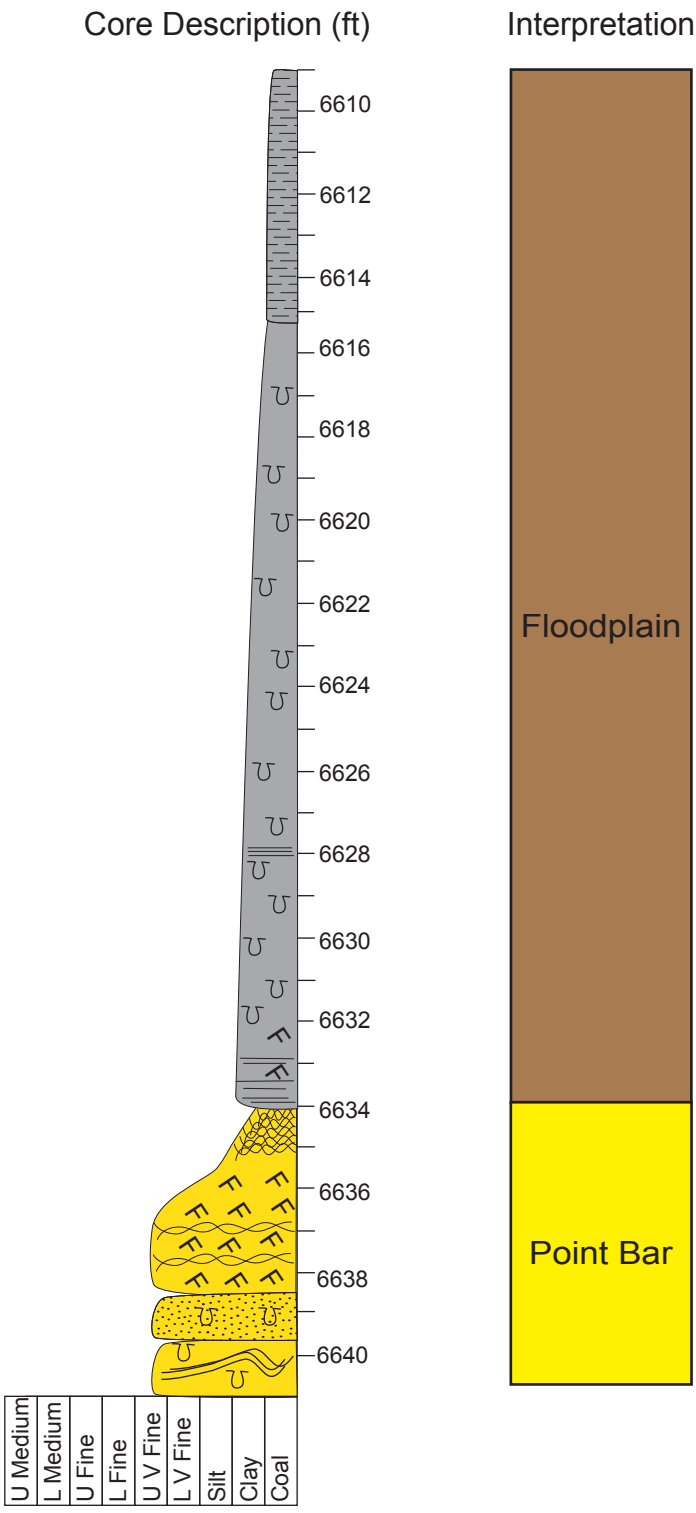
Core Description (ft)
Interpretation
6610
6612
6614
6616
6618
6620
6622
6624
6626
6628
6630
6632
6634
6636
6638
6640
Floodplain
Point Bar
U Medium
L Medium
U Fine
L Fine
U V Fine
L V Fine
Silt
Clay
Coal

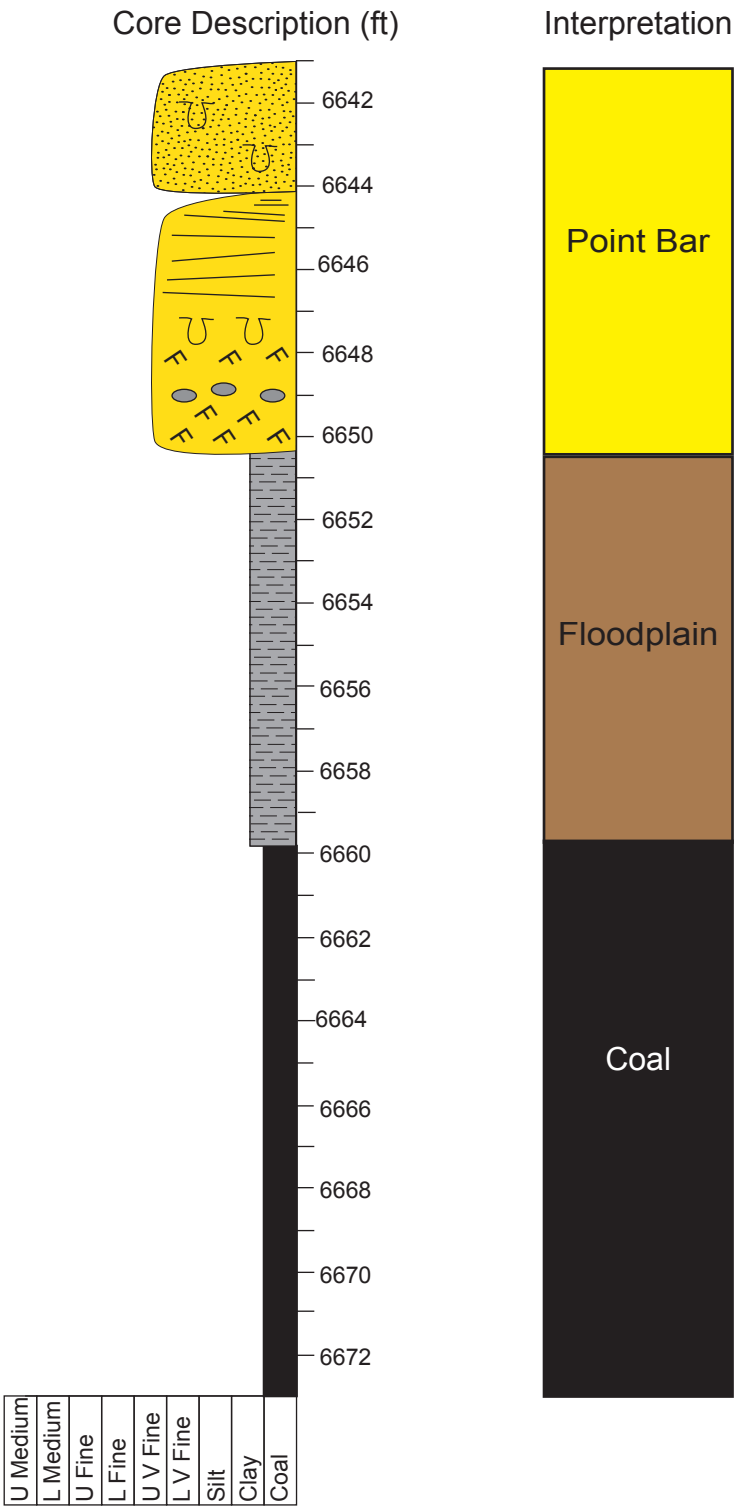
Core Description (ft)
Interpretation
6642
6644
6646
6648
6650
6652
6654
6656
6658
6660
6662
6664
6666
6668
6670
6672
Point Bar
Floodplain
Coal
U Medium
L Medium
U Fine
L Fine
U V Fine
L V Fine
Silt
Clay
Coal

Appendix E

Reservoir Maps

Appendix E shows maps created to evaluate the variability of sandstone-body deposits within the lower Williams Fork Formation at Grand Valley Field. The following maps were created: gross-interval isopach, sandstone percent, point-bar percent, and crevasse-splay percent.

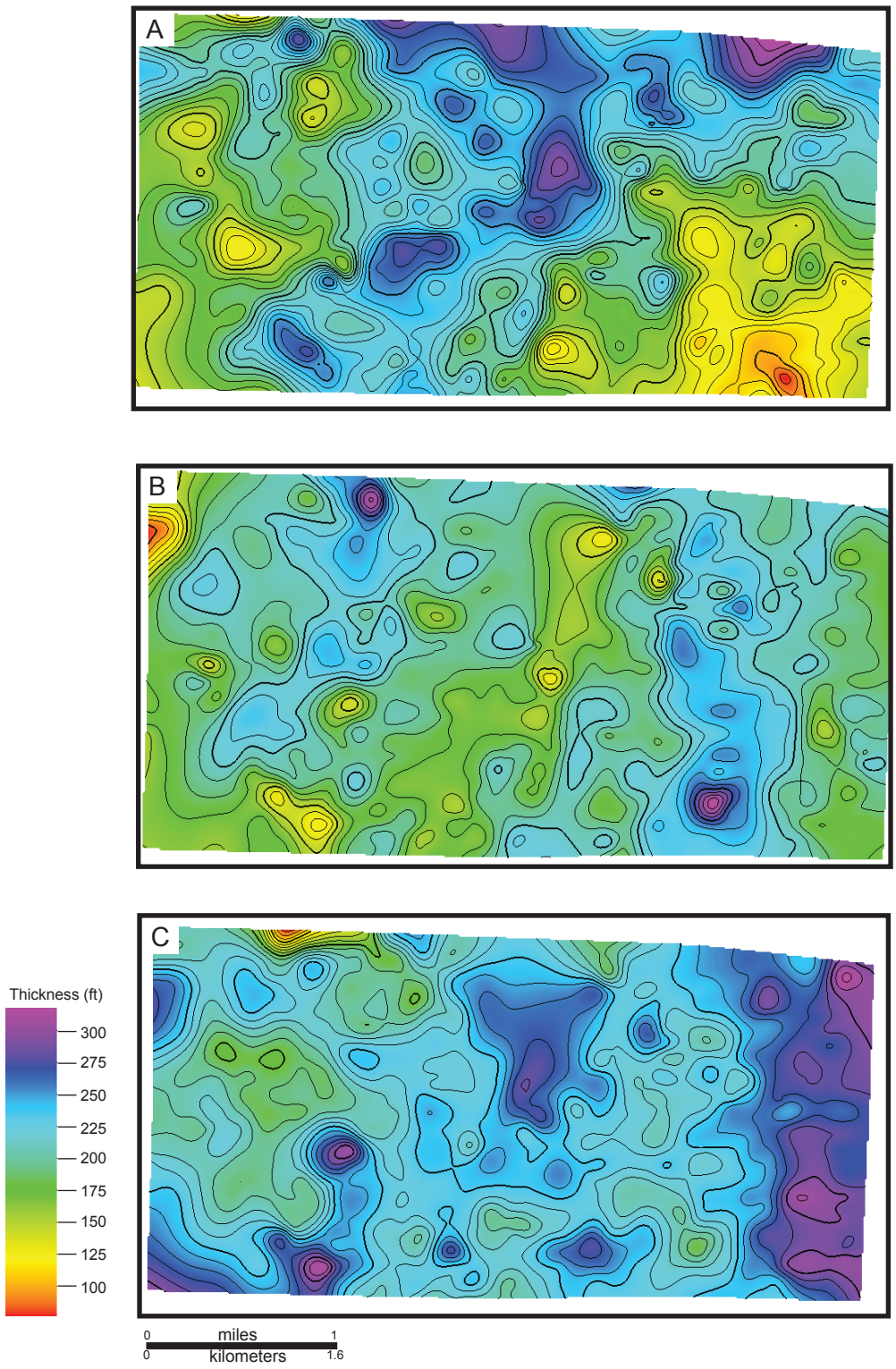

Gross-interval isopach of A) Top lower Williams Fork Formation to Coal Ridge (180 ft) . B) Coal Ridge to Regressive marker (344 ft). C) Regressive marker to Middle Sandstone (172 ft).

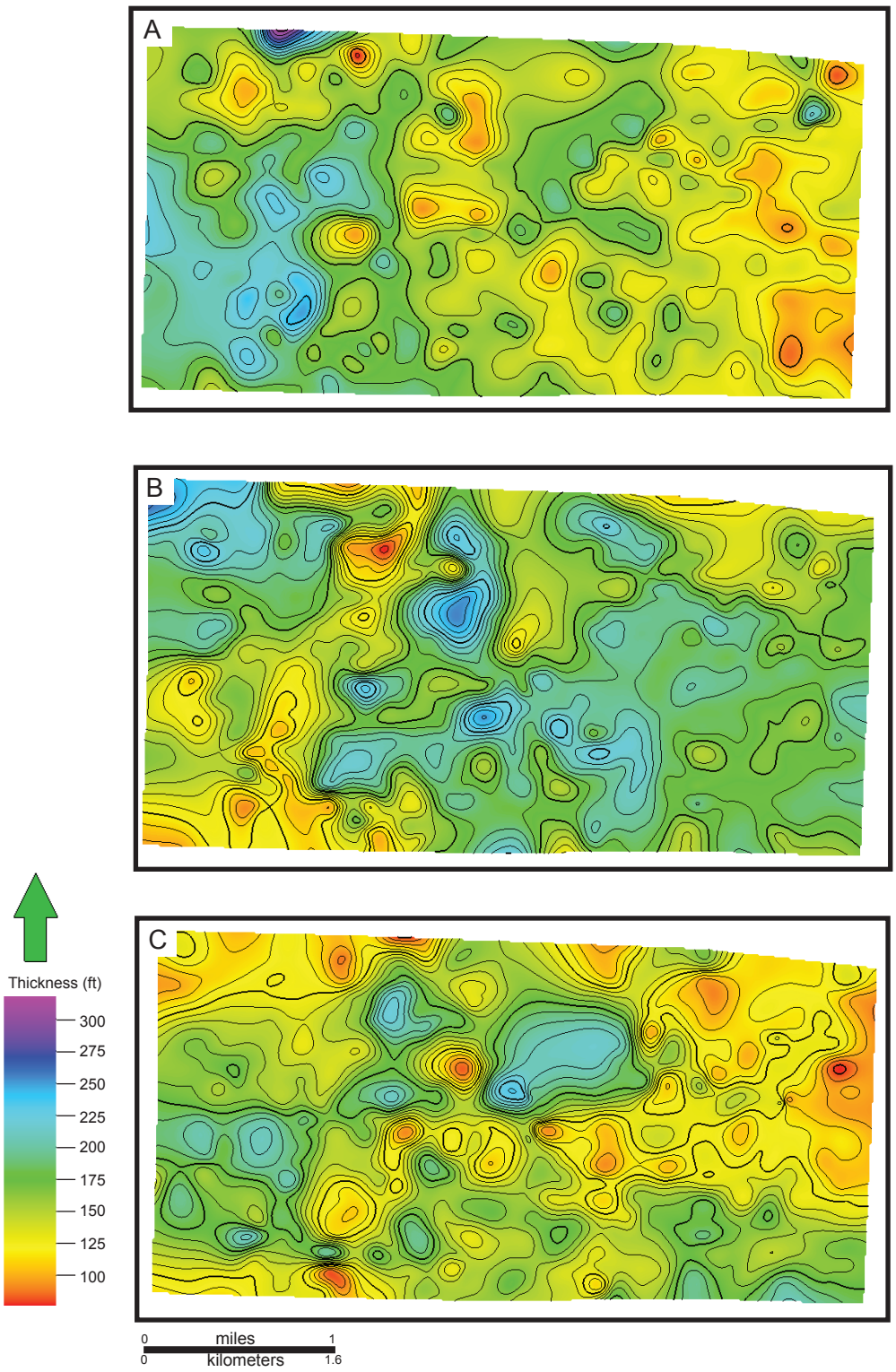

Gross-interval isopach of A) Middle Sandstone to FS Middle Sandstone (200 ft) . B) FS Middle Sandstone to Coal F (144 ft). C) Coal F to Coal E (128 ft).

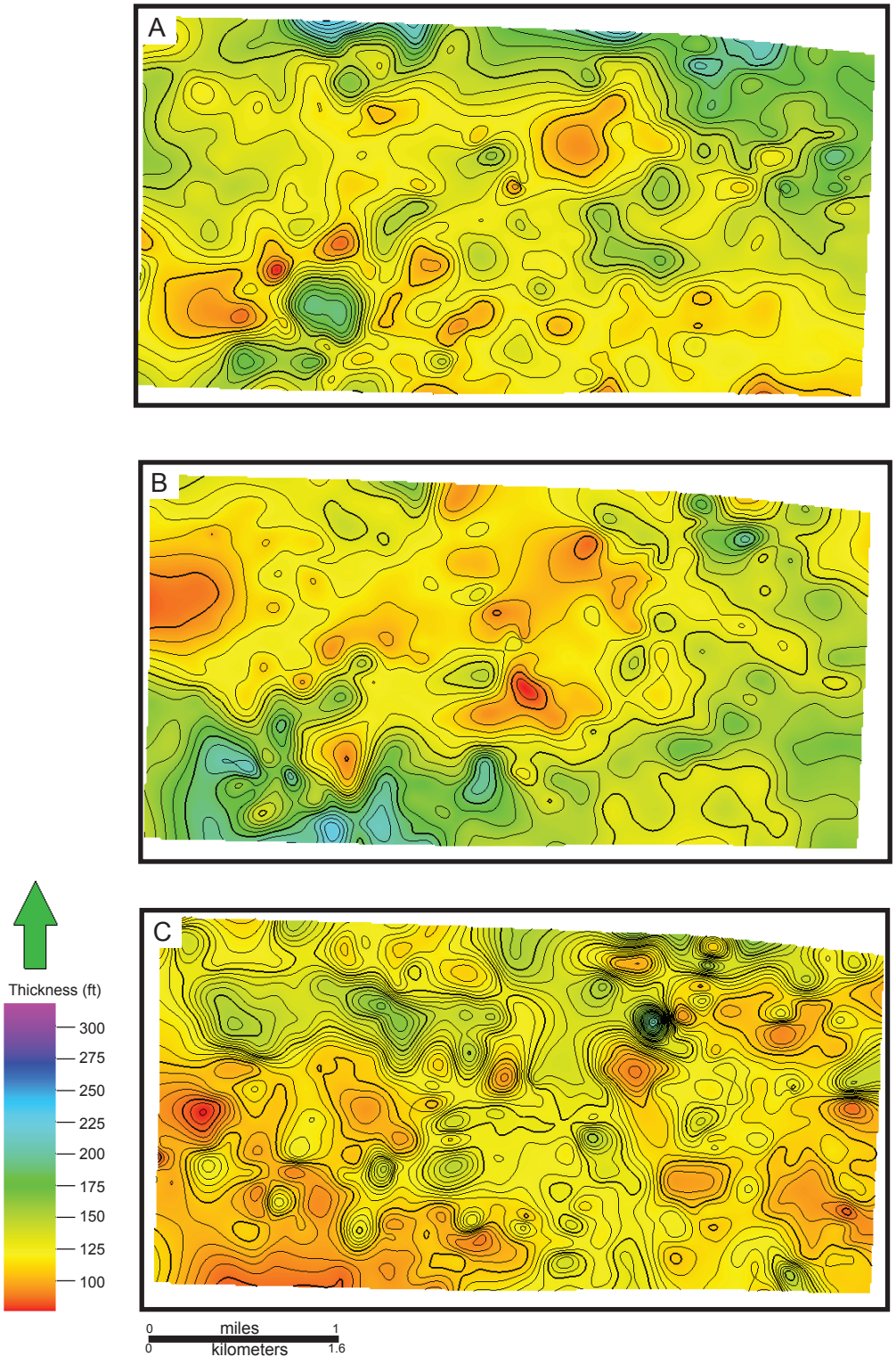

Gross-interval isopach of A) Coal E to Coal D (80 ft). B) Coal D to Coal B (72 ft). C) Coal B to Coal A5 (60 ft).

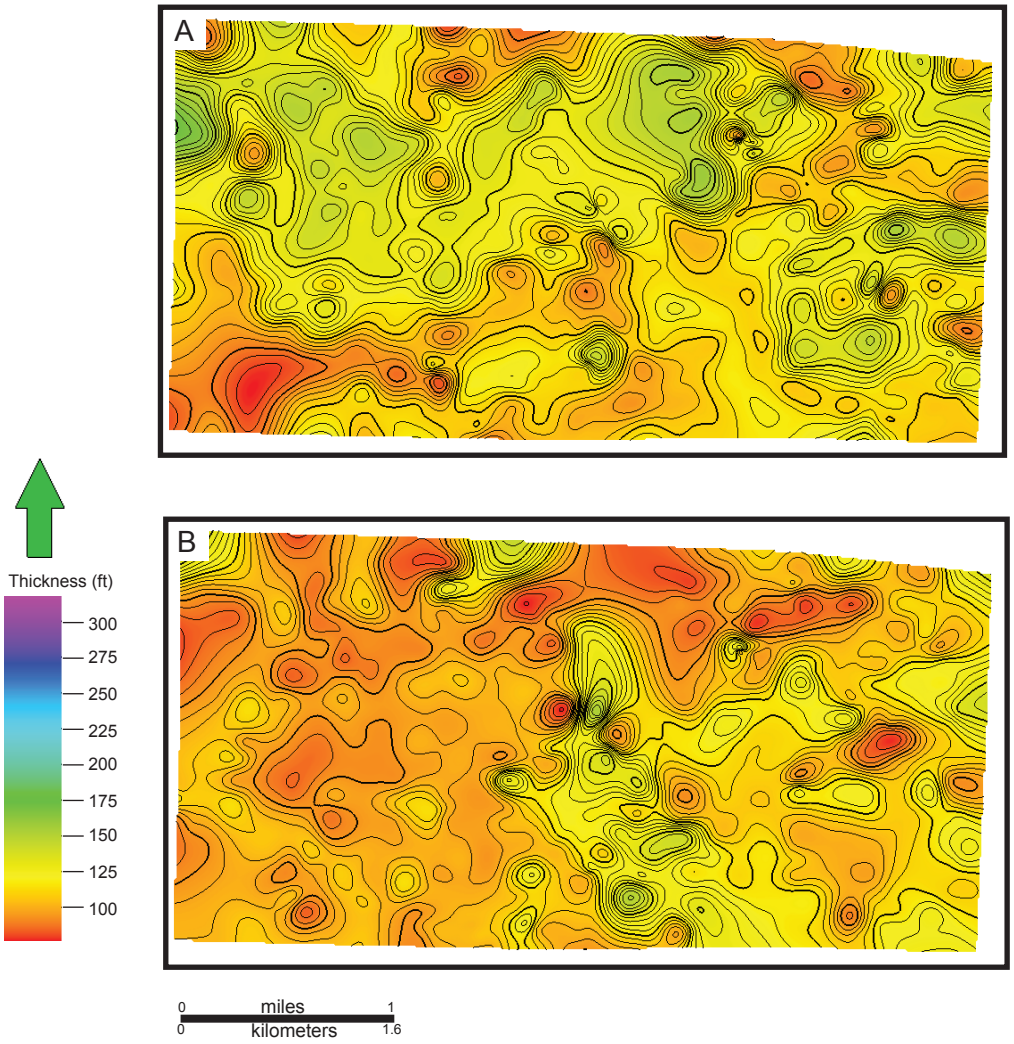

Gross-interval isopach of A) Coal A5 to Coal A (56 ft) . B) Coal A to Rollins Sandstone Member (36 ft).

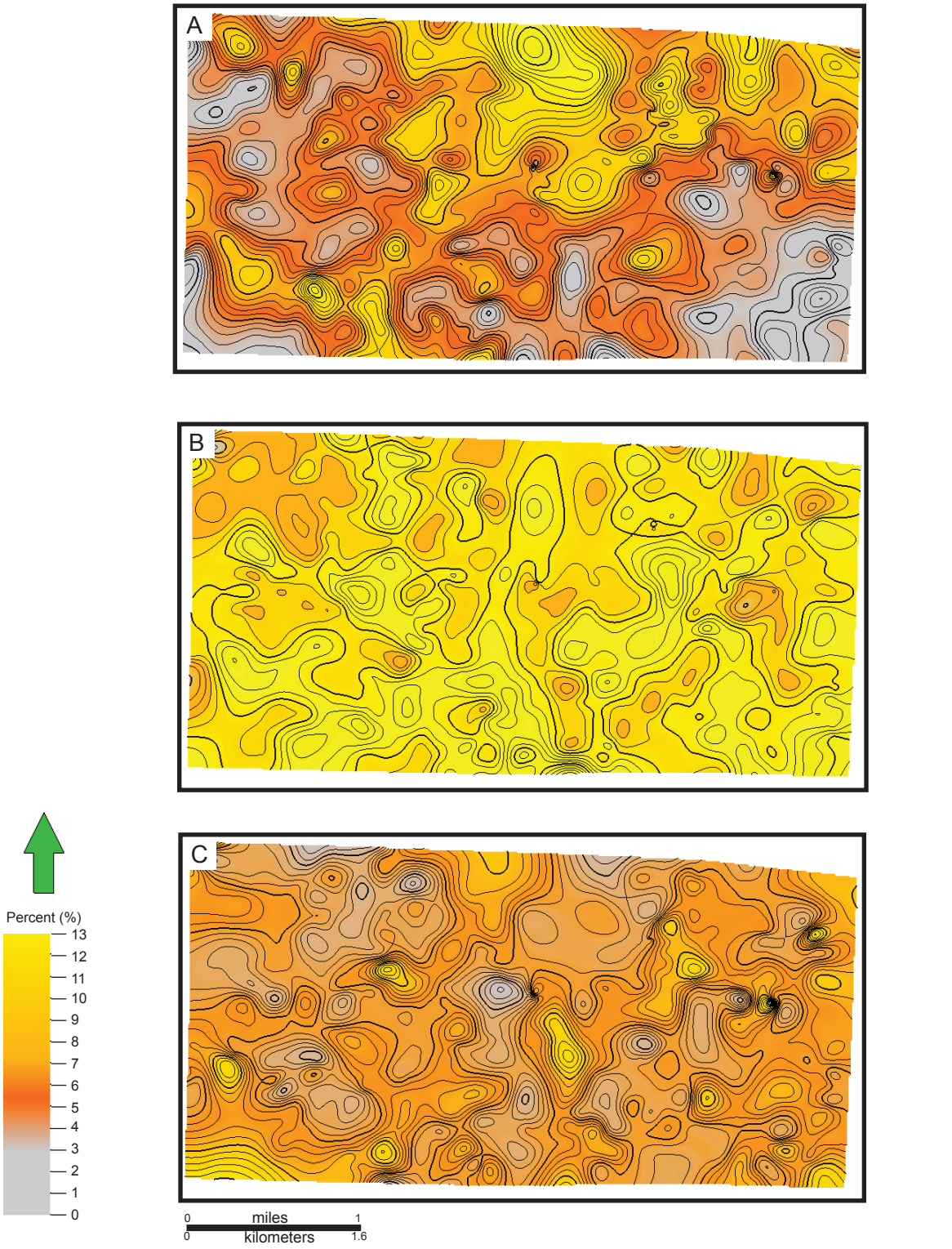

Percent of sandstone present in zones within the lower Williams Fork Formation. A) Top lower Williams Fork Formation to Coal Ridge (180 ft) . B) Coal Ridge to Regressive marker (344 ft). C) Regressive marker to Middle Sandstone (172 ft).

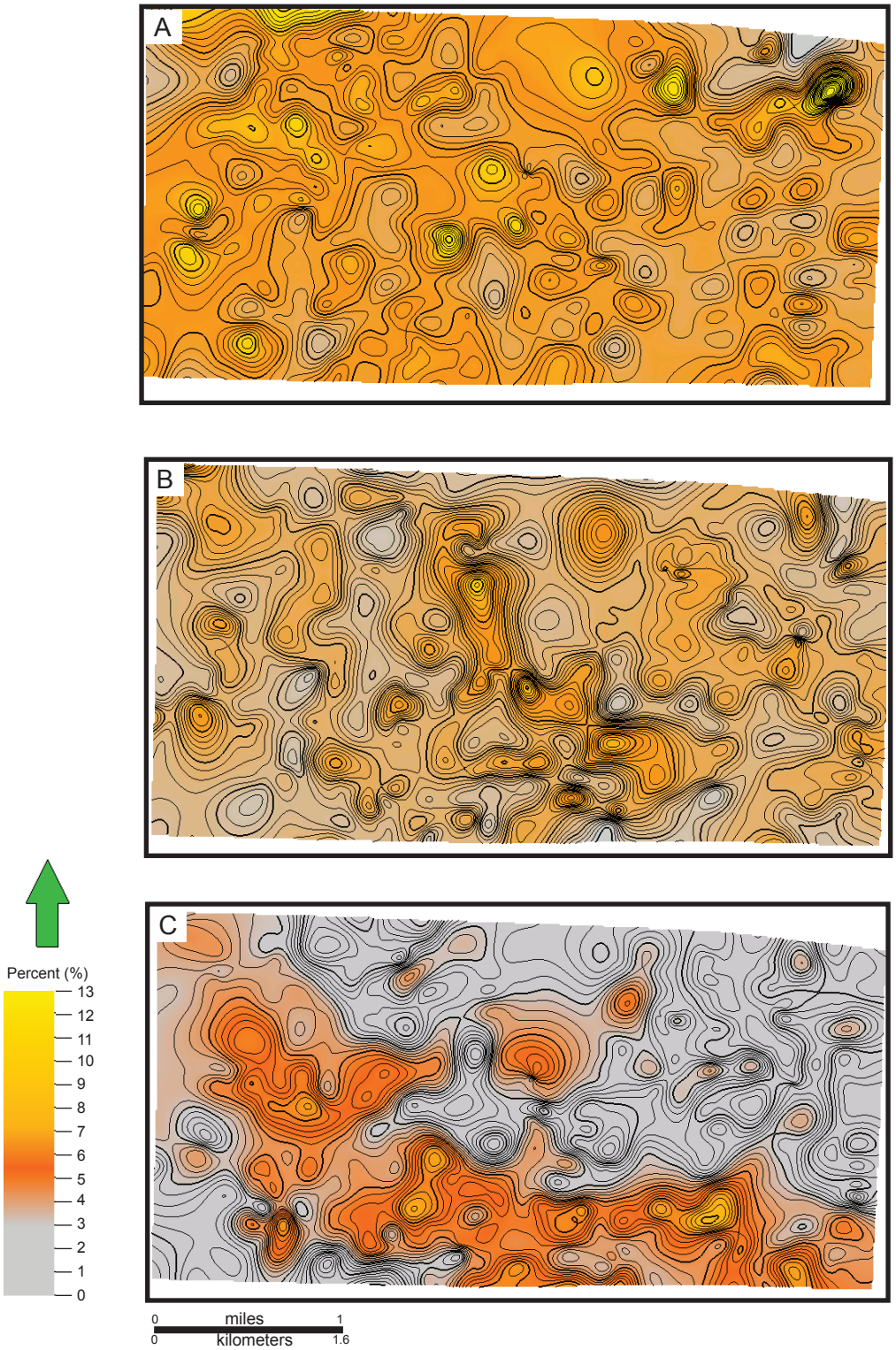

Percent of sandstone present in zones within lower Williams Fork Formation. A) Middle Sandstone to FS Middle Sandstone (200 ft) . B) FS Middle Sandstone to Coal F (144 ft). C) Coal F to Coal E (128 ft).

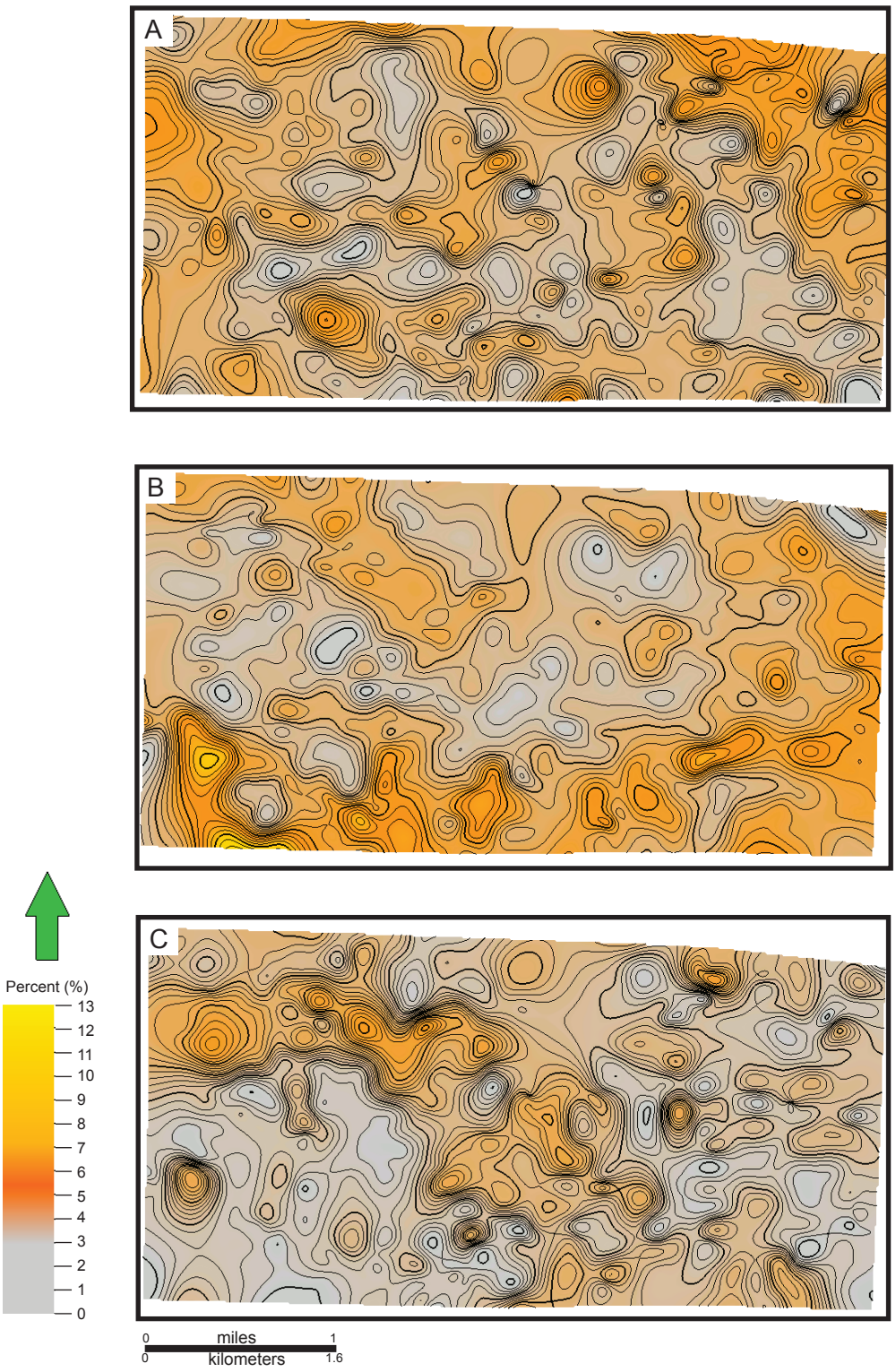

Percent of sandstone present in zones within lower Williams Fork Formation. A) Coal E to Coal D (80 ft) . B) Coal D to Coal B (72 ft). C) Coal B to Coal A5 (60 ft).

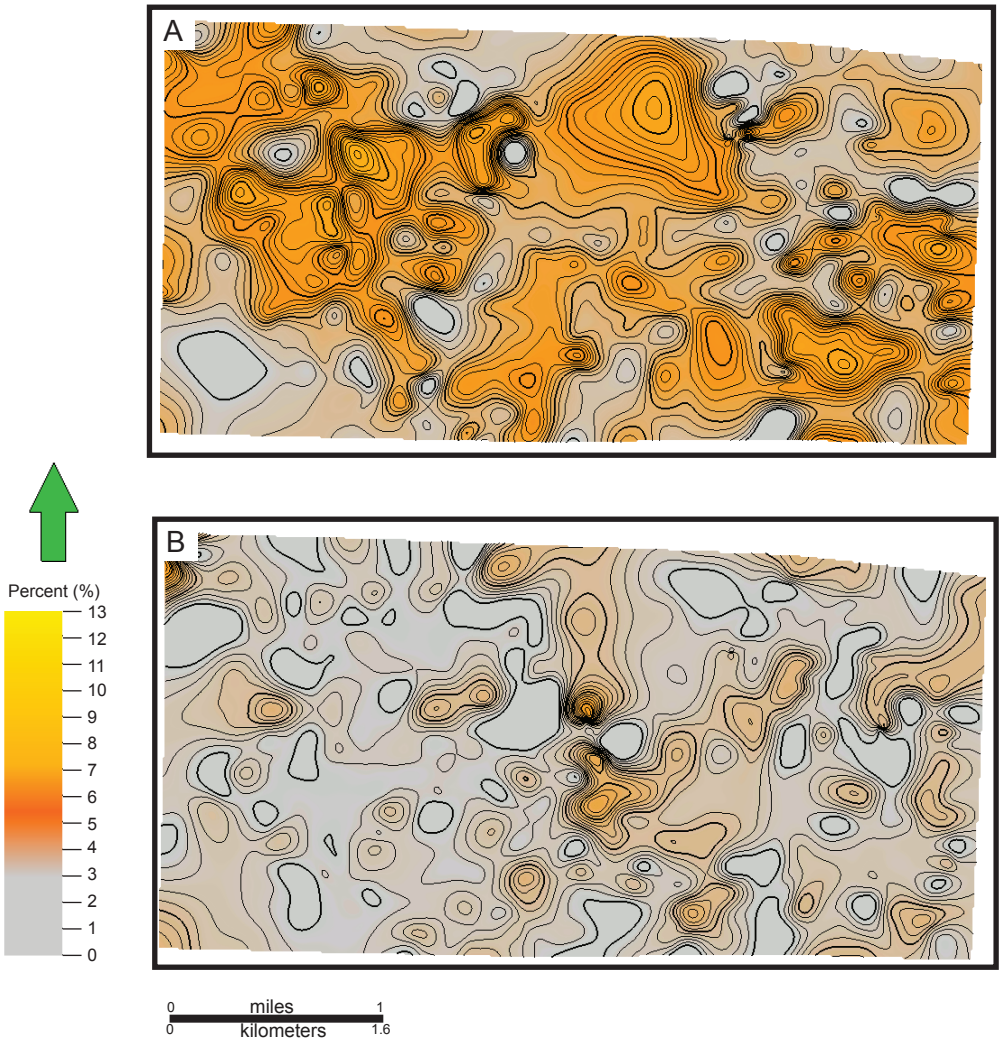

Percent of sandstone present in zones within lower Williams Fork Formation. A) Coal A5 to Coal A (56 ft) . B) Coal A to Rollins Sandstone Member (36 ft).

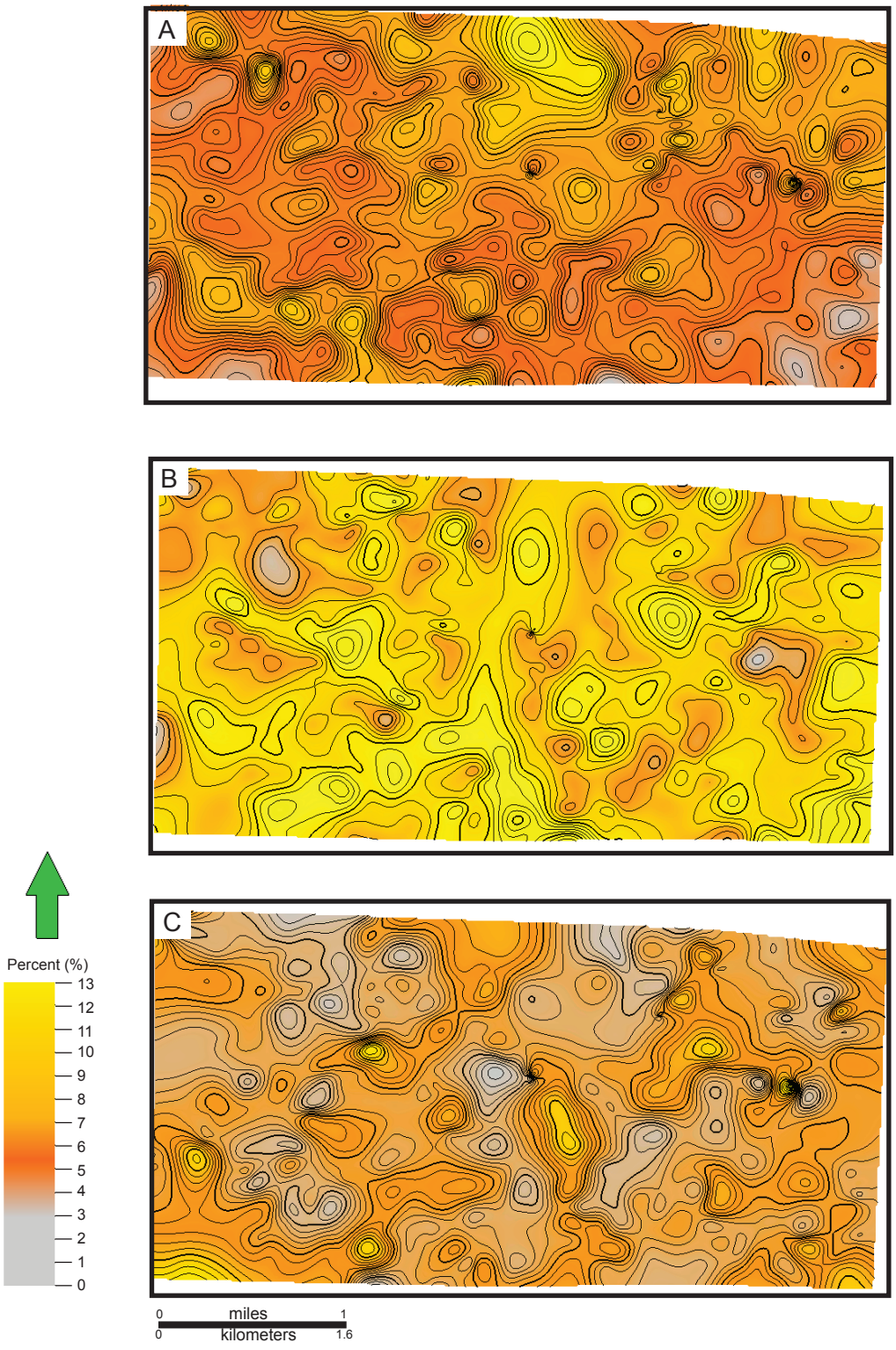

Percent of point bar deposits present in zones within lower Williams Fork Formation. A) Base middle Williams Fork Formation to Coal Ridge (180 ft) . B) Coal Ridge to Regressive marker (344 ft). C) Regressive marker to Middle Sandstone (172 ft).

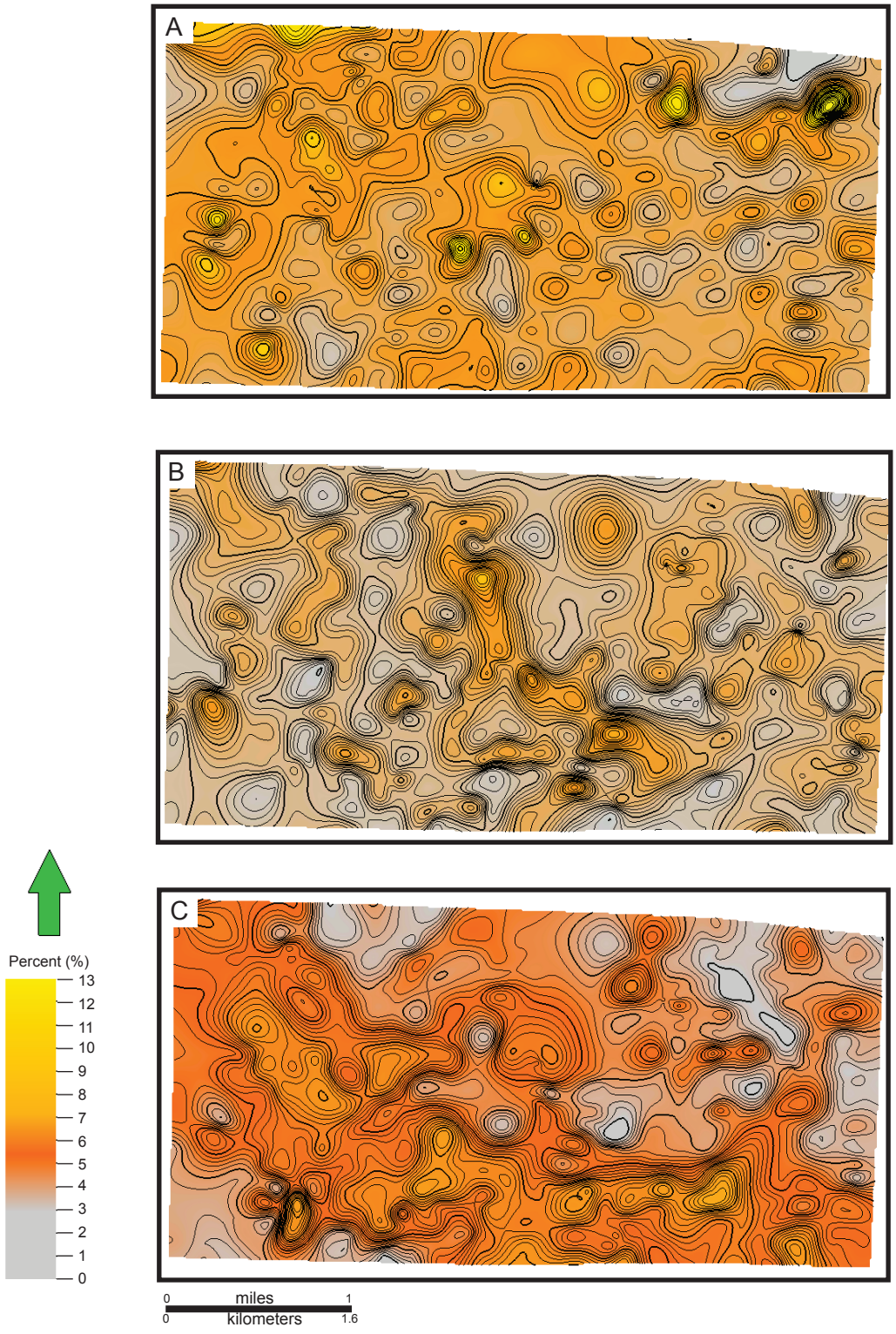

Percent of point bar deposits present in zones within lower Williams Fork Formation. A) Middle Sandstone to FS Middle Sandstone (200 ft) . B) FS Middle Sandstone to Coal F (144 ft). C) Coal F to Coal E (128 ft).

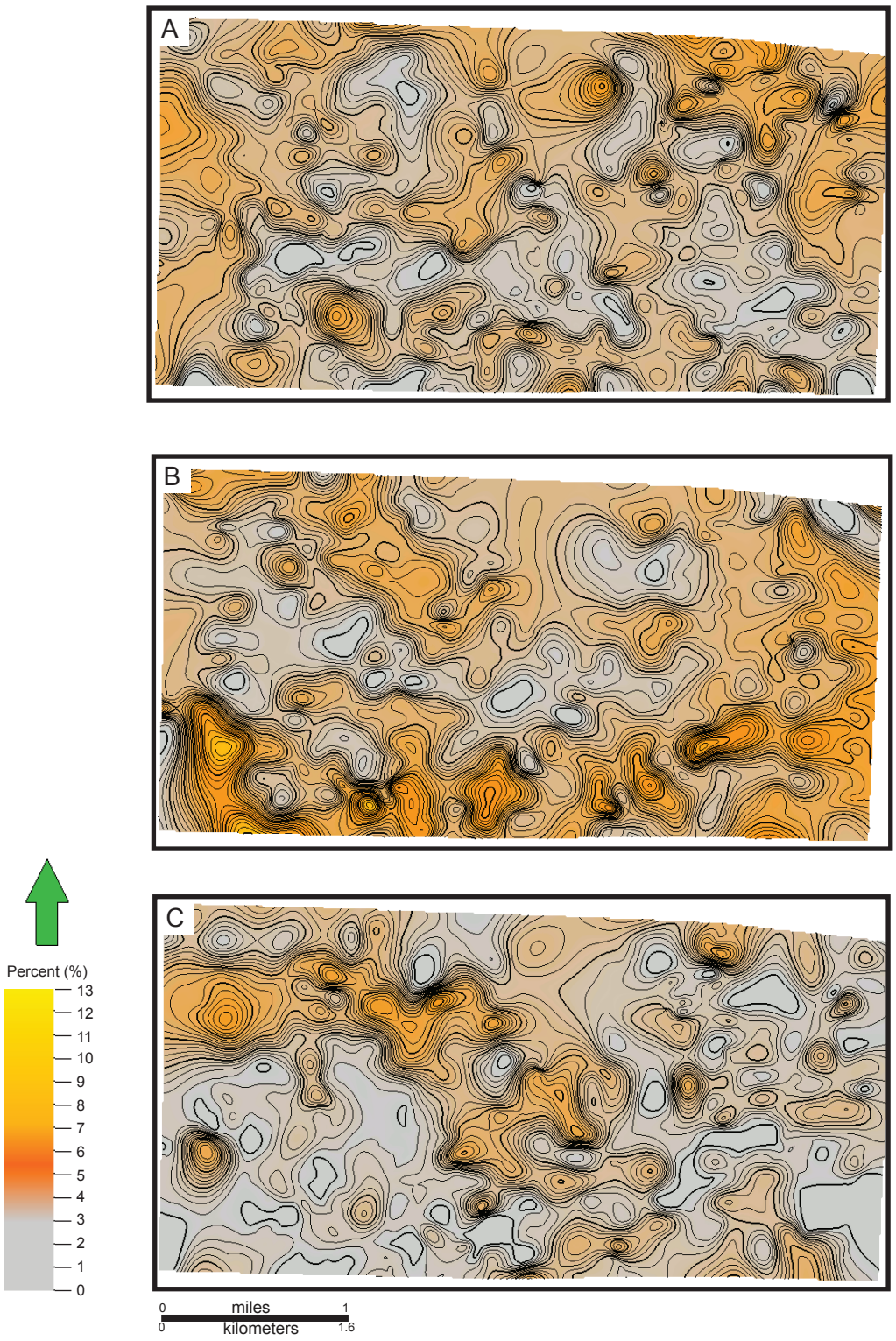

Percent of point bar deposits present in zones within lower Williams Fork Formation. A) Coal E to Coal D (80 ft) . B) Coal D to Coal B (72 ft). C) Coal B to Coal A5 (60 ft).

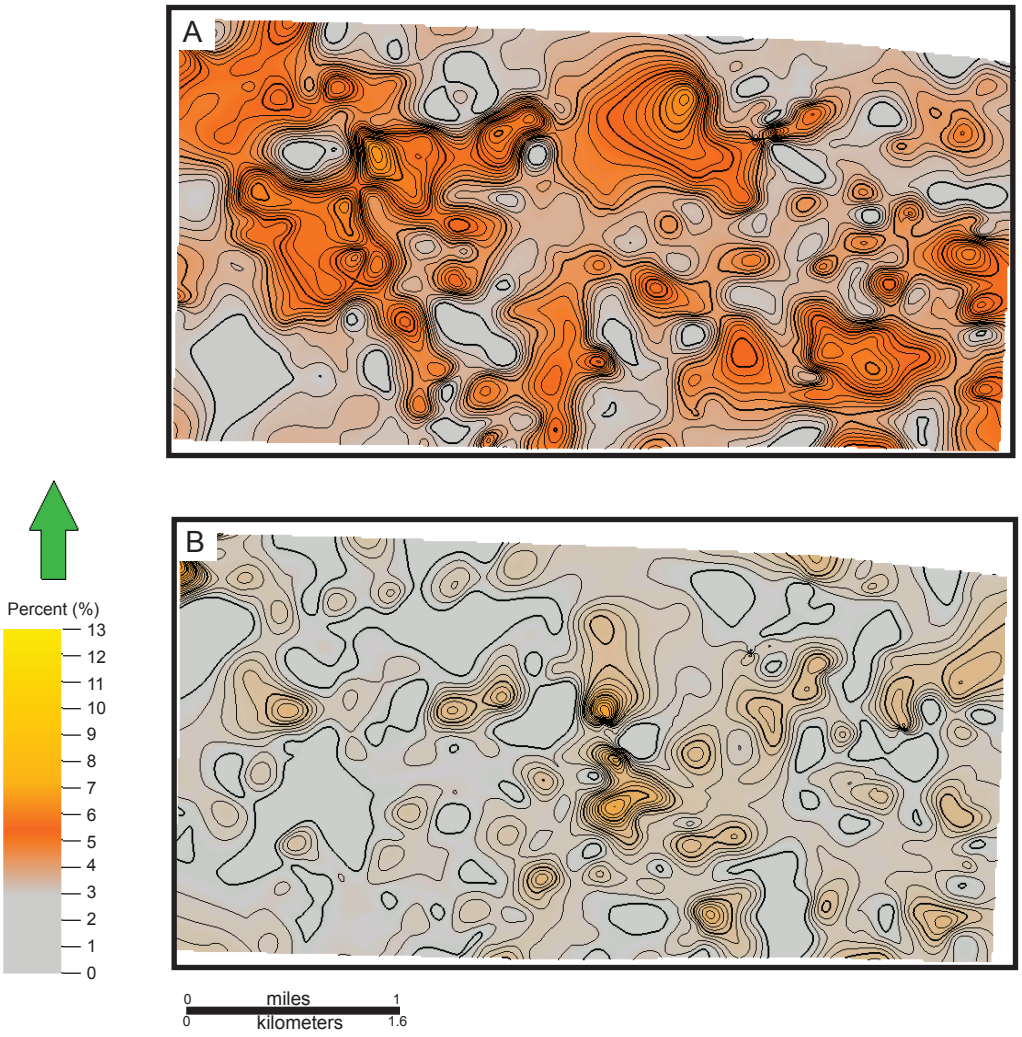

Percent of point bar deposits present in zones within lower Williams Fork Formation. A) Coal A5 to Coal A (56 ft) . B) Coal A to Rollins Sandstone Member (36 ft).

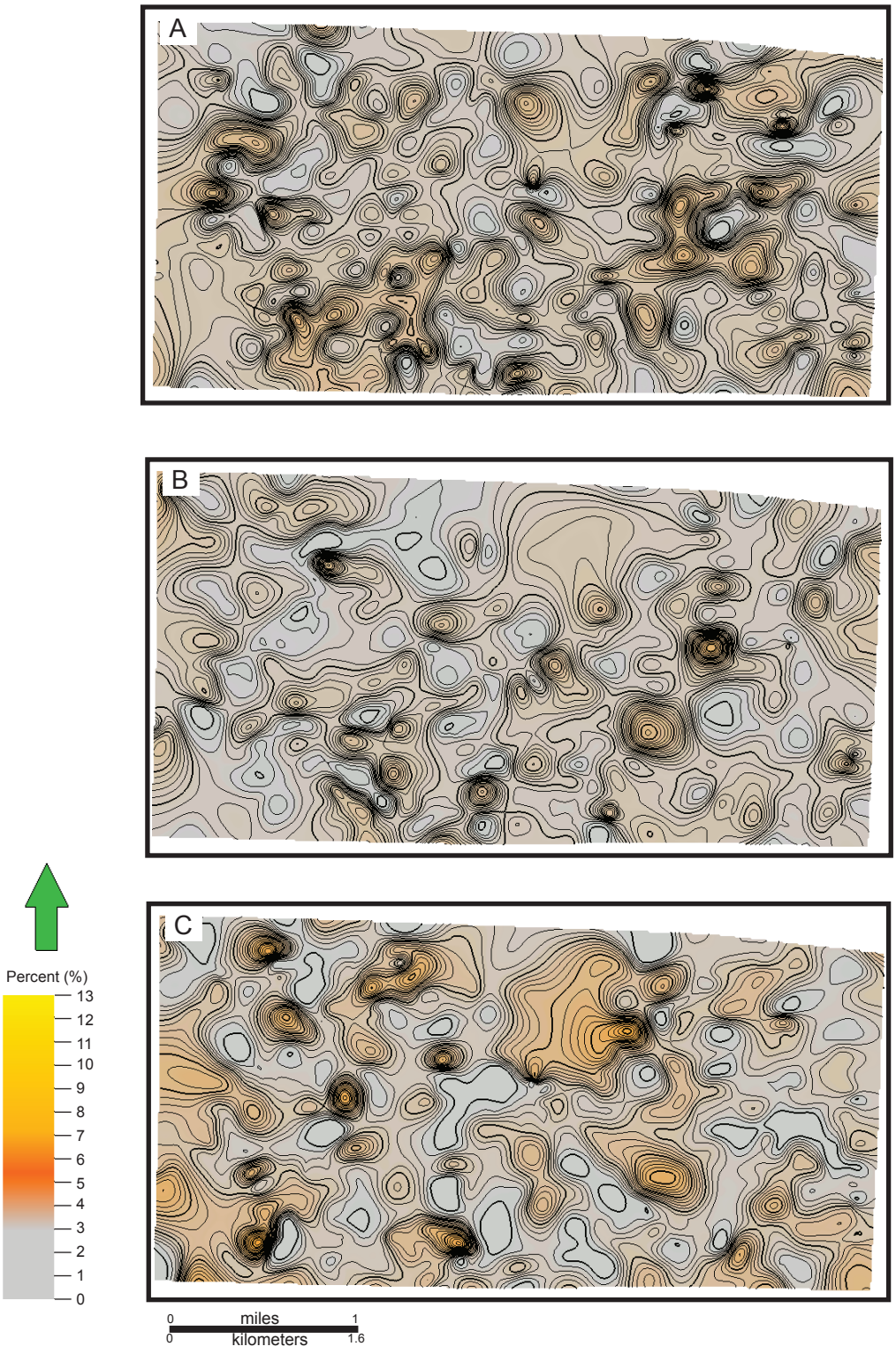

Percent of crevasse splay deposits present in zones within lower Williams Fork Formation. A) Middle Sandstone to FS Middle Sandstone (200 ft). B) FS Middle Sandstone to Coal F (144 ft). C) Coal F to Coal E (128 ft).

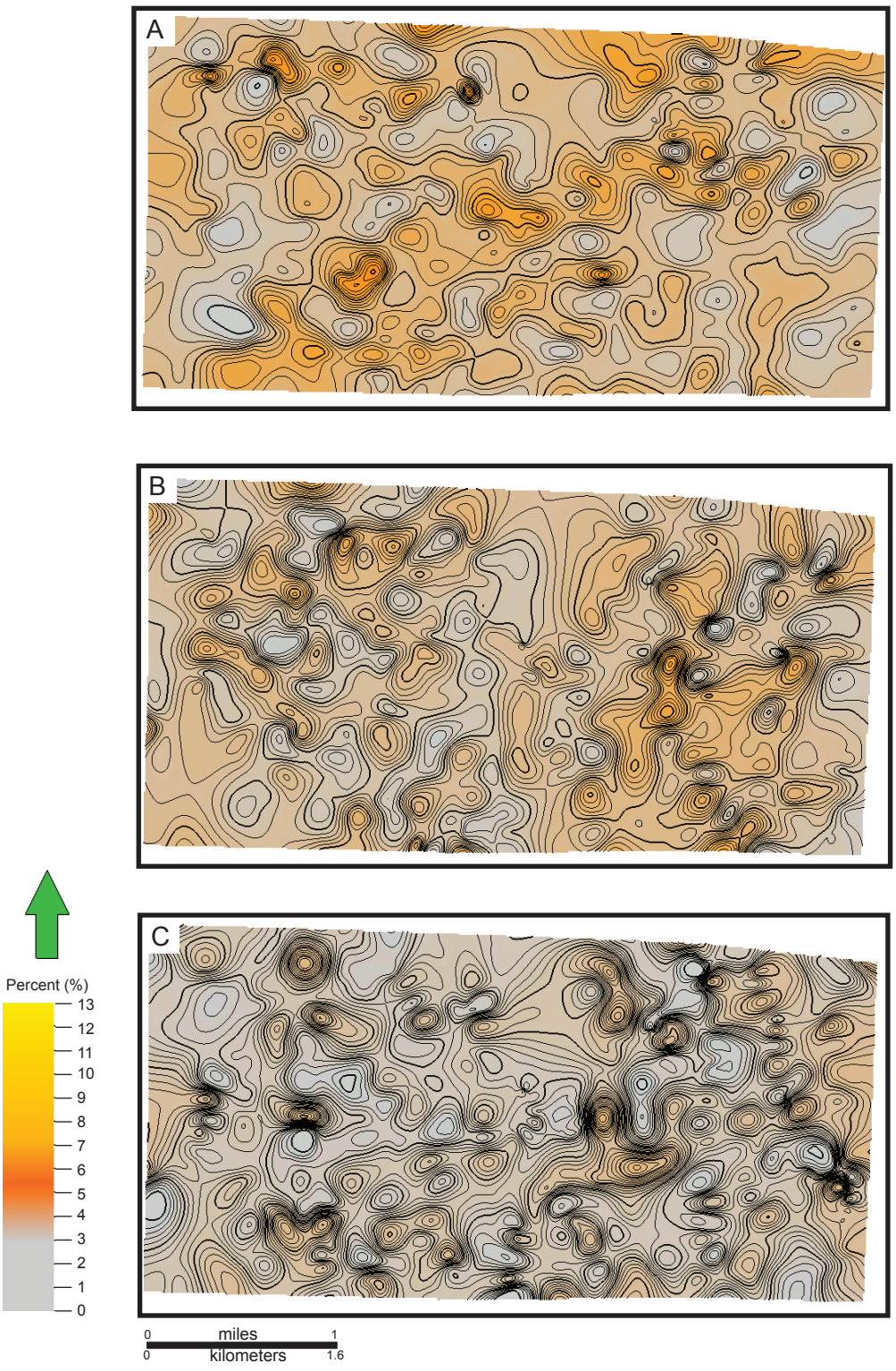

Percent of crevasse splay deposits present in zones within lower Williams Fork Formation. A) Base middle Williams Fork Formation to Coal Ridge (180 ft) . B) Coal Ridge to Regressive marker (344 ft). C) Regressive marker to Middle Sandstone (172 ft).

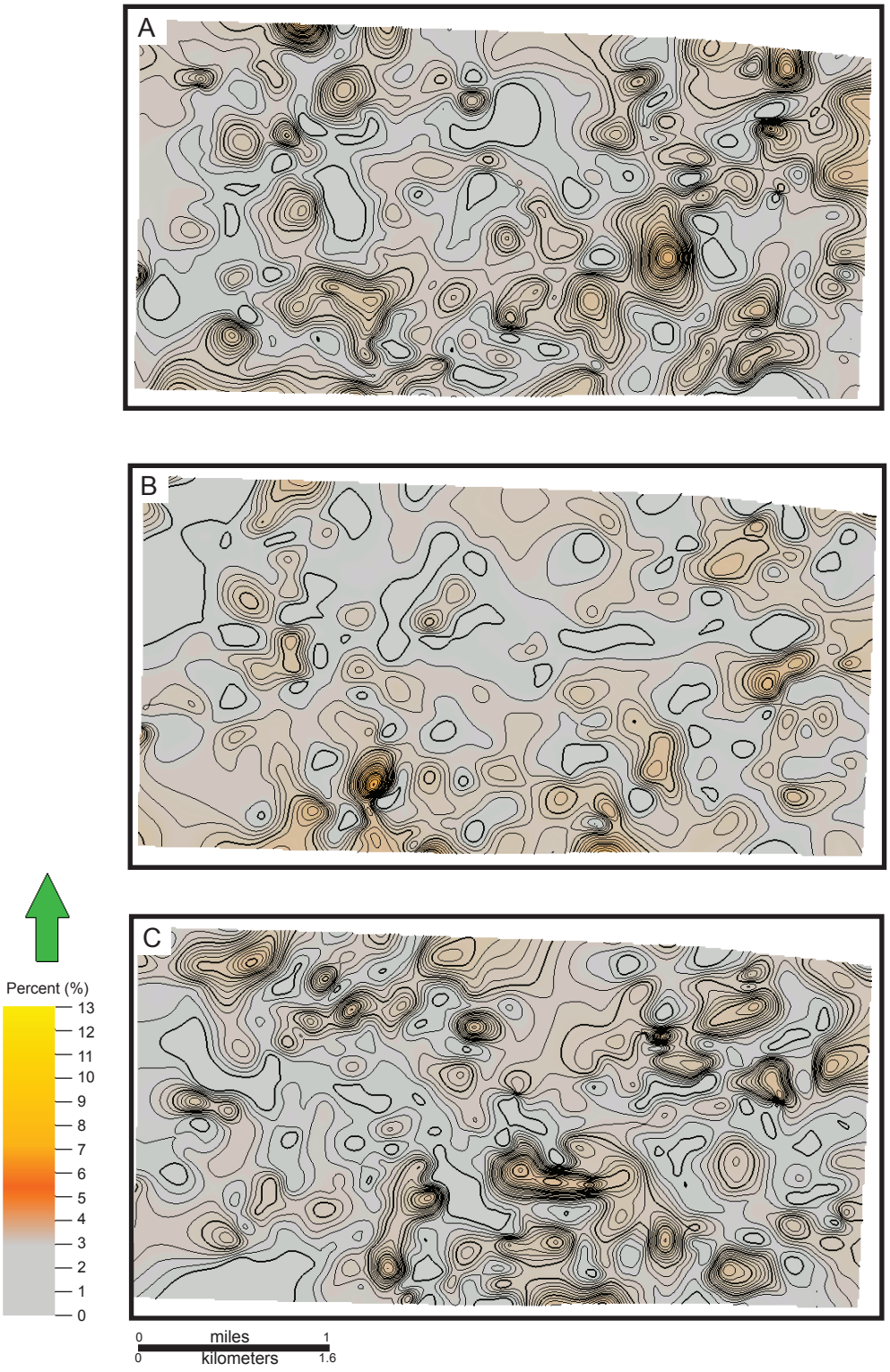

Percent of crevasse splay deposits present in zones within lower Williams Fork Formation. A) Coal E to Coal D (80 ft) . B) Coal D to Coal B (72 ft). C) Coal B to Coal A5 (60 ft).

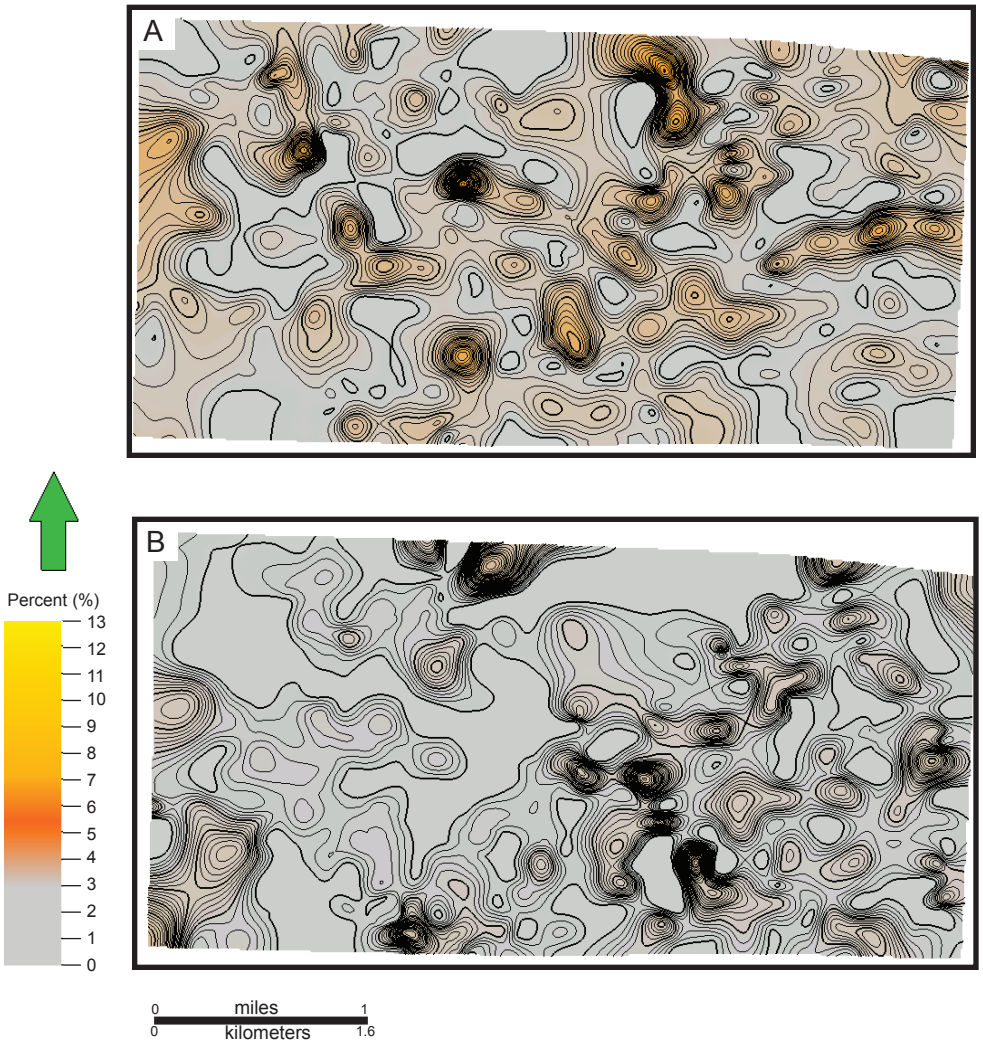

Thickness of crevasse splay deposits present in zones within lower Williams Fork Formation. A) Coal A5 to Coal A (56 ft) . B) Coal A to Rollins Sandstone Member (36 ft). Contour intervals of 10 ft are used.

Appendix F

Training Image Testing Scenarios

Appendix F documents the 25 trial scenarios carried out to determine the appropriate training image grid and cell size, search mask shape and radius, number of multi-grids, number of informed nodes, scaling, rotation, conditioning, and constraint to the vertical proportion curve to be used to carry out MPS modeling within the lower Williams Fork Formation at Grand Valley Field.

Training Image Trial Parameters used in Testing										
Trial	Grid Size	Cell Size	Search Mask	Search Mask Size	Multi-Grids	Informed Nodes	Constrained to VPC?	Scaling? (IxJxK)	Rotation?	Conditioning?
1	79x80x17	22x22x1	ellipsoid	8 x 3 x 2	4	32	Y	N	N	N
2	58x58x17	30x30x1	ellipsoid	N/A	4	64	N	N	N	N
3	58x58x17	30x30x1	ellipsoid	N/A	4	64	N	N	N	N
4	58x58x17	30x30x1	ellipsoid	N/A	4	64	N	2x2x2	5 degrees	Smoothed AE Model
5	79x80x17	22x22x1	ellipsoid	N/A	4	64	N	N	N	N
6	58x51x17	45x45x5	ellipsoid	N/A	2	32	N	N	N	N
7	88x76x17	30x30x5	ellipsoid	7x9x2	3	32	N	N	N	N
8	105x91x17	25x25x5	ellipsoid	10x25x2	3	64	N	N	N	N
9	105x91x17	25x25x6	ellipsoid	15x25x2	3	64	N	N	N	N
11	53X46X17	50X50X15	ellipsoid	7x6x2	3	64	N	N	N	N
12	65x56x17	50X50X15	ellipsoid	8x7x2	3	64	N	N	N	N
13	65x56x17	50X50X15	ellipsoid	8x3x2	3	64	N	N	N	N
14	114x98x17	50X50X15	ellipsoid	7x12x2	3	64	N	N	N	N
15	114x98x17	50X50X15	ellipsoid	N/A	3	64	N	N	N	N

Training Image Trial Parameters used in Testing										
Trial	Grid Size	Cell Size	Search Mask	Search Mask Size	Multi-Grids	Informed Nodes	Constrained to VPC?	Scaling? (IxJxK)	Rotation?	Conditioning?
14	114x98x17	50X50X15	ellipsoid	7x12x2	3	64	N	N	N	N
15	114x98x17	50X50X15	ellipsoid	N/A	3	64	N	N	N	N
16	35x35x17	50X50X15	ellipsoid	4x4x2	3	64	N	N	N	N
17	65x56x17	50X50X15	ellipsoid	12x10x2	2	64	N	N	N	N
18	65x56x17	50X50X15	ellipsoid	12x10x2	2	64	N	N	N	N
19	65x56x17	50X50X15	ellipsoid	12x10x2	2	64	N	N	N	N
20	65x56x17	50X50X1	ellipsoid	12x10x2	2	64	N	N	N	N
21	65x56x17	50X50X1	ellipsoid	12x10x2	2	128	N	N	N	N
22	65x56x17	50X50X1	ellipsoid	12x10x2	2	128	N	N	N	N
23	65x56x17	50x50x1	ellipsoid	12x10x2	2	128	N	N	N	N
24	65x56x17	50x50x1	ellipsoid	12x10x2	2	100	N	N	N	N
25	65x56x17	50x50x1	ellipsoid	12x10x2	2	100	N	N	N	N
Final	**65x56x17**	**50x50x1**	**ellipsoid**	**12x10x2**	**2**	**64**	**N**	**N**	**N**	**N**

Trial	Notes from Result	Notes from Testing Scenario
1	% good-lots of pixilation	Architectural element orientation drawn incorrectly
2	Pixilated	Architectural element orientation drawn incorrectly
3	Pixilated	Architectural element orientation drawn incorrectly
4	Identical to SIS AE Model	Architectural element orientation drawn incorrectly
5	Pixilated	Architectural element orientation drawn incorrectly
6	much better but still pixilated	
7	Better than previous trials	
8		
9	best so far	
11	curved features modeled but isolated	
12	curved features modeled but isolated	
13	curved features modeled but isolated	
14	curved features modeled but isolated	one channel drawn per level in training image rather than two
15	curved features modeled but isolated	one channel drawn per level in training image rather than two
16		one channel drawn per level in training image rather than two
17		one channel drawn per level in training image rather than two
18		only drew one strand of point bars in TI and worked MUCH better, was over training before
19		
20		
21	not as good as using more straight line PBs	irregularity creates noise and PB A and B connected in circles; coal still crazy
22	with more informed nodes (128) PBs looked better	still somewhat pixilated but that isn't going to change, with irregular PB's getting circles of them rather than strand
23	bad	tried coal in upper zones and it is modeled between wells so will have to merge models
24	circular point bars eliminated so use more than 64 informed nodes to create training image and it will yield a better result, as it should	tried more informed nodes in training image creation
25	test to see if what coal looks like merged from another model	
Final	**Best trial out of 25, maintains geostatistical parameters**	**Best trial out of 25, maintains geostatistical parameters**

Appendix G

Sequential Gaussian Simulation Parameters

Appendix G shows the parameters used to carry out sequential gaussian simulation (SGS). SGS was used to create property models of porosity.

MPS Model Variogram Settings by Zone and Architectural Element for SGS Petrophysical Modeling								
Zone	**Architectural Element**	**Variogram Type**	**Dip (degrees)**	**Nugget**	**Major Range**	**Minor Range**	**Vertical**	**Azimuth (degrees)**
1	Point Bar	Spherical	0	0	300	200	20	60
	Crevasse Splay				300	200	20	-60
	Floodplain	Assign Value=0						
	Mudstone Plug	Assign Value=0						
2	Point Bar	Spherical	0	0	300	200	20	90
	Crevasse Splay				300	200	20	25
	Floodplain	Assign Value=0						
	Mudstone Plug	Assign Value=0						
3	Point Bar	Spherical	0	0	300	200	20	-43
	Crevasse Splay				300	200	20	55
	Floodplain	Assign Value=0						
	Mudstone Plug	Assign Value=0						
4	Point Bar	Spherical	0	0	300	200	20	73
	Crevasse Splay				300	200	20	-83
	Floodplain	Assign Value=0						
	Mudstone Plug	Assign Value=0						
5	Point Bar	Spherical	0	0	300	200	20	45
	Crevasse Splay				300	200	20	75
	Floodplain	Assign Value=0						
	Mudstone Plug	Assign Value=0						
6	Point Bar	Spherical	0	0	300	200	20	40
	Crevasse Splay				300	200	20	25
	Floodplain	Assign Value=0						
	Mudstone Plug	Assign Value=0						
7	Point Bar	Spherical	0	0	300	200	20	-55
	Crevasse Splay				300	200	20	-76
	Floodplain	Assign Value=0						
	Mudstone Plug	Assign Value=0						
8	Point Bar	Spherical	0	0	300	200	20	-50
	Crevasse Splay	Assign Value=1						
	Floodplain	Assign Value=0						
	Mudstone Plug	Assign Value=0						

MPS Model Variogram Settings by Zone and Architectural Element for SGS Petrophysical Modeling								
Zone	**Architectural Element**	**Variogram Type**	**Dip (degrees)**	**Nugget**	**Major Range**	**Minor Range**	**Vertical**	**Azimuth (degrees)**
1	Point Bar	Spherical	0	0	300	200	20	60
	Crevasse Splay				300	200	20	-60
	Floodplain	Assign Value=0						
	Mudstone Plug	Assign Value=0						
2	Point Bar	Spherical	0	0	300	200	20	90
	Crevasse Splay				300	200	20	25
	Floodplain	Assign Value=0						
	Mudstone Plug	Assign Value=0						
3	Point Bar	Spherical	0	0	300	200	20	-43
	Crevasse Splay				300	200	20	55
	Floodplain	Assign Value=0						
	Mudstone Plug	Assign Value=0						
4	Point Bar	Spherical	0	0	300	200	20	73
	Crevasse Splay				300	200	20	-83
	Floodplain	Assign Value=0						
	Mudstone Plug	Assign Value=0						
5	Point Bar	Spherical	0	0	300	200	20	45
	Crevasse Splay				300	200	20	75
	Floodplain	Assign Value=0						
	Mudstone Plug	Assign Value=0						
6	Point Bar	Spherical	0	0	300	200	20	40
	Crevasse Splay				300	200	20	25
	Floodplain	Assign Value=0						
	Mudstone Plug	Assign Value=0						
7	Point Bar	Spherical	0	0	300	200	20	-55
	Crevasse Splay				300	200	20	-76
	Floodplain	Assign Value=0						
	Mudstone Plug	Assign Value=0						
8	Point Bar	Spherical	0	0	300	200	20	-50
	Crevasse Splay	Assign Value=1						
	Floodplain	Assign Value=0						
	Mudstone Plug	Assign Value=0						

17	Point Bar	Spherical	0	0	300	200	20	-40
	Crevasse Splay	Assign Value=1						
	Floodplain	Assign Value=0						
	Coal	Assign Value=0						
	Mudstone Plug	Assign Value=0						
18	Point Bar	Spherical	0	0	300	200	20	-63
	Crevasse Splay				300	200	20	89
	Floodplain	Assign Value=0						
	Coal	Assign Value=0						
	Mudstone Plug	Assign Value=0						
19	Point Bar	Spherical	0	0	300	200	20	45
	Crevasse Splay				300	200	20	-45
	Floodplain	Assign Value=0						
	Coal	Assign Value=0						
	Mudstone Plug	Assign Value=0						
20	Point Bar	Spherical	0	0	300	200	20	-10
	Crevasse Splay				300	200	20	-88
	Floodplain	Assign Value=0						
	Coal	Assign Value=0						
	Mudstone Plug	Assign Value=0						

Appendix H

Variogram Polar Plots

Appendix H contains the parameters used to create variogram polar plots within the modeling area at Grand Valley Field. Variogram polar plots were created to determine the azimuth of greatest continuity for point bar and crevasse splay deposits within the lower Williams Fork Formation prior to property modeling.

Variogram Polar Plot Settings by Zone and Architectural Element					
Zone	Architectural Element	Number of lags (x-direction)	Number of Lags (y-direction)	Search Distance (x-direction)	Search Distance (Y-Direction)
1	Point Bars	6	6	2640	2640
	Crevasse Splays	7	7	2640	2640
2	Point Bars	6	6	2640	2640
	Crevasse Splays	7	7	2640	2640
3	Point Bars	6	6	2640	2640
	Crevasse Splays	7	7	2640	2640
4	Point Bars	6	6	2640	2640
	Crevasse Splays	7	7	2640	2640
5	Point Bars	6	6	2640	2640
	Crevasse Splays	7	7	2640	2640
6	Point Bars	6	6	2640	2640
	Crevasse Splays	7	7	2640	2640
7	Point Bars	6	6	2640	2640
	Crevasse Splays	7	7	2640	2640
8	Point Bars	6	6	2640	2640
	Crevasse Splays	7	7	2640	2640
9	Point Bars	6	6	2640	2640
	Crevasse Splays	7	7	2640	2640
10	Point Bars	6	6	2640	2640
	Crevasse Splays	7	7	2640	2640
11	Point Bars	6	6	2640	2640
	Crevasse Splays	7	7	2640	2640
12	Point Bars	6	6	2640	2640
	Crevasse Splays	7	7	2640	2640
13	Point Bars	6	6	2640	2640
	Crevasse Splays	7	7	2640	2640
14	Point Bars	6	6	2640	2640
	Crevasse Splays	7	7	2640	2640
15	Point Bars	6	6	2640	2640
	Crevasse Splays	7	7	2640	2640
16	Point Bars	6	6	2640	2640
	Crevasse Splays	7	7	2640	2640
17	Point Bars	6	6	2640	2640
	Crevasse Splays	7	7	2640	2640
18	Point Bars	6	6	2640	2640
	Crevasse Splays	7	7	2640	2640
19	Point Bars	6	6	2640	2640
	Crevasse Splays	7	7	2640	2640
20	Point Bars	6	6	2640	2640
	Crevasse Splays	7	7	2640	2640

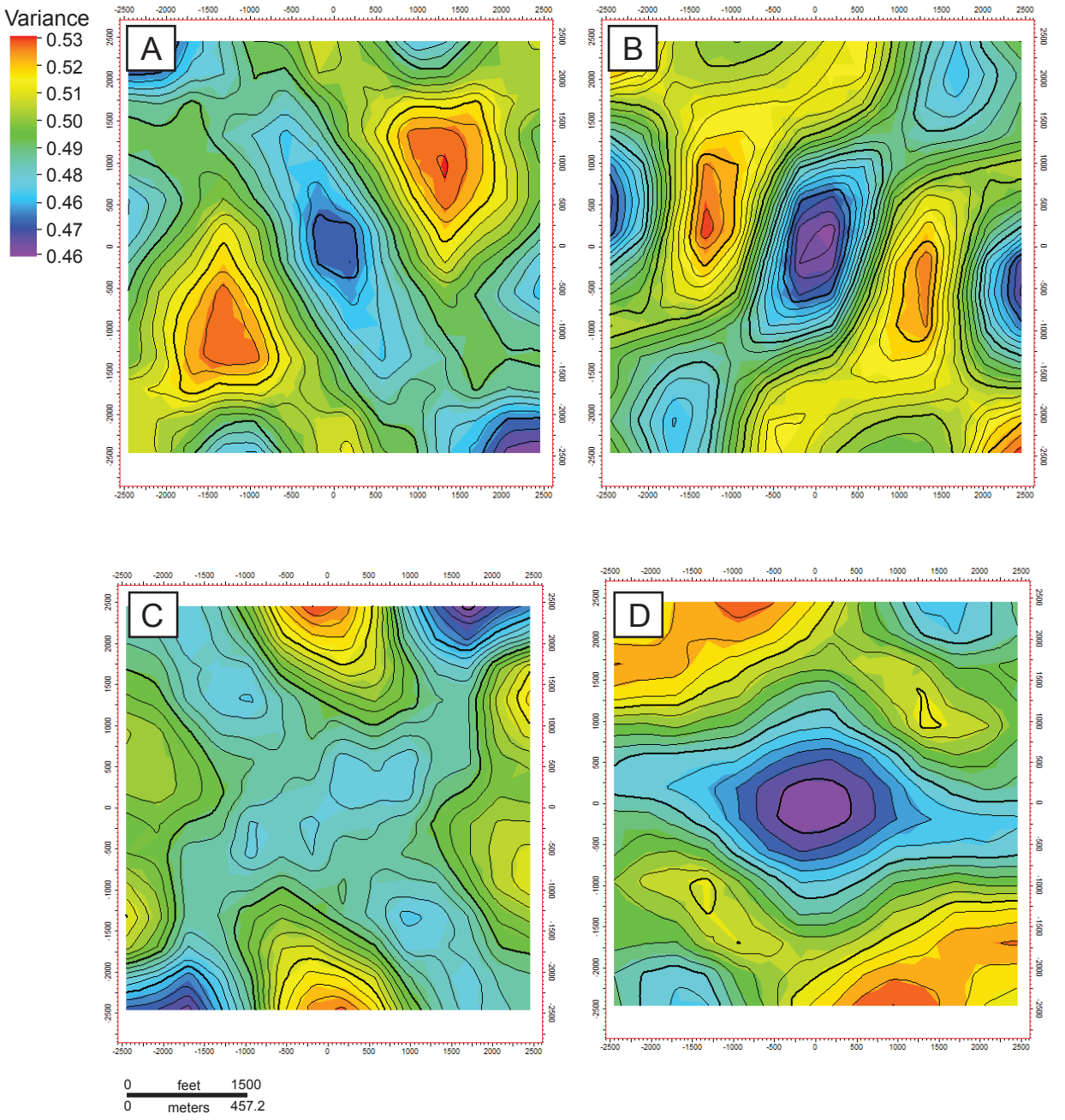

Variogram polar plots created for use in property modeling. A) Base middle Williams Fork to layer 14 (57 ft; azimuth of 60 degrees). B) Layer 14 to layer 31 (68 ft; azimuth of 90 degrees). C) Layer 31 to Coal Ridge Coal Zone marker (57 ft; azimuth of -43 degrees). D) Coal Ridge Coal Zone marker to layer 87 (168 ft; azimuth of 73 degrees).

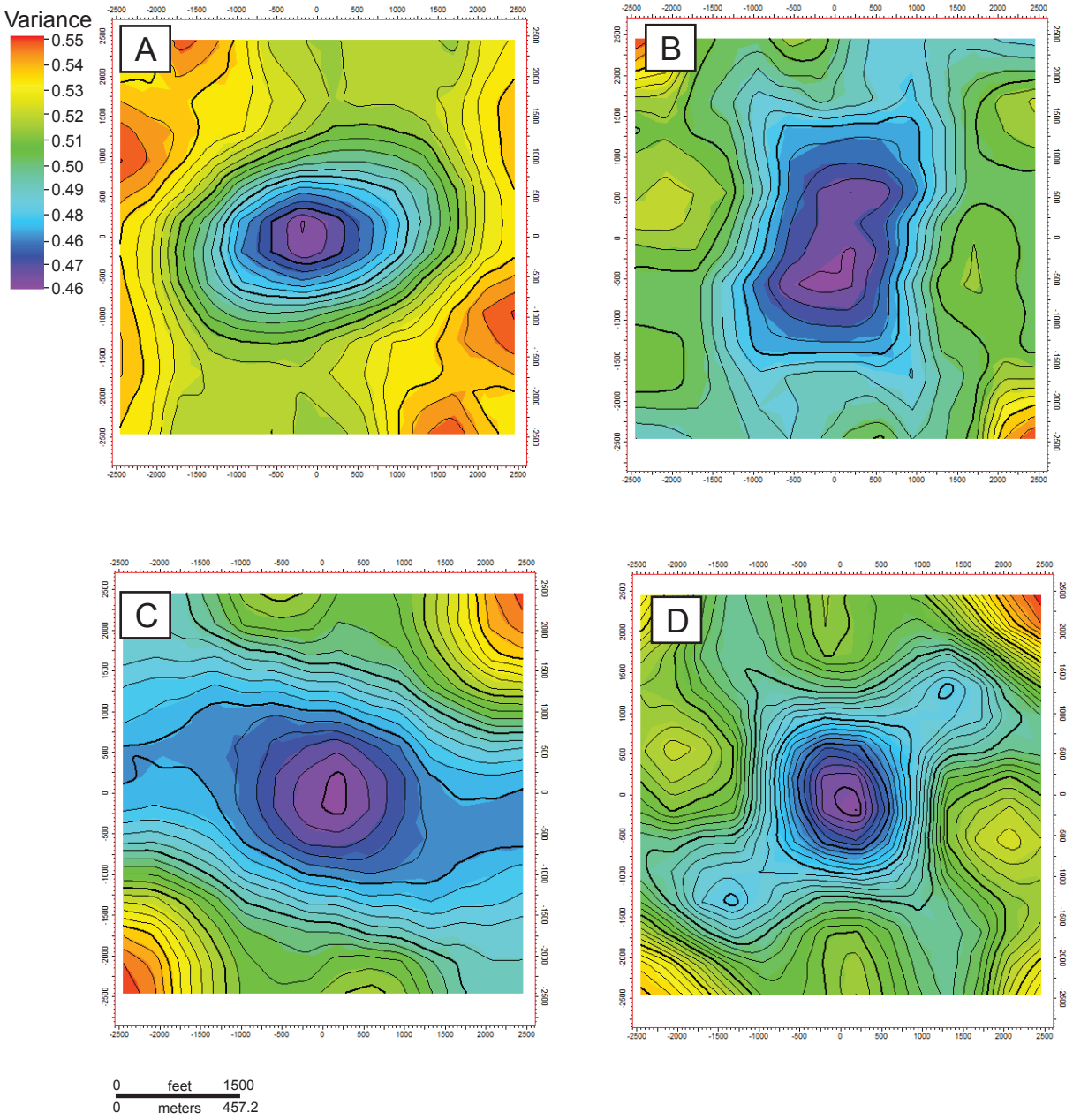

Variogram polar plots created for point bar deposits and used in property modeling. A) Layer 87 to Regressive Marker (180 ft). B) Regressive Marker to layer 160 (112 ft). C) Layer 160 to Middle Sandstone (63 ft). D) Middle Sandstone to layer 190 (55 ft). Contour interval of 0.005 ft.

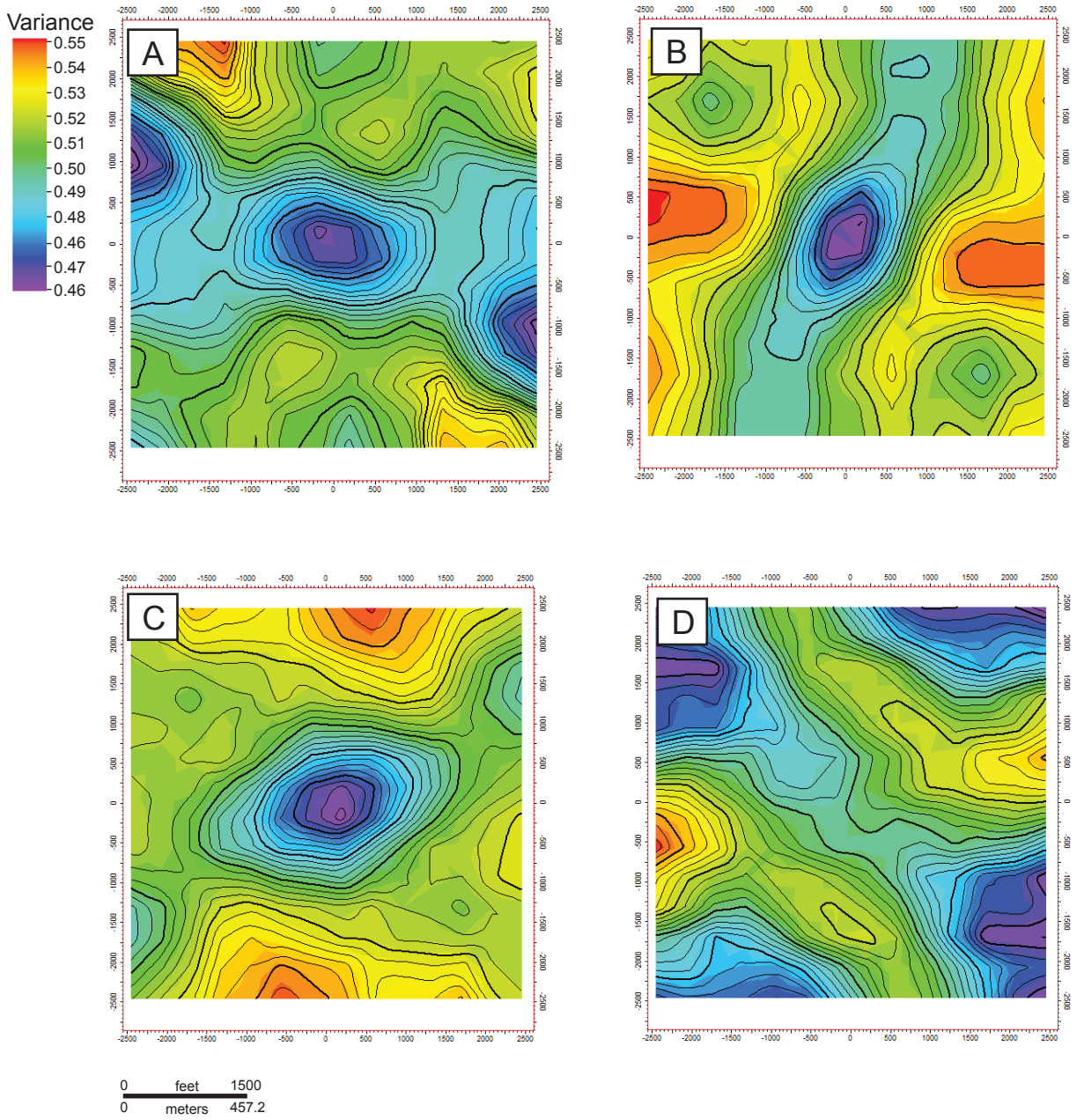

Variogram polar plots created for point bar deposits and used in property modeling. A) Layer 190 to layer 197 (30 ft; azimuth of 88 degrees). B) Layer 197 to Flooding Surface (119 ft; azimuth of 34 degrees). C) Flooding surface to layer 250 (94 ft; azimuth of 55 degrees). D) Layer 250 to Coal F (48 ft; azimuth of -55 degrees). Contour interval of 0.005 ft.

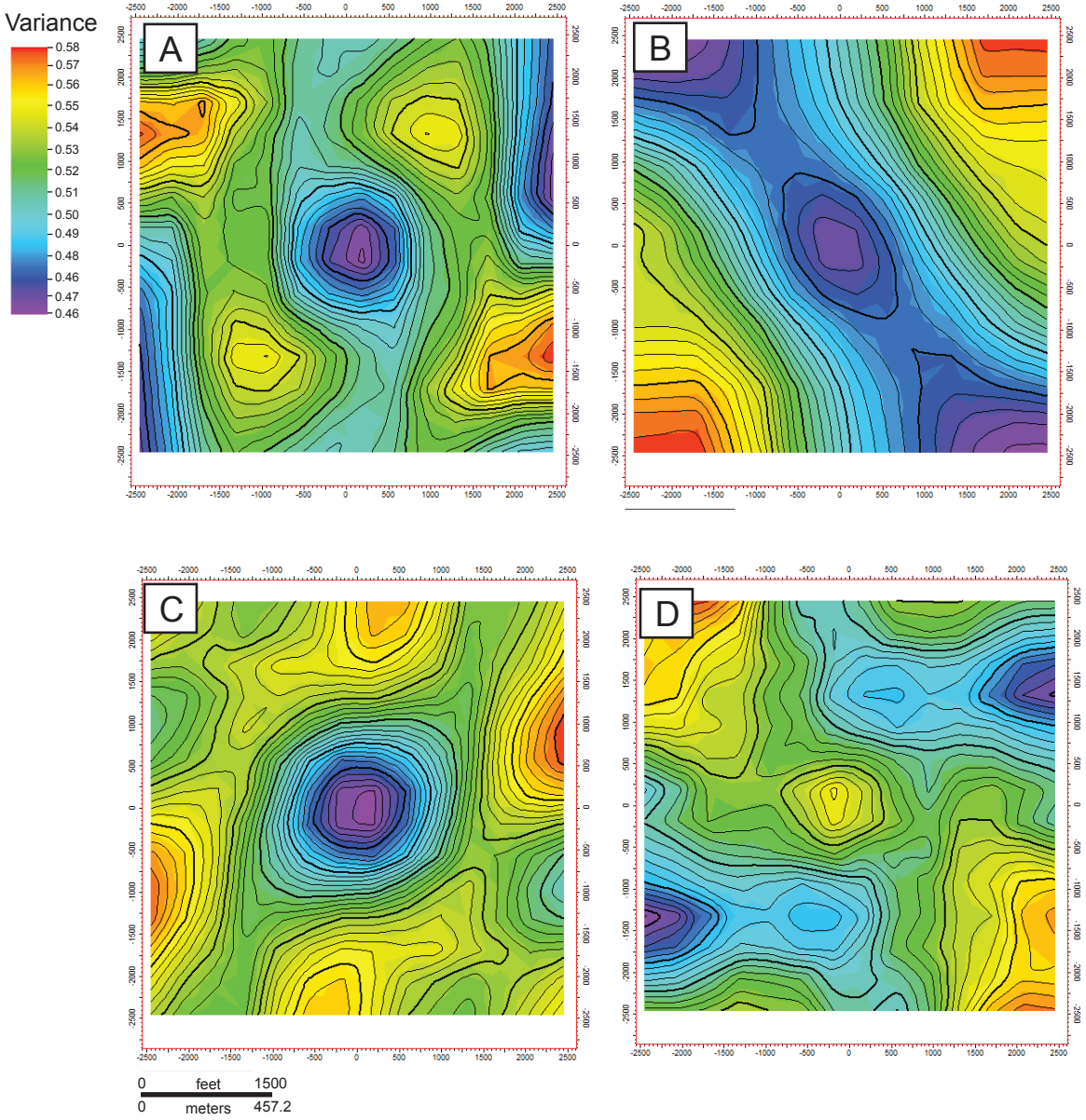

Variogram polar plots created for point bar deposits and used in property modeling. A) Coal F to layer 276 (48 ft; contour interval of 0.005 ft; azimuth of -9 degrees). B) Layer 276 to Coal E (83 ft; contour interval of 0.01 ft; azimuth of -25 degrees). C) Coal E to Coal D (322 ft; contour interval of 0.005 ft; azimuth of -53 degrees). D) Coal D to layer 322 (16 ft; contour interval of 0.01; azimuth of 55 degrees).

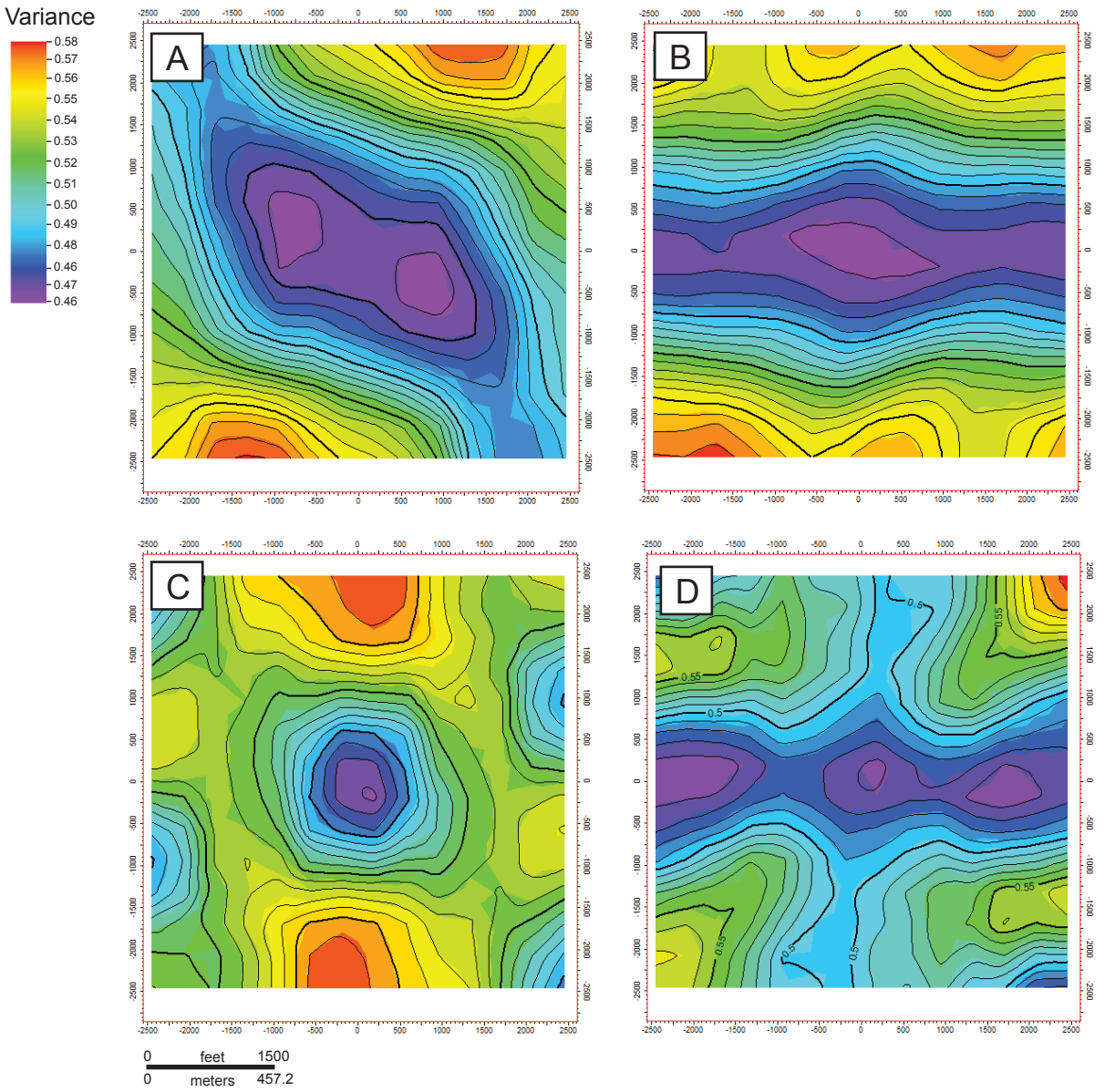

Variogram polar plots created for point bar deposits and used in property modeling. A) Layer 322 to Coal B (60 ft; azimuth of -40 degrees). B) Coal B to Coal A5 (63 ft; azimuth of -63 degrees). C) Coal A5 to Coal A (60 ft; azimuth of 45 degrees). D) Coal A to Rollins Sandstone Member (39 ft' azimuth of -10 degrees). Contour interval of 0.01 ft.

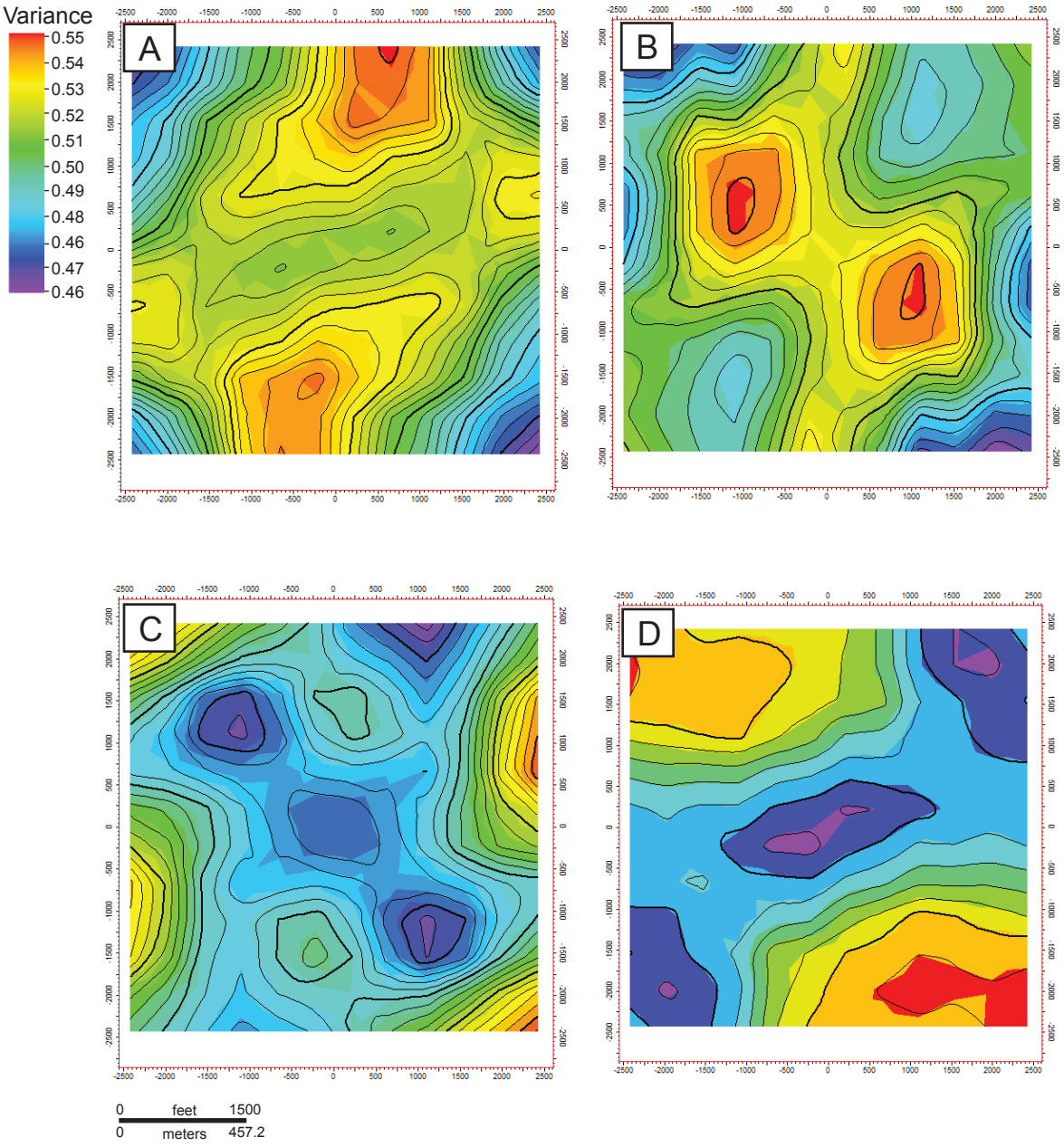

Variogram polar plots created for crevasse splay deposits and used in property modeling. A) Base middle Williams Fork to layer 14 (57 ft; azimuth of -60 degrees). B) Layer 14 to layer 31 (68 ft; azimuth of 25 degrees). C) Layer 31 to Coal Ridge Coal Zone marker (57 ft; azimuth of 55 degrees). D) Coal Ridge Coal Zone marker to layer 87 (168 ft; azimuth of -83 degrees). Contour interval of 0.005 ft.

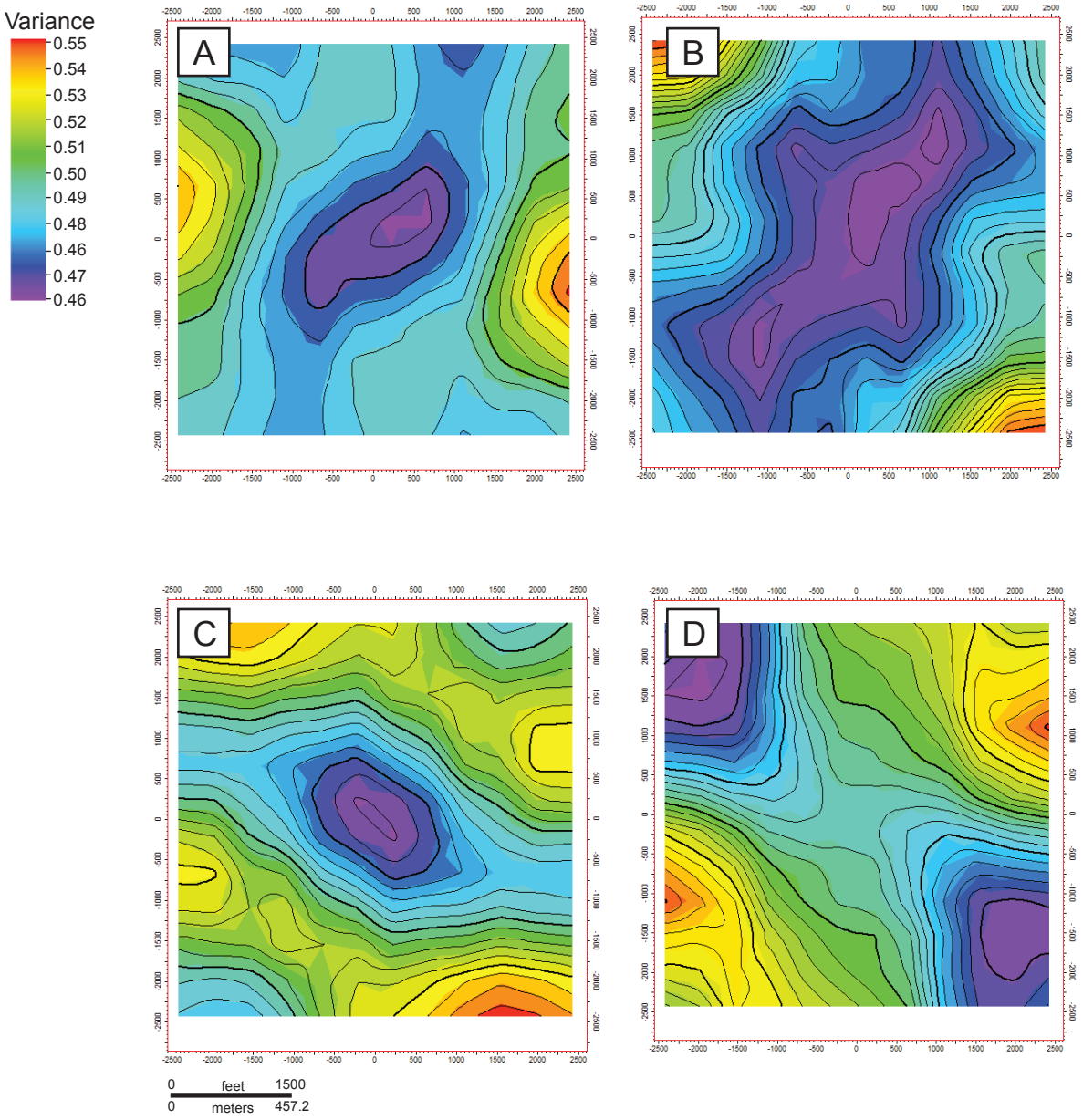

Variogram polar plots created for crevasse splay deposits and used in property modeling. A) Layer 87 to Regressive Marker (180 ft; azimuth of 75 degrees). B) Regressive Marker to layer 160 (112 ft; azimuth of 25 degrees). C) Layer 160 to Middle Sandstone (63 ft; azimuth of -76 degrees). D) Middle Sandstone to layer 190 (55 ft; assign value=1). Contour interval of 0.005 ft.

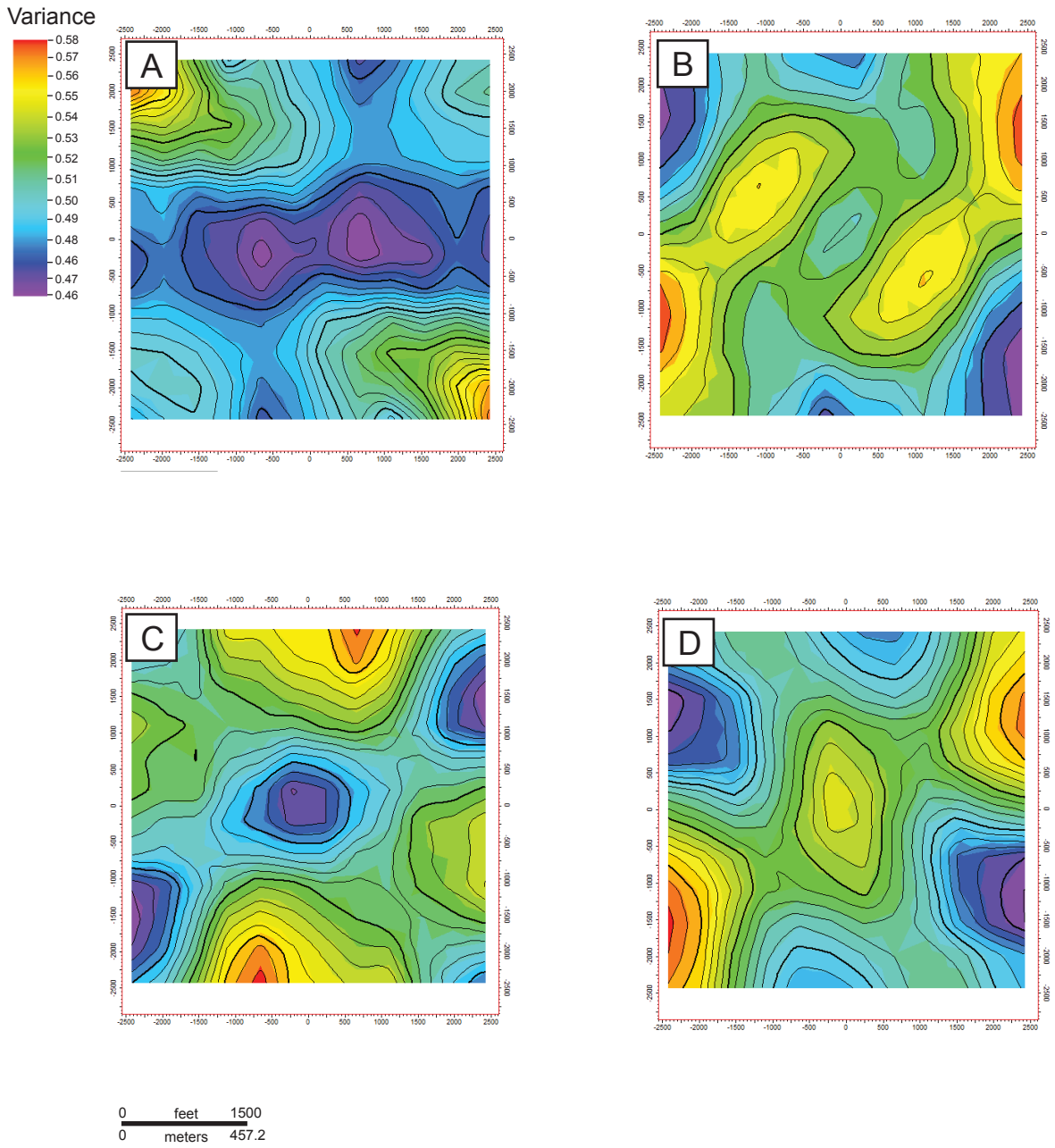

Variogram polar plots created for crevasse splay deposits and used in property modeling. A) Layer 190 to layer 197 (30 ft; assign value=1). B) Layer 197 to Flooding Surface (119 ft; azimuth of 30 degrees). C) Flooding surface to layer 250 (94 ft; azimuth of 65 degrees). D) Layer 250 to Coal F (48 ft; assign value=1;contour interval of 0.01). Contour interval of 0.005 ft.

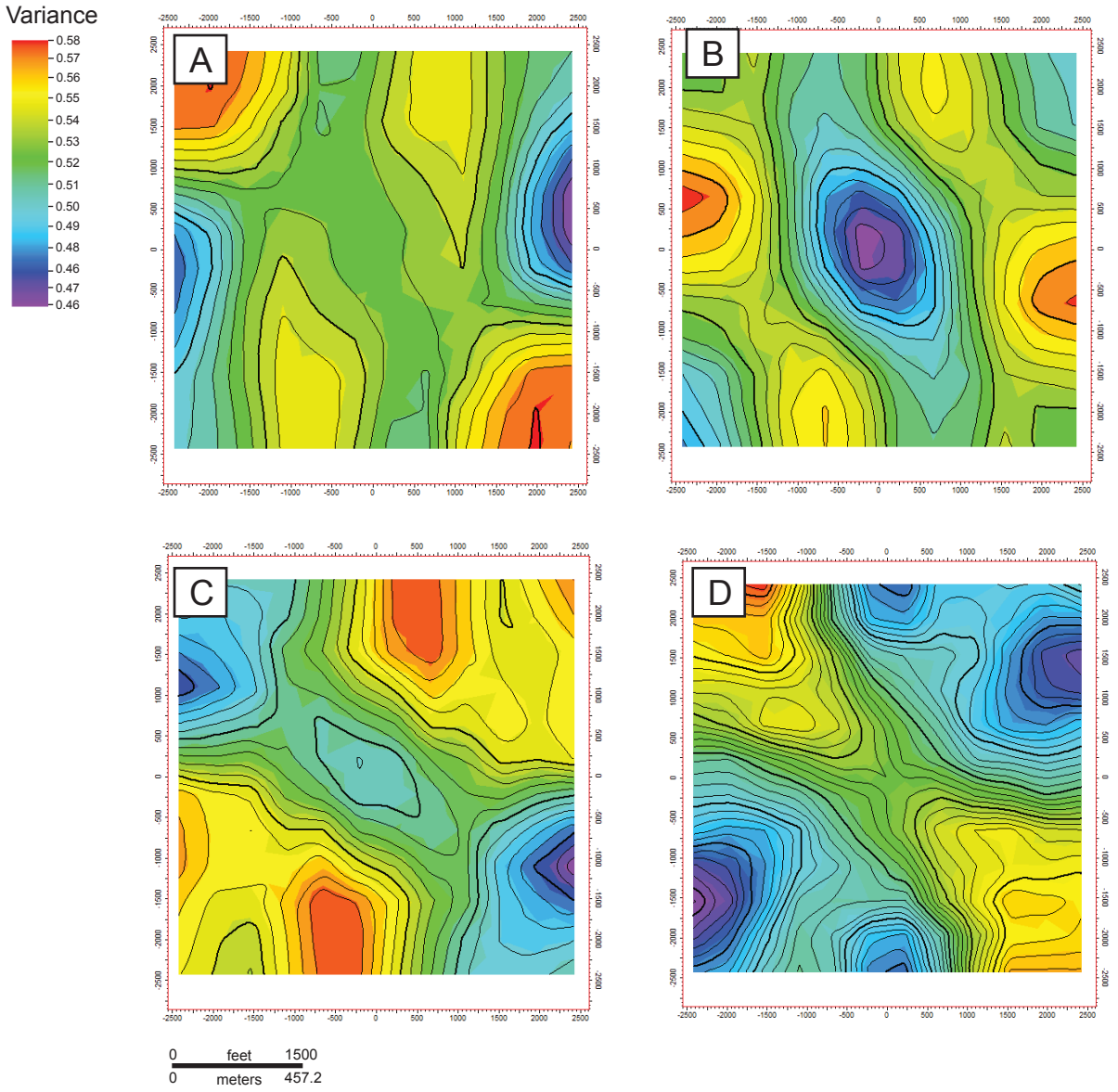

Variogram polar plots created for crevasse splay deposits and used in property modeling. A) Coal F to layer 276 (48 ft; contour interval of 0.01 ft; assign value=1). B) Layer 276 to Coal E (83 ft; contour interval of 0.005 ft; azimuth of -33 degrees). C) Coal E to Coal D (322 ft; contour interval of 0.005 ft; azimuth of 50 degrees). D) Coal D to l;ayer 322 (16 ft; contour interval of 0.01 ft; assign value=1).

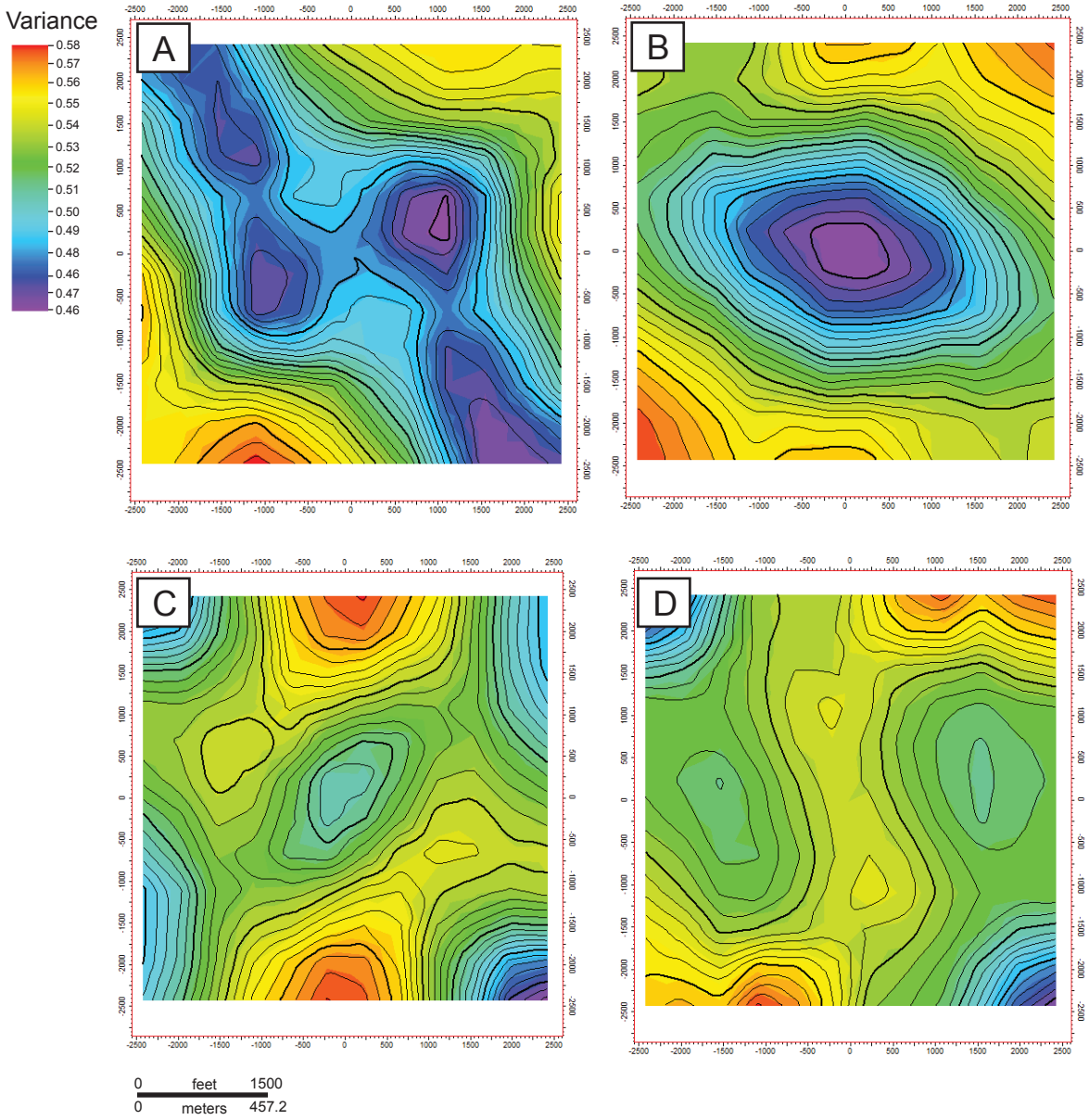

Variogram polar plots created for crevasse splay deposits and used in property modeling. A) Layer 322 to Coal B (60 ft; assign value=1). B) Coal B to Coal A5 (63 ft; azimuth of 89 degrees). C) Coal A5 to Coal A (60 ft; azimuth of -45 degrees). D) Coal A to Rollins Sandstone Member (39 ft; contour interval of 0.01; azimuth of -88 degrees). Contour interval of 0.005 ft.

Appendix I

Net-to-Gross Calculation

Appendix I contains results of the net-to-gross calculations for the three MPS modeled scenarios.

Statistical summary of net-to-gross percentage for partial mudstone-plug model

Stratigraphic Zone	Percent of Point Bars from Upscaled Logs	Percent of Crevasse Splays from Upscaled Logs	Percent of Floodplain from Upscaled Logs	Percent of Coal from Upscaled Logs	Percent of Mudstone Plugs From Upscaled Logs	Total Achitectural Elements	Total Reservoir*	Total Non-Reservoir**	Net-to-Gross Percentage
1	18.3%	4.5%	74.0%	0.0%	3.2%	100.0%	22.8%	77.2%	22.8%
2	31.8%	3.0%	61.0%	0.0%	4.2%	100.0%	34.8%	65.2%	34.8%
3	22.1%	2.5%	72.0%	0.0%	3.3%	100.0%	24.7%	75.3%	24.7%
4	23.6%	3.5%	69.0%	0.0%	3.8%	100.0%	27.2%	72.9%	27.2%
5	25.1%	3.2%	68.3%	0.0%	3.4%	100.0%	28.3%	71.8%	28.3%
6	12.4%	4.3%	80.7%	0.0%	2.6%	100.0%	16.7%	83.3%	16.7%
7	46.6%	1.5%	49.1%	0.0%	2.9%	100.0%	48.0%	52.0%	48.0%
8	34.2%	2.1%	60.2%	0.0%	3.5%	100.0%	36.3%	63.7%	36.3%
9	19.1%	3.5%	75.0%	0.0%	2.5%	100.0%	22.6%	77.4%	22.6%
10	25.1%	3.1%	68.9%	0.0%	2.9%	100.0%	28.2%	71.8%	28.2%
11	17.3%	3.8%	76.5%	0.0%	2.4%	100.0%	21.1%	78.9%	21.1%
12	12.3%	3.9%	81.6%	0.1%	2.2%	100.0%	16.2%	83.8%	16.2%
13	15.2%	3.4%	79.2%	0.1%	2.1%	100.0%	18.6%	81.4%	18.6%
14	44.7%	1.8%	48.0%	0.8%	4.8%	100.0%	46.5%	53.5%	46.5%
15	26.3%	2.7%	64.4%	2.7%	4.0%	100.0%	29.0%	71.1%	28.9%
16	4.3%	2.0%	64.8%	28.2%	0.6%	100.0%	6.4%	93.6%	6.4%
17	21.9%	3.1%	71.5%	0.6%	3.0%	100.0%	25.0%	75.0%	25.0%
18	28.2%	1.8%	52.6%	14.3%	3.2%	100.0%	29.9%	70.1%	29.9%
19	38.1%	1.6%	50.4%	4.9%	5.0%	100.0%	39.7%	60.3%	39.7%
20	10.3%	2.0%	56.6%	30.0%	1.1%	100.0%	12.3%	87.7%	12.3%

* Point bars and crevasse splays are considered to be reservoir architectural elements

** Floodplain, coal, and mudstone plugs considered to be non-reservoir architectural element

Net-to-gross ratio (%) for the partial-mudstone-plugs MPS model. Net-to-gross ratio is calculated as reservoir quality sandstone (point bars and crevasse splays) divided by the volume of the total rock volume and times 100.

Statistical summary of net-to-gross ratio (%) for the mudstone-plug MPS model

Stratigraphic Zone	Percent of Point Bars from Upscaled Logs	Percent of Crevasse Splays from Upscaled Logs	Percent of Floodplain from Upscaled Logs	Percent of Coal from Upscaled Logs	Percent of Mudstone Plugs From Upscaled Logs	Total Achitectural Elements	Total Reservoir*	Total Non-Reservoir**	Net-to-Gross Percentage
1	15.7%	4.5%	74.6%	0.0%	5.2%	100.0%	20.2%	79.9%	20.2%
2	27.4%	3.0%	61.5%	0.0%	8.1%	100.0%	30.4%	69.6%	30.4%
3	19.3%	2.5%	72.5%	0.0%	5.7%	100.0%	21.8%	78.2%	21.8%
4	20.7%	3.5%	69.5%	0.0%	6.2%	100.0%	24.2%	75.8%	24.2%
5	22.1%	3.2%	69.1%	0.0%	5.6%	100.0%	25.3%	74.7%	25.3%
6	11.4%	4.3%	80.6%	0.0%	3.6%	100.0%	15.7%	84.3%	15.7%
7	36.9%	1.5%	56.6%	0.0%	5.0%	100.0%	38.4%	61.6%	38.4%
8	30.2%	2.1%	61.5%	0.0%	6.1%	100.0%	32.4%	67.6%	32.4%
9	15.5%	3.5%	76.8%	0.0%	4.3%	100.0%	19.0%	81.0%	19.0%
10	21.1%	3.1%	70.5%	0.0%	5.2%	100.0%	24.3%	75.8%	24.2%
11	15.1%	3.8%	77.9%	0.0%	3.2%	100.0%	18.9%	81.1%	18.9%
12	10.4%	3.9%	82.3%	0.1%	3.3%	100.0%	14.3%	85.7%	14.3%
13	13.0%	3.4%	80.2%	0.1%	3.3%	100.0%	16.4%	83.6%	16.4%
14	37.7%	1.8%	51.4%	0.8%	8.4%	100.0%	39.4%	60.6%	39.4%
15	21.4%	2.7%	66.6%	2.7%	6.7%	100.0%	24.1%	75.9%	24.1%
16	3.3%	2.0%	65.3%	28.2%	1.2%	100.0%	5.3%	94.7%	5.3%
17	20.3%	3.1%	71.1%	0.6%	5.0%	100.0%	23.4%	76.6%	23.4%
18	22.8%	1.8%	55.2%	14.3%	5.9%	100.0%	24.6%	75.5%	24.6%
19	33.7%	1.6%	50.5%	4.9%	9.3%	100.0%	35.4%	64.7%	35.3%
20	8.6%	2.0%	57.0%	30.0%	2.5%	100.0%	10.6%	89.5%	10.6%

* Point bars and crevasse splays are considered to be reservoir architectural elements

** Floodplain, coal, and mudstone plugs considered to be non-reservoir architectural elements

Net-to-gross ratio (%) for the mudstone-plug MPS model. Net-to-gross ratio is calculated as reservoir quality sandstone (point bars and crevasse splays) divided by the volume of the total rock volume and times 100.

Statistical summary of net-to-gross ratio (%) for the string-of-beads MPS model

Stratigraphic Zone	Percent of Point Bars from Upscaled Logs	Percent of Crevasse Splays from Upscaled Logs	Percent of Floodplain from Upscaled Logs	Percent of Coal from Upscaled Logs	Percent of Mudstone Plugs From Upscaled Logs	Total Achitectural Elements	Total Reservoir*	Total Non-Reservoir**	Net-to-Gross Percentage
1	17.6%	4.5%	76.3%	0.0%	1.6%	100.0%	22.1%	77.9%	22.1%
2	32.4%	3.0%	63.6%	0.0%	1.0%	100.0%	35.5%	64.6%	35.5%
3	22.4%	2.5%	73.7%	0.0%	1.4%	100.0%	24.9%	75.1%	24.9%
4	24.5%	3.5%	70.6%	0.0%	1.4%	100.0%	28.0%	72.0%	28.0%
5	25.8%	3.2%	70.0%	0.0%	1.0%	100.0%	29.0%	71.1%	29.0%
6	12.7%	4.3%	81.6%	0.0%	1.5%	100.0%	17.0%	83.0%	17.0%
7	47.2%	1.5%	50.8%	0.0%	0.5%	100.0%	48.7%	51.3%	48.7%
8	34.5%	2.1%	62.2%	0.0%	1.3%	100.0%	36.6%	63.4%	36.6%
9	19.9%	3.5%	76.1%	0.0%	0.6%	100.0%	23.3%	76.7%	23.3%
10	25.1%	3.1%	70.7%	0.0%	1.2%	100.0%	28.2%	71.8%	28.2%
11	17.0%	3.8%	77.9%	0.0%	1.3%	100.0%	20.8%	79.3%	20.8%
12	11.7%	3.9%	83.2%	0.1%	1.1%	100.0%	15.6%	84.4%	15.6%
13	15.1%	3.4%	80.4%	0.1%	0.9%	100.0%	18.5%	81.5%	18.5%
14	45.9%	1.8%	50.5%	0.8%	1.1%	100.0%	47.7%	52.4%	47.6%
15	26.3%	2.7%	66.7%	2.7%	1.7%	100.0%	29.0%	71.0%	29.0%
16	3.6%	2.0%	65.8%	28.2%	0.4%	100.0%	5.6%	94.4%	5.6%
17	21.9%	3.1%	72.4%	0.6%	2.1%	100.0%	25.0%	75.0%	25.0%
18	29.7%	1.8%	53.7%	14.3%	0.5%	100.0%	31.4%	68.6%	31.4%
19	37.1%	1.6%	53.9%	4.9%	2.5%	100.0%	38.7%	61.3%	38.7%
20	10.2%	2.0%	57.5%	30.0%	0.3%	100.0%	12.2%	87.9%	12.1%

* Point bars and crevasse splays are considered to be reservoir architectural elements

** Floodplain, coal, and mudstone plugs considered to be non-reservoir architectural elements

Net-to-gross ratio (%) for the string-of-beads MPS model. Net-to-gross ratio is calculated as reservoir quality sandstone (point bars and crevasse splays) divided by the volume of the total rock volume and times 100.

Appendix J

Static Connectivity Calculation

Appendix J contains results of the static connectivity calculation for the three MPS modeled scenarios.

Statistical summary of three-dimensional static connectivity of sandstone bodies within the string-of-beads MPS model

Stratigraphic Zone	Sandstone Volume	Point Bar Volume Connected to Wells	Crevasse Splay Volume Connected to Wells	Sandstone Connected to Wells	Point-Bar Connectivity	Crevasse-Splay Connectivity	Sandstone Connectivity
1	6.48E+14	4.46E+14	76694800	6.05E+14	68.76%	0.00001183%	93.24%
2	1.27E+15	1.02E+15	53096400	1.22E+15	80.36%	0.00000420%	96.27%
3	7.33E+14	5.75E+14	50146600	7.04E+14	78.55%	0.00000685%	96.04%
4	2.47E+15	1.89E+15	168138600	2.38E+15	76.60%	0.00000680%	96.23%
5	2.74E+15	2.14E+15	91443800	2.63E+15	78.17%	0.00000334%	96.00%
6	9.99E+14	6.46E+14	76694800	9.27E+14	64.67%	0.00000767%	92.72%
7	1.64E+15	1.40E+15	23598400	1.59E+15	85.73%	0.00000144%	97.34%
8	1.07E+15	8.90E+14	32447800	1.03E+15	82.81%	0.00000302%	96.03%
9	3.43E+14	2.54E+14	20648600	3.18E+14	74.06%	0.00000603%	92.80%
10	1.77E+15	1.39E+15	67845400	1.70E+15	78.28%	0.00000382%	95.72%
11	1.00E+15	7.13E+14	44247000	9.35E+14	71.13%	0.00000441%	93.31%
12	4.59E+14	2.92E+14	61945800	4.09E+14	63.71%	0.00001350%	89.27%
13	4.66E+14	3.34E+14	26548200	4.32E+14	71.73%	0.00000570%	92.77%
14	2.10E+15	1.79E+15	67845400	2.04E+15	85.06%	0.00000323%	96.92%
15	1.28E+15	1.02E+15	53096400	1.21E+15	79.91%	0.00000416%	94.64%
16	4.74E+13	2.40E+13	5899600	3.08E+13	50.62%	0.00001246%	65.03%
17	7.86E+14	6.06E+14	56046200	7.42E+14	77.13%	0.00000713%	94.41%
18	1.06E+15	8.75E+14	50146600	1.01E+15	82.90%	0.00000475%	96.06%
19	1.22E+15	1.03E+15	67845400	1.17E+15	84.57%	0.00000556%	96.15%
20	2.55E+14	1.74E+14	386423800	2.24E+14	68.24%	0.00015154%	87.78%

Three-dimensional static connectivity of point bars, crevasse spalys, and total sandstone within the string-of-beads MPS model. Connectivity is calculated by dividing the volume of sandstone connected to wells within the model zone by the total volume of sandstone within the zone.

Statistical summary of three-dimensional static connectivity of sandstone bodies within the partial-mudstone-plugs MPS model

Stratigraphic Zone	Sandstone Volume	Point Bar Volume Connected to Wells	Crevasse Splay Volume Connected to Wells	Sandstone Connected to Wells	Point-Bar Connectivity	Crevasse-Splay Connectivity	Sandstone Connectivity
1	6.61E+14	4.41E+14	76694800	6.17E+14	66.63%	0.00000791%	93.20%
2	1.23E+15	9.73E+14	53096400	1.18E+15	79.17%	0.00000432%	95.74%
3	7.16E+14	5.45E+14	50146600	6.83E+14	76.03%	0.00000700%	95.41%
4	2.37E+15	1.77E+15	168138600	2.23E+15	74.62%	0.00000711%	94.41%
5	2.64E+15	2.00E+15	91443800	2.50E+15	75.73%	0.00000347%	94.78%
6	9.70E+14	5.89E+14	76694800	8.65E+14	60.74%	0.00000791%	89.20%
7	1.59E+15	1.34E+15	23598400	1.54E+15	84.30%	0.00000148%	96.62%
8	1.05E+15	8.62E+14	32447800	1.01E+15	81.73%	0.00000308%	95.84%
9	3.28E+14	2.30E+14	20648600	2.95E+14	70.22%	0.00000630%	89.86%
10	1.75E+15	1.34E+15	67845400	1.64E+15	76.50%	0.00000387%	93.76%
11	1.01E+15	7.08E+14	44247000	9.27E+14	70.33%	0.00000439%	92.00%
12	4.70E+14	2.87E+14	61945800	4.09E+14	61.07%	0.00001319%	87.17%
13	4.64E+14	3.20E+14	26548200	4.18E+14	69.10%	0.00000573%	90.21%
14	2.03E+15	1.70E+15	67845400	1.95E+15	83.99%	0.00000335%	96.28%
15	1.26E+15	9.86E+14	53096400	1.19E+15	78.16%	0.00000421%	94.16%
16	5.29E+13	2.34E+13	5899600	3.53E+13	44.25%	0.00001116%	66.82%
17	7.77E+14	5.81E+14	56046200	7.28E+14	74.73%	0.00000721%	93.61%
18	9.92E+14	8.01E+14	50146600	9.43E+14	80.66%	0.00000505%	95.06%
19	1.24E+15	1.03E+15	67845400	1.18E+15	83.08%	0.00000549%	95.57%
20	2.55E+14	1.73E+14	386423800	2.17E+14	67.88%	0.00015133%	85.0

Three-dimensional static connectivity of point bars, crevasse spalys, and total sandstone within the partial-mudstone-lug MPS model. Connectivity is calculated by dividing the volume of sandstone connected to wells within the model zone by the total volume of sandstone within the zone.

Statistical summary of three-dimensional static connectivity of sandstone bodies within the mudstone-plugs MPS model

Stratigraphic Zone	Sandstone Volume	Point Bar Volume Connected to Wells	Crevasse Splay Volume Connected to Wells	Sandstone Connected to Wells	Point-Bar Connectivity	Crevasse-Splay Connectivity	Sandstone Connectivity
1	5.12E+14	2.76E+14	76694800	4.41E+14	54.03%	0.00001499%	86.10%
2	9.37E+14	6.82E+14	53096400	8.72E+14	72.80%	0.00000567%	93.08%
3	5.53E+14	3.74E+14	50146600	5.07E+14	67.66%	0.00000906%	91.70%
4	1.85E+15	1.22E+15	168138600	1.70E+15	66.10%	0.00000911%	92.13%
5	2.07E+15	1.42E+15	91443800	1.89E+15	68.90%	0.00000442%	91.42%
6	7.99E+14	4.19E+14	76694800	6.80E+14	52.44%	0.00000959%	85.08%
7	1.11E+15	8.71E+14	23598400	1.05E+15	78.29%	0.00000212%	94.02%
8	8.22E+14	6.25E+14	32447800	7.71E+14	76.06%	0.00000395%	93.88%
9	2.41E+14	1.47E+14	20648600	2.05E+14	61.24%	0.00000857%	85.19%
10	1.32E+15	9.22E+14	67845400	1.20E+15	69.92%	0.00000514%	90.71%
11	7.88E+14	4.89E+14	44247000	7.01E+14	62.03%	0.00000562%	88.99%
12	3.63E+14	1.89E+14	61945800	3.01E+14	52.05%	0.00001709%	83.12%
13	3.58E+14	2.12E+14	26548200	3.13E+14	59.34%	0.00000742%	87.50%
14	1.50E+15	1.17E+15	67845400	1.40E+15	78.11%	0.00000452%	93.24%
15	9.17E+14	6.46E+14	53096400	8.28E+14	70.42%	0.00000579%	90.31%
16	3.87E+13	9.80E+12	5899600	1.62E+13	25.33%	0.00001525%	41.94%
17	6.36E+14	4.35E+14	56046200	5.75E+14	68.43%	0.00000882%	90.50%
18	7.12E+14	5.14E+14	50146600	6.44E+14	72.10%	0.00000704%	90.37%
19	9.62E+14	7.47E+14	67845400	8.95E+14	77.69%	0.00000706%	93.08%
20	1.91E+14	9.70E+13	386423800	1.57E+14	50.67%	0.00020193%	81

Three-dimensional static connectivity of point bars, crevasse spalys, and total sandstone within the mudstone-plug MPS model. Connectivity is calculated by dividing the volume of sandstone connected to wells within the model zone by the total volume of sandstone within the zone.

Appendix K

Net-to-Gross Ratio and Static Connectivity Results

Appendix K contains results of net-to-gross ratio and static connectivity calculation for the three MPS modeled scenarios.

Statistical summary of net-to-gross ratio (%) versus three-dimensional point-bar connectivity

Stratigraphic Zone	Net-to-Gross %			Point Bar Connectivity			Total Sandstone Connectivity		
	String-of-Beads	Mudstone-Plugs	Partial Mudstone-Plugs	String-of-Beads	Mudstone-Plugs	Partial Mudstone-Plugs	String of Beads	Partial Mudstone Plugs	Mudstone Plugs
1	22.07%	20.15%	22.78%	69.31%	54.03%	66.63%	93.24%	93.20%	86.10%
2	35.45%	30.38%	34.83%	80.99%	72.80%	79.17%	96.27%	95.74%	93.08%
3	24.93%	21.80%	24.66%	79.23%	67.66%	76.03%	96.04%	95.41%	91.70%
4	28.03%	24.24%	27.15%	77.24%	66.10%	74.62%	96.23%	94.41%	92.13%
5	28.95%	25.33%	28.25%	78.81%	68.90%	75.73%	96.00%	94.78%	91.42%
6	17.00%	15.74%	16.70%	65.16%	52.44%	60.74%	92.72%	89.20%	85.08%
7	48.72%	38.36%	48.04%	86.41%	78.29%	84.30%	97.34%	96.62%	94.02%
8	36.57%	32.36%	36.29%	83.52%	76.06%	81.73%	96.03%	95.84%	93.88%
9	23.32%	18.97%	22.57%	74.75%	61.24%	70.22%	92.80%	89.86%	85.19%
10	28.18%	24.24%	28.19%	78.94%	69.92%	76.50%	95.72%	93.76%	90.71%
11	20.75%	18.89%	21.11%	71.72%	62.03%	70.33%	93.31%	92.00%	88.99%
12	15.62%	14.28%	16.17%	64.21%	52.05%	61.07%	89.27%	87.17%	83.12%
13	18.50%	16.44%	18.62%	72.30%	59.34%	69.10%	92.77%	90.21%	87.50%
14	47.64%	39.44%	46.47%	85.73%	78.11%	83.99%	96.92%	96.28%	93.24%
15	28.97%	24.08%	28.94%	80.57%	70.42%	78.16%	94.64%	94.16%	90.31%
16	5.64%	5.33%	6.37%	51.06%	25.33%	44.25%	65.03%	66.82%	41.94%
17	24.97%	23.36%	24.98%	77.81%	68.43%	74.73%	94.41%	93.61%	90.50%
18	31.42%	24.55%	29.89%	83.59%	72.10%	80.66%	96.06%	95.06%	90.37%
19	38.73%	35.34%	39.69%	85.27%	77.69%	83.08%	96.15%	95.57%	93.08%
20	12.14%	10.55%	12.31%	68.84%	50.67%	67.88%	87.78%	85.03%	81.87%

A statistical summary of net-to-gross ratio and three-dimensional point-bar connectivity by stratigraphic zone.

Appendix L

Porosity and Permeability Data

Appendix L contains the porosity and permeability data used to create models used in the conceptual dynamic flow simulation.

Depth	Porosity (%)	Permeability	Core
5766.3	3.2	0.005	8-4 MV
5766.8	4.2	0.015	8-4 MV
5767.3	3.8	0.009	8-4 MV
5790.8	4.1	0.006	8-4 MV
5792.7	9.4	0.018	8-4 MV
5793.2	5.9	0.007	8-4 MV
5793.7	6.3	0.013	8-4 MV
5794.2	7.1	0.015	8-4 MV
5794.7	7	0.027	8-4 MV
5795.2	7.4	0.034	8-4 MV
5795.7	8	0.039	8-4 MV
5796.2	8.2	0.043	8-4 MV
5796.7	7.2	0.026	8-4 MV
5797.2	8.5	0.042	8-4 MV
5797.7	9.6	0.045	8-4 MV
5798.2	9.7	0.037	8-4 MV
5798.7	9.4	0.053	8-4 MV
5800	6.2	0.019	8-4 MV
5834	4.6	0.023	8-4 MV
5834.5	4.9	0.019	8-4 MV
5835	5.5	0.044	8-4 MV
5837.3	5.4	0.031	8-4 MV
5837.8	5.6	0.032	8-4 MV
5851	3.9	0.014	8-4 MV
5851.5	8	0.037	8-4 MV
5852	7.7	0.037	8-4 MV
5852.5	8.9	0.05	8-4 MV
5853	8.5	0.075	8-4 MV
5853.5	9.1	0.059	8-4 MV
5854	9.6	0.047	8-4 MV
5856.5	8.8	0.025	8-4 MV
5857	8.6	0.045	8-4 MV
5857.5	8.5	0.048	8-4 MV
5858	9	0.049	8-4 MV
5858.5	9.2	0.045	8-4 MV
6579-6580	10.5	0.07	MV 24-20 Chevron
6580-6581	8.3	0.04	MV 24-20 Chevron
6580.1	5.3	0.0077	MV 24-20 Chevron
6581-6582	9.8	0.05	MV 24-20 Chevron
6582-6583	8.9	0.05	MV 24-20 Chevron
6583-6584	10.1	0.05	MV 24-20 Chevron
6591.3	3.1	0.0085	MV 24-20 Chevron
6591.9	3.4	0.0037	MV 24-20 Chevron